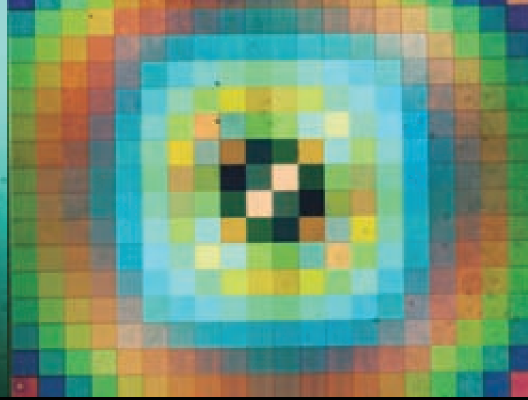

Fabrication of Soft X-ray Diffractive Lenses with Resolution in the Nanometer Range

PhD Thesis — December 2007

Joan Vilà Comamala

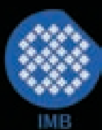

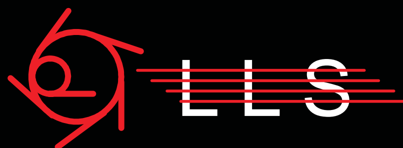

Universitat Autònoma de Barcelona

Fabrication of Soft X-ray Diffractive Lenses with Resolution in the Nanometer Range

Doctoral Dissertation submitted to the
Universitat Autònoma de Barcelona
in partial fulfilment of the requirements of
the degree of Doctor of Philosophy in Applied Physics

by

Joan Vilà Comamala
Laboratori de Llum Sincrotró

under the supervision of

Dr. Salvador Ferrer Fàbregas
CELLS
ALBA Font de Llum Sincrotró

Dr. Juan Campos Coloma
Departament de Física
Universitat Autònoma de Barcelona

Dr. Xavier Borrisé Nogué
Instituto de Microelectrónica de Barcelona
Centro Nacional de Microelectrónica

December 2007

This work was partly funded by EU project “Integrating Activity on Synchrotron and Free Electron Laser Science Contract under the contract Nr. RII3-CT-2004-506008 part JRA3”, by “Departament d’Educació i Universitats de la Generalitat de Catalunya i del Fons Social Europeu” and by “Ministerio de Ciencia y Tecnología (FIS2006-13037-C02-01)”.

Als meus pares
que sempre han estat al meu costat.

To my parents
that have always been by my side.

Contents

Preface **9**

1 Introduction **11**

1.1 X-rays and Synchrotron Radiation 12

1.2 X-ray Microscopy 14

1.3 Soft X-ray Microscopy Beamline at ALBA Synchrotron 15

1.4 Micro- and Nanofabrication 17

1.5 Motivation, Framework, Objectives and Scheme of this Report 19

I Theoretical Issues **21**

2 X-ray Focusing and Soft X-ray Microscopy **23**

2.1 X-ray Interaction with Matter 23

2.2 X-ray Focusing Elements 29

2.3 Soft X-ray Microscopy 31

2.3.1 Full-field Transmission X-ray Microscopy (TXM) 33

2.3.2 Scanning Transmission X-ray Microscopy (STXM) 33

2.4 Fresnel Zone Plates and Diffractive Optical Elements 34

3 Fresnel Zone Plate Theory **35**

3.1 Fresnel Zone Plate Basics 35

3.1.1 Fundamental Parameters for a Fresnel Zone Plate 38

3.1.2 Fresnel Zone Plate Diffraction Efficiency 44

3.1.3 Materials for a Soft X-ray Fresnel Zone Plate 45

3.2 Zone-Doubling Technique for Ultrahigh Resolution 49

3.3 Design of a Beamshaping Condenser Lens 55

II Nanofabrication Methods and Results **59**

4 Electron Beam Lithography **61**

4.1 Introduction to Electron Beam Lithography 61

4.1.1 LEO 1530 SEM RAITH ELPHY PLUS System 63

4.1.2 Leica LION LV-1 E-Beam Lithography System 64

4.2 Electron Beam Lithography Exposure 65

4.2.1 Resist Layer Preparation 66

4.2.2 Fresnel Zone Plate Exposure Strategies 67

4.2.2.1 LEO 1530 SEM RAITH ELPHY PLUS System 67

4.2.2.2 Leica LION LV-1 E-Beam Lithography System 69

4.3 E-beam Exposure Results 73

4.3.1 LEO 1530 SEM RAITH ELPHY PLUS System 73

4.3.2 Leica LION LV-1 E-Beam Lithography System 74

5 Nickel Fresnel Zone Plates **77**

5.1 Nickel Evaporation and Resist Lift-off 77

5.2 Nickel Electroplating using a PMMA Mold 81

5.3 Nickel Electroplating using a Polyimide Mold 83

5.3.1 Substrate Preparation 83

5.3.2 Polyimide Reactive Ion Etching 85

5.3.3 Nickel Electroplating Deposition 86

6 Silicon Fresnel Zone Plates **91**

6.1 Fresnel Zone Plates made of a Silicon Single Crystal Substrate 92

6.2 Silicon Fresnel Zone Plate Fabrication 94

6.2.1 Silicon Membrane Fabrication 95

6.2.2 E-beam Lithography and Chromium Reactive Ion Etching 98

6.2.3 Silicon Reactive Ion Etching 101

6.3 Silicon Fresnel Zone Plate Characterization 105

6.3.1 Silicon Fresnel Zone Plate 105

6.3.2 Silicon Beamshaping Condenser Lens 109

6.3.3 Full-Field Transmission X-ray Microscopy (TXM) 112

6.3.4 Scanning Transmission X-ray Microscopy (STXM) 116

7 Iridium-Silicon Fresnel Zone Plates **127**

7.1 Iridium-Silicon Fresnel Zone Plate Fabrication 128

7.2 Iridium-Silicon Fresnel Zone Plate Characterization 133

7.2.1 Iridium-Silicon Fresnel Zone Plate 133

7.2.2 Scanning Transmission X-ray Microscopy (STXM) 135

7.2.2.1 15 nm Outermost Zone Width Ir-Si Fresnel Zone Plate 136

7.2.2.2 20 nm Outermost Zone Width Ir-Si Fresnel Zone Plate 140

Conclusions and Outlook **149**

Acknowledgements **151**

Bibliography **153**

Preface

During the last decades, the construction of electron storage rings exclusively dedicated to the production of *synchrotron radiation* has been a key reason to explain the large development of *x-ray optics*. New optical elements are required for an optimal exploitation of the properties of this *light*, which can be used to find out the secrets of matter and to reveal the microscopic world. The use of synchrotron light as a *probe* has made possible a large quantity of experiments to expand the knowledge in many scientific areas. Little by little, synchrotron radiation sources have become an indispensable tool for the research of lots of scientists, who work in very different disciplines such as biology, chemistry, physics, material science or even archaeology.

X-ray microscopy has emerged as a technique to observe structures which are not accessible with conventional optical microscopy, and that has advantages in respect to electron microscopy due to the longer penetration depth and chemical sensitivity of the x-ray radiation. The optics of the x-ray microscopes includes components such as the Fresnel zone plate lenses which are made by means of microfabrication techniques.

Within this work, Fresnel zone plate lenses were produced using different approaches and they have been tested in several Synchrotron Light Sources. We will describe in detail the micro- and nanofabrication techniques that are necessary for the production of such elements, from the electron beam lithography to the pattern transfer into different materials. In particular, we will present lenses for soft x-rays made of silicon. We show that they perform well at the current light sources and we think that due to their robustness they will also be suitable for the 4th generation x-ray sources. We also prepared a diffractive optical element which produces a square flat top illumination spot, and that can be used as a condenser lens in full-field transmission x-ray microscopy. Finally, we will also demonstrate a novel fabrication method which can push the ultimate spatial resolution of x-ray diffractive lenses. Fresnel zone plates with an outermost zone width of 20 nm have been fabricated and 15 nm lines have been clearly resolved in scanning transmission x-ray microscopy.

This work has been carried out in the *Laboratori de Llum Sincrotró* in Barcelona, with the participation of the *Centro Nacional de Microelectrónica de Barcelona (CSIC - CNM)* and the *Grup d'Òptica del Departament de Física de la Universitat Autònoma de Barcelona*. At the same time, essential parts of this work have been done in close collaboration with Dr. C. David and Dr. K. Jefimovs from the *Labor für Mikro- und Nanotechnologie* at the *Paul Scherrer Institut* in Villigen (Switzerland).

CHAPTER 1

Introduction

Since the Ancient Times, human beings have been making efforts to comprehend the world around them and to give explanation to the phenomena that occur by their side. In this chore to understand the world, which *science* has systematized, *observation* is the first essential step. This is the reason why mankind has, slowly but surely, endowed themselves with more and more sophisticated tools to overcome the limitations of their own biological senses. Optical microscopes and telescopes are obvious instances of such tools. In both instruments, *light*, which comes from the observed object, is collected and manipulated to make the observation possible. At this point, it is important to notice the essential difference between the *instrument* (our eye or tool plus our eye) and the *probe* (light) which interacts with the object under observation. According to this dichotomy, to enlarge our observational scope we can improve either the instrument capabilities or the probe properties. The first endeavours to find out the world that is not directly visible with our own eyes were mainly concerned about the instruments (for instance, lens cutting and polishing were gradually improved).

Light has always been a natural and powerful probe. At the present time, the resolution and the magnification achieved by optical devices are really so good that the only limitation comes from the fact that light has a non-zero wavelength. When an object is illuminated only structures which are comparable or bigger than the wavelength of the light can be resolved. We are in *the diffraction limit*, which arises from the fundamental nature of light. As a matter of fact, features with a size half of the wavelength can be distinguished and so, the smallest details that optical microscopy can resolve are around 250 nm. To observe smaller sized object we should use other kinds of probes with a wavelength smaller than the one of the ordinary visible light. Electrons [1, 2], neutrons [3] or x-rays [4] are three candidates as alternative probes for matter. Electron

microscopes are widely used everyday in many laboratories and few neutron sources are also available to probe the matter all around the world. Advantages and disadvantages of these three kinds of radiation will be shortly discussed in the next sections. However, in this work we are interested in x-rays, especially in the ones which are produced in Synchrotron Radiation Facilities, and x-ray microscopy. We are concerned about the design, fabrication and characterization of Fresnel zone plates lenses and diffractive optical elements, which are essential optical elements in x-ray microscopes.

1.1 X-rays and Synchrotron Radiation

X-rays were discovered by W. C. Röntgen in 1895. Despite their nature was unknown for a while, it was clear from the very beginning that they could be used to observe structures inside thick samples, due to their small attenuation in materials and negligible scattering. Since that time it has been shown that they are electromagnetic radiation with a very short wavelength, from 10 to 0.01 nm, and that they are an excellent probe to find out the secrets of matter structure. For instance, the x-ray utilization was crucial to unravel the complexities of the DNA molecule, and nowadays, they are used to establish the protein structure [5], which finally determines its functionality in living tissues. X-rays have also been decisive to verify the structure of the inorganic compounds and so, to give experimental evidences to the theories developed by crystallography and by the more modern material sciences [6]. Even confectioner industry takes benefit from x-rays and uses synchrotron radiation to design new methods for the production high-quality chocolate [7].

A synchrotron radiation facility is basically a circular particle accelerator ring where a beam of electrons is accelerated up to relativistic speeds. According to the classical electrodynamics theory, it is well-established that when a particle with electric charge is being accelerated (in this case, to turn at the curved sections), it radiates electromagnetic waves, i.e. it emits energy. In the storage ring of a synchrotron radiation facility, since the charged particles are moving at relativistic velocities, this emission is quite particular. The radiation is concentrated in a narrow cone around the tangential direction to the particle trajectory.

Synchrotron radiation may have a *wide spectral range* which runs continuously from the infrared to the hard x-rays and the achieved intensity and brilliance (density of photons in phase space) is truly high. This is especially interesting in the x-ray spectral range, since there is not any other conventional source which offers the same features (at lower energies, lasers and other sources give the same or better capabilities). Besides, *polarization* (linear in the plane of the electron orbit and circular above and beneath this plane) and *temporal structure* (owing to fact that the beam is not continuous but bunched) are two additional characteristics of the radiation emitted by the electrons going around the storage ring. One last point is to realize that the electron beam smallness leads to a very tiny size source and that, due to the relativistic effects in the emission, the divergence of the emitted light is also very small. Indeed, the beam

cross-section is less than 1 mm^2 at several tens of meters away from the emission point. Nowadays not only the radiation emitted in the curved sections of the storage ring is harnessed but some extra radiation is obtained in its straight sections. This additional emission is generated when the electron beam goes through a lattice of little magnets, referred as *insertion devices*, where it is forced to execute small-amplitude oscillations.

All these characteristics turn synchrotron light into an exceptional probe, which is used for lots of scientists as a fundamental tool for their research in many different disciplines (biology [8], chemistry [9], magnetism [10], archaeology [11]...). Without synchrotron radiation sources many experiments could not be attainable, since the intensity in conventional laboratory sources is too low. Nevertheless, there are only a very limited amount of cases where the raw synchrotron light beam emanating from the storage ring can be directly used to illuminate the sample under study. Certainly, some devices, which are usually referred as optical elements, are always necessary to manipulate the radiation before it impinges on the sample. The set composed by these optical elements, the sample and the radiation detector is the so-called beamline. As a whole, they form the experimental station which is dedicated to a very concrete type of scientific research. The details in each beamline vary considerably depending in the particular experimental requirements. In every synchrotron a large quantity of different beamlines can be installed, around 35 for a typical medium-sized facility. The scheme of a synchrotron radiation source and beamline are shown in figure 1.1.

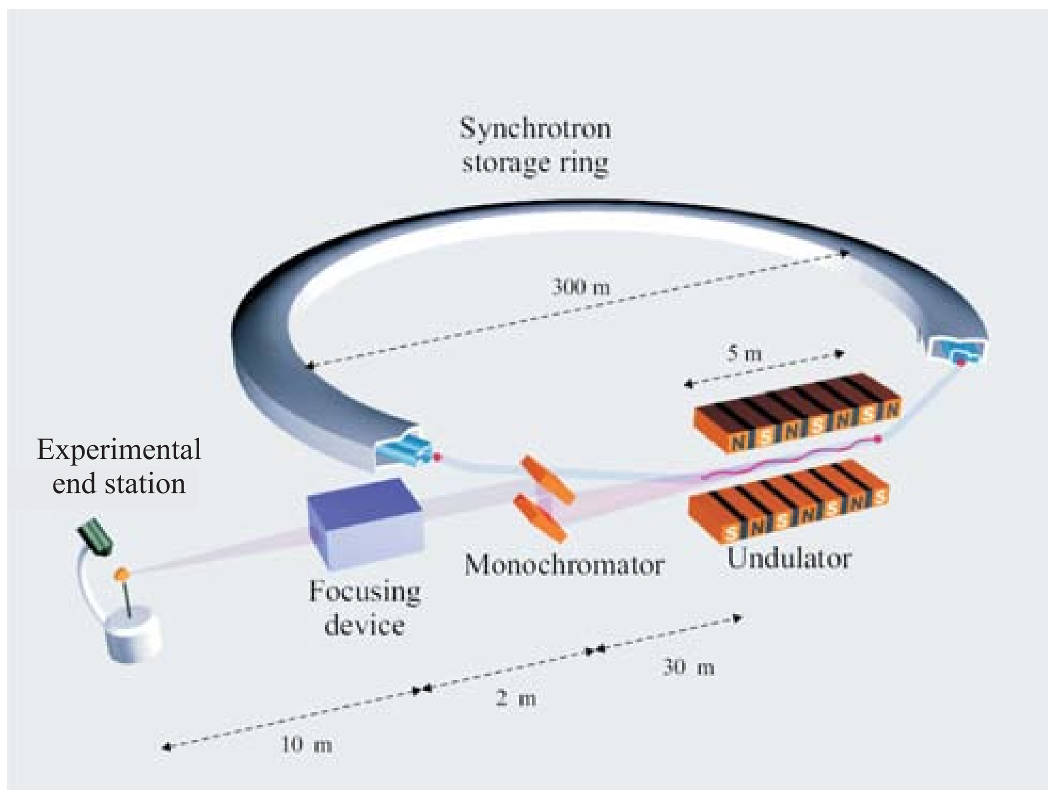

Figure 1.1: Scheme of an x-ray beamline at a synchrotron radiation facility, extracted from *Als-Nielsen* & *McMorrow* [12].

Synchrotron radiation sources have evolved through three different generations [13]. 1st generation storage rings were originally built for high energy physics research and the use of synchrotron radiation was completely subsidiary. 2nd generation storage rings are those designed and constructed to be exploited as light sources. 3rd generation light sources, the newest ones, have many straights sections for insertion devices and lower electron beam emittance to increase the brilliance and intensity of x-ray beam. 4th generation light sources, known as Free Electron Lasers (FEL), have been already devised. They will consist of a long linear accelerator followed by a long insertion device, and the electrons will emit highly coherent x-ray radiation as in a conventional visible laser. Several FEL sources are under design and construction and they will be quite demanding on the optical devices due to their extremely intense x-ray radiation beam [14].

1.2 X-ray Microscopy

Since the discovery of x-rays, it was clear they could be an extremely useful tool for imaging. However, the impossibility of using conventional optics was also obvious from the very beginning. Without appropriate focusing devices, x-ray microscopy remained as a speculative subject for more than half a century until the pioneering developments by *P. Kirkpatrick* & *A. Baez* in 1948, using reflective optics at grazing incidence [15]. Since that time, x-ray microscopy has been considered as a promising technique, because in terms of specimen size and resolution, it should fill the gap between electron and light microscopy, and thus be well-suited to image extremely large and complex structures. X-ray microscopy relies on a combination of resolution, penetrating power and analytical sensitivity, compatibility with wet specimens and the ease of image interpretation. However, its development involved so many complexities that it has been only during the last decades that the technique has been consolidated. A complete review on x-ray microscopy can be found in *Sayre* & *Chapman* [16].

X-ray microscopy is commonly performed in synchrotron radiation facilities, despite there are efforts to build x-ray microscopes based on table-top sources [17]. X-ray microscopy has several advantages over optical, electron and neutron microscopy. In one hand, due to the smaller wavelength, the ultimate resolution for x-ray microscopes should be almost two orders of magnitude below the achieved resolution by visible microscopy. On the other hand, due to the high penetrating power, x-ray microscopy is able to obtain information from thick samples demanding little or no specimen preparation, which is a cumbersome must in electron microscopy. This is extremely exciting when considering biological specimens which could be almost observed in their original environment. In relation to neutron microscopy [20], despite this technique is sharing most of the advantages of x-ray microscopy and could become a respectable competitor in the future, it is currently limited by the lack of sufficiently bright sources. As particular examples, x-ray microscopy can be used for the high resolution protein localization [18] and for x-ray imaging of plants and fungi [19]. In addition and due to the feasible energy tun-

ing, x-rays microscopes can be used to observe local chemical composition and binding states.

Several types of x-ray microscopy arrangements can be used depending on the energy of the x-ray beam, the specific setup and the nature of the detected signal. They are the scanning transmission x-ray microscope, the scanning photoemission microprobe, the scanning x-ray fluorescence microprobe, the photoemission electron microscope and the full-field transmission x-ray microscope. Focusing devices are needed in all these setups and Fresnel zone plates are one of the best choices. It will be shown in the next chapters that the spatial resolution achieved in x-ray microscopy depends on the performance of optical elements and that the optimization in the design and fabrication of Fresnel zone plates and diffractive optical elements can provide enhanced performance to x-ray microscopes.

In the recent years, a new imaging technique, commonly referred as coherent diffractive imaging, is under development to extend the methodology of x-ray crystallography and to enable imaging of micrometer-sized non-crystalline samples [21]. In this approach the crystallographic phase problem, i.e. the usually inevitable loss of phase information in the diffraction intensity, is overcome by oversampling the diffraction pattern and the image is obtained using an iterative phase retrieval algorithm [22, 23]. *A priori*, these techniques do not require any high-resolution x-ray optical elements, but it has been recently shown that the use of a curved beam illumination produced by means of a Fresnel zone plate provides some striking benefits [24].

1.3 Soft X-ray Microscopy Beamline at ALBA Synchrotron

ALBA is the new electron storage ring under construction near Barcelona. This facility will cover the requirements of the Spanish synchrotron radiation users and it will also be opened wide to the international research groups. ALBA facility has been conceived as a 3rd generation light source, with a storage ring full of straight sections to accommodate a large amount of insertion devices. A 400 mA electron beam will be accelerated up to energy of 3.0 GeV. The circumference will be around 268 m long, and owing to the lattice design (the array of magnets installed along the perimeter) the achieved horizontal emittance will be truly small (4.3 nm·rad). ALBA synchrotron is devised to cover a photon energy range up to 30 keV, despite the installation of special insertion devices (superconducting wiggler) could push this limit to 80 keV. The bending magnets (BM) that keep the electron beam in the orbit are producing a magnetic field of 1.42 T, and they deliver x-ray radiation with a critical energy[1], E_c, of 8.5 keV. Main ALBA machine and bending magnet parameters are summarized in table 1.1. Despite being beyond of this report, they determine the major characteristics of the light source and they

[1]By definition half of the photon flux is emitted above the critical energy while the other half is emitted below. Roughly, the useful photon flux extends up to maximum energy of $2 \cdot E_c$, thus, 17 keV in ALBA bending magnets.

establish the primary limitations on the experiments that can be done using synchrotron radiation.

Parameter	Symbol	Unit	Value
Circumference	C	m	268.8
Electron Energy	E	GeV	3.0
BM Magnetic Field	B	T	1.42
BM Critical Energy	E_c	keV	8.5
BM Horizontal Source Size	S_x	μm	133.3
BM Vertical Source Size	S_y	μm	76.4

Table 1.1: Some ALBA storage ring parameters [25, 26].

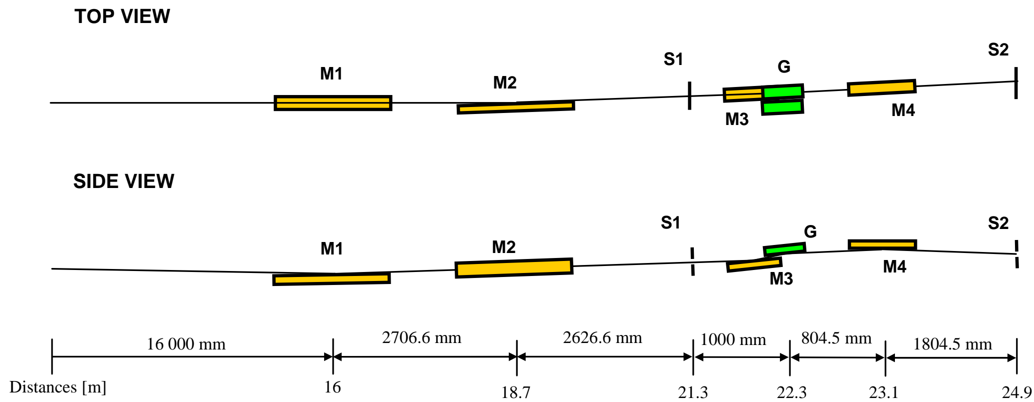

Figure 1.2: Optical layout of the full-field transmission x-ray microscopy beamline at ALBA synchrotron radiation facility [26].

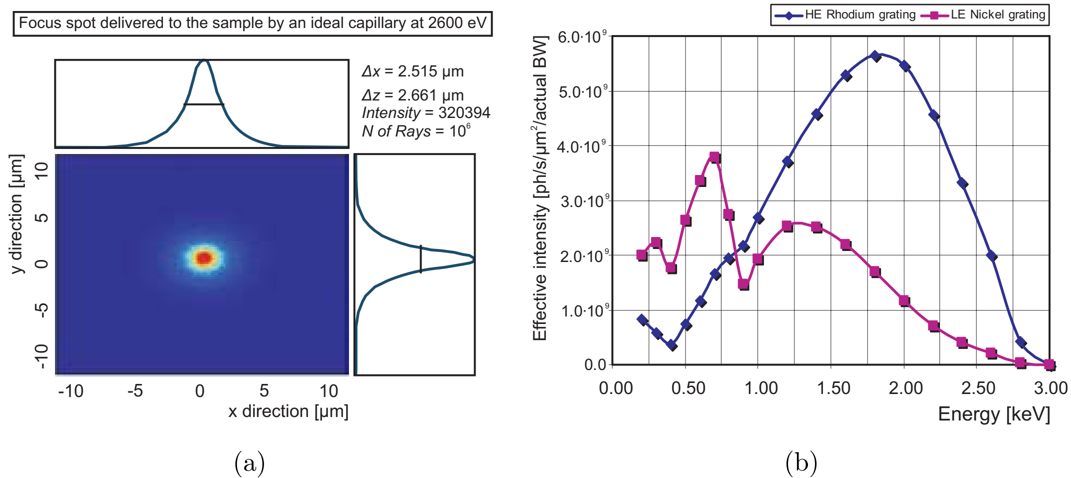

Figure 1.3: (a) Focus spot size delivered to illuminate the sample at 2600 eV. (b) Photon flux at the sample as function of the energy for both nickel and rhodium grating monochromators [26].

A full-field transmission x-ray microscope operating at soft x-ray regime specialized in imaging *thick biological specimens* from 275 eV to 3.0 keV at cryo-temperatures is foreseen to be installed in ALBA facility. The optical design of the microscopy beamline at ALBA has been done with the following goals: *i)* Water window for carbon imaging, to acquire tomographic data sets with 30 nm spatial resolution in a short period of time. *ii)* Higher photon energies for accessing K and L shells of light elements (Fe, Co, Ni, Cu, Zn...). *iii)* Energy resolution to perform spectroscopic imaging.

The wide range in energies offers several possibilities. In one hand, in the range of energies between the carbon (284 eV) and the oxygen (543 eV) absorption edges, which is usually referred as *water window*, the organic materials show strong absorption contrast between the cellular structures which are rich in carbon and the intracellular aqueous medium which is highly transmissive. On the other hand, higher energies allow the possibility to reach several interesting edges for biological, environmental and material science applications as well as to image thicker biological samples by means of phase contrast (1.5 — 3.0 keV). In addition, at higher energies the focal length and the depth of focus of the Fresnel zone plate lenses are significantly larger and this is an advantage to provide room to rotate the sample for the acquisition of tomographic data. A very important characteristic of the optical design is the possibility of obtaining energy resolved images thanks to the monochromator placed before the microscope. This will allow a fast energy tuning to record images with chemical binding state sensitivity.

The optical layout, shown in figure 1.2, is based on varied line spacing plane grating monochromator (VLS PGM) that will deliver monochromatic light to an elliptical hollow glass capillary, which will be used as a condenser to deliver light on the sample. Two interchangeable gratings for low and high energies respectively made of nickel and rhodium will be available. The simulated focal spot size and intensity to illuminate the sample produced by the capillary condenser is shown in figure 1.3. Upstream several mirror systems will prepare the radiation beam before it enters into the grating monochromator. After the sample, the transmitted radiation will be collected by an objective Fresnel zone plate and a magnified image of the sample will be projected on the active area of a soft x-ray CCD detector. As extensively discussed in next chapters, the spatial resolution of the microscope, that is the smallest details that can be distinguished in the sample, is limited by the quality of the objective Fresnel zone plate.

Despite some Fresnel zone plates will be delivered by the microscope suppliers, in-house fabrication of these optical elements would be advantageous since their commercial availability is very limited and costly[2].

1.4 Micro- and Nanofabrication

One of the main topics of this report deals with the technological fabrication requirements to produce Fresnel zone plate lenses. A scheme of a Fresnel zone plate is given in

[2]In addition, lifetime of Fresnel zone plate can be rather short (typically < 1 year), and they are indispensable for the operation of the x-ray microscope.

figure 1.4, they are circular diffractive transmission gratings with a radially increasing line density. The outermost zone width determines the ultimate resolution that can be reached by the x-ray microscope, and should therefore be as small as possible. Since the wavelength of the x-rays is below 10 nm, the structures that can diffract this radiation must have dimensions of the same other of magnitude. Typical Fresnel zone plate diameters, D, range from 50 to 500 μm, while common outermost zone widths, Δr, vary from 500 down to 30 nm. In addition, these structures must be located on a thin support membrane to yield sufficient transmission of the incoming x-ray beam.

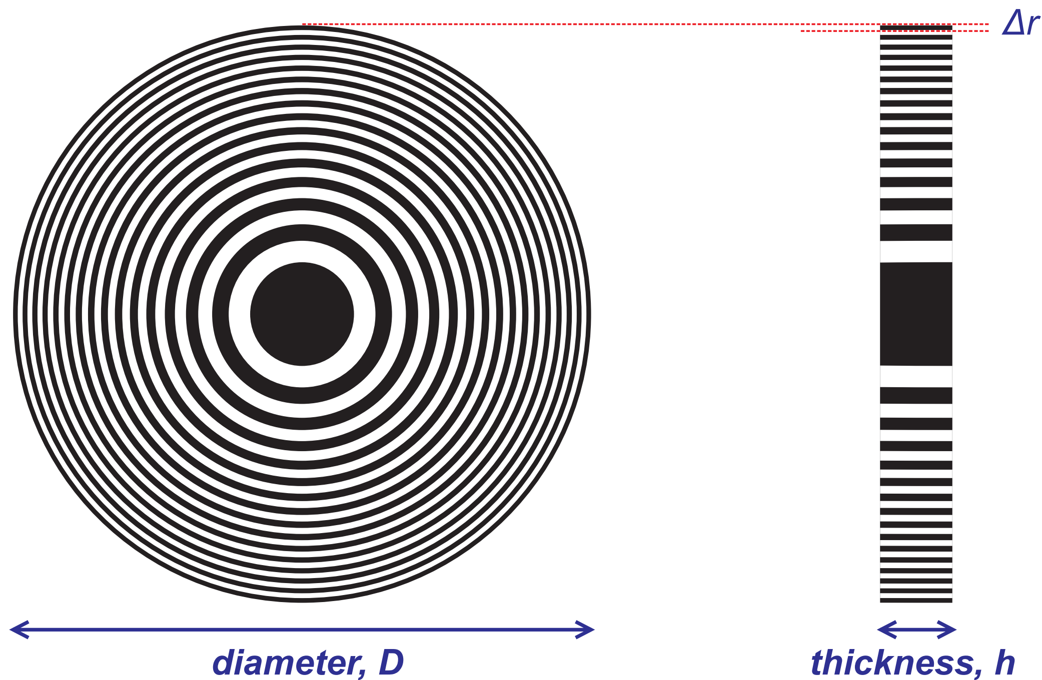

Figure 1.4: Scheme of a Fresnel zone plate lens.

In fact, the impossibility of producing such structures delayed for a long time the development of x-ray microscopy. So, special fabrication methods are required and micro- and nanofabrication technology becomes indispensable. Microfabrication has been developing during the last 40 years because of miniaturisation in electronics. Thin film deposition, optical and electron beam lithography and pattern transfer etching processes among other ordinary techniques in microelectronics fabrication must be adapted, combined and optimized for the fabrication of Fresnel zone plate lenses. Later in this report we will describe the most suitable techniques, and explain in detail the processes and the parameters that were used for the fabrication of the structures. We will compare several techniques and point out the advantages and drawbacks of each one. A complete introduction to nanotechnology can be found in *Ziaie et al.* [27].

1.5 Motivation, Framework, Objectives and Scheme of this Report

As we mentioned before, the fabrication of Fresnel zone plate lenses and diffractive optical elements is essential for x-ray microscopy and quite challenging from the technological point of view. Fresnel zone plate lenses are fabricated by a few research groups all around the world and they are commercially available only at a high cost. In the *Laboratori de Llum Sincrotró*, which is involved in the design and construction of ALBA synchrotron light source, a project was started to develop the technology for the manufacture of Fresnel zone plates in collaboration with the *Centro Nacional de Microelectrónica de Barcelona (CSIC - CNM)* and the *Grup d'Òptica del Departament de Física de la Universitat Autònoma de Barcelona*. Thus, developing the knowledge and technology for the in-house fabrication of Fresnel zone plate lenses has been a primary motivation for the work presented in this report.

An essential part of the results have been obtained in collaboration with Dr. C. David and Dr. K. Jefimovs from the *Labor für Mikro- und Nanotechnologie* at the *Paul Scherrer Institut* in Switzerland.

This report is divided in two parts. In the first part, an introduction to x-ray interaction with matter and x-ray microscopy is given (not going into much detail but suggesting some suitable references). There is also an introduction to theory that describes Fresnel zone plate lenses and some relevant calculations for the subsequent chapters that are presenting the experimental work.

In the second part we describe the fabrication techniques that have been used in the laboratory to produce the optical elements. We describe in detail some problems that had to be overcome during the fabrication of the elements, and taking into account that the solutions had to be compatible with the other steps involved in the fabrication process. In addition, in this second part the fabricated structures are shown and the experimental works done at the synchrotron light sources to check their performance are described. It will be shown that the main goals have been achieved, despite there is always room for improvement.

Part I

Theoretical Issues

CHAPTER 2

Basic Concepts in X-ray Focusing and Soft X-ray Microscopy

In this chapter, we briefly discuss the basic concepts involved in x-ray focusing and soft x-ray microscopy. Some fundamentals of x-ray interaction with matter are shortly reviewed, since they will be used later in chapter 3 to obtain the focusing efficiencies of the Fresnel zone plate lenses. Then, we give a short overview of the existing focusing devices comparing their potentialities, performance and state of art.

Later, we give some more details about soft x-ray microscopy, showing that this technique is particularly suitable for imaging biological samples at high resolution. The common x-ray microscopes layouts are described in detail pointing out the requirements on the focusing elements.

In the last section of the chapter there is a short discussion on Fresnel zone plates and diffractive optical elements.

2.1 X-ray Interaction with Matter

X-rays are electromagnetic radiation, i.e. electromagnetic waves or photons, with wavelengths in the nanometer and angstrom scale, from 10 to 0.01 nm. Thus, they have the same nature that radiowaves and light but they have a much shorter wavelengths or complementary, a much higher photon energy. A numerical equation, in suitable units, relating the photon energy and the wavelength is given by

$$\boxed{\lambda[\text{nm}] = \frac{hc}{E} = \frac{1239.8 \text{ eV}\cdot\text{nm}}{E[\text{eV}]}} \tag{2.1}$$

Following quantum mechanical approach, x-rays can be described either as waves or photons depending on the particular phenomena under study. Clearly, latter expression give us the connection between the two descriptions. In addition, this numerical relationship is very useful from the practical point of view. Figure 2.1 exposes that part of the electromagnetic spectrum extending from the infrared to the x-ray region. Principal spectral regions shown are the infrared, which is associated with heat and molecular resonances; the visible region from red to violet, which is perceived by human eye; the ultraviolet (UV), which we associate with sunburn and ionizing radiation, and finally the x-rays, in which we are interested in this report. Numerical values for photon energy and wavelength of these electromagnetic spectrum regions are shortly listed in table 2.1.

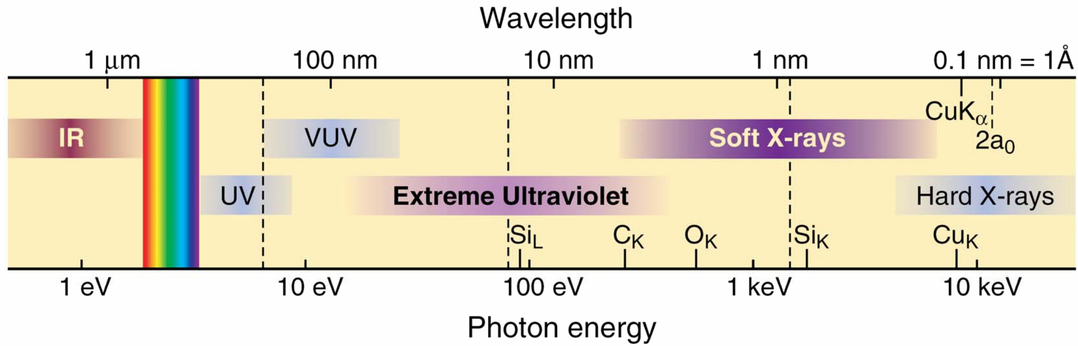

Figure 2.1: Electromagnetic spectrum from the infrared to the hard x-rays, extracted from *Attwood* [28].

The region between ultraviolet and soft x-ray radiation has been the last to be exploited since there are a large amount of atomic resonances which lead to absorption in very short distances, typically measured in micro- or nanometers. That is the reason why the experimental setups of soft x-ray microscopes must be in vacuum, which is a liability in terms of beamline complexity when comparing to hard x-ray microscopes.

Spectral Region	Energy Range [eV]	Wavelength Range [nm]
Infrared	$\sim$1	$\sim$1000
Visible	1.58 — 3.18	650 — 390
Ultraviolet (UV)	3.0 — 10.0	400 — 125
Vacuum Ultraviolet (VUV)	10.0 — 20.0	125 — 60
Extreme Ultraviolet (EUV)	30 — 200	40 — 5
Soft X-rays	150 — 3500	8 — 0.35
Hard X-rays	$3500 — 120 \cdot 10^3$	0.35 — 0.01
γ-rays	$\geq 120 \cdot 10^3$	$\leq$0.01

Table 2.1: Energy and wavelength for some of the electromagnetic spectral regions.

Electromagnetic radiation interacts with matter through several processes depending on the energy/wavelength of the incoming beam. Following the standard definitions

in particle and radiation physics, these phenomena are usually described introducing the total cross-section concept [29], which when multiplied by the incoming flux gives the number of particles that indeed interact with the target. Conventionally [30], the total interaction cross-section σ_{tot} is understood as a sum over the individual photon interaction cross-sections so that

$$\sigma_{tot} = \sigma_{coh} + \sigma_{incoh} + \sigma_{ph} + \tau + \kappa_e + \kappa_n \tag{2.2}$$

The total interaction cross-section is decomposed in σ_{coh} and σ_{incoh}, which describe the *elastic* and *inelastic scattering*, τ and σ_{ph}, which account for *photoelectric* and *photonuclear absorption*, and κ_e and κ_n, which are only relevant for γ-rays and stand for the *pair production* in the electronic and nuclear field. Photon interaction cross-sections for carbon and lead atoms are shown in figure 2.2 for energies above 10 eV.

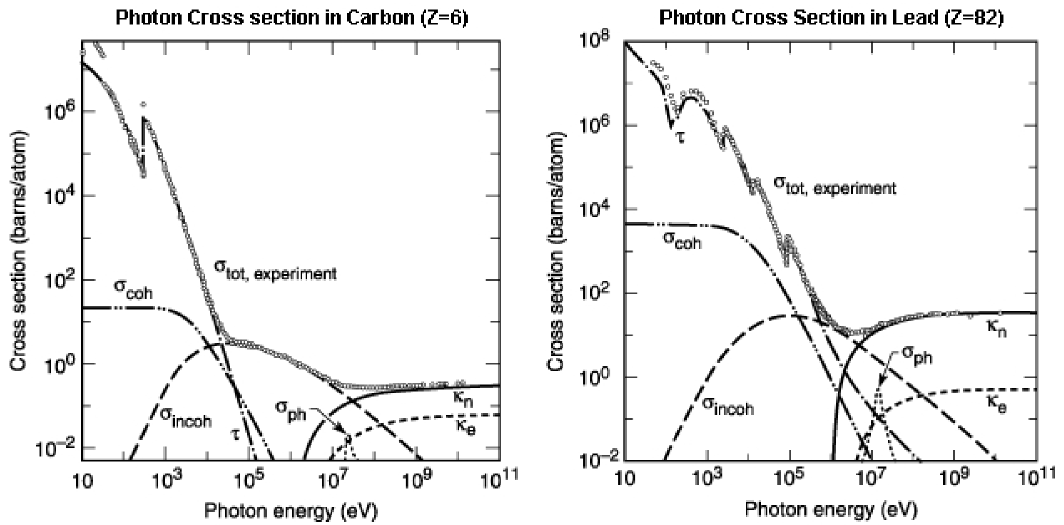

Figure 2.2: Total experimental photon cross-section for carbon and lead decomposed in the individual cross-section for each interaction process of photons with matter, extracted from *Thompson et al.* [31].

From figure 2.2, one can observe that not all the interaction processes are significant at a given photon energy. At soft x-ray regime, photons interact with matter in three ways: *elastic scattering*, *inelastic scattering* and *photoelectric absorption*. Elastic or coherent scattering can be described using classical electrodynamics, and is caused by two processes: Thomson scattering from single atomic electrons that may be considered as free in the low-energy limit, and Rayleigh scattering which occurs from strongly bound electrons acting cooperatively. As a result, some of the incoming photons are elastically (no change in their energy) dispersed in all directions. Inelastic or incoherent scattering, which is also referred as Compton scattering, must be described using relativistic dynamics and occurs from poorly bound electrons when a fraction of energy of the incoming photon is transferred to the electron. The outgoing photon has lower energy and a different direction from the original photon, so that the overall momentum of the system

is conserved. Absorption, via the photoelectric effect, happens when the x-ray photon transfers all of its energy to an inner atomic electron and the atom is ionized. Thus, a *photoelectron* has been ejected. The atom with a core vacancy readjusts itself when a higher lying shell electron makes a transition to the vacancy, either with the emission of a *fluorescent* energy photon or through the non-radiative *Auger* recombination, in which a second electron is ejected by the atom. Fluorescent emission and Auger process are competitive. Despite being beyond the scope of this report, photoabsorption is used in many synchrotron beamlines to extract information from the photoelectronic, fluorescence and Auger signal. From figure 2.2, we can derive that incoherent scattering is negligible while the coherent scattering cross-section is at least two orders of magnitude lower than the photoabsorption cross-section for soft x-rays. However, despite of the relatively small size of the atomic elastic cross-section, it would be erroneous to conclude that elastic scattering is insignificant in soft x-ray optical systems. If the amplitudes scattered by the atoms in an element of matter are added coherently, the total scattered intensity scales with the square of the volume of the element while the total absorbed intensity scales only linearly with volume. Therefore, as the element becomes larger, elastic scattering is increasingly favoured versus absorption so long as the superposition continues to be coherent. This feature is exploited in optical elements such as Fresnel zone plate lenses.

Latter approach is mainly microscopic. From a macroscopic point of view, the x-ray propagation in a medium of uniform atomic density can be described using the Maxwell equations and supposing that the electromagnetic wave induces an oscillatory motion on the electrons. Despite this is a non-rigorous semiclassical approach, most of the results do not differ significantly from the accurate quantum mechanical description. In these electron oscillatory motions, resonance effects occur when the frequency of the incoming radiation coincides with any one of the absorbing/emitting frequencies of the material. Even though for x-rays these frequencies correspond to the atomic transitions, this formalism can also be applied at molecular level for ultraviolet, visible and infrared radiation. When the electromagnetic wave penetrates into medium, the oscillatory motions of the electrons start and the generated current density alters the incoming radiation. This effect of the material on the electromagnetic wave propagation can be taken into account introducing the refraction index of the material, which can be linked to the microscopic properties of the atoms developing the Maxwell equations. Details of this derivation can be found in *Attwood* [28]. It is shown that

$$n(w) = \left[1 - \frac{e^2 n_a}{\varepsilon_0 m} \sum_s \frac{g_s}{(w^2 - w_s^2) - i\gamma w} \right]^{\frac{1}{2}} \tag{2.3}$$

where n_a is the atomic density in the medium, m is the electron mass, w_s are the resonance frequencies, γ is a dissipative factor and g_s is called the oscillator strength (i.e the number of the electrons involved for each resonance frequency). The refraction index depends strongly on the radiation energy/frequency and the medium is referred as *dispersive*. At the x-ray spectral region, w^2 is very large compared to the quantity

$\frac{e^2 n_a}{\varepsilon_0 m}$ and so, to a high degree of accuracy the refraction index can be written as

$$n(w) = 1 - \frac{1}{2}\frac{e^2 n_a}{\varepsilon_0 m}\sum_s \frac{g_s}{(w^2 - w_s^2) - i\gamma w} \tag{2.4}$$

which can be further simplified with the introduction of

$$\left.\begin{array}{ll} \text{classical electron radius} & r_e = \dfrac{1}{4\pi\varepsilon_0}\dfrac{e^2}{mc^2} = 2.817\cdot 10^{-15}\ \text{m} \\[2ex] \text{atomic scattering factor} & f^0(w) = \displaystyle\sum_s \frac{g_s w^2}{(w^2 - w_s^2) - i\gamma w} = f_1^0 + i f_1^0 \end{array}\right\}$$

to finally obtain

$$n(w) = 1 - \frac{n_a r_e \lambda^2}{2\pi}[f_1^0(w) + i f_2^0(w)] = 1 - \delta - i\beta \quad \rightarrow \quad \begin{cases} \delta = \dfrac{n_a r_e \lambda^2}{2\pi} f_1^0 \\ \beta = \dfrac{n_a r_e \lambda^2}{2\pi} f_2^0 \end{cases} \tag{2.5}$$

$f^0(w)$ is the complex atomic scattering factor in the forward direction. The *complex atomic scattering factors* are closely related with the cross-sections discussed above. f_1^0 and f_2^0 are measured experimentally and they are tabulated for all the elements and for an energy range that goes from 30 eV to 30 keV [32].

The refractive index at soft x-ray regime deviates only a small amount from unity, and the expression $n = 1 - \delta - i\beta$ is a standard notation. Typical values are $\delta \sim 10^{-5}$ and $\beta \sim 10^{-6}$. Such a small deviation from unity justifies the impossibility of using conventional optics to concentrate an x-ray beam and some of the limitations in the existing x-ray focusing devices.

Once the refraction index is known, we can easily represent the effect that a medium produces on a propagating wave. For this purpose, we compare the two monochromatic plane waves shown in figure 2.3. Wave ① is propagating in vacuum, while wave ② travels through a material volume of thickness r. As a result of the propagation inside the medium, wave ② undergoes an amplitude decrease due to absorption and a phase variation in relation to wave ①. The dephase between the two waves is caused by the fact the wavelength inside the material is modified by the refraction index. In opposition to visible optics and due to the negative sign in the index refraction expression, the x-ray wavelength becomes longer inside a medium and the wave phase is delayed in relation to the wave travelling in vacuum. In addition, the fact that the refraction index is less than unity introduces some interesting effects that are missing in visible optics (like total external reflection).

From Maxwell's equations, it can be shown that the phase velocity (the speed at which fixed phase crest travels) in a medium differs from the one in vacuum, c, according to the relation

$$v_\phi = \frac{w}{k} = \frac{c}{n(w)} = \frac{c}{1 - \delta - i\beta} \tag{2.6}$$

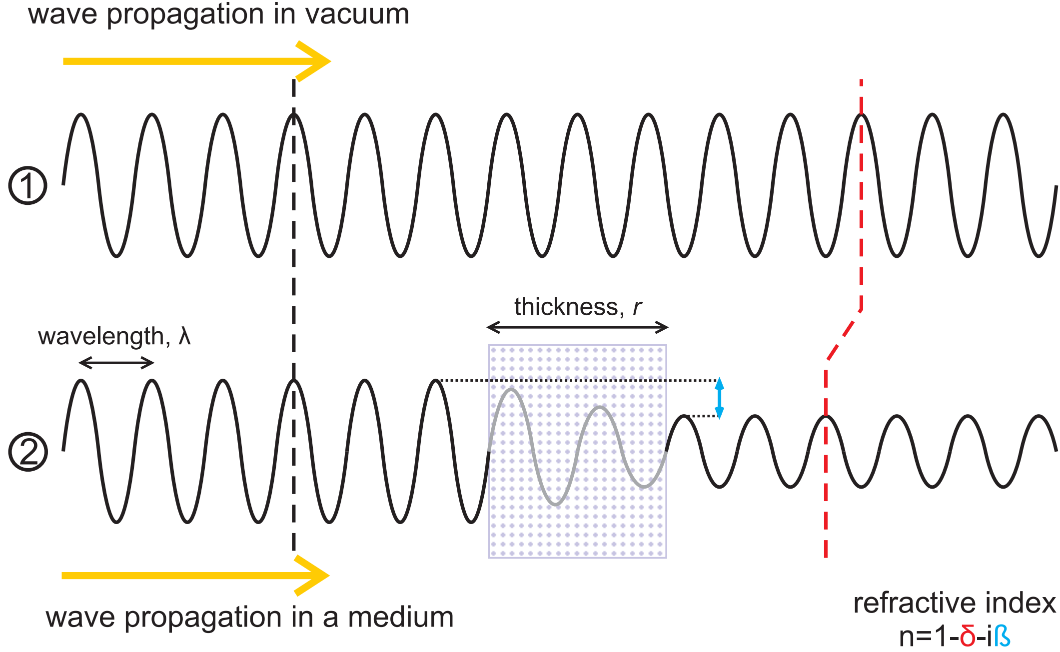

Figure 2.3: X-ray beam through a material volume. The effect of the material on the radiation can be described by the refraction index and it involves a decay of the wave amplitude and a shift of its phase.

A monochromatic plane wave is commonly represented by

$$\boldsymbol{E}(\boldsymbol{r},t) = \boldsymbol{E}_0 e^{i(wt-\boldsymbol{k}\cdot\boldsymbol{r})} \tag{2.7}$$

where $\boldsymbol{E}_0$ is the initial amplitude of the electromagnetic wave. Solving the former expression for k, and considering the forward propagation direction as in figure 2.3 which leads to $\boldsymbol{k}\cdot\boldsymbol{r} = kr$, one gets

$$\boldsymbol{E}(\boldsymbol{r},t) = \boldsymbol{E}_0 e^{i\left[wt-\frac{w}{c}(1-\delta-i\beta)\cdot r\right]} = \boldsymbol{E}_0 \underbrace{e^{iw(t-\frac{r}{c})}}_{\substack{\text{vacuum}\\\text{propagation}}} \underbrace{e^{-i(2\pi\frac{\delta}{\lambda})r}}_{\phi-\text{shift}} \underbrace{e^{-(2\pi\frac{\beta}{\lambda})r}}_{\substack{\text{absorption}\\\text{decay}}} \tag{2.8}$$

This expression describes wave ② after its propagation in the material volume. The first exponential term represents the phase advance as if the wave has only been propagating in vacuum, i.e. as wave ①. The second factor stand for the extra phase shift due to the material. The last exponential introduces the decay of the wave amplitude since part of the energy carried by the wave have been absorbed by the medium. Therefore, δ and β coefficients are directly related to the phase shift and the absorption of the incoming beam in the material. Later on, this expression describing the phase shift and the absorption decay introduced by a material will be essential to derive the effects that Fresnel zone plates produce on an x-ray photon beam.

Further details on the x-ray interaction with matter can be found in *Attwood* [28], *Kirz et al.* [33], *Michette* [34] and the references therein.

2.2 X-ray Focusing Elements

As discussed in previous sections, x-ray focusing entails some difficulties and it was even considered unfeasible for a while due to the weak interaction[1] of x-rays with matter, which translates to refraction index that is extremely close to unity. However, x-ray focusing into small spots is an essential requirement in many microanalysis techniques. Some experiments merely benefit from having a higher flux of photons on the region of interest of the sample to enhance the detected signal. In other experimental stations, a tiny x-ray spot is produced and scanned on the sample to acquire a line scan or a two dimensional map. In this case, the spatial resolution is fundamentally limited by the spot size produced by the focusing element. In full-field microscopy, an x-ray lens located downstream is used as objective lens to produce a magnified image of the sample on a spatially resolving detector. Resolving power is again limited by the lens performance. While in the latter case only attenuation or phase shift of the object can be recorded, an x-ray scanning station can provide a much wider range of information depending on the detected signal (this includes x-ray fluorescence, photoelectrons as well as the non-absorbed x-rays). All these argumentations justify the efforts to develop and improve the x-ray focusing devices.

Various systems have been developed for focusing of x-rays. They are based on reflection (mirrors, capillaries and waveguides), on refraction (compound refractive lenses) or on diffraction (Fresnel zone plates and diffractive optical elements).

- MIRRORS $\Longrightarrow$ Mirrors are the most widely used devices by far. Reflectivities at high glancing angles are so low that to ensure enough reflectivity, they must be used in grazing incidence (typically a few mrad) so that total external reflection condition is achieved. However, grazing incidence implies that very large mirrors (up to 1 m) must be used even to accept small synchrotron radiation beams. In addition, high reflectivities are only obtained when the residual roughness on the mirror surface is comparable to the x-ray wavelength, i.e. below 1 nm. Polishing of a surface with this precision is an effortful task and in addition, residual slope errors[2] must be also very small. A particular arrangement suggested by *Kirkpatrick & Baez* [15], in which a couple of mirrors are arranged in a particular disposition so that one focuses the radiation tangentially and the other one sagitally is very commonly used. The main accomplishment of such a system is that the astigmatism which results from the first mirror is compensated by that of the second mirror. Kirkpatrick-Baez systems are specially interesting at hard x-rays, where x-ray focusing is difficult to achieve with other devices. They have the advantage of being achromatic, which is of special interest when the primary photon energy is scanned to obtain spectroscopic information. Nevertheless, high performance mirrors system are difficult to align. Spot sizes in the submicron range can be obtained in routine operation, although spot sizes down to 50 nm have been recently

[1] Excluding absorption in case of soft x-rays.

[2] Slope error measures the difference between the real and the ideal shape of the reflecting surface.

demonstrated [35, 36], specially when introducing the multilayer technology [37].

- CAPILLARIES ⟹ Capillary optics [38, 39] is based on total external reflection on a smooth glass surface. Two different arrangements are commonly used. A polycapillary lens [40] is made of bundles of many hollow glass fibers that compress the x-ray beam into sizes of ten of micrometers with multiple reflections at the capillary walls. On the other hand, monocapillaries [41] consist of a single hollow glass tube and the focusing is achieved by a single reflection at the internal capillary surface. In this case the capillary needs a well defined shape of a paraboloid or ellipsoid. While polycapillaries can accept a large solid angle subtending many degrees, monocapillaries subtend less than 1° of angular acceptance. Fabrication of capillaries has been developing during the last decade. Current capillaries have good efficiency and micron and submicrometer spot sizes can be achieved.

- WAVEGUIDES ⟹ A waveguide consist of a two-dimensional cavity that confines the x-ray beam [42, 43]. The beam is concentrated to a very small spot at the exit of the waveguide and it can also be used for the generation of coherent x-ray point sources by resonant coupling of the incoming beam.

- COMPOUND REFRACTIVE LENSES ⟹ Since the refraction index is very close to unity, a single refractive lens would have an extremely long focal length and refractive lenses were considered unfeasible for a long time. However, this difficulty can be overcome by stacking several lenses in a row, so that the resulting focal length is cut down to reasonable values. However, materials with low atomic number and photon energies above 10 keV must be used in order to avoid extreme absorption losses, i.e. while they focus hard x-ray radiation efficiently, they are not useful for soft x-ray radiation. Another important disadvantage of compound refractive lenses is that they are chromatic devices and focal distances change with the photon energy. Nevertheless, they are very interesting focusing devices which can offer interesting features. There is a broad range of techniques to fabricate compound refractive lenses [44, 45, 46, 47].

- FRESNEL ZONE PLATES ⟹ Zone plates are the diffractive optical elements which can offer the best focusing at soft x-ray and hard x-ray regimes with a large beam acceptance. Routine working spot sizes are around 30 nm for soft x-rays [48] and around 50 nm for hard x-rays [49]. They work similar to a visible thin lens, but only a part of the radiation is delivered to the focus due to the diffraction. However, at hard x-rays their efficiency is limited because of the difficulties on the fabrication of high aspect ratio structures.

- BRAGG-FRESNEL LENSES ⟹ Bragg-Fresnel lenses can efficiently concentrate a hard x-ray beam combining the Bragg reflection of a crystal with the focusing properties of a Fresnel zone plate structure patterned into the crystal [50].

Main parameters and features of the described x-ray focusing devices are compared in table 2.2. The parameters are chosen so that the comparison can be done easily

despite not all the parameters are really relevant for every device. Collected values in the table try to be as illustrative as possible.

	KB Mirror	**Capillary**	**Waveguide**	**Compound Refractive Lens**	**Fresnel Zone Plate**	**Bragg-Fresnel Lens**
Minimum spot size	50 nm	$< 1\ \mu$m	100 nm	100 nm	15 nm (SXR) 30 nm (HXR)	$\sim 1\ \mu$m
Energy range	$<$ 30 keV	$<$ 30 keV	$>$ 4 keV	$>$ 10 keV	$<$ 10 keV	$>$ 10 keV
Efficiency	high, 70%	high	low	20%	10—20%	10%
Device Dimensions	large$\rightarrow --$	small$\rightarrow +$	small$\rightarrow +$	small$\rightarrow +$	small$\rightarrow ++$	small$\rightarrow ++$
Alignment	$--$	$\pm$	$+$	$++$	$++$	$\pm$
Working Distance	$\sim$ 30 mm	$<$ 10 mm	$<$ 1 mm	$\sim$ 1 m	1 to 100 mm	$\sim$ 500 mm
Chromaticity	$+++$	$+++$	$--$	$\frac{1}{\lambda^2} \rightarrow --$	$\frac{1}{\lambda} \rightarrow -$	$---$
Imaging	Not good	Not good	Not possible	Good	Very Good	Good

Table 2.2: This table compares the existing x-ray focusing devices. It gives illustrative values for some their relevant parameters and points out their advantages and disadvantages.

2.3 Soft X-ray Microscopy

As stated in section 1.2, x-ray microscopy gives the chance of imaging micro- and nanostructures at higher resolution with regard to optical microscopy, but without the cumbersome preparation requirements of electron microscopy. In particular, soft x-ray microscopy ($\approx$ 100 — 3000 eV) is specially suitable for biological material. Extended reviews on this subject can be found in *Adam et al.* [17], *Kirz et al.* [33], *Michette* [34] and references therein.

Biologist are mainly interested in observing the phenomena that occur inside the cell. This would require a resolution in the range of 20 — 40 nm with a good contrast between the details and its surroundings, and field of view of 5 — 20 μm, which is the typical cell size. In addition, taking advantage of the higher penetration depths of x-ray radiation, three dimensional imaging would be desirable since two dimensional imaging has some limitations when dealing with thick samples.

Between the K absorption edges of carbon (284 eV, 4.37 nm) and oxygen (543 eV, 2.28 nm), there exists a quite strong natural contrast between the intracellular aqueous medium and the carbon rich cellular organelles. Figure 2.4(a) shows the penetration depth, as function of the energy, for x-ray radiation and electrons. Clearly, the x-ray radiation penetrating power is almost two orders of magnitude higher than that of the electrons. In addition, the absorption of x-rays in carbon (cellular structures, black) increases substantially in comparison to that in oxygen (aqueous medium, blue) above the K absorption edge of carbon at 284 eV. The maximum contrast is obtained for an energy slightly below the oxygen edge at 543 eV. Besides, higher photon energies are advantageous during the imaging of thick samples because, due to its lower absorption, more photons are disposable for the image formation and lower dose is deposited in the

sample reducing the risk of damage. At 500 eV, 10 μm of water transmits 30% of the incoming fotons, which open the possibility of performing tomography of a whole cell. Figure 2.4(b) shows a detailed plot of differential transmission in the water window energy range for ordinary biological substances. One can see that the different components in a cell (lipids, proteins and carbohydrates) have slightly different contrast and they could be recognised and distinguished. Note the effect of the nitrogen L absorption edge at 410 eV on the protein transmission, even though nitrogen represents only an 8% of protein composition.

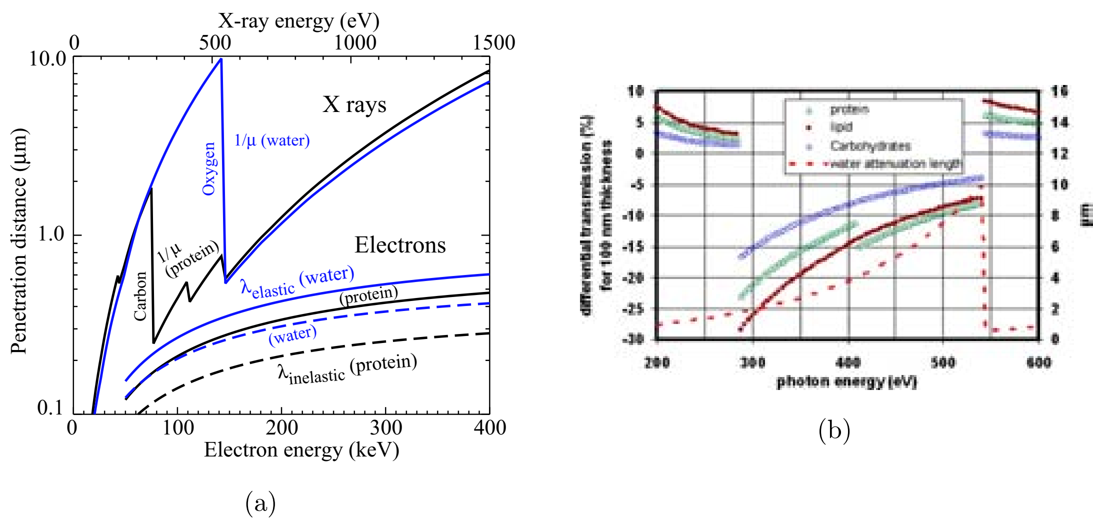

Figure 2.4: (a) Penetration distance as function of the energy for x-ray and electron beams, extracted from *Kirz et al.* [33]. (b) Differential transmission for 100 thickness of ordinary biological material, extracted from *Adam et al.* [17].

Above 500 eV, phase contrast techniques must be exploited to obtain good images from the biological samples. This can be done using Zernike phase contrast microscopy [51], or using special diffractive optical elements which are phase-sensitive [52]. As stated before, the use of higher energies reduces the delivered dose to the specimens during the image recording. High doses will partly destroy the cellular structures and eventually kill the cell. Usually, biological samples are frozen to decrease the risk of the radiation damage. Regarding x-ray lenses, radiation damage minimization demands optical devices and detectors as efficient as possible. Details on radiation damage can be found in the above mentioned references.

Despite x-ray microscopy has a great potential, only a few soft x-ray microscopes are installed at some synchrotron radiation facilities (BESSY in Germany, ALS in United States, ASTRID in Denmark, ELETTRA in Italy). This fact has precluded the wide use of x-ray microscopy, but this situation is likely to improve due to the new microscopes which are planned in the new facilities (SAGA in Japan, DIAMOND in United Kingdom, SOLEIL in France and ALBA in Spain).

Two main setups for x-ray microscopy can be arranged and they are shortly described in the following sections.

2.3.1 Full-field Transmission X-ray Microscopy (TXM)

Full-field transmission x-ray microscopy is based on the same optical arrangement as in conventional light microscopy. As shown in figure 2.5, the incoming x-ray radiation is focused onto the specimen by a condenser device and an objective lens is placed behind the sample to form a magnified image on a spatially resolving detector (typically a CDD chip which is either directly illuminated or by means of a visible scintillator). Whereas a large Fresnel zone plate lens was commonly used as condenser device in the past, monocapillaries are becoming more frequently used in the novel setups. On the other hand, Fresnel zone plate lenses are the best option as objective device to do imaging at very high spatial resolution. This technique can be used for continuous imaging and can be easily adapted to perform phase contrast microscopy introducing some extra optical elements [51]. Main limitations of this arrangement, when it refers to biological specimens, comes from the typically low efficiency of both objective lens and detector, since only a few percentage of the radiation can be used to produce the image and the sample can be damaged if too long acquisition times are required.

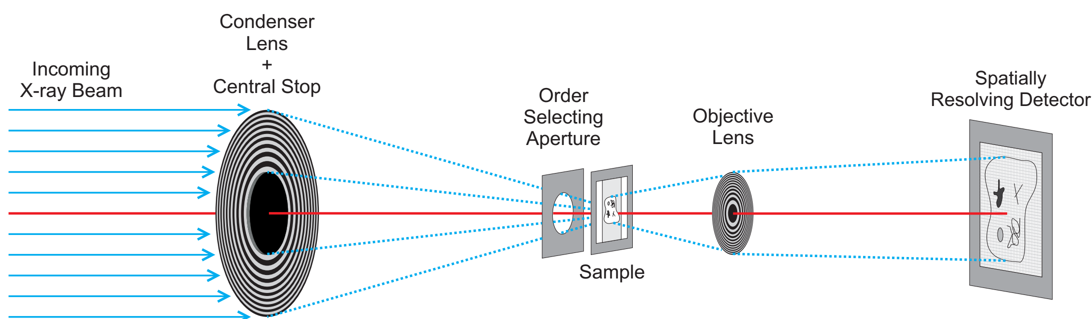

Figure 2.5: Full-field transmission x-ray microscope scheme.

2.3.2 Scanning Transmission X-ray Microscopy (STXM)

In terms of optical elements, scanning transmission x-ray microscopy setup is simpler than a full-field TXM setup. As shown in figure 2.6, a single lens is used to concentrate the incoming x-ray radiation and the specimen is mechanically scanned across the focused x-ray probe. A radiation detector located behind the sample records the transmitted signal sequentially at each position. Main STXM assets in relation to TXM are that no post-specimen optics and no spatially resolving detector are required. Both facts represent that low signals can be detected and as a result less dose has to be delivered into the specimen. In addition and depending on the detector sensitivity, fluorescence or photoelectron signals can be recorded as well as the transmitted photon beam. However, acquisition times for a single image are much longer in STXM (from minutes to hours) than in TXM (from milliseconds to a few tens of seconds). Nowadays, mechanical scanning of the specimens can be done with a precision of 5 nm or less and the current limitation of STXM resolution directly comes from the focusing devices.

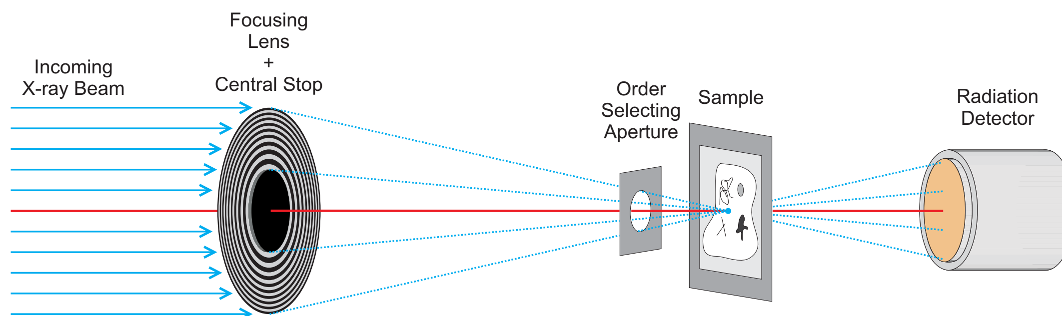

Figure 2.6: Scanning transmission x-ray microscope scheme.

2.4 Fresnel Zone Plates and Diffractive Optical Elements

As discussed in the previous sections, Fresnel zone plates are a well established focusing element for x-rays, and they are the best choice to perform x-ray imaging in terms of spatial resolution. However, their fabrication have just been implemented during the last two decades, and there are still some limitations that spoil the theoretical diffraction efficiency and resolution that could be achieved. Up to now, smallest lines ever resolved in x-ray microscopy, which are 15 nm, were a direct consequence of improvements on the Fresnel zone plate fabrication [53]. This fact already justifies the endeavours to learn and ameliorate the design and the manufacture of Fresnel zone plates.

Nevertheless, a Fresnel zone plate is one of the simplest diffractive optical elements that can be designed. At this stage, one should realize that the fundamental idea which lays in any optical element is that the amplitude and phase[3] of the wave impinging on the device must be appropriately changed so that the wave achieves the desired behaviour (collimation or focusing in the simplest cases) as it propagates away from the optical element. An ideal diffractive optical element (or hologram) would modify the amplitude and phase of the wavefront of the incoming radiation at will. Therefore, diffractive optical elements would be able to perform new optical functions beyond focusing, and they could redistribute the radiation intensity with almost complete freedom at a given downstream plane. Ideally in the context of x-ray microscopy, one could even optimize the optical device according to the sample requirements. While in visible light, holography techniques have been developing during the last 50 years, at the x-ray regime, they are in a very early stage [54]. Main restrictions in the production of diffractive optical elements come from the manufacture processes. Clearly, mastery of Fresnel zone plate fabrication techniques is a must in order to accomplish any progress in the design and fabrication of diffractive optical elements.

[3]Wave amplitude carries the information related with the energy or the number of photons, while the wave phase contains the information about the wave propagation.

CHAPTER 3

Fresnel Zone Plate Theory

In this chapter we discuss Fresnel zone plate lenses concepts in detail. They are introduced from an intuitive point of view and main formulas relating their relevant parameters are given. A complete derivation of the formulas will not be presented since they can be found in *Attwood* [28], *Kirz et al.* [33], *Michette* [34] and the references therein. Focusing diffraction efficiency and spatial resolution are shortly treated from a theoretical point of view. Exhaustive diffraction efficiency calculations for several appropriate materials at the soft x-ray regime are shown.

Later, we introduce a novel concept of Fresnel zone plate lens, which combines a layer of high refractive index material deposited onto a low refraction index material template. Despite the diffraction efficiency is diminished, there is a gain of a factor two in terms of spatial resolution. Detailed diffraction efficiencies calculations for such structures are also presented.

In the last part of the chapter, we describe a beamshaping condenser lens designed to produce a square flat-top illumination at its focal plane.

3.1 Fresnel Zone Plate Basics

A Fresnel zone plate consists of circular diffractive transmission grating with a radially increasing line density. These optical elements are suitable for focusing and imaging with x-ray photons as well as other types of particles, like atoms [55] or neutrons [56], for which refractive lenses are inappropriate (commonly due to excessive absorption). First examples of Fresnel zone plates developed for visible light were attributed to *Lord Rayleigh*

and *Soret*[1] on the basis of some earlier works by *J. A. Fresnel*.

Figure 3.1 shows the equivalence of a refractive lens and a Fresnel zone plate. In the *refractive lens*, a), the length, d, gives the distance that a wave has to travel inside the lens material to undergo a phase change of π in relation to a wave travelling in vacuum. Then, one must notice that only the regions (in dark gray) close to the edge of the lens play a role in introducing a phase lag in the wavefront. In case of a non-absorbing medium, the rest of the material would not affect the wave propagation at all. As a result, most part of the lens is dispensable and can be removed, while the relevant regions can be rearranged as in b). This disposition, referred as *Fresnel lens*, was firstly realised by *J. A. Fresnel* when improving the visibility of lighthouses, and enables the construction of lenses with large aperture and short focal lenses saving a lot in volume and weight of material in comparison to a conventional refractive lens. At the x-ray regime, where the absorption is not negligible at all, Fresnel lenses would be very appropriate since the saving of material implies an important diminution of the attenuation suffered by the beam when travelling through the lens. However, typical outermost periods of such structures must be in the sub-100 nm range in case of x-ray radiation and the ideal profile of the Fresnel lens is not feasible to be manufactured. Further simplification is demanded. As a solution, a Fresnel zone plate structure, c) and d), which is a binary approximation to a Fresnel lens, are proposed. An ideal *phase zone plate*, c), would introduce a π phase lag in the rays going through the structures, but again this is not feasible. A real *Fresnel zone plate* is represented in d), in which the dark region represents a highly absorbing material while the light gray regions are quite transmissive.

Fresnel zone plates can also be understood in terms of a diffractive grating. Figure 3.2 shows the comparison of a grating, a circular grating and a Fresnel zone plate. In a transmission grating, figure 3.2a), the incoming beam is divided in an infinite number of beams, one for each diffraction order, which emerge from the element at different angles. In the figure only the zeroth, first and minus first orders are shown. The direction of the diffracted beams are determined by the constructive interference that occurs at the angles where path length is increased by an integer number of wavelengths, such that

$$\boxed{\sin\theta_m = \frac{m\lambda}{d}} \tag{3.1}$$

where θ_m is the outgoing angle of the mth diffraction order, λ is the wavelength of the incoming radiation, and d is the period in the grating. This expression is known as the *grating equation*.

In the circular grating, figure 3.2b), the incoming beam is split in a different way. Due to the circular symmetry of the element, positive convergent orders are partly focused into a segment on the optical axis of the element, while the negative orders are divergent from a virtual focus which also consist of a segment but located upstream of the element. Then, we easily understand that, in a Fresnel zone plate, figure 3.2c), the local line period

[1] *J. L. Soret*, Ann. Phys. Chem. 156, 99 (1875)

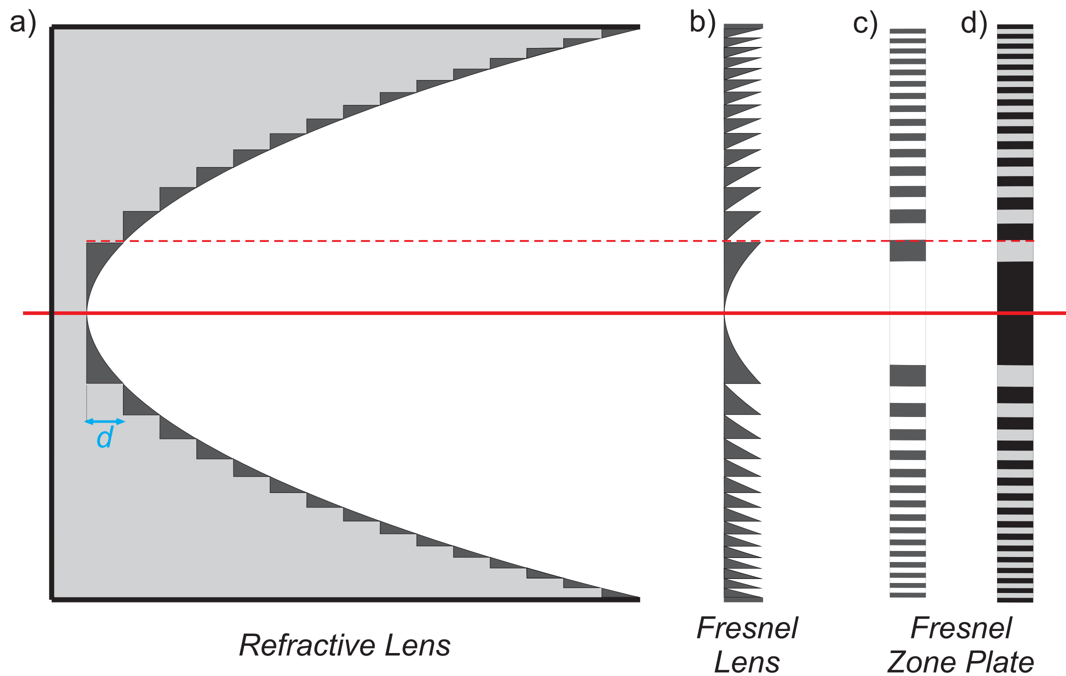

Figure 3.1: Equivalence of a refractive lens and a Fresnel zone plate. Length d in the refractive lens, **a)**, gives the distance that a wave has to travel inside the material to undergo a dephase π in relation to a wave travelling in vacuum. Only the shaded parts in dark gray near the edge of the lens are introducing a non-uniform dephase on the wavefront. The refractive lens can be reduced to a Fresnel lens, **b)**. A Fresnel zone plate, **c)** and **d)**, is a binary approximation to a Fresnel lens.

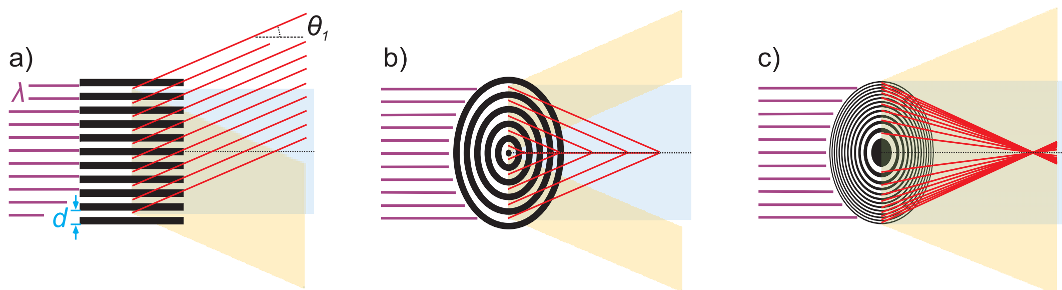

Figure 3.2: Comparison of a grating, **a)**, a circular grating, **b)** and a Fresnel zone plate, **c)**. Zeroth (blue), first (red) and minus first (yellow) orders are shown for each element. While the grating is only splitting the incoming beam, the circular grating and the Fresnel zone plate are respectively focusing the radiation into a segment and into a point of the optical axis.

is arranged so that all the rays from the first order converge into a point, which is, by construction, the focus of the element. Since the deflection angle is proportional to the line density[2], the grating period has to be bigger at the inner part of the element, while smaller at the outer regions. The negative orders, which are also divergent, have point virtual focus upstream of the element. The generation of infinite diffraction orders in a Fresnel zone plate is a consequence of the binarization of the Fresnel Lens, figure 3.1b), which would ideally concentrate all incoming radiation in a single point.

3.1.1 Fundamental Parameters for a Fresnel Zone Plate

Main parameters in a Fresnel zone plate are depicted in figures 3.3 and 3.4. Lens characteristics, which describe its optical performance are the *diameter* D, its *focal length* f, its *numerical aperture*, its *spatial resolution* and its *depth of focus*. All of them will be determined in terms of the radiation wavelength λ, the total number of zones N, and the outermost zone region Δr. The thickness of the zones h, will become an important parameter when considering the diffraction efficiency of the device.

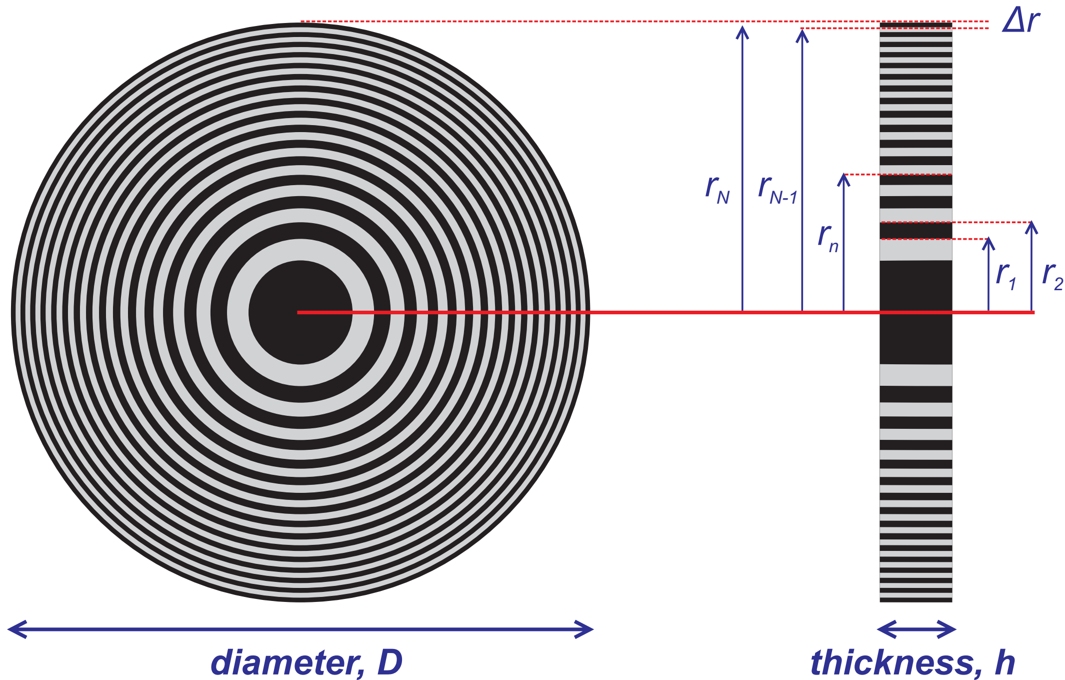

Figure 3.3: Main geometrical parameters in a Fresnel zone plate: the lens diameter D, zone radii r_n, zone thickness h, and the outermost zone width Δr. Zone radii are defined at the edge of the zones. While zone thickness will be important when concerning the diffraction efficiency of the lens, the outermost zone width is directly related to its spatial resolution.

[2]Strictly from the grating equation, this statement is only true for small numerical apertures, which is almost always the case at x-ray regimes.

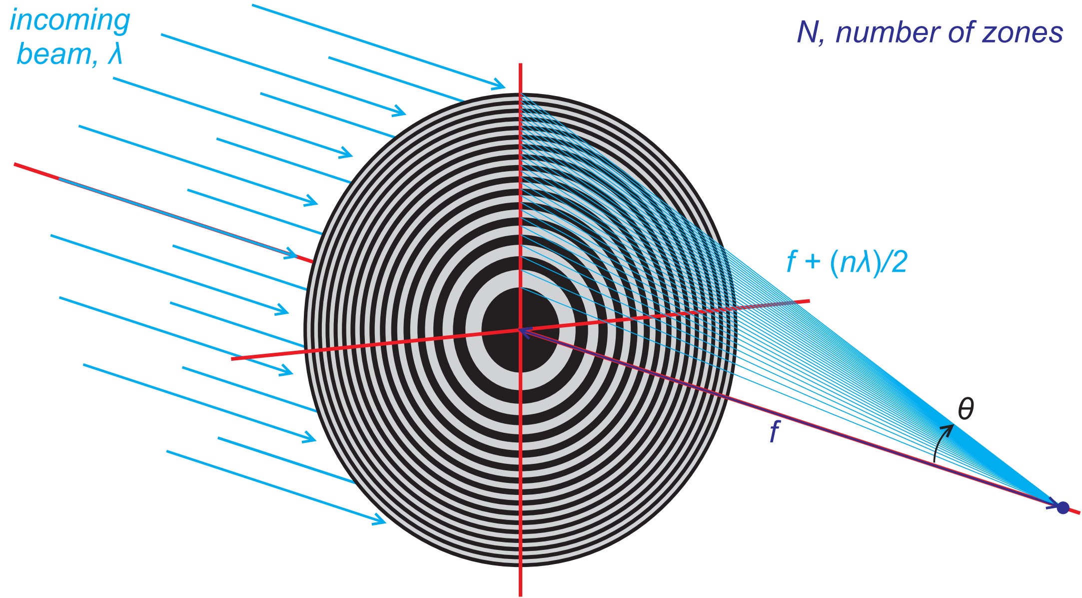

Figure 3.4: A Fresnel zone plate illuminated by a plane wave, λ. The first convergent diffraction order is concentrated at the focal plane at a distance f downstream of the lens. The radiation is concentrated in a cone of angle θ around the optical axis. N is the total number of zones, both opaque and transparent.

Fresnel zone plates are, in its simplest version, a pattern of alternating opaque and transparent radial zones located in such a way that the increased path lengths through sequential transparent zones differ by one wavelength each. Hence, an incoming wave travelling through the Fresnel zone plate is modified in such a way that the radiation is added in phase at the focal spot. According to this statement, the optical path of the rays going through the transparent zones must differ by one wavelength and the condition on the zone radii is given by

$$f^2 + r_n^2 = \left(f + \frac{n\lambda}{2}\right)^2 \tag{3.2}$$

which can arranged as,

$$\boxed{r_n = \sqrt{n\lambda f + \left(\frac{n\lambda}{2}\right)^2} \simeq \sqrt{n\lambda f}} \tag{3.3}$$

The term $n^2\lambda^2/4$ can be ignored when $f \gg n\lambda/2$, which turns out to be true in case of small numerical apertures. The numerical aperture of lens is defined as $\mathrm{NA} = \sin\theta$ where θ is the half angle measured from the optical axis back to the lens. From the grating equation 3.1, and considering that the period at the edges of the lens is given by two times the outermost zone width Δr, the numerical aperture NA of the Fresnel zone plate can be expressed as,

$$\boxed{\mathrm{NA} = \sin\theta = \frac{\lambda}{2\Delta r}} \tag{3.4}$$

In case of small numerical apertures, lens focal length and diameter are easily determined. Since $\text{NA} = \sin\theta \simeq \theta = \frac{D}{2f}$, and using equation 3.2 for the outermost radius, $\frac{D^2}{4} = N\lambda f$, one gets

$$\boxed{D = 4N\Delta r} \tag{3.5}$$

$$\boxed{f = \frac{4N(\Delta r)^2}{\lambda} = \frac{N\lambda}{2}\frac{1}{\text{NA}^2}} \tag{3.6}$$

This expression shows that the focal length of a Fresnel zone plate varies inversely proportional to the radiation wavelength, meaning that they are highly chromatic devices. Despite this is usually a disadvantage in relation to reflection based elements, a Fresnel zone plate in combination with a pinhole can be used as a monochromator.

The above analysis indicates the position of the focus but it does not give any information about the intensity distributions (that is, the diffraction patterns) produced at the focal plane by the Fresnel zone plate. These may be obtained using the Fresnel-Kirchoff diffraction integral, and the detailed investigation [28] shows that, as the total number N of zones increases, the diffraction pattern at a given focus resembles to that of a refractive lens, i.e. an Airy pattern. For $N > 100$ the difference is negligible. The spatial resolution δ_{res} in an image can be defined by the Rayleigh criterion as the radius of the first dark ring in the diffraction pattern. And then one gets,

$$\boxed{\delta_{res} = 1.22\Delta r} \tag{3.7}$$

Last expression shows the intimate relation between the spatial resolution of a Fresnel zone plate and its outermost zone width, the two of them being essentially comparable. This formula gives an estimation of the diffraction limited spot size which can be obtained by the Fresnel zone plate lens under coherent illumination. In complex imaging systems such as microscopes, the spatial resolution analysis depends on extra parameters such as the illumination. However, the fundamental proportionality between both parameters is always kept, despite the numerical factor can be slightly modified. This relationship justifies the endeavours to manufacture Fresnel zone plate with an outermost zone width as small as possible.

Two other important parameters in any imaging device are the depth of focus and maximum spectral bandwidth acceptance, which in case of a Fresnel zone plate are also derived in *Attwood* [28].

$$\boxed{\text{Depth of Focus,} \quad DOF = \pm\frac{1}{2}\frac{\lambda}{[\text{NA}]^2} = \pm\frac{(\Delta r)^2}{\lambda}} \tag{3.8}$$

$$\boxed{\text{Maximum Spectral Bandwidth,} \quad \frac{\Delta\lambda}{\lambda} \leq \frac{1}{N}} \tag{3.9}$$

There is an allowed shift, away from the focal or image plane, in any lens based imaging systems, for which the intensity on axis is decreased by some acceptable small

amount, or the image is only slightly deteriorated. By definition, this displacement is referred as the depth of focus of the lens. This is a very important parameter in x-ray microscopes when imaging thick samples and considering the acquisition of tomographic data. On the other hand, due to the wavelength dependence of the focal length of the Fresnel zone plate, monochromatic radiation must be used in order to reduce the chromatic aberration. The maximum spectral bandwidth sets an upper limit for spectral impurity of the incoming beam in order to have the expected focal spot size and resolution.

As pointed out in the beginning of this section, a Fresnel zone plate is a multifocal device. This is shown in figure 3.5. Positive and negative diffraction orders exist, which are respectively convergent and divergent. The existence of several diffraction orders demands the use of a pinhole located close to the selected order to prevent the residual radiation coming from the rest of orders go further. The pinhole is usually referred as order selecting aperture (OSA). Locating the order selecting aperture close to the focal position in combination with a central stop ensures the obtention of a clean focal spot.

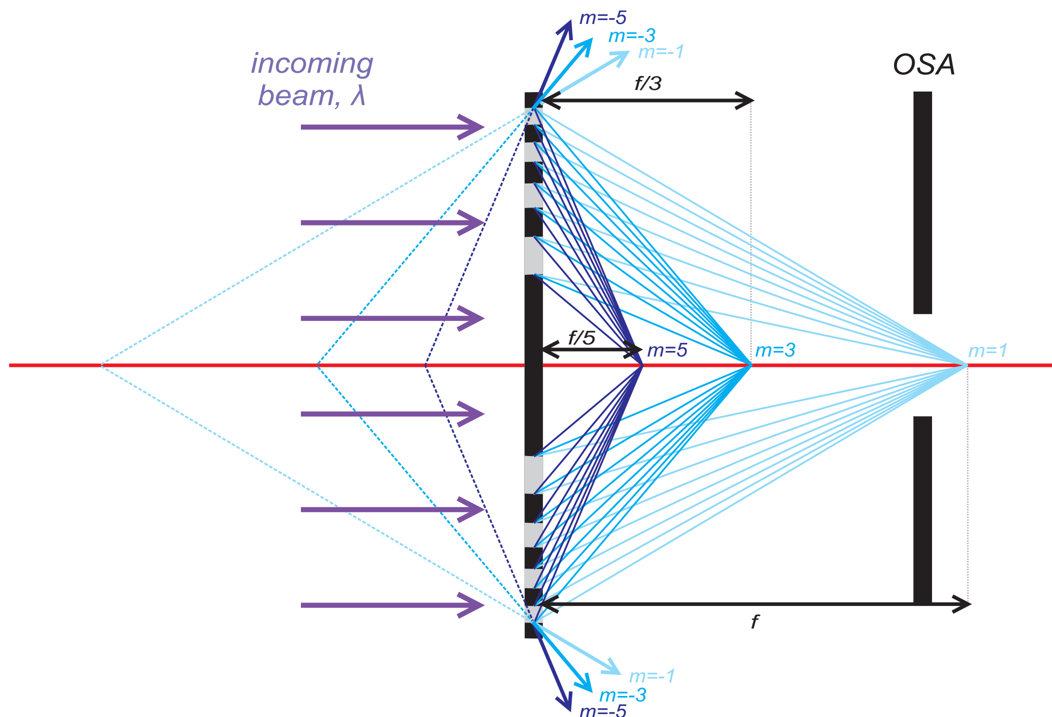

Figure 3.5: Diffractive focusing of a Fresnel zone plate for the first three positive orders. Three negative divergent orders, which have virtual foci upstream of the lens, are also shown. An order selecting aperture located near the first order focus can block most of the radiation of the remaining orders.

Formulas given above at first diffraction order must be slightly modified to be useful at higher orders. Table 3.1 summarizes the formulas for any diffraction order and gives illustrative values for all the parameters. One should note that at mth order diffraction the spatial resolution of the zone plate is increased, by a factor m. However, as will be

seen in the next section the diffraction efficiency decreases also by a factor m and as a matter of fact, even the third order is hardly ever used.

Parameter	Notation	Typical Values at Soft X-rays
Radiation Wavelength	λ	8 — 0.35 nm
Outermost Zone Width	Δr	20 — 100 nm
Number of Zones	N	100 — 1000
Diffraction Order	m	1, 3
Focal Length	$f = \dfrac{4N(\Delta r)^2}{m\lambda}$	0.5 — 10 mm
Diameter	$D = 4N\Delta r$	0.05 — 1 mm
Numerical Aperture	$\mathrm{NA} = \dfrac{m\lambda}{2\Delta r}$	0.01 — 0.06
Spatial Resolution	$\delta_{res} = \dfrac{1.22\Delta r}{m}$	30 — 120 nm
Depth of Focus	$DOF = \pm\dfrac{(\Delta r)^2}{m^2\lambda}$	0.3 — 4 μm
Maximum Spectral Bandwidth	$\dfrac{\Delta\lambda}{\lambda} \leq \dfrac{1}{mN}$	0.01 — 0.001

Table 3.1: Main parameters of a Fresnel zone plate in terms of the wavelength λ, the total number of zones N and the outermost zone width Δr. Illustrative values at the soft x-ray regime are given.

In what follows we present an alternative derivation of the zone radii of the Fresnel zone plate when considering a point source P located at a finite distance. We consider that the Fresnel zone plate is forming an image point Q of the point source P, as shown in figure 3.6. With an analogous derivation of equation 3.3, we have that,

$$p_n + q_n = p + q + \frac{n\lambda}{2} \tag{3.10}$$

$$\left(q^2 + r_n^2\right)^{\frac{1}{2}} + \left(p^2 + r_n^2\right)^{\frac{1}{2}} = p + q + \frac{n\lambda}{2}$$

from which r_n can be exactly expressed as,

$$\boxed{r_n = \frac{\left(2pq(p+q)\frac{n\lambda}{2} + \left[(p+q)^2 + pq\right]\left(\frac{n\lambda}{2}\right)^2 + (p+q)\left(\frac{n\lambda}{2}\right)^3 + \left(\frac{n\lambda}{2}\right)^4\right)^{\frac{1}{2}}}{p+q+\frac{n\lambda}{2}}} \tag{3.11}$$

Even though this expression is a bit more exact than equation 3.3, it is only strictly valid for the point source P and image Q. This expression can be simplified in case $p + q \gg n\lambda$ so that,

$$r_n^2 = \frac{n\lambda pq}{p+q} + \left(\frac{n\lambda}{2}\right)^2 \frac{p^3+q^3}{(p+q)^3} + \ldots$$

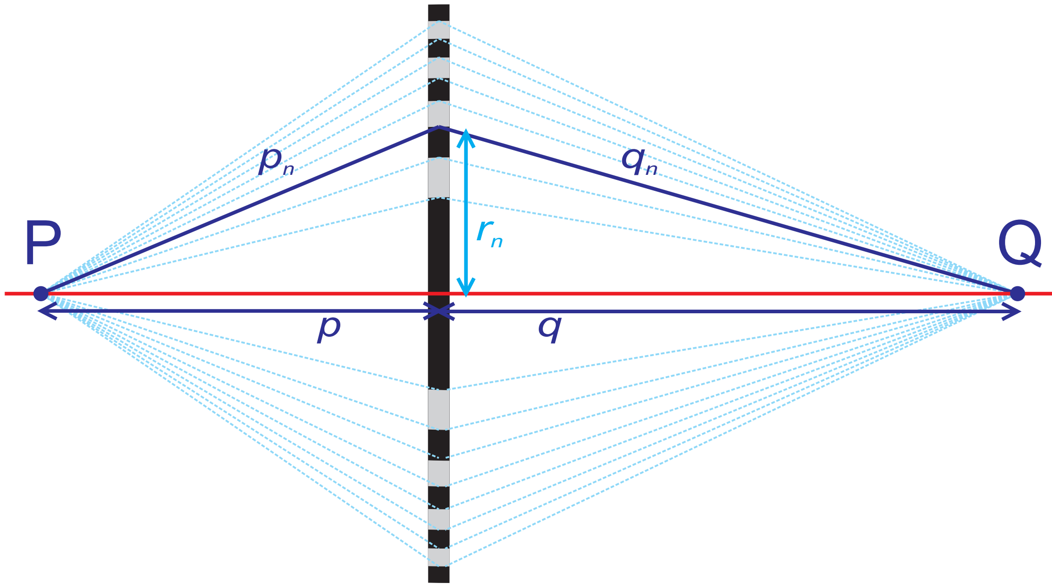

Figure 3.6: A Fresnel zone plate lens is forming a image point Q of the object point P. The difference in optical path through the center of each zone must be one wavelength and this can be used to establish the zone radii in the Fresnel zone plate.

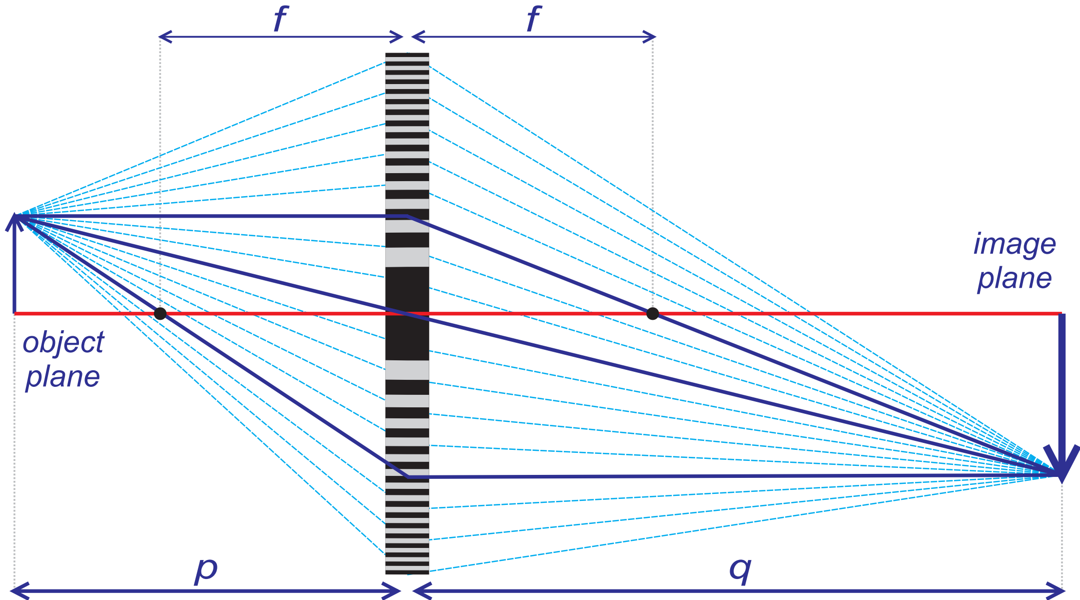

Figure 3.7: A Fresnel zone plate forming an image of an object. Fresnel zone plates resemble thin refractive lenses, and analogous analysis for the image formation can be used.

which can be further simplified to

$$r_n^2 = n\lambda f + \left(\frac{n\lambda}{2}\right)^2 \frac{M^3+1}{(M+1)^3} + \dots \tag{3.12}$$

where we introduced the typical relations for a thin lens,

$$\boxed{\frac{1}{p} + \frac{1}{q} = \frac{1}{f}} \tag{3.13}$$

$$\boxed{\frac{q}{p} = M} \tag{3.14}$$

As matter of fact, Fresnel zone plates lenses are used in focusing, $M \gg 1$, or magnified imaging, $M \ll 1$, so that equation 3.12 tends to equation 3.3. Note that last expressions are analogous to those of a refractive thin lens, that is, the Fresnel zone plate behaves like a refractive thin lens. Then, the position of the image of a given object can be found using equation 3.13 once the focal length is known and the magnification is given by equation 3.14. Same theory and results used in a thin lens analysis apply to a Fresnel zone plate system, as shown in figure 3.7.

3.1.2 Fresnel Zone Plate Diffraction Efficiency

Diffraction efficiency of a Fresnel zone plate gives the fraction of the incoming radiation intensity that is diffracted into a particular diffraction order. In case of a Fresnel zone plate with completely opaque and transparent zones the diffraction efficiency is given by [28],

$$\eta_m = \frac{I_m}{I_{incoming}} = \begin{cases} \frac{1}{4} & m = 0 \\ \frac{1}{m^2\pi^2} & m \text{ odd} \\ 0 & m \text{ even} \end{cases} \quad \text{and} \quad \frac{1}{4} + \sum_{m \text{ odd}} \frac{1}{m^2\pi^2} = 0.5 \tag{3.15}$$

As a result, 25% of the incident radiation is transmitted in the forward direction ($m = 0$) without being focused. Diffraction efficiency to the first order focus ($m = 1$) is about 10%, another 10% goes to the first divergent ($m = -1$), and less than 5% goes to the remaining orders. On the other hand, only half of the radiation is transmitted beyond the lens, since the other half is absorbed in the opaque rings. Thus, a binary Fresnel zone plate is, by construction, a low focusing efficiency device.

As a matter of fact at x-ray regime, Fresnel zone plates with completely opaque zones are difficult to manufacture. In order to absorb all the radiation, the demanded zone thickness h should be a few microns for common materials and when combining this with the requirement of a narrow outermost zone width Δr, the resulting high aspect ratio structures are not straightforwardly produced.

In order to include the case of real zone plate equation 3.15 must be recalculated, as shown by *Kirz* [57]. The effect of a real material zone thickness is introduced using equation 2.8. Then, the difference between the electromagnetic wave field alternatively transmitted through transmissive and opaque zone is given by a factor,

$$A = e^{-i(2\pi\frac{\delta}{\lambda})h} e^{-(2\pi\frac{\beta}{\lambda})h} \tag{3.16}$$

As previously discussed, the first term gives the extra phase while the second one accounts for the absorption[3]. Then the diffraction efficiency can be recalculated with analogous development of equation 3.15 and one gets,

$$\eta_m = \begin{cases} \left|\frac{1+A}{2}\right|^2 & m = 0 \\ \left|\frac{1-A}{m\pi}\right|^2 & m \text{ odd} \\ 0 & m \text{ even} \end{cases} \tag{3.17}$$

for which the odd diffraction orders can be arranged as

$$\boxed{\eta_m = \frac{1}{(m\pi)^2}\left[1 + e^{-2\frac{2\pi}{\lambda}\beta h} - e^{-\frac{2\pi}{\lambda}\beta h}\cos(\tfrac{2\pi}{\lambda}\delta h)\right]} \tag{3.18}$$

This expression shows that the diffraction efficiency depends on the material thickness and refraction index, $n = 1 - \delta - i\beta$. Due to the extra phase change introduced by the material the constructive interference in the focal spot may be reinforced and this effect will translate into an increase of the diffraction efficiency of a Fresnel zone plate when the material and zone thickness are conveniently chosen. Concrete values are provided in the next section. If the product βh is large enough the expression tends to the result of equation 3.15, since all the radiation that goes through the opaque zones is absorbed. In the opposite case, when βh tends to zero, the diffraction efficiency is maximized when $\frac{2\pi}{\lambda}\delta h = \pi$. This case would correspond to pure phase Fresnel zone plate, since the zone thickness could be chosen to introduce a phase lag π in the radiation going through the zones, for which up to 40% diffraction efficiencies could be achieved.

3.1.3 Materials for a Soft X-ray Fresnel Zone Plate

By using expression 3.18 introduced in the last section, calculations to determine the diffraction efficiency of Fresnel zone plate for different zone materials can be performed. Silicon (Si, Z=14), nickel (Ni, Z=28), iridium (Ir, Z=77) and gold (Au, Z=79) will be considered in the calculations. Si, Ni and Ir were used in the experimental works presented in the next chapters while Au is also included for comparison since it is a very common material in Fresnel zone plate production. Diffraction efficiency can be calculated as function of photon energy, zone material, and zone thickness, h.

[3]Note that A is a complex number.

Refraction index coefficients, δ and β are calculated using relationships 2.5 and the atomic form factors tabulated in [32]. Material densities are given in table 3.2. Due to their dependence on photon energy a small computing code was implemented to do the calculations. Figure 3.8 shows the diffraction efficiency at 1st order focus of a Fresnel zone plate as function of the zone thickness considering Si, Ni, Ir and Au as zone materials. At 500 eV, Ni and Si are the best materials and a maximum theoretical efficiency around 22% could be reached. Oscillations in the Ni curve are typical and show the consecutive constructive and destructive interference induced at the focal spot as the thickness (and dephase) is increased. Note, Ir and Au are quite absorbing at this energy and for zone thicknesses above 300 nm the diffraction efficiency asymptotically approaches that of a totally absorbing Fresnel zone plate. At 1000 eV, Ir and Au perform better than Ni, and efficiencies around 15% can be reached with both materials. Si could offer even higher values up to 30%. However, zone heights around 1 μm would be necessary and that is extremely challenging from the fabrication point of view. Generally speaking *at soft x-ray regime, diffraction efficiencies between 15 and 25% should be reached for any energy choosing an appropriate material and thickness.* Table 3.2 gives the optimum zone material thickness and the maximum theoretical diffraction efficiency that can be attained at 500 eV and 1000 eV.

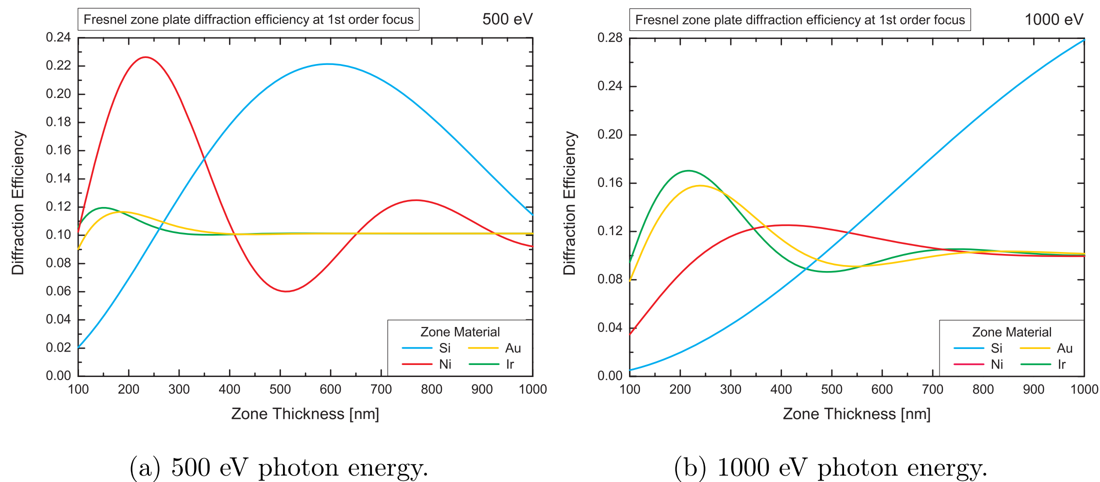

(a) 500 eV photon energy.

(b) 1000 eV photon energy.

Figure 3.8: Diffraction efficiency at 1st order focus of Fresnel zone plate as function of zone thickness, h, considering Si, Ni, Ir, Au as zone materials.

Figures 3.9 and 3.10 show the diffraction efficiency as function of the photon energy for several zone thicknesses. These graphs can be used to select the zone thickness when the Fresnel zone plate lens is meant to be used at given range of photon energies. For instance, from figure 3.9, a Fresnel zone plate with zone thicknesses of 400 nm Si or 200 nm Ni would provide diffraction efficiencies over 12% at the water window energy. In general, *maximum diffraction efficiency peaks get higher as the zone thickness increases but at the same time they are shifted towards higher energies.* Higher zone thickness translates into an increment on the phase shift strengthening the constructive interference but, at the same time, absorption is reinforced at lower photon energies. The sharp

Material	Density $\rho\left[\frac{g}{cm}^3\right]$	Photon Energy 500 eV		Photon Energy 1000 eV	
		Thickness [nm]	Diffraction Efficiency	Thickness [nm]	Diffraction Efficiency
Si, Z=14	2.330	596	0.22	1320	0.32
Ni, Z=28	8.902	234	0.23	410	0.13
Ir, Z=77	22.420	150	0.12	216	0.17
Au, Z=79	19.320	186	0.12	240	0.16

Table 3.2: 1st order focus diffraction efficiency of a Fresnel zone plate at 500 and 1000 eV photon energies for Si, Ni, Ir and Au as zone material. Material densities used in the calculations are also given.

decrease of the efficiency around 850 eV in the Ni curve originates as consequence of the existence of two absorption edges at 852.7 and 870.0 eV. A Ni Fresnel zone plate would not be very convenient for these photon energies.

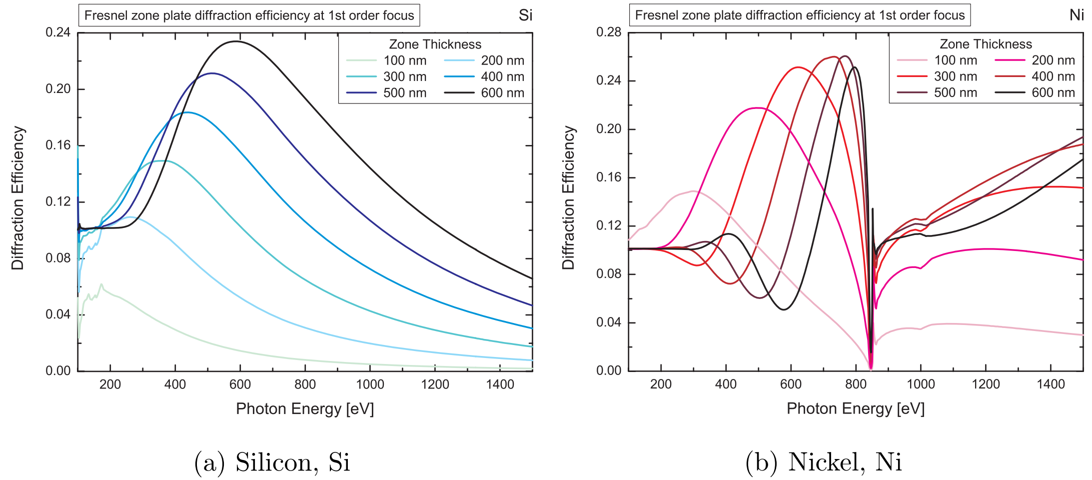

(a) Silicon, Si

(b) Nickel, Ni

Figure 3.9: 1st order focus diffraction efficiency of Si (a) and Ni (b) Fresnel zone plates as function of the photon energy, 100 — 1000 eV, for several zone thicknesses.

Figure 3.10 demonstrates that Ir and Au are suitable zone materials for photon energies above 800 up to 2000 eV providing diffraction efficiencies above 15% with moderate zone thicknesses between 200 and 400 nm. As a rule of thumb, higher atomic number materials perform better at higher photon energies unless extremely high zone thicknesses could be achieved with low atomic number materials.

So far, one has been considering free standing Fresnel zone plate structures for the diffraction efficiency calculations, while the patterns are usually supported by a membrane. Particularly at soft x-ray energies, these membranes must be extremely thin in order to minimize the absorption and to yield sufficient beam transmission. For a Fresnel zone plate, one usually distinguishes between *the total diffraction efficiency*, which takes into account the absorption of the supporting membrane, and *the groove diffraction efficiency*, for which the effect of the membrane is subtracted. Calculations shown

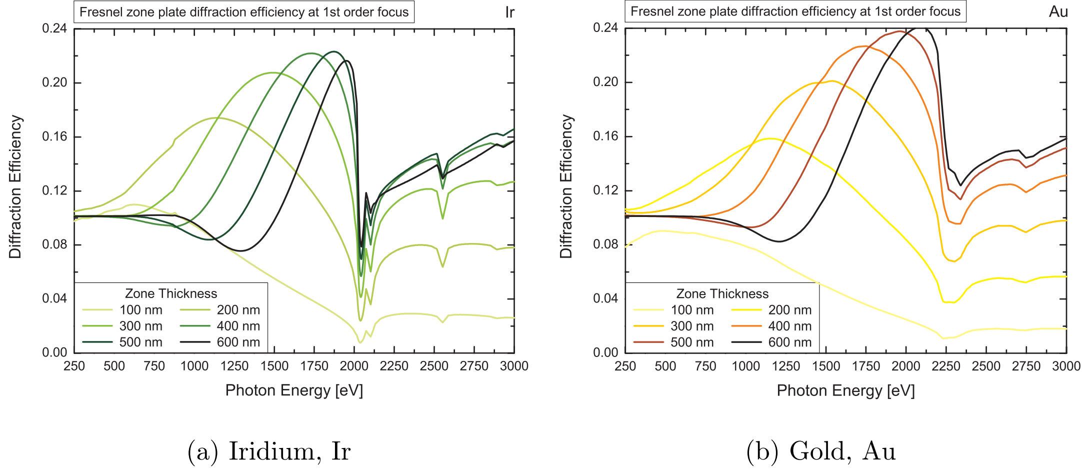

(a) Iridium, Ir (b) Gold, Au

Figure 3.10: 1st order focus diffraction efficiency of Ir (a) and Au (b) Fresnel zone plates as function of the photon energy, 250 — 3000 eV, for several zone thicknesses.

in figures above give the groove diffraction efficiency of the respective structures. Both diffraction efficiencies differ by a factor that stand for the transmission of the supporting membrane. X-ray transmission through a material thickness, h, can be calculated using the imaginary coefficient of the refraction index. One gets that

$$I = I_{incoming} e^{-4\pi \frac{\beta}{\lambda} h} \tag{3.19}$$

Silicon and silicon nitride, Si_3N_4, x-ray transmissions for a photon energy range between 250 — 2000 eV are shown in figure 3.11. Both materials are feasible to be used as supporting substrate of a Fresnel zone plate.

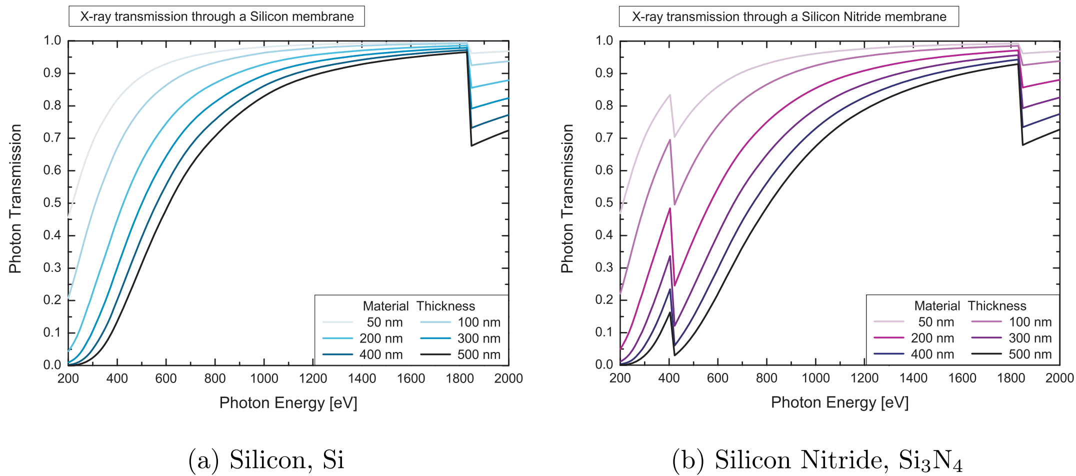

(a) Silicon, Si (b) Silicon Nitride, Si_3N_4

Figure 3.11: Transmission of an x-ray beam as function of the photon energy, 200 — 2000 eV, for Si and Si_3N_4 membranes.

In order to ensure reasonable transmission, thicknesses under 250 nm are required. Si_3N_4 is more commonly used as substrate for Fresnel zone plate patterns because Si_3N_4

membranes are more easily manufactured and they are even commercially available. However, in comparison to Si membranes, they have a couple of disadvantages: they are weaker and they have the nitrogen absorption edge (409 eV) that reduces noticeably the transmission in the water window energy range. Curiously, it can be stated that whereas for energies below the nitrogen edge both materials have the same transmission for a given thickness, above it Si layers can be twice thicker for a given transmission. On the other hand, weakness must be here understood in terms of handling, endurance to processing, and lifetime in the x-ray beam. Main inconvenient of Si membranes is that their fabrication is not straightforward.

3.2 Zone-Doubling Technique for Ultrahigh Resolution

In this section, we introduce a modified Fresnel zone plate structure to achieve higher spatial resolution. As discussed in the previous sections, spatial resolution essentially depends on the outermost zone width of the Fresnel zone plate pattern. The following development directly arises from the limitations on the fabrication techniques. As described in detail in the following chapters, Fresnel zone plates are mostly patterned using electron beam lithography and the finest outer zones widths are limited by the broadening of the electron beam, which is caused by the scattering of the electrons in the recording resist layer. This effect is particularly important when exposing dense features instead of isolated lines, as it is the case in the outer regions of a Fresnel zone plate.

The steps to construct the modified Fresnel zone plate structure are shown in figure 3.12. The new pattern, figure 3.12b), is constructed by replacing the opaque zones of a conventional Fresnel zone plate, figure 3.12a), which have variable width, by a set of zones which have a constant width, w, equal to that of the outermost zone, positioned at proper position. This pattern can be generated by depositing a layer of a *high refractive index* material on the top of the template structure, figure 3.12c), made of a *low refractive index* material, as shown in figure 3.12d). The combination of a low and high refractive index materials is essential so that the low refractive index zones of the template and the open zones can be considered equivalent, in a first raw approximation. In this case, the number of zones of the Fresnel zone plate template, figure 3.12c), has been doubled in the modified Fresnel zone plate pattern figure 3.12d).

This greatly facilitates the fabrication by nanolithographic techniques since the template structure in figure 3.12c), which is the one to be exposed, is clearly less dense than the patterns in figures 3.12a), b). As a matter of fact, the effective outermost zone width has been divided by a factor two resulting in a subsequent improvement of the spatial resolution by a factor two. The diffraction efficiency of the zone-doubled Fresnel zone plate will be lower than that of a standard Fresnel zone plate mainly for three reasons: *i)* the thickness of the deposited high index material is constant, meaning that the width of the zone is only optimum at the outer regions, and the diffraction efficiency decreases substantially at the center of the structure. *ii)* The continuous layer of the high index

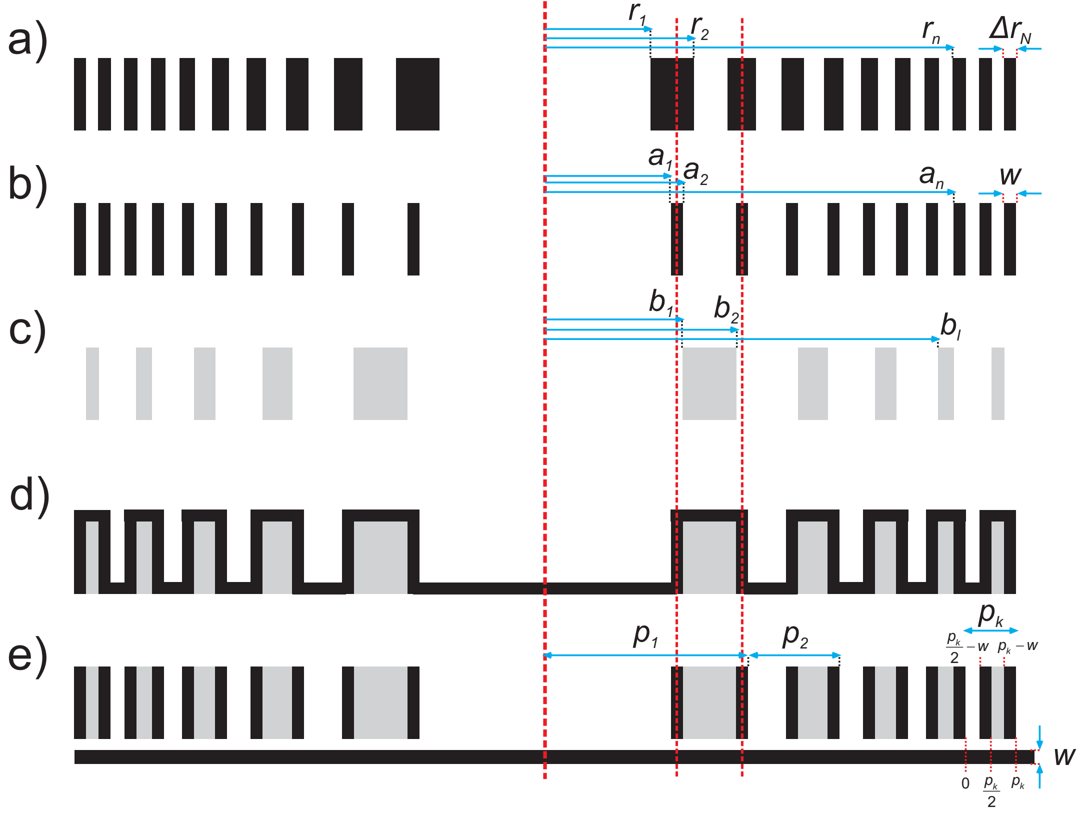

Figure 3.12: Zone-doubling technique in comparison to a conventional Fresnel zone plate. **a)** Schematic drawing of a Fresnel zone plate. **b)** Fresnel zone plate with constant width of the even zones equal to w. **c)** Low refractive index template structure. **d)** Zone-doubled Fresnel zone plate: low refractive index template structure coated by high refractive index material. **e)** Equivalent structure to the one in d), showing that the high refractive index material deposited onto ridges and grooves of the low refractive index template is acting as a thin absorbing layer.

material leads to additional absorption losses. *iii)* The low refraction index template introduces some attenuation and phase shift reducing the obtainable constructive interference. However, as it will be shown in the following, the impact of these effects can be rather weak depending on the used materials and geometry for relative high photon energies. Generally speaking, *high ratio between the index refraction coefficients of the coating and template materials is required.*

Following the analogous development used in by *Kirz* [57] to derive the equation 3.18 of last section, we can write the diffracted intensity due to the kth local period of the coated template as:

$$I_k = |A_1 + A_2 + A_3 + A_4|^2 \tag{3.20}$$

where

$$A_1 = \frac{C}{p_k} e^{-\frac{2\pi}{\lambda}\beta_{high} w} \int_0^{\frac{p_k}{2}-w} e^{-2\pi i \frac{mx}{p_k}}\, dx \tag{3.21}$$

$$A_2 = \frac{C}{p_k} e^{-\frac{2\pi}{\lambda}\beta_{high} w} e^{-\frac{2\pi}{\lambda}\beta_{high} h} e^{-\frac{2\pi}{\lambda}\delta_{high} h} \int_{\frac{p_k}{2}-w}^{\frac{p_k}{2}} e^{-2\pi i \frac{mx}{p_k}} dx \tag{3.22}$$

$$A_3 = \frac{C}{p_k} e^{-\frac{2\pi}{\lambda}\beta_{high} w} e^{-\frac{2\pi}{\lambda}\beta_{low} h} e^{-\frac{2\pi}{\lambda}\delta_{low} h} \int_{\frac{p_k}{2}}^{p_k-w} e^{-2\pi i \frac{mx}{p_k}} dx \tag{3.23}$$

$$A_4 = \frac{C}{p_k} e^{-\frac{2\pi}{\lambda}\beta_{high} w} e^{-\frac{2\pi}{\lambda}\beta_{high} h} e^{-\frac{2\pi}{\lambda}\delta_{high} h} \int_{p_k-w}^{p_k} e^{-2\pi i \frac{mx}{p_k}} dx \tag{3.24}$$

are the amplitudes contributed by the four different zones of the kth local template period p_k and the pairs β_{high}, δ_{high} and β_{low}, δ_{low} are the high and low refractive index coefficients. In addition,

$$I_{incoming} = |C|^2 \quad \text{is the incoming intensity.} \tag{3.25}$$

The interpretation of this expressions is easier when noticing the equivalence between structures in figures 3.12d) and 3.12e). The first exponential terms in four expressions corresponds to the absorption in the uniform layer of high refractive index material. The second and third terms in A_2, A_3 and A_4 stand for the absorption and the phase shift by the coating and template materials. The borders of the Fresnel integral define a different pass of the beam from different zones to a focal plane of the mth diffraction order. Since the number of local periods of high refractive index zones is doubled comparing to the template structure, the efficiency η_k due to a pair of high refractive index periods is calculated as

$$\eta_k = \frac{I_k}{I_{incoming}} \quad \text{by substitution of } m = 2 \tag{3.26}$$

Since the area of each period is, in very good approximation, equal for all the values of k template periods, the overall efficiency of the zone plate can be calculated as the average of the local efficiencies.

$$\eta = \frac{1}{L}\sum_{l=1}^{K} \eta_k \quad \text{where } L \text{ is the number of periods in the template} \tag{3.27}$$

These expressions can be implemented in a computing code to perform a numerical optimization of the diffraction efficiency of the zone-doubled Fresnel zone plate as a function of the coating layer thickness, w, and the template height, h, for given set of materials and photon energy.

Silicon and polymers are suitable as template materials since they have a low refractive index material in a wide range of energies and there exist well developed methods for their nanostructuring. The choice of the coating material greatly depends on the energy to be used. Iridium or gold are two feasible candidates, for which layer deposition techniques are available.

Figure 3.13 shows the calculated diffraction efficiency at first order of Ir/Si and Ir/Polyimide[4] zone-doubled Fresnel zone plates at 500 and 1000 eV photon energies.

[4]Polyimide is current polymer resist used in micro- and nanofabrication.

Diffraction efficiency is presented as function of the structure height, h, and the width of the high refractive index material coating, w. One must realize that the diffraction efficiency of this new patterns depends on diameter of the Fresnel zone plate. For a given outermost zone width, their diffraction efficiency increases for larger diameters since the area which has structures with an almost *tuned period* is larger. The calculations shown in figure 3.13 are for a zone-doubled Fresnel zone plate of 100 μm diameter and an outermost zone width of 20 nm.

One can observe that there exists a diffraction efficiency peak for each combination of materials at a given energy. The height, h, and the width, w, can be optimized. The optimal width, w, is always a bit higher than the outermost zone width of the equivalent standard Fresnel zone plate. Ir/Si and Ir/Polyimide combinations result in about 4% diffraction efficiency at 500 eV, being the value slightly higher for the second case. Ir is quite absorbing material at 500 eV, and low atomic number materials, such Ni, would be better at this energy range. However, at 1000 eV expected diffraction efficiencies are higher, around 9%, which is already a resonable value.

Table 3.3 summarizes the calculations and comparisons between the achieved values can be easily established. Ir/Si combination at 1000 eV photon energy has a special interest because the performance of this system was checked experimentally, as detailed in chapter 7. Table 3.3 also shows the theoretical diffraction efficiency at 8000 eV, already in the hard x-ray range. Due to the decrease in the absorption, specially in the Si or Polyimide template, the achievable diffraction efficiencies are quite high.

Energy [eV]	**Ir standard Fresnel zone plate**			**Ir/Si zone-doubled Fresnel zone plate**			**Ir/Polyimide zone-doubled Fresnel zone plate**		
	h	Δr	DE	h	w	DE	h	w	DE
500	150	20.0	0.12	135	21.7	0.035	143	22.1	0.040
1000	215	20.0	0.17	225	24.8	0.091	222	24.4	0.095
8000	1350	20.0	0.31	1400	25.6	0.229	1390	26.0	0.237

Table 3.3: Maximum theoretical diffraction efficiency, DE, and optimized parameters, height of the structures, h, and width of the coating layer, w, for the Ir/Si and Ir/Polyimide material combinations. A Fresnel zone plate with $D = 100$ μm and $\Delta r = 20$ nm is considered.

Other pairs of materials could also be investigated. At 500 eV, combinations of Ni/Si and Ni/Polyimide are expected to perform better because Ni has significant less absorption than Ir. Expected values can be extracted from figure 3.14. Diffractions efficiencies of 9% and 12% are respectively expected in this case.

A last comment on this new type of Fresnel zone plate pattern can be done observing figure 3.15. It compares the focusing of a conventional structure in relation to a zone-doubled pattern. The focal length corresponding to the high refractive index of the zone-doubled structure, f_B, is half of the correspondent one for the conventional template, f_A. In fact, in the zone-doubled structure a focus should exist at position f_A which is originated by the template structure which has a periodicity which is half of the high

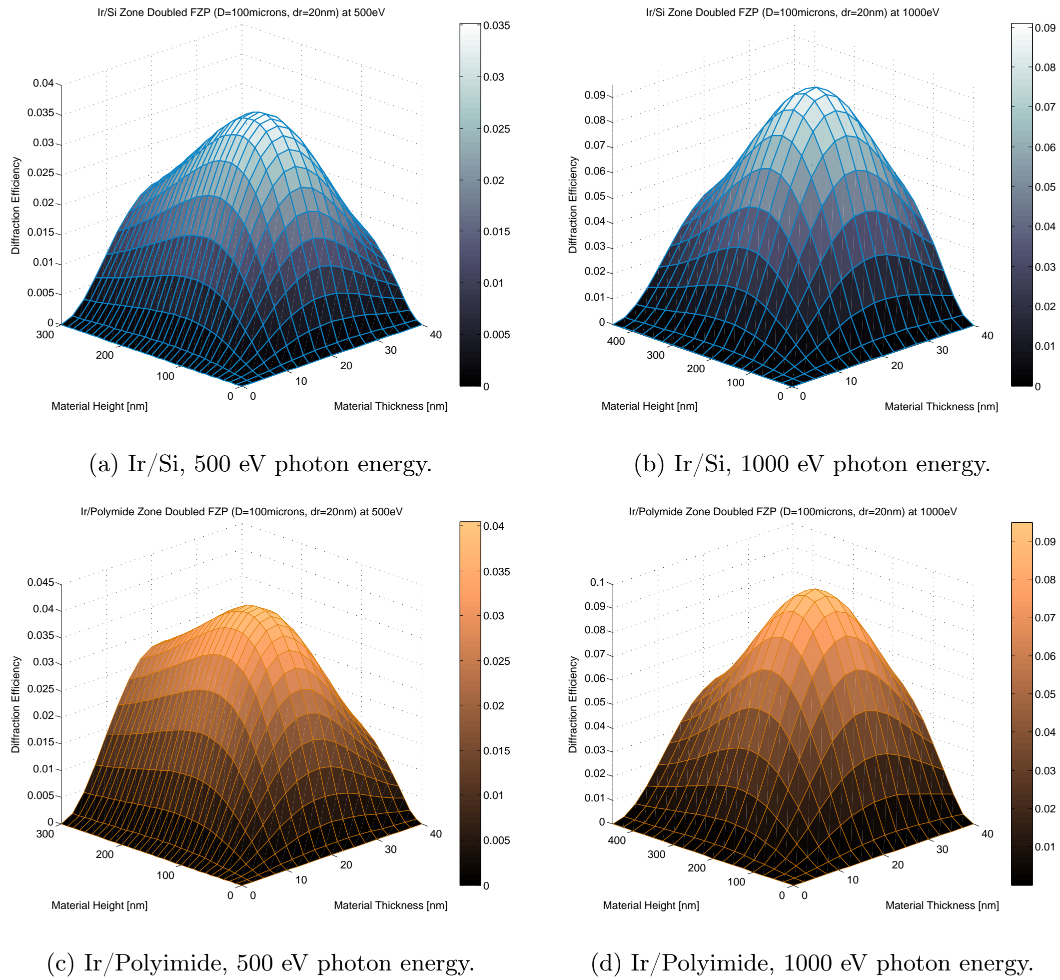

(a) Ir/Si, 500 eV photon energy.

(b) Ir/Si, 1000 eV photon energy.

(c) Ir/Polyimide, 500 eV photon energy.

(d) Ir/Polyimide, 1000 eV photon energy.

Figure 3.13: Diffraction efficiency at 1st order for a zone-doubled Fresnel zone plate ($D = 100\ \mu$m and $\Delta r = 20$ nm). Ir/Si and Ir/Polyimide patterns at 500 and 1000 eV photon energy.

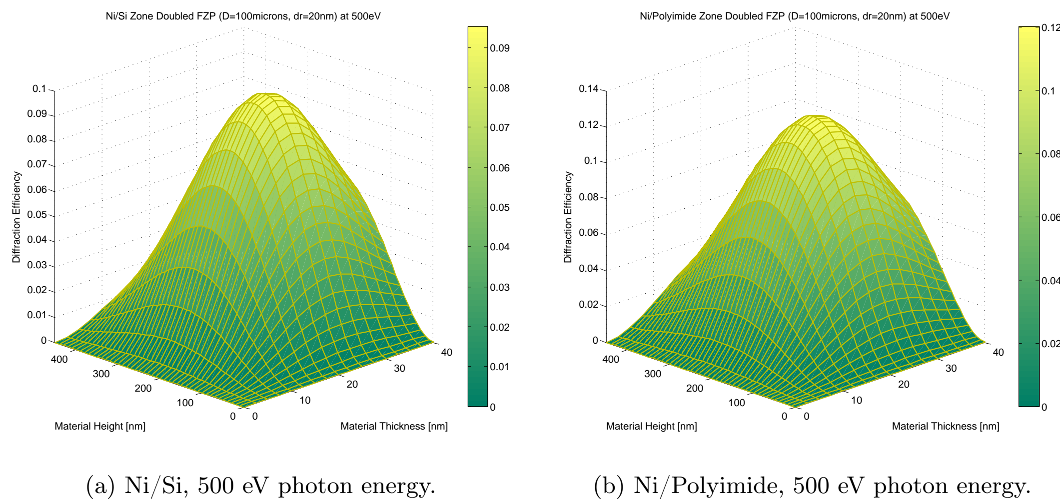

(a) Ni/Si, 500 eV photon energy.

(b) Ni/Polyimide, 500 eV photon energy.

Figure 3.14: Diffraction efficiency at 1st order for a zone-doubled Fresnel zone plate ($D = 100\ \mu$m and $\Delta r = 20$ nm). Ni/Si and Ni/Polyimide patterns at 500 eV photon energy.

refractive index coating. On the other hand, whereas for a conventional Fresnel zone plate the spatial resolution must be comparable to the outermost zone width Δr, in a zone-doubled pattern one should expect a spatial resolution close to one-fourth of the template period, as shown in figure 3.15. The width in the outer regions, w, should not necessary coincide to this value, according to the diffraction efficiency calculations shown above.

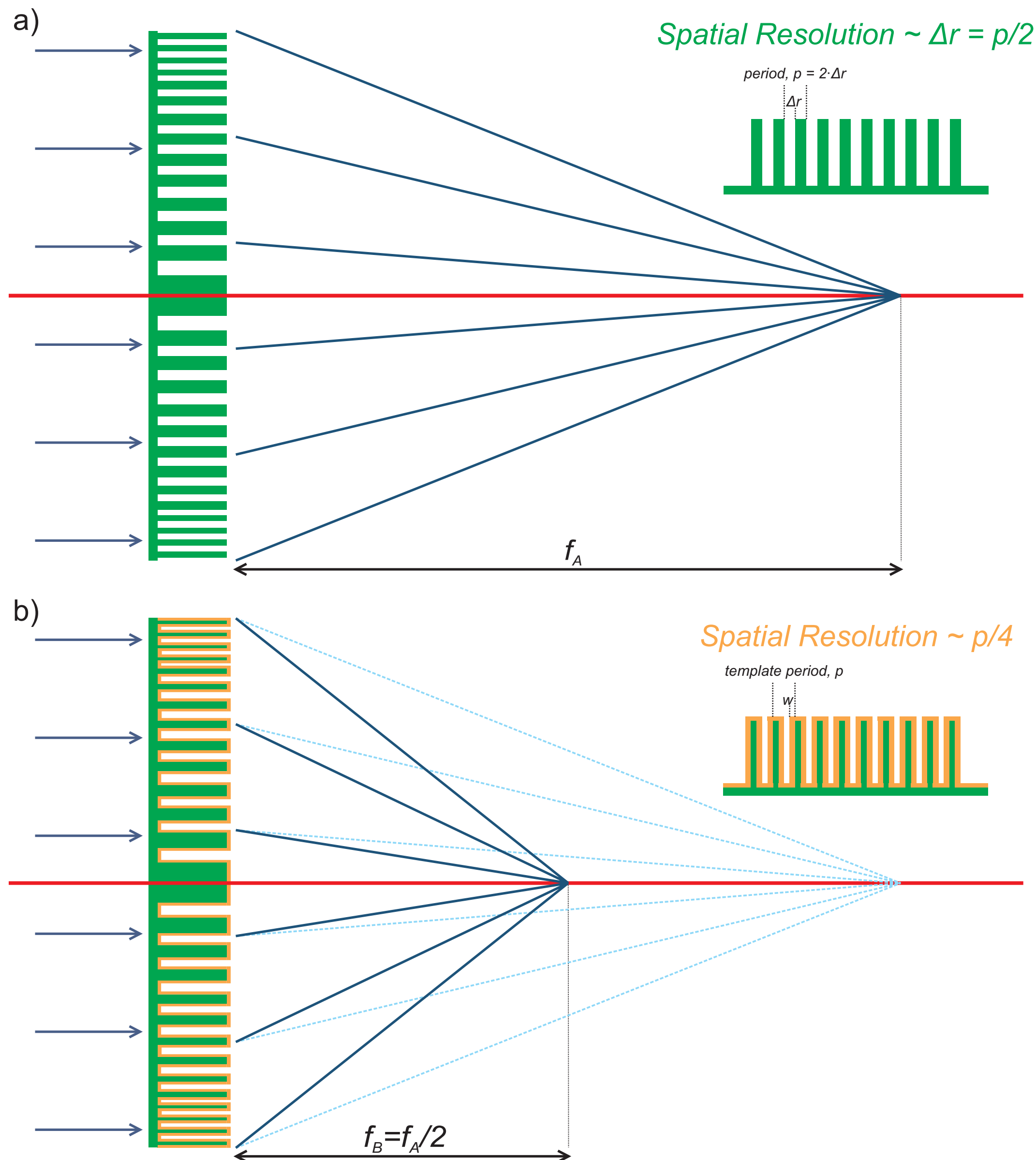

Figure 3.15: Comparison between a conventional Fresnel zone plate **a)** and zone-doubled Fresnel zone plate **b)**. The focal length corresponding to the high refractive index structure, f_B, is half of the correspondent one for the low refractive index template, f_A. The spatial resolution is improved by a factor two.

Previous analyses are based on the assumption that the Fresnel zone plate structure

is thin enough so that *the kinematical diffraction theory* can be applied. This supposition implies that the wavefront interacts punctually with the structure and multiple scatterings effects are neglected. This approximation is good enough when the aspect ratio of the structures is not very high, that is, when the ultimate zones are not extremely narrow nor the height of the structures is too high. However, *the dynamical diffraction theory* should be applied in case of a pattern with very thick structures or very narrow outermost zones. The dynamical diffraction approach takes into account that the wave is confined during its propagation inside the Fresnel zone plate pattern and all multiple scattering effects are included. Despite being beyond the scope of this report, a couple of references on this topic are suggested [58, 59]. While having outermost zones above 20 nm and structure thicknesses below 1 μm kinematical diffraction description gives accurate results.

3.3 Design of a Beamshaping Condenser Lens

The design and fabrication of diffractive optical elements for x-ray radiation has been demonstrated in recent works by *Di Fabrizio et al.* in [54, 60, 61]. The utilization of beamshapers with complex optical functionality was proven in these references, and their advantages were pointed out. On the other hand, the feasibility of extending holography techniques, which are well established in case of visible light, to the x-ray energy range was demonstrated by *Firsov et al.* [62]. In fact, a Fresnel zone plate lens can be understood as the hologram of point source when a plane wave is taken as a reference wave[5]. However, diffractive optical element design entails some difficulties due to two main reasons: *i)* the incoming x-ray beams are not easily modelized and *ii)* there exists some restrictions due to the fabrication limitations. As a result, the fabrication and use of diffractive optical element for x-ray beams is at a very early stage of development. In this short section, we introduce a beamshaping condenser lens, based on a very simple design, which can produce a flat-top illumination. Later in chapter 5, one will show that Fresnel zone plate fabrication techniques can be used to implement and fabricate this optical element.

As briefly suggested in section 2.3.2, one of the key optical elements in full-field transmission x-ray microscopes is a condenser device to provide illumination of the sample. The illumination should be as homogeneous and intense as possible and the numerical aperture should be matched to that of the objective lens in order to obtain an optimum resolution [64]. Fresnel zone plates [65], tapered capillaries [66], mirrors [67], and combinations of these elements [68] are commonly used as condensers. Nevertheless, these devices are focusing the beam into a spot which is smaller than the field of view of the microscope, which in practise forces to raster scan the focused beam across the sample to be imaged.

[5]Based on this approach, a new technique to expose Fresnel zone plate patterns is under development [63].

Recently, a simple approach of a beamshaping condenser element was proposed and tested in a soft x-ray full-field microscope [69]. The idea of the design was to divide a conventional Fresnel zone plate into sectors keeping local spatial frequency within each sector constant. As a result, such a device produces a flat-top illumination spot in the focal plane. However, the superposition of non-symmetric radially distributed shapes forms an approximately round spot with significant "tails". Based on the same idea of dividing a Fresnel zone plate, we propose an improved design made of square gratings.

The beamshaping condenser lens design is sketched in figure 3.16 in comparison to a standard Fresnel zone plate. The beamshaping condenser lens is composed of square subfields of side d. Each subfield consists of a linear grating with constant line orientation and period, which corresponds to the local period of the equivalent Fresnel zone plate pattern. Since both elements have the same diameter[6] and outermost zone width, they have the same focal length. The first diffraction order of every subgrating of the beamshaping element will form an exactly coinciding square illumination in its focal plane with the illuminated area equal to the size, d, of the gratings, as shown in figure 3.17. As a result, a square flat-top intense focal spot is produced by the beamshaping condenser lens. In addition, using square shaped illumination is very convenient since the active area of the detector is usually square too.

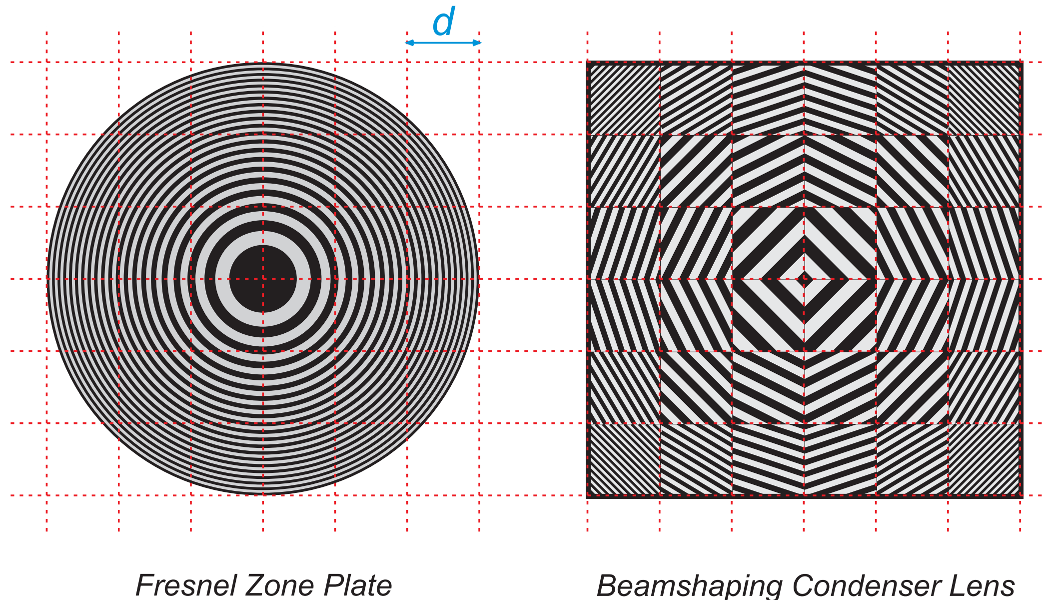

Figure 3.16: Equivalence between the beamshaping condenser lens in comparison to a conventional Fresnel zone plate lens. The beamshaping element is made of square subfields which consist of a linear grating with line orientation and constant period, which correspond to the local orientation and period of the equivalent Fresnel zone plate pattern.

Several parameters like the size of the element, the size of the subfields and the period

[6]To be precise, diameter stands for the diagonal line segment in case of the beamshaping condenser element, which is by construction a square shaped element.

in the outermost gratings are easy to address during the design in order to fulfill the geometrical conditions of the specific experimental station (beam size, focal distance, sample size, active area of the detector). The diagonal of the beamshaping condenser element can be as big as the size of the incoming x-ray beam and the size of the subfields can be changed in order to have a spot size on the focal spot that matches the field of view of the microscope. Typical beamshaping element sides should be from 500 μm to 2 mm, with an outermost zone width from 100 nm down to 50 nm. The size of the subfields, d, could commonly range from 10 to 50 μm, which is the size of the usually required field of views.

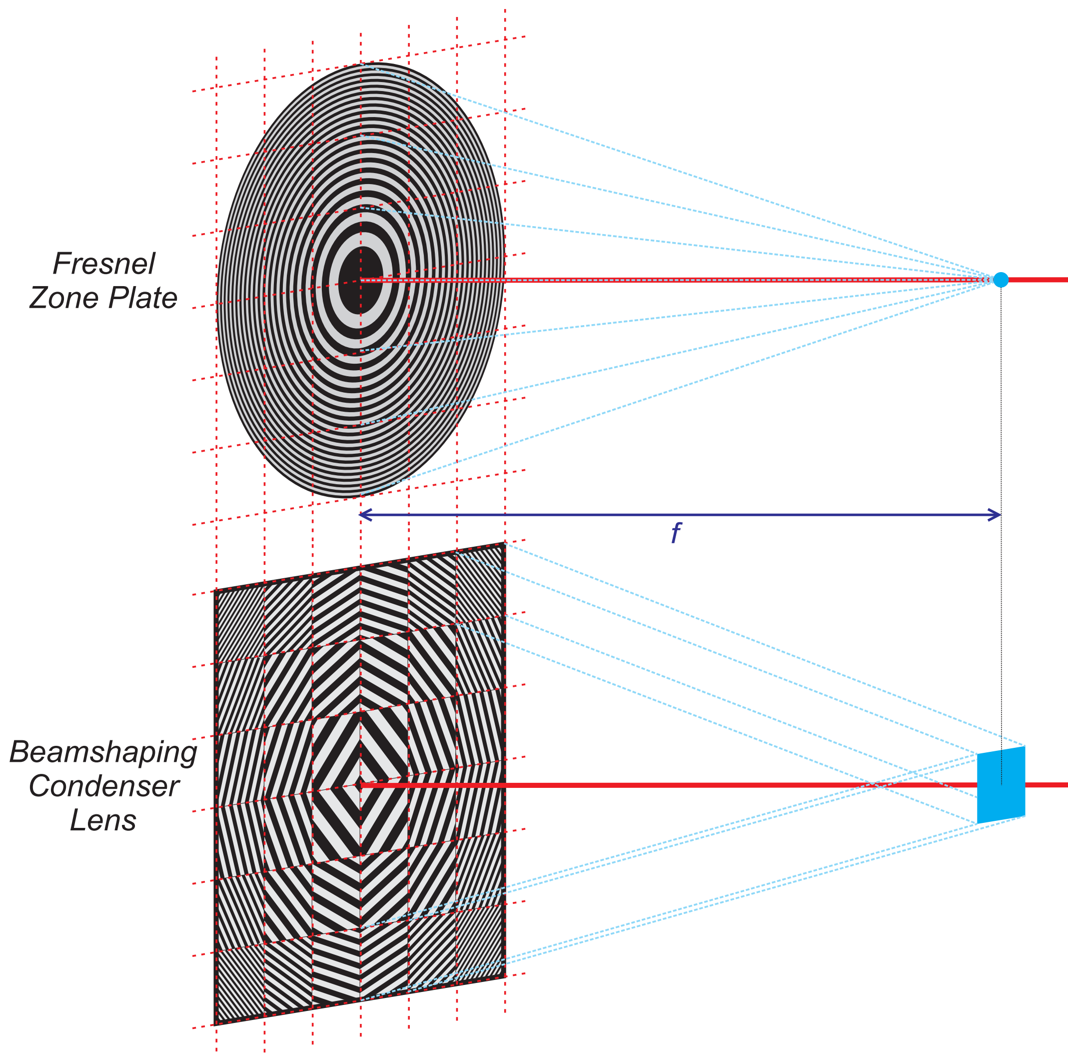

Figure 3.17: The beamshaping condenser lens produces a square spot of uniform illumination at the focal position. The first order diffracted beams coming from each subfield add themselves at the same position where the equivalent Fresnel zone plate has a tiny focal spot.

To have a closer insight to the beamshaping condenser lens, figure 3.18 depicts the scheme of full-field transmission x-ray microscopy setup using this element. As it can be

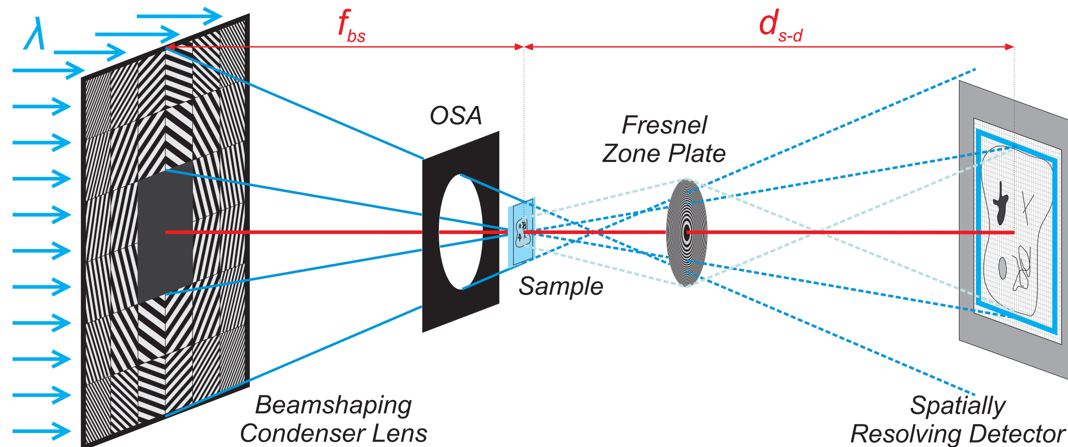

Figure 3.18: Scheme of full-field transmission x-ray microscopy setup using the beamshaping condenser lens to illuminate the sample.

seen, a central stop on the beamshaping element in combination to an order selecting aperture must be added in the setup. They are both necessary to remove the zeroth and the higher diffraction orders so that beyond the order selecting aperture no more light apart from the first order radiation of the beamshaping element is transmitted. The sample is located at the focal distance of the beamshaping condenser lens, and a Fresnel zone plate situated behind works as objective lens and projects a magnified image of the sample on a spatially resolving detector. Notice that due to the limited focusing efficiency of the objective lens not all the radiation that goes through the sample is collected to produce the image on the detector. This fact is schematically shown in figure 3.18 where only very light blue rays are indeed forming the image. Darkish blue rays travel through the Fresnel zone plate without being deflected[7] and they produce one bright peak for each subgrating of the beamshaping lens on the detector. In principle, all this peaks would be uniformly spread in an area around the optical axis hindering the image acquisition on the detector. As a consequence, the use of a central stop is also required to produce a shadow on the detector and to remove these spots from the field of view of the detector. The geometric shadow of the central stop can be easily calculated once the focal length of the beamshaping condenser lens, f_{bs}, and the distance sample-detector, d_{s-d}, are known. In figure 3.18, the shadow of the central stop would fall inside the darkish blue frame drawn on the active area of the detector, which should be perfectly matched for an ideal case.

Thus, we have a beamshaping condenser lens design which is likely to produce a square flat-top spot at the focal plane in order to illuminate uniformly the sample in the field of view of a full-field transmission x-ray microscope.

[7] Zeroth order radiation of the objective lens.

Part II

Nanofabrication Methods and Experimental Results

CHAPTER 4

Electron Beam Lithography

This is the first chapter dealing with the micro- and nanofabrication techniques that are indispensable for the production of Fresnel zone plates and diffractive optical elements for x-ray radiation. A general introduction to these structuring methods can be found in *Ziaie et al.* [27]. Despite these techniques were originally developed for microelectronics, they are now spreading to other scientific fields (like optics, mechanics or biology) and they are used to produce miniaturized systems with amazing functionalities [70].

This chapter intends to give an overview on electron beam lithography techniques emphasizing some details that are more relevant for the patterning of Fresnel zone plate structures and that are not easily found elsewhere. E-beam lithography is used to generate a pattern in a radiation sensitive material layer (resist), which is later transferred to the underlying substrate by several techniques.

Two different e-beam lithography systems were used during the realization of the work presented here. Both systems will be described and compared, pointing out their advantages and drawbacks. We will summarize all the steps involved in the preparation, exposure and development of the resist layer, while the pattern transferring techniques will be extensively treated in the succeeding chapters.

4.1 Introduction to Electron Beam Lithography

Almost any micro- or nanostructuring process starts with the definition of the pattern by means of lithography techniques. In these techniques, electrons, photons or ions are used to locally deliver energy into a thin layer of sensitive material —referred as *resist*—. Energy transferral results in a local change of the solubility properties of the resist layer

when after the exposure the sample is dipped into a developing solution. Either the exposed regions or the non-exposed regions can be removed during the development process depending on the particular resist and lithography technique. One distinguishes between *positive resists*, when the exposed regions are removed, and *negative resists*, when the non-exposed regions are cleaned. After the development, the pattern with a given size, shape and details, as small as 10 nm in case of e-beam lithography, is ready to be transferred to the underlying substrate by several processes of etching or deposition techniques.

A general and complete overview on electron beam lithography can be found in *McCord* & *Rooks* [75]. In an e-beam lithography system a beam of electrons is generated by a small metal tip or filament, usually referred as *electron gun*. By travelling through several *electromagnetic lenses* and *apertures*, the original electron beam is prepared and focused before impinging on the sample. In addition, there is also an *electromagnetic deflection system* which is used to deviate the electron beam with extreme placement accuracies of a few nanometers (1 — 20 nm). The electron beam is sequentially deflected to draw the requested pattern on the resist layer. Another important component in any e-beam lithography tool is the *beam blanker*, which deflects the electron beam at very high frequencies in order to prevent it from reaching the sample. Thus, the beam blanker controls the exposure times and determines the minimum dose that can be delivered for a given current intensity.

Comparing to other lithography techniques, e-beam lithography provides the highest resolution being the smallest details ever patterned under 10 nm [71]. Despite optical lithography has the advantage that a whole pattern is exposed in a single step, resulting in a much higher throughput in comparison to a sequential e-beam exposure, only details in the submicron range can be depicted. Deep ultraviolet (DUV) lithography using a wavelength of 193 nm from ArF excimer laser is currently used to pattern computer microprocessors with features down to 65 nm half-pitch[1]. On the other hand and due to shorter wavelength, extreme ultraviolet (EUV) lithography is becoming a competitor of e-beam lithography in terms of resolution [72]. Ion lithography [73] can also be used to expose very thick resist layers ($\sim$10 μm) but its resolution in the micrometer[2] range precludes its use for the fabrication of Fresnel zone plate lenses.

Fresnel zone plate lenses and diffractive optical elements for x-ray radiation have been almost exclusively produced by means of e-beam lithography because very high accuracy in the placement of the zones is required, and as discussed in the previous chapters the resolution of the elements is totally determined by the outermost zone width which must be as narrow as possible. Nevertheless, Fresnel zone plate fabrication using EUV radiation is under development [63] and focused ion beam systems have been already used [74].

[1]Even smaller features (down to 32 nm half pitch) are expected to be patterned using immersion DUV lithography that replaces the usual air gap between the final lens and the wafer surface with a liquid medium that has a refractive index over 1.

[2]However, there are efforts to obtain resolutions in the sub-50 nm using non-commercial lithography tools under development.

During an e-beam exposure the electron beam is deflected inside a given region of the sample, i.e. the *writing field* which is typically as large as few hundred of micrometers. In case of bigger patterns, they have to be split in subfields which are exposed sequentially. This approach is usually referred as *field-stitching*. Due to inaccuracies in sample stage movement and in the deflection system, one usually gets some overlap or gap between the contiguous subfields. These errors may occur with a periodicity given by the size of the stitching-field and for the production of diffractive optical elements such periodic errors can cause problems as they result in unwanted diffraction artifacts of the optical device. An example of stitching errors can be appreciated in figure 4.1(a), where a linear Fresnel zone plate was exposed on PMMA resist layer.

Another usual problem in e-beam lithography systems is the *proximity effect*. When the electron beam reaches the resist layer, the primary and secondary electrons are scattered by the resist layer and by the substrate. As a result, the energy and dose delivered by the electron beam, which was supposed to be confined to the shapes that the lithography system is depicting, is indeed spread over a much wider region resulting in pattern specific line width variations, known as the proximity effect. Typically proximity effects can be observed at the edges of the patterned structures. Proximity effect error can be observed in figure 4.1(b) where the very last line was exposed with the same dose of the contiguous ones but turns to be much narrower.

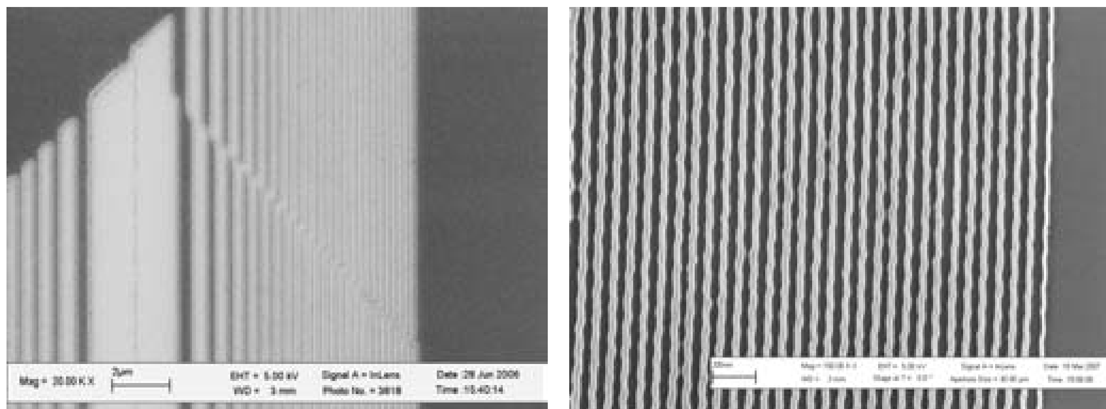

(a) Stitching Error. (b) Proximity Effect.

Figure 4.1: (a) When exposing patterns larger than the writing field, stitching errors can arise. (b) Despite the very last line was exposed with the same dose of the contiguous ones, it turns out to be much narrower due to the proximity effect.

During the realization of this work two different e-beam lithography systems were used. They are introduced in the next sections. The results of their exposures are also presented later in this chapter.

4.1.1 LEO 1530 SEM RAITH ELPHY PLUS System

One of the e-beam lithography tools used is a system based on a LEO 1530 scanning electron microscope (SEM) and RAITH ELPHY PLUS controller and software [76].

This system is installed at *the Nanofabrication Laboratory* in the *Centro Nacional de Microelectrónica* in Barcelona (Spain). The scanning electron microscope LEO 1530 has an electron gun based on Schottky field-emission cathode which provides a very stable electron current and has a wide working range of electron beam energies from 100 eV to 30 keV. Nominal resolution, that is, beam size focused on the sample, is 1.0 nm at 20 KeV and 2.1 nm at 1 keV. Several apertures (7.5, 10, 20, 30, 60 and 120 μm) are available so that several current intensities can be selected. Two detectors are disposable, they are both sensitive to the secondary electrons generated in the sample by the primary beam. One of them is located inside the electron optical column, and is usually referred as *InLens detector*. This detector is suitable when using short working distances[3]. A second detector, referred as *SE2 detector*, is appropriate when using long working distances and high electron beam energies. It is located sideways next to sample stage. All scanning electron microscope functions are controlled by a computer software that runs under Windows NT. LEO 1530 SEM electron optical column is schematically shown in figure 4.2a).

The subsystem for the e-beam lithography tool consists of a beam blanker and a deflection unit installed by Raith GbmH. The beam blanker applies a 200 V voltage that abruptly deflects the electron beam to avoid its impingement on the sample with a maximum frequency of 2.6 MHz so that the minimum exposure time is around 0.00385 ms. Beam deflection during the exposures is controlled by ELPHY PLUS software which also includes routines for the design of the patterns to be exposed and for the calibration of the system before each exposure. GDSII data format is the standard file format for the pattern generation. A Faraday cup that must be manually pushed into electron beam trajectory is available to measure the current intensities just before the exposure begins.

4.1.2 Leica LION LV-1 E-Beam Lithography System

A Leica LION LV-1[4] electron beam lithography system was also used within this work [75, 77, 78]. This system is installed at the *Labor für Mikro- und Nanotechnologie* at the *Paul Scherrer Institut* in Villigen (Switzerland). A SEM electron optical column allows electron energies ranging from 1 to 20 keV and provides a gaussian beam with spot sizes as small as 5 nm at 1 keV and 3 nm at 20 keV. LION LV-1 electron optical column is shown in figure 4.2b). Low electron energies are suitable to avoid both substrate damage and proximity effect complications. An interferometric sample stage equipped with an He-Ne laser ensures a positioning accuracy of 10 nm. Beam deflection system is controlled by a built-in pattern generator allowing the exposure of several types of data formats (GDSII, BITMAPS. . .). In addition this system has a unique exposure mode —a continuous path control (CPC)— which allows the writing of curved lines without stitching errors. In this exposure mode the sample stage is moving under the electron

[3]The working distance is the length between the end of the electron optical column and the sample, typically ranging from 2 to 20 mm.

[4]LION LV-1 stands for Lithography for Integrated Optics and Nanostructures — Low Voltage 1 keV.

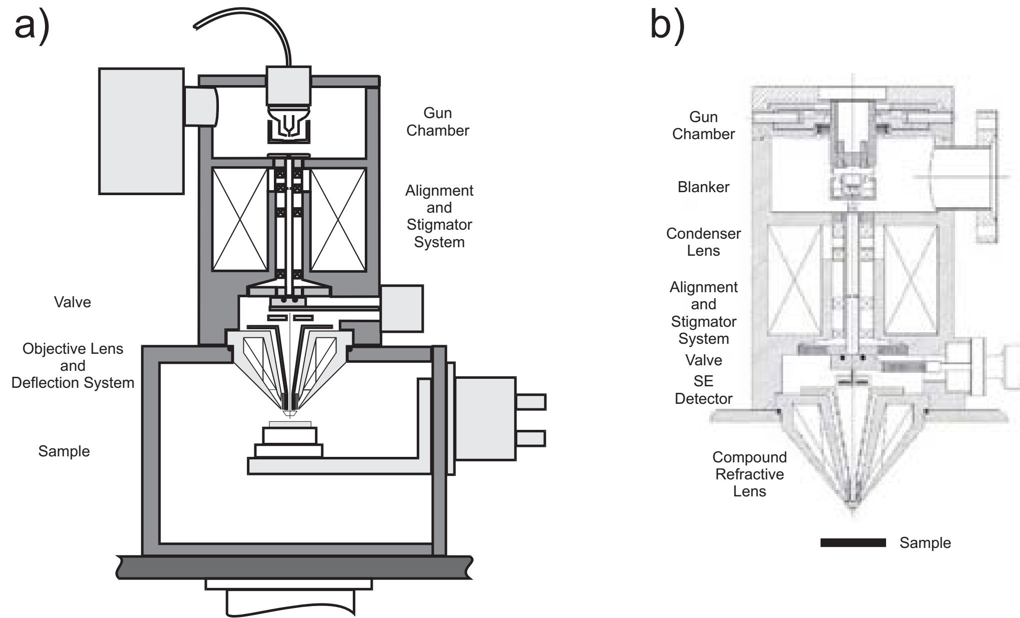

Figure 4.2: Electron optical columns of the e-beam lithography systems: **a)** LEO SEM 1530 column and **b)** LION LV-1 column. Note that both equipments are very similar.

beam, and the mechanical movement inaccuracies of the stage which are measured by the interferometric system are on-the-fly corrected by the pertinent deflection of the electron beam. The remaining deviations from the ideal electron beam path according to the pattern design are under 10 nm and they are not at all periodic as the case of stitching fields. CPC exposures in LION LV-1 tool require a very special file format that will be explained in the next sections.

Figure 4.2 shows that both electron lithography systems are indeed very similar. However, the interferometric stage of LION LV-1 tool turns out to be very useful to expose large patterns with high accuracies in the positioning which are not expectable in the LEO 1530 SEM system[5], which is not an exclusively dedicated system to lithography.

4.2 Electron Beam Lithography Exposure

In this section we describe the procedures involved in any e-beam lithography exposure which include the resist preparation, the pattern design and generation and the exposure itself. Since two different e-beam lithography tools were used, two different exposure strategies will be presented.

[5]Due to columns specifications smaller features can be patterned using the LEO 1530 SEM system, which is a newer equipment.

4.2.1 Resist Layer Preparation

A requirement for almost any lithography technique is the ability of preparing resists layers of uniform and well-specified thickness with high reproducibility. This is commonly accomplished using spin-coating techniques, in which a drop of resist/solvent[6] solution is applied onto the substrate and immediately distributed by rotating the substrate at high speeds. Most of the solvent is expelled from the substrate and the resulting resist layer is highly uniform and its thickness is exclusively determined by the solution composition and the rotational speed[7]. Immediately after spin-coating most of the resist layers must be baked in an oven or in a hot plate to outgas the residual solvent and to enable the relaxation of the strain within the resist layer. Resist layer thicknesses were measured with an ellipsometer or with a profilometer[8].

Polymethyl Methacrylate (PMMA) and Calixarene resists were used in the exposures. PMMA was one of the first materials developed for e-beam lithography. It is an organic polymer with molecules typically composed of 10000 monomers, which solid form is commonly referred as acrylic glass. When the electron beam impinges onto a PMMA layer, the extreme long molecules are broken and in consequence the exposed regions become soluble in an appropriate developer, such as methyl isobutyl ketone (MIBK). Therefore, for moderate doses, PMMA resist is positive. PMMA in two molecular weight forms (950k or 495k) dissolved in anisole or chlorobenzene were used. Since MIBK turns out to be a too strong developer, a mixture of it with isopropyl alchohol (IPA) is more commonly used. 1:3 MIBK:IPA solution produces a very high contrast, which is very appropriate for high resolution patterning. Temperature control is very important during the development since a variation of a few degrees destroys the reproducibility of the process. PMMA layers were always developed with solutions at 23°C.

Thicknesses of the resulting PMMA layers for a given solution and spinning speed are usually determined experimentally. Curves shown in figure 4.3 give the thickness PMMA layers as function of rotational speed for several solutions. PMMA spin coated samples were usually baked at 180°C in a hot plate for 3 min.

The use of Calixarenes as a high resolution negative resists was firstly suggested by *Fujita et al.* [79]. Calixarenes are nonpolymer materials which have a cyclic structure and are roughly ring-shaped molecules about 1 nm in diameter. They are commonly dissolved in o-dichlorobenzene. Calixarene resists are around 20 times less sensible than PMMA. Within this work, their use was required to expose sub-50 nm lines as will be later discussed. Calixarene solution was spin coated on the silicon substrates at 3000 rpm and baked at 90°C in a hot plate for 3 min to obtain a layer thickness of 20 nm. In order to ensure enough adherence of the resist, an oxygen plasma etching was applied on

[6]Electron sensitive material is dissolved in a solution. When the solution is spread on a surface substrate, a thin layer layer of electron sensitive material is formed.

[7]Providing that sufficient amount of solution is dropped on the substrate and that the rotational acceleration is enough high to reach the final rotational speed before the final layer thickness is reached.

[8]By scratching the resist layer at one corner of the chip.

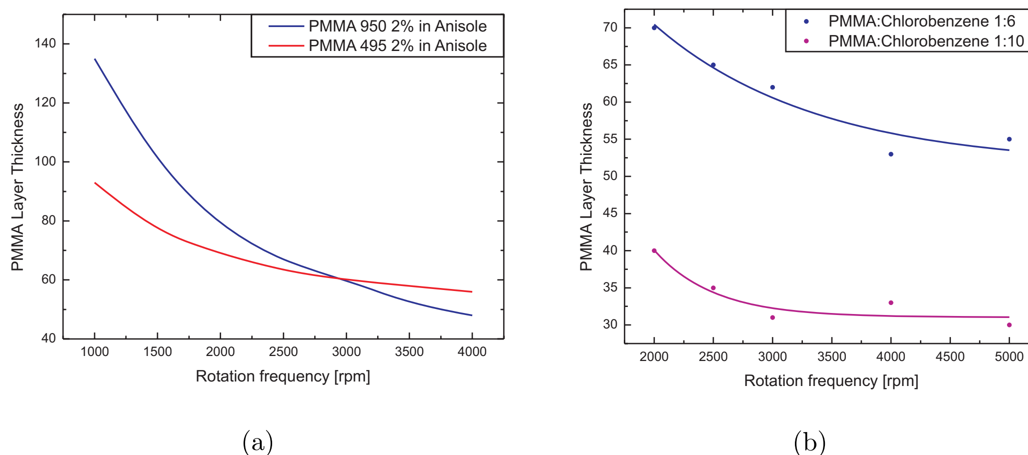

(a) (b)

Figure 4.3: (a) PMMA solution in anisole, around 100 nm thickness can be achieved, from the manufacturer. (b) PMMA solutions in chlorobenzene, layer thicknesses from 50 down to 35 nm can be obtained, experimentally determined.

the substrates for 30 s just before the spinning process. After the exposure Calixarene layers were developed in pure IPA at 20°C for 30 s and dried with a N_2 blow.

4.2.2 Fresnel Zone Plate Exposure Strategies

As explained in chapter 2, a Fresnel zone plate pattern consists of concentric rings with decreasing widths as the radius increases. In this section we introduce the two different approaches for the pattern generation, one for each one of the e-beam lithography systems that were used.

4.2.2.1 LEO 1530 SEM RAITH ELPHY PLUS System

During the fabrication trials at *the Nanofabrication Laboratory* in the *Centro Nacional de Microelectrónica* in Barcelona, we were pursuing the exposure of relatively thick resist layers (∼ 200 nm) which could be later used as a mold during the metal deposition (by evaporation or electroplating) to produce the final Fresnel zone plate pattern.

Raith pattern generator installed in the LEO 1530 SEM uses a gaussian beam with a *vector scan* mode[9]. The Fresnel zone plate pattern design was prepared as GDSII file format using the ELPHY PLUS software. Structures can be defined using polygonal areas or single pixel lines. When polygonal areas are used, the pattern generator divides the region and its parts are scanned sequentially. When single pixel lines are exposed the beam is deflected sequentially following a linear path. After several exposures using both approaches, it was established that the single pixel line mode was faster and more

[9] In this exposure mode the beam is only scanned over the areas that are indeed exposed in contrast to the *raster scan* mode, in which the beam is scanned sequentially over the full writing field and the exposure is controlled by switching on and off the beam.

accurate for lines under 300 nm. Exposure approach is shown in figure 4.4. Since the dose delivered to each individual line was quite low and in order to expose thicker lines several single pixel lines were concentrically scanned. Lateral distance between two consecutive lines and distance to edge of the zone according to the design were taken as parameters. The dose for each individual line could also be controlled.

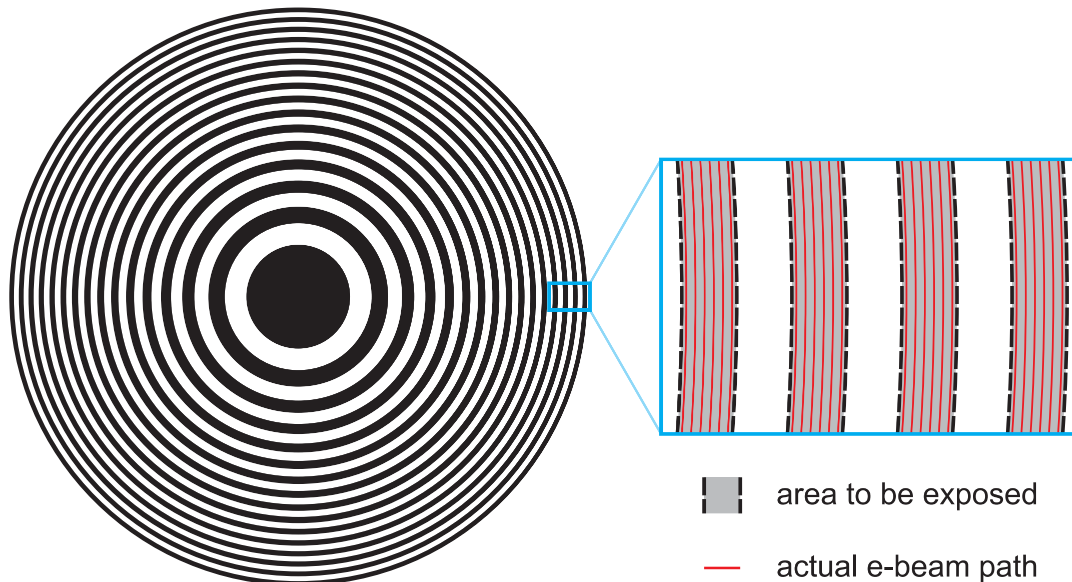

Figure 4.4: Exposure strategy for the LEO 1530 SEM RAITH ELPHY PLUS system. Each zone is made of a set of single pixel lines which are consecutively exposed.

During the first trials, when exposing 100 nm thick resist layers, an electron energy of 10 keV was used. Later, when using 200 nm thick resist layers, the electron energy was switched to 20 keV and the dose was suitably increased[10]. Despite 100 nm lines were exposed several times, reproducibility problems were encountered when exposing lines in the sub-200 nm range. These difficulties mainly come from the lack of system that controls the distance between the sample and the electron optical column. This way, the field alignment and preparation of the beam is done manually and becomes critical when exposing extremely small features. Resist layer details and exposure parameters of the machine for more successful exposures are presented in table 4.1.

As it can be observed in the table, the e-beam exposure was done on a bilayer combining PMMA resists of two molecular weights. A layer of PMMA 950k was spun

[10]Higher energies must be used to expose thicker resist layers. The dose has to be increased, since solubility changes in the resist layer are produced by the secondary electron with energies from 2 to 50 eV. Secondary electrons are produced when the primary electrons slow down inside the resist layer. Low electron beam energies translate into a higher production of secondary electrons and less dose is required despite only very thin resist layer can be exposed. However, higher electron beam energies also translate into an increase of the proximity effects since the primary electrons can be scattered several times before completely losing their energy.

E-BEAM LITHOGRAPHY PARAMETERS	
Substrate	Si chip 1 cm $\times$ 1 cm
Resist	PMMA 495k + PMMA 950k 2% anisole
Resist thickness	90 nm + 200 nm spun at 1500 rpm
Electron beam current	192.0 pA
Electron beam energy	20 keV
Doses	300, 350, 400, 450 pC/cm
Step size	5 nm
Dwelltime	0.78, 0.91, 1.04, 1.12 μs
Column aperture	20 μm
Z stage position	15.500 mm
Working distance	8.880 mm
Exposure field	100 μm $\times$ 100 μm
Magnification	1500

Table 4.1: Exposure parameters for the e-beam lithography performed with the LEO 1530 SEM RAITH ELPHY PLUS system.

on a PMMA 495k layer. Lower molecular weight PMMA layers require less dose to be exposed. After several trials, it was realized that in order to achieve aspect ratios above 2 for 100 nm wide lines the use of combined PMMA bilayer was preferable to the use of a single PMMA 950k layer of the same thickness. A feasible explanation to this fact takes into account that we were using an electron beam energy of 20 keV. The broadening of the exposed lines because of the proximity effect increases at higher electron beam energies. However, the use of less dense low molecular weight PMMA resist at the bottom reduces the scattering of the electrons in the resist which at the same times reduces the undesired proximity effects in the patterned structures. A complementary feasible explanation could be the generation of a large undercut between the PMMA 950k and the PMMA 495k layers during the development due to the lower critical dose required for the PMMA 495k layer.

4.2.2.2 Leica LION LV-1 E-Beam Lithography System

During the exposures carried out at *Labor für Mikro- und Nanotechnologie* at the *Paul Scherrer Institut*, we intended to pattern the structures on very thin resist layer (typically $\leq$ 50 nm) which were later transferred to an underlying material layer. This was very convenient since we were operating the LION LV-1 e-beam tool at an electron beam energy of 2.5 keV. Thick resist layers can not be exposed at this energy when we are intending to obtain lines widths in the sub-100 nm range. As a matter of fact, such a low electron beam energy implies that only aspect ratios below 2 are feasible and, as a consequence, only very thin resist layers can be exposed at high resolution.

To expose the Fresnel zone plate structure consisting of concentric rings which are

densely patterned at the outermost regions, we were using the Continuous Path Control (CPC) exposure mode of the LION LV-1 e-beam tool. This exposure mode is a very specific attribute of this system. Within LION-software *only* rational Bézier curves [80] (of 1st, 2nd and 3rd order) can be used to define the path of the electron beam during a CPC mode exposure and as a result a very particular input data format is required [78]. Basically, the pattern must be decomposed in rational Bézier curves which parameters must be written in a suitable ASCII-text-format. As described by *Nöhammer* [78], a circle can be decomposed with minimum of 3 rational Bézier curves of 2nd order. LION LV-1 input data files were automatically generated with Matlab scripts which took as input the defining parameters of the Fresnel zone plate structure.

The second important characteristic of the CPC mode of the LION LV-1 e-beam tool concerns the line width control. During the exposure of a Fresnel zone plate each ring is exposed by a single electron beam pass, since the actual line width of each ring is controlled by changing the dose and the electron beam defocus as described by *Nöhammer* [78], and *David* & *Hambach* [81]. Figure 4.5 schematically shows this exposure strategy. When exposing a line with a given linear dose, D_l, and a defocus, d_f, only the region of the resist layer that receive a dose above a critical value, D_c, will be removed during the development. As a result, the line width is both controlled by the linear dose and the electron beam defocus. Detailed mathematical expressions describing these relationships can be encountered in the above mentioned references. They were implemented in the Matlab scripts to generate the input files for the LION LV-1 e-beam tools and some of the parameters were slightly adjusted until optimal exposed patterns were obtained.

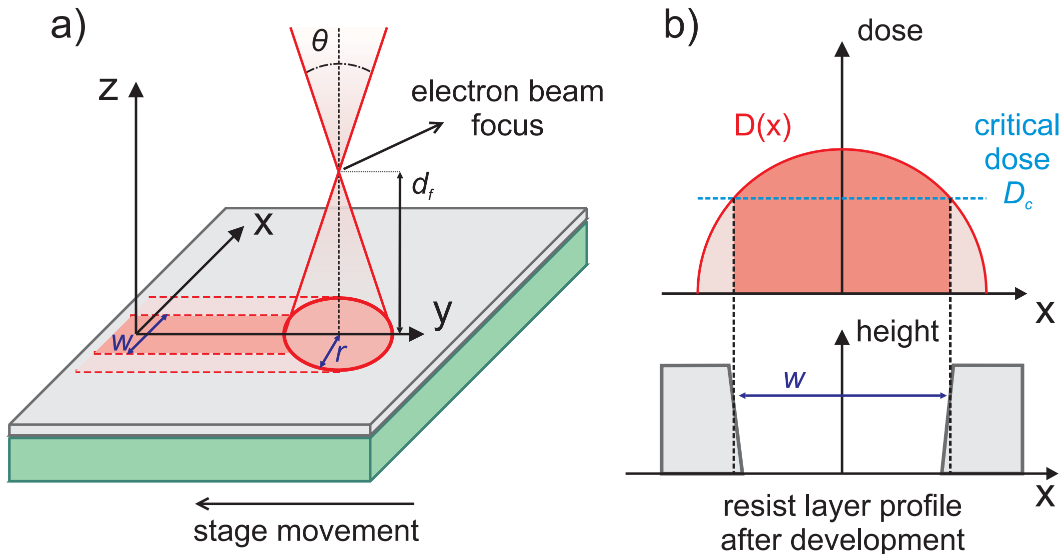

Figure 4.5: LION LV-1 e-beam system exposure strategy. **a)** Scheme showing the line width control for a CPC mode exposure with the LION LV-1 e-beam tool. **b)** Only the region that receive a dose above the critical dose, D_c, will be removed during the development.

Figures 4.6 and 4.7 show the optimal linear dose, D_l, and electron beam defocus, d_f, that was applied to expose a 100 μm diameter Fresnel zone plate patterns on PMMA and Calixarene resist layers with the LION LV-1 e-beam tool.

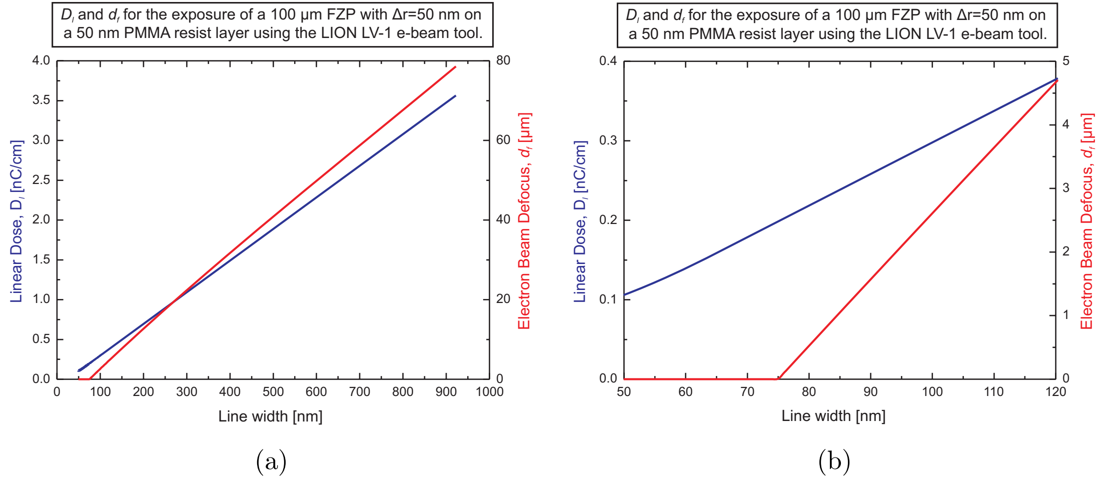

Figure 4.6: Optimal linear doses, D_l, the electron beam defocuses, d_f, as function of line width that were applied to expose a 100 μm diameter Fresnel zone plate patterns on 50 nm PMMA resist layer with the LION LV-1 e-beam tool. (a) Full line width range. (b) Detail for the sub-120 nm line width range.

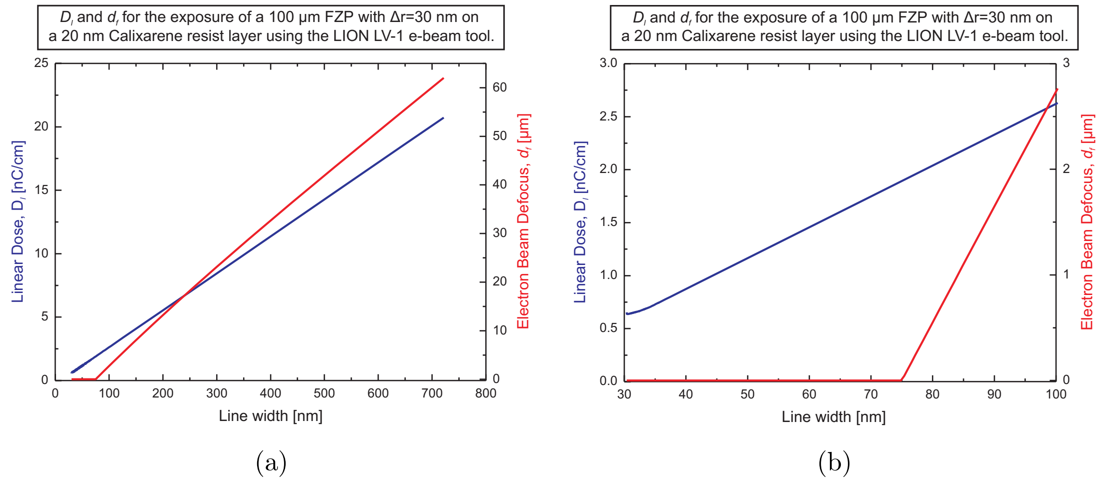

Figure 4.7: Optimal linear doses, D_l, the electron beam defocuses, d_f, as function of line width that were applied to expose a 100 μm diameter Fresnel zone plate patterns on 20 nm Calixarene resist layer with the LION LV-1 e-beam tool. (a) Full line width range. (b) Detail for the sub-100 nm line width range.

One should notice that we were able to pattern smaller features using Calixarene resist, since a 20 nm thick Calixarene layer is almost 12 times less sensitive than a 50 nm thick PMMA layer. In order to justify this point, some more details about the LION LV-1 e-beam tool must be explained. In one hand, the delivered linear dose is the quotient between electron beam current and the sample stage velocity. On the

other hand, when exposing a given pattern, the sample stage is moving in a square grid with a fixed step size (typically, 10 or 5 nm for high resolution applications). The sample stage velocity can achieve a maximum value of 1 mm/s when using a step size of 10 nm and 0.5 mm/s for a step size of 5 nm[11]. Considering a given electron beam current, the maximum stage velocity determines the minimum linear dose that can be delivered by the machine, thus giving the minimum feature size that can be patterned. When exposing features in the sub-50 nm, a 5 nm step size is mandatory. However, the decrease in the maximum stage velocity, put up the minimum dose that can be delivered and a less sensitive resist layer is required to expose features of a given size.

When exposing Fresnel zone plate patterns with outermost regions in the sub-50 nm range it was realized that the line width was varying periodically as a function of the azimuthal angle, θ. This effect has to do with the sample stage movement during the exposure, which is limited to individual points of the square grid with a given step size. As shown in figure 4.8, when exposing a short segment l at an angle θ, the actual exposure path can decomposed as the sum of segments a and b.

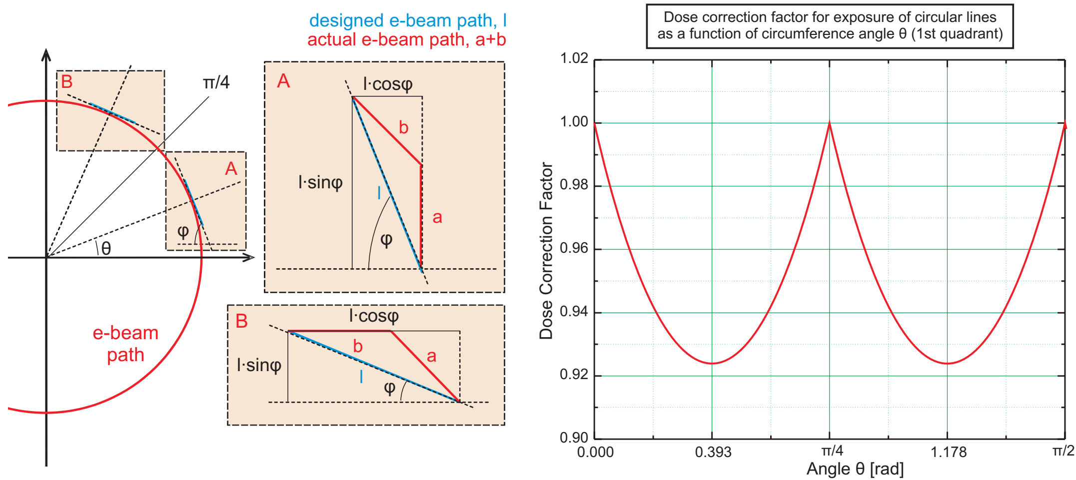

Figure 4.8: Dose correction factor required from the fact that the sample stage movement is limited to a discreet square grid of points in the LION LV-1 e-beam tool.

One of the segments corresponds to stage movement in a parallel direction of the square grid, while the other one corresponds to stage movement in diagonal direction. Line width variation is originated due to the fact that $l \leq a + b$. Complementary, one can also consider that the square grid in which the sample stage is moving introduces a linear dose variations depending on the direction. When exposing very narrow and dense lines (as small as 30 nm lines/spaces), this linear dose variations become critical up to the point that structures are not well patterned. This can be corrected by splitting the circular lines in pieces and introducing a dose correction factor, D_{cor}, which is given

[11]This limitation arises from the working frequency of the electronics that controls the systems involved in the e-beam exposure.

by

$$\text{in case A, } 0 < \pi/4 \quad D_{cor} = \frac{l}{a+b} = \frac{1}{\cos\theta + \left(\sqrt{2}-1\right)\sin\theta} \tag{4.1}$$

$$\text{in case B, } \pi/4 < \pi/2 \quad D_{cor} = \frac{l}{a+b} = \frac{1}{\sin\theta + \left(\sqrt{2}-1\right)\cos\theta} \tag{4.2}$$

The dose correction factor, D_{cor}, as function of the azimuthal angle θ is represented in figure 4.8 for angles ranging from 0 to $\pi/2$. The maximum dose correction, $D_{cor} = 0.924$, is needed for angles $\theta = \frac{\pi}{8}(1 + n/2)$ with n=1, 2, 3, 4, 5, 6, 7, 8. Splitting of the circular path for each ring of the Fresnel zone plate and the corresponding dose correction factor was implemented in the Matlab script that was generating the input data files for the LION LV-1 exposures. A substantial improvement was obtained when patterning 100 μm diameter Fresnel zone plates with an outermost zone width of 30 nm (further details can be encountered in section 6.2.2).

One of the strongest points of the LION LV-1 e-beam tool is the high reproducibility during the exposures. This asset results from the fact that the machine has a system to accurately control the distances between the end of the electron optical column and the sample. This system is essential to apply the appropriate electron beam defocus during the exposure. In addition, there exists a well defined operation protocol to prepare and calibrate the machine just before each exposure.

4.3 E-beam Exposure Results

Whenever it was possible the samples were developed just after the exposure. Since they degradate under the scanning electron microscopy (SEM) inspection, they were hardly ever observed at this stage.

4.3.1 LEO 1530 SEM RAITH ELPHY PLUS System

After the exposure the samples were manually developed dipping them into a solution of 1:3 MIBK:IPA for 45 s and rinsed in pure IPA for another 45 s. The samples were dried by a N_2 blow. Since the exposed resist layer was relatively thick longer developing times were used in some cases.

Since the PMMA layer was meant to be directly used as a mold during the metal deposition, a reactive ion etching of O_2 was used to totally remove the resist remains of the exposed areas, which could hinder the metal adherence to substrate. From the metal structures that were generated following the methods extensively described in chapter 5, one can infer that 100 nm lines were properly patterned in a 250 nm PMMA resist layer. This is shown in the gold structures from figure 4.9.

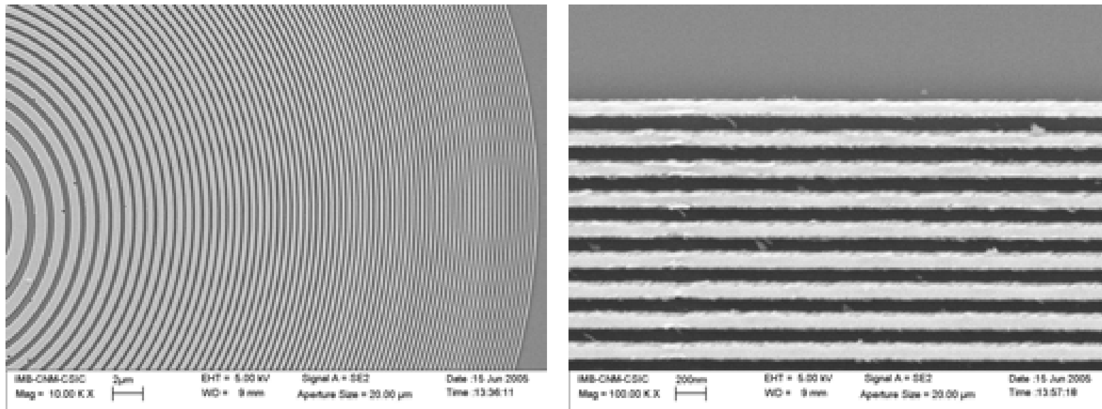

Figure 4.9: Scanning electron micrographs of gold patterns when using PMMA molds exposed by the LEO 1530 SEM RAITH ELPHY PLUS system. 100 nm lines/spacings were produced.

4.3.2 Leica LION LV-1 E-Beam Lithography System

In the *Labor für Mikro- und Nanotechnologie* all the exposed PMMA resist samples were developed using a HAMATECH (Steag-Hamatech HME 500) developing machine, providing a fully automated and highly reproducible processing. In a first step the samples were sprayed with a 1:3 MIBK:IPA solution for 30 s while rotating at moderate speed to ensure a uniform spreading of the developing liquid. In a second step the sample was rinsed with pure IPA and afterwards dried by rotating the sample at high speed. The machine was accurately controlling all the parameters that are essential for the development process (time, temperature, solution compositions. . .).

As mentioned above, the patterned structures in the thin PMMA layer were transferred to an underlying material layer. Specifically, we were using a thin chromium layer of 20 nm, and the e-beam exposed pattern was transferred by dry etching. A BMP Plasmafab 100 from BMP was used for this process. A reactive ion etching chlorine-based process with 1:1 Cl_2:CO_2 plasma was the standard technique for transferring a pattern into the chromium layer, while using the exposed PMMA layer as a mask. Typical etching times range from 40 to 60 s. Main parameters concerning this process are summarized in table 4.2.

E-beam exposures were usually inspected with a scanning electron microscope after the chromium mask etching, since this layer is not damaged by the electron beam. PMMA exposed Fresnel zone plate patterns transferred into the chromium layer are shown in figures 4.10 and 4.11. 50 nm lines are perfectly patterned at the outer regions of a 100 μm diameter structure.

When Calixarene resist was used during the e-beam exposure, the samples were manually developed by dipping them into pure IPA at 20°C for 30 s and dried with a N_2 blow. After several trials to adjust the linear doses that should be delivered to the Calixarene resist layer, we were able to expose Fresnel zone plate patterns with outermost line widths as small as 30 nm. In particular, figure 4.12 shows a successful exposure of a 100 μm diameter structure with an outermost zone width of 30 nm.

Chromium Reactive Ion Etching	
CO_2 Flow	100 sccm
Cl_2 Flow	100 sccm
Pressure	260 mTorr
Temperature	300 K
DC Bias	$\sim$ 0 V
Time	40 — 60 s
Etching Rate	$\sim$ 0.5 nm/s

Table 4.2: Main parameters in the chlorine-based reactive ion etching for the pattern transfer into the chromium layer.

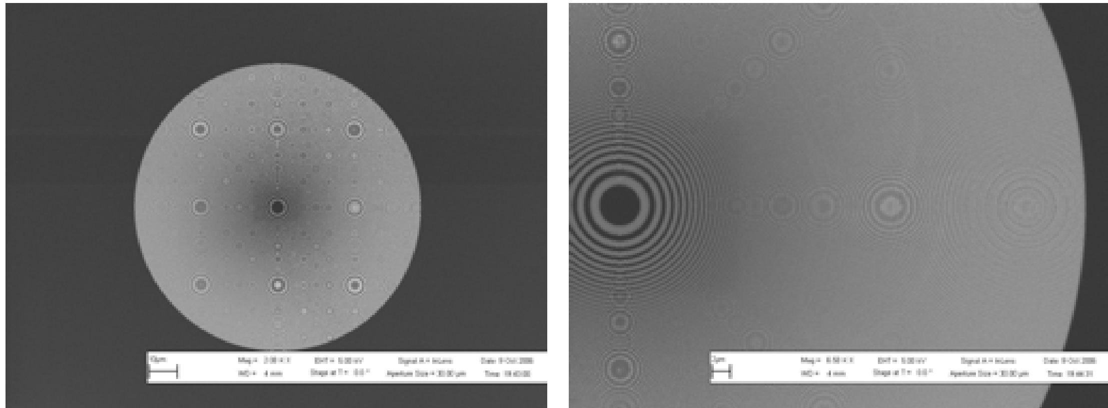

Figure 4.10: General views of a PMMA exposed Fresnel zone plate pattern transferred into an underlying chromium layer. The diameter of the structure is 100 μm and the total number of zones is 504.

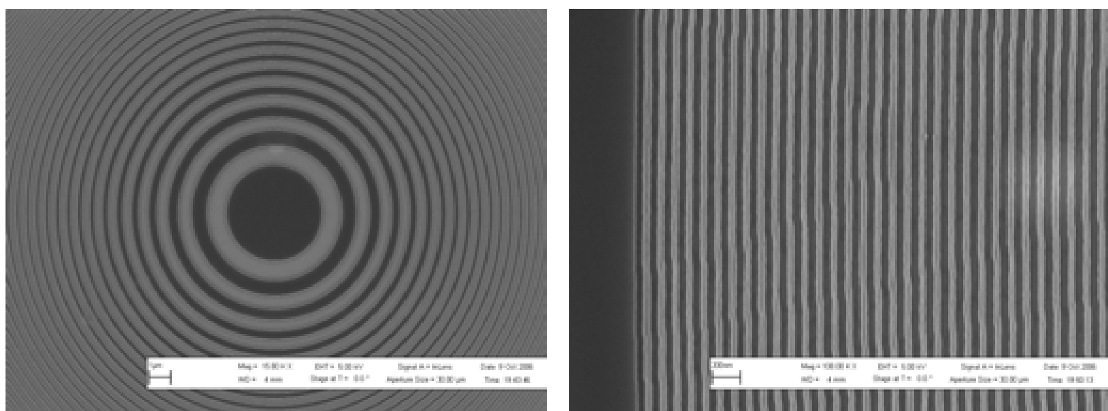

Figure 4.11: Detail of the central and the outermost regions of a PMMA exposed Fresnel zone plate pattern transferred into an underlying chromium layer. Outermost zones of 50 nm are perfectly patterned.

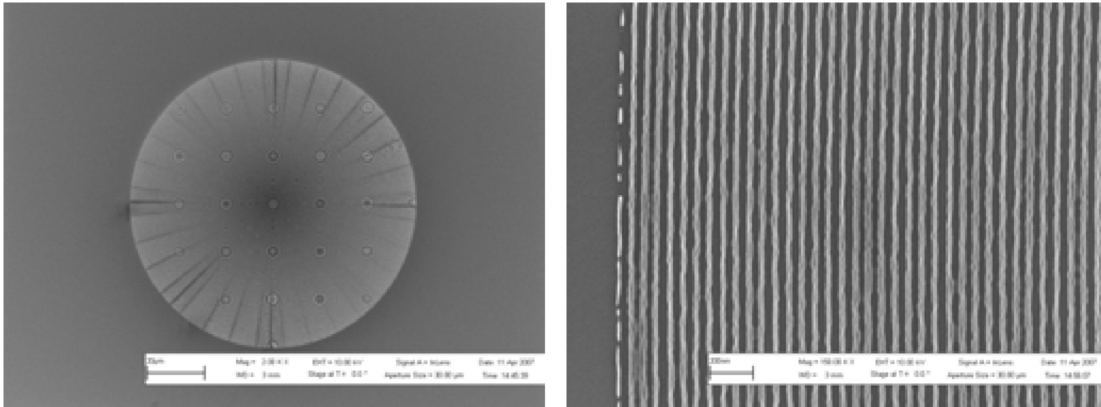

Figure 4.12: General view and detail of a Calixarene exposed Fresnel zone plate pattern transferred into an underlying chromium layer. The diameter of the structure is 100 μm and the outermost zone width is 30 nm.

Calixarene exposures were not as reproducible as the PMMA exposures, since we were pushing the fabrication process to its limit. As a matter of fact and after many trial-and-error tests to determine the optimal exposure doses, only half of the e-beam exposure were successful enough for further processing, which is a very reasonable throughput indeed. One of the difficulties when exposing Fresnel zone plates with extremely narrow outermost zones is that the lines are densely patterned. As suggested when explaining about the proximity effects, while e-beam tools such as LION LV-1 are capable of writing with nanometer spot sizes and position accuracies, the obtainable structure sizes are indeed determined by the range of secondary electrons created in the resist layer. The effect of the electron beam broadening in the resist layer has particularly detrimental consequences when writing dense patterns of lines such as in Fresnel zone plate. In fact, much narrower but less dense lines were patterned in Calixarene resist during the dose adjustment trials. Figure 4.13 shows 10 nm wide lines with a 50 nm period exposed in a Calixarene resist layer and transferred into the chromium layer.

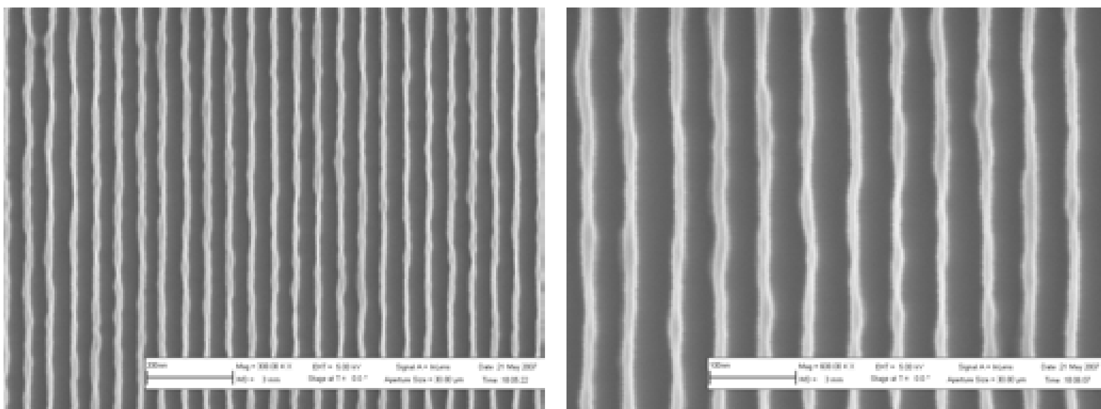

Figure 4.13: 10 nm wide lines with a period of 50 nm exposed in a Calixarene resist layer and transferred to chromium layer by reactive ion etching.

CHAPTER 5

Nickel Fresnel Zone Plates

Once the Fresnel zone plate structure has been patterned into the resist layer several techniques can be used to generate the final functional x-ray focusing structure. In this and following chapters, we will be describing several fabrication approaches to this purpose.

As discussed in section 3.1.3, nickel is a very suitable material to focus soft x-ray radiation. From the theoretical analysis, a Fresnel zone plate made of nickel with zone thickness of 230 nm is expected to have a diffraction efficiency of 23% at 500 eV photon energy. We will explain in detail three different fabrication processes for the production of nickel structures. One of them is based on metal evaporation, while the other two are using metal electrodeposition. Metal electrodeposition (also referred as electroplating) has been one of the most successful approaches to manufacture Fresnel zone plates [48, 49, 53, 82].

Despite some structures were patterned on thin membranes so that they were ready to be used, no experiments were done in order to check the performance of these lenses in an x-ray beamline. However, images from scanning electron microscopy inspections will show the effectiveness of the manufacturing processes.

5.1 Nickel Evaporation and Resist Lift-off

A first very simple approach that was used to generate metal structures as small as few hundreds of nanometers was the metalization through evaporation, using the prepatterned structure on an e-beam exposed PMMA resist mold. This manufacturing procedure, based on a lift-off process, is shown in figure 5.1 and was developed in *the*

Nanofabrication Laboratory in the *Centro Nacional de Microelectrónica* in Barcelona (Spain). During the lift-off after the *metal evaporation*, the resist is dissolved in the appropriate solution, and only the metal structures attached to the substrate remain. The process entails some difficulties during the removal of the resist since the metal that has been deposited on the ridges of the resist layer sometimes prevents the dissolving liquid from reaching the resist structure.

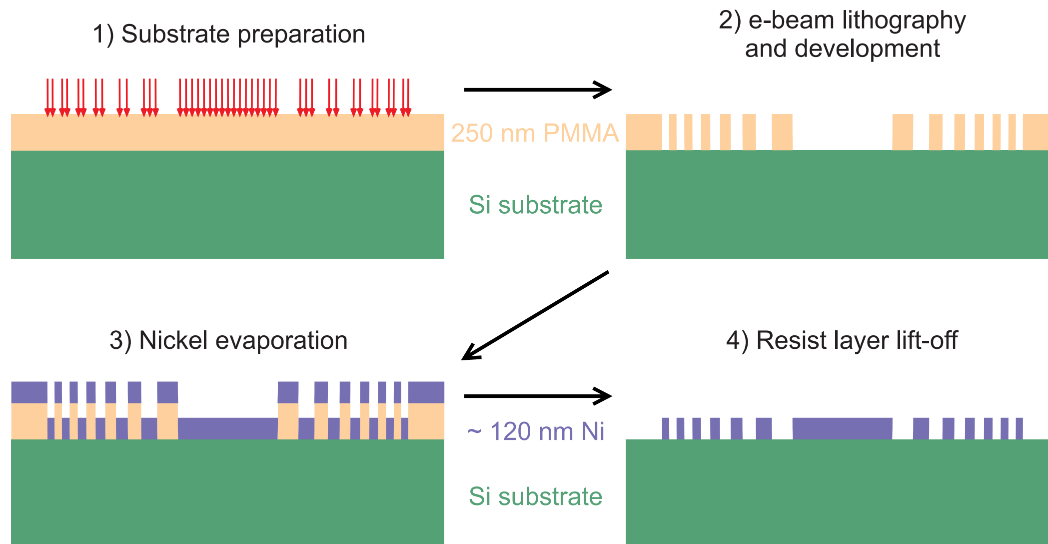

Figure 5.1: Nanofabrication approach based on metal evaporation. After the resist layer patterning by e-beam lithography, **1)** and **2)**, a nickel evaporation was done, **3)**. Later on, during the lift-off process, **4)**, the resist layer and the metal which have been deposited on ridges of the structures were removed using the suitable solution and only the metal which has been deposited inside the patterned mold grooves remains.

During the evaporation, the metal source (pellets or powder) is placed in a small container with tapered walls (referred as crucible or boat), and heated up to a temperature at which the evaporation of the metal occurs. Several techniques are utilized to reach the high temperatures including electrical heating or bombardment of the source material with an electron beam. The process requires high vacuum conditions (pressure $\leq 10^{-5}$ Torr), since the mean free path of the vaporized metal atoms must be much longer than source-sample distance. Evaporation has some advantages over other deposition techniques such as *metal sputtering* due to fact that all atoms that reach the substrate have a well defined direction trajectory, provided that the substrate is located far away enough from the source[1]. In our case, with a perpendicular placement of the sample substrate (which contains the patterned resist mold) respect to the metal atom flow, the direction of the evaporated atoms should be as parallel as possible to the walls of the resist structure. This way, the step coverage is highly reduced, that is, we avoid

[1] In metal sputtering techniques, a flux of accelerated ions impinges on the metal source and agglomerations of several atoms are ejected from the source to the target without a so well defined trajectory.

the coating of the walls of the resist structure that would later hinder the resist layer lift-off.

Within this work, nickel depositions were done using an electron beam evaporator. The evaporation trials were performed at the *Department de Física de la Universitat Autònoma de Barcelona*. The e-beam evaporator equipment was a UNIVEX 450 from LEYBOLD company. The vacuum system consisted of a rotative pump and a turbomolecular pump (turbovac with pumping velocity of 1150 l/s for N_2). The electron beam was generated with 3 kW power and 8 kV voltage and four targets could be loaded at the same time. Before the nickel evaporation, 5 nm of chromium were evaporated on the patterned resist mold because the adhesion of the nickel structures to the substrate is improved a lot using this intermediate extremely thin layer. Otherwise, the nickel structures were likely to be completely removed during the lift-off process.

After the nickel evaporation the PMMA resist layer was lifted-off in an ultrasound assisted acetone bath warmed up to 50°C. The use of ultrasounds was very useful to get a successful lift-off for the smallest structures. However, ultrasounds are not compatible with the use of thin membranes, which break as soon as the ultrasonic vibration starts. Since the use of thin membranes substrate is a strong requirement for soft x-ray radiation, this manufacturing technique would not be very useful unless the membranes could be produced after the fabrication of the structures on bulk silicon. On the other hand, and in order to ensure a successful lift-off, the maximum metal height that can be deposited should not exceed half of the resist layer thickness. Many unsuccessful fabrication trials can be justified with this argument.

As a mold we were using a 250 nm PMMA resist layer patterned on a silicon bulk chip. Following the above described steps we were able to obtain nickel structures as small as 125 nm in width and 150 nm in height. Scanning electron microscope inspections of such structures are shown in figures 5.2, 5.3 and 5.4.

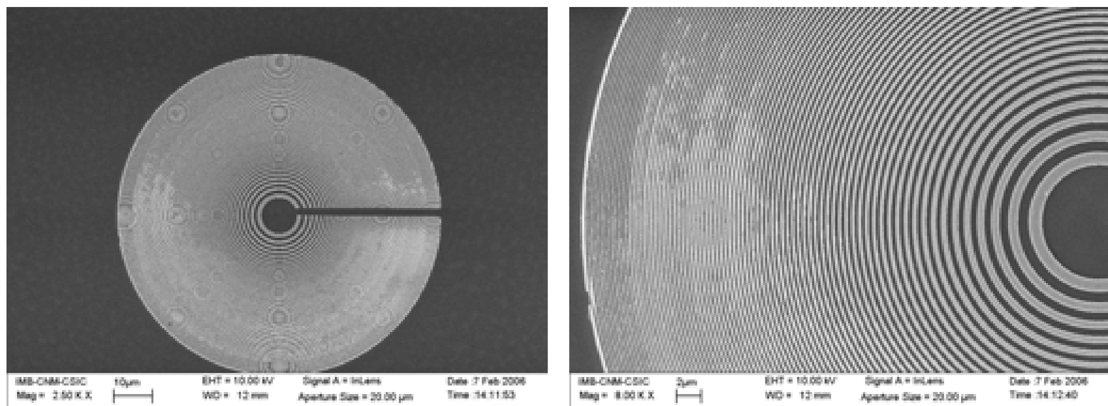

Figure 5.2: Scanning electron microscopy images of a 80 μm diameter Fresnel zone plate pattern made of nickel which has an outermost zone width of 125 nm produced by means of metal evaporation and resist lift-off.

All the structures are well patterned despite there are some resist remains that have

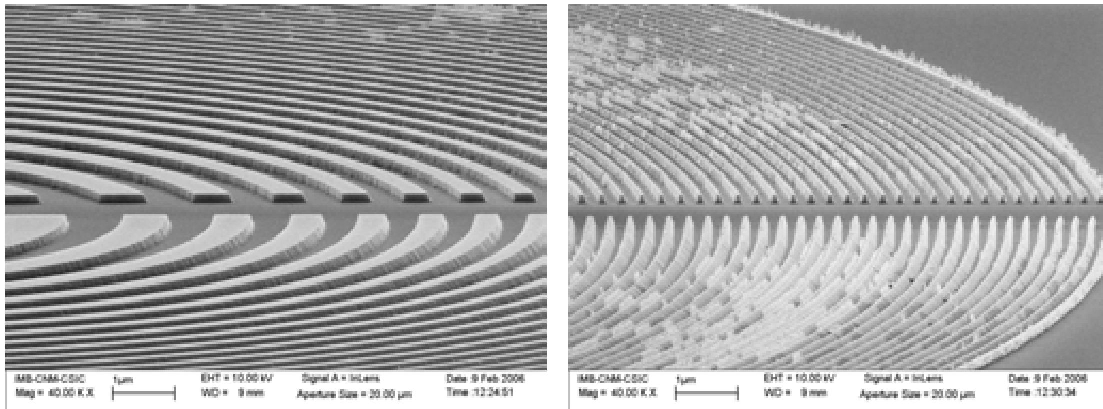

Figure 5.3: Detail of the central and outermost regions of the nickel Fresnel zone plate structure. Sometimes there are some resist remains that are not completely removed during the lift-off process.

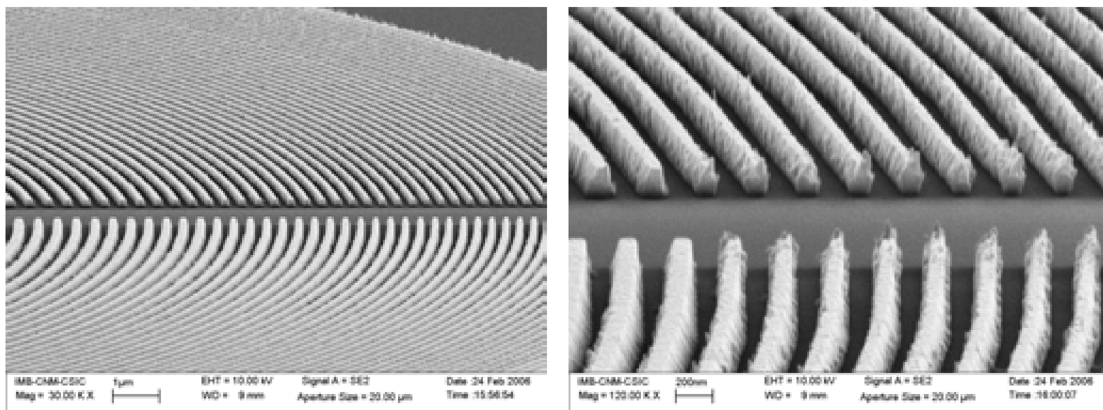

Figure 5.4: Detail of the outermost regions another nickel Fresnel zone plate structure produced by evaporation. In this case, the nickel zones are very well defined without any resist remains, they are 150 nm high and 125 nm wide.

not been totally removed during the lift-off. Smaller lines have triangular shape like in figure 5.3. It probably results from a combination of the resist groove shape and the evaporation direction. Figure 5.4 shows 125 nm walls with much more vertical slope. The work and results of evaporation and lift-off techniques to produce Fresnel zone plates were summarized in *Vila-Comamala et al.* [102].

In summary, we were able to produce 80 μm diameter Fresnel zone plate pattern with an outermost zone width of 125 nm and a zone thickness of 150 nm, i.e. densely patterned structures with an aspect ratio up to 1.20 on a silicon bulk substrate. No further developments were investigated since no thicker resist layer above 250 nm were exposed by the LEO SEM 1530 system and because the use of ultrasounds was not compatible with the use of thin membrane substrates.

5.2 Nickel Electroplating using a PMMA Mold

In order to overcome the limitations encountered in the metal evaporation approach, we switched our developments to metal electrodeposition process. This technique, also known as electroplating, uses an electrical current to coat an electrically conductive surface with a layer of metal, with thicknesses ranging from a few hundreds of nanometers to a few hundreds of micrometers. The process is identical to a galvanic cell acting in reverse. The object to be plated is immersed into the *electrolyte* solution and is attached to the cathode of the circuit. An external power supply generates a direct current and the electrolyte solution contains several dissolved salts of the metal allowing the flow of electricity through the migration of metal ions from the anode to the cathode. When the metal ions in the electrolyte solution reach the cathode, they lose their charge and plate on it. When the anode is made of the plating metal, it slowly dissolves replenishing the ions in the bath. Otherwise metal salts must be added in the solution from time to time. Electrodeposition is a standard technique in the industry to coat plenty of surfaces. Using a suitable patterned resist mold metal electrodeposition processes can also be used to produce structures with micro- and nanometer dimensions. Manufacturing steps are shown in figure 5.5.

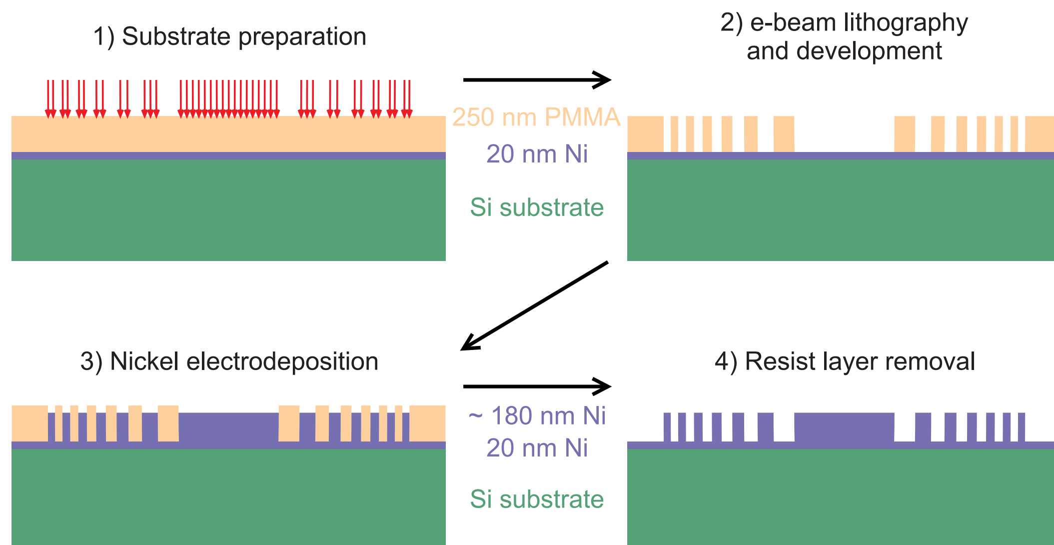

Figure 5.5: Nanofabrication approach based on metal electroplating. After the resist layer patterning by e-beam lithography, **1)** and **2)**, nickel structures are grown by electrodeposition, **3)**. Later on, the resist layer is easily removed as long as no overplating exists, **4)**. Note that a conductive seed layer is required beneath the e-beam resist.

In order to guarantee the growth of the metal structures on a low electrical conductive silicon substrate, a thin conductive layer, commonly referred as *seed layer*, must be deposited before the resist layer preparation. The seed layer facilitates electrical contact to the cathode and ensures high electrical conductivity.

In the fabrication trials performed at *the Nanofabrication Laboratory* in the *Centro Nacional de Microelectrónica*, we were using as a substrate a silicon chip coated with seed layer made of 10 nm titanium and 20 nm nickel. A 250 nm thick PMMA resist layer exposed by the LEO SEM 1530 system. The electrolyte solution was prepared with concentrations of $[NiSO_4] = 280$ g/l, $[NiCl_2] = 45$ g/l and $[H_3BO_3] = 30$ g/l. The solution was kept at 23°C and it had a bright dark green color. The solution pH was monitored and stabilized at 3. A nickel wire of 0.5 mm was used as anode.

Several samples were electroplated to determine the optimal electrical current intensity and plating time to grow nickel structures of 200 nm thickness in the PMMA resist mold. However, not enough exhaustive tests were done to give conclusive values of both parameters. The samples were immersed in acetone to remove the PMMA resist layer after the plating. In comparison to the samples prepared with metal evaporation, there were no problems to remove the resist after the metal deposition with acetone at room temperature. Ultrasonic vibrations were not necessary at all, and the restriction on the use thin membrane substrates did not apply anymore.

Figures 5.6 and 5.7 show a successful 80 μm diameter Fresnel zone plate structure grown by electroplating. The plated structures are 200 nm high and the smallest zone widths are 100 nm with a period of 250 nm. In this case, the duty cycle in the outermost regions does not fit the design specifications due to a lack of dose during the e-beam lithography. However, one can see that the nickel structures with an aspect ratio of 2.0 are perfectly defined and that no resist remains are left. The structures were slightly overplated and the ridges are quite rough. This roughness could be probably diminished by changing the component concentrations in the electrolyte bath to obtain smaller nucleation grains or reducing the electrical current to slow down the plating process. Thus, this manufacturing approach is working and only further fabrication trials would be required to optimize the electroplating procedure.

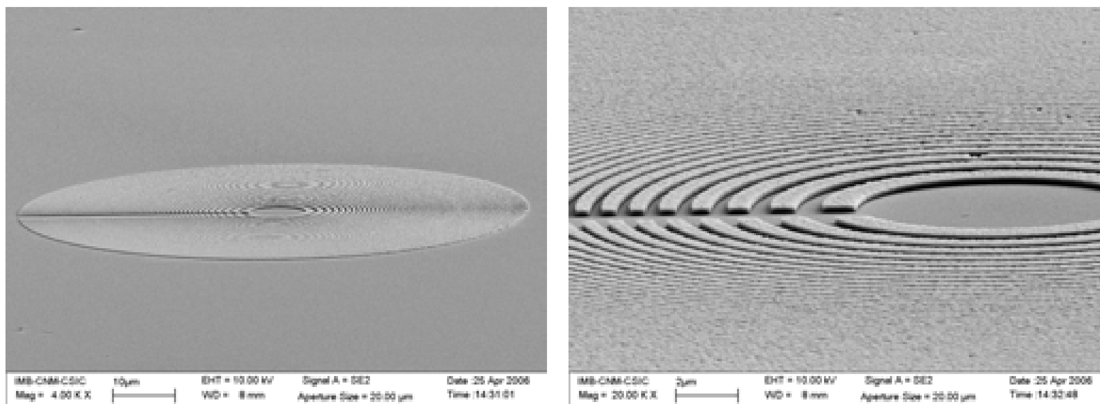

Figure 5.6: Scanning electron microscopy images of a 80 μm diameter Fresnel zone plate pattern made of nickel which have an outermost zone width of 125 nm produced by means of metal electrodeposition.

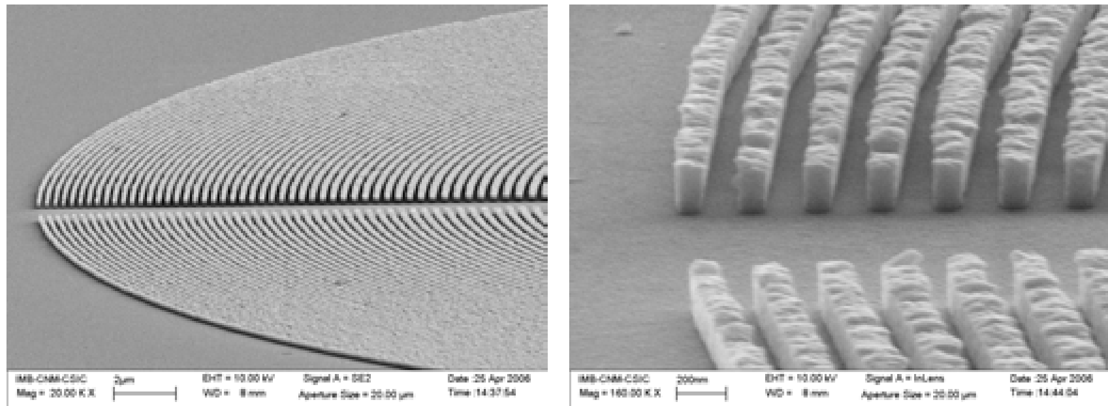

Figure 5.7: Detail of the central and outermost regions of the nickel Fresnel zone plate structure. 125 nm wide nickel zones are 200 nm high.

5.3 Nickel Electroplating using a Polyimide Mold

In this section we describe the fabrication technique that was developed at the *Labor für Mikro- und Nanotechnologie* at the *Paul Scherrer Institut* in Villigen (Switzerland). Despite that within this work we are concerned on nickel Fresnel zone plates for soft x-rays, these manufacturing processes were previously used to produce high aspect ratio Fresnel zone plates made of gold for hard x-ray focusing, by *Jefimovs et al.* [49]. Like in previous section, metal electrodeposition is the essential step to create the functional focusing structures, but in this case the preceding processes are a bit more complex. However, nickel structures with a higher aspect ratio are achievable.

Figure 5.8 schematically shows the manufacturing steps. In this case silicon nitride membranes were used as a substrate. After the preparation of the seed layer, a 250 nm thick resist layer is spun and a thin chromium layer is evaporated on the top of it. The e-beam lithography and the pattern transfer to the chromium mask by plasma dry etching is done following the procedures explained in the previous chapter. Later, the resist layer is etched by reactive ion etching and the nickel electrodeposition is performed. Finally, the chromium mask and the resist layer are removed and only the nickel structures are left on the silicon nitride membrane substrate.

5.3.1 Substrate Preparation

Even though the first structures were grown on a bulk silicon substrate, several Fresnel zone plates were produced on a very thin silicon nitride membrane ($\leq$ 100 nm). A seed layer for electroplating made of 10 nm chromium and 20 nm germanium was deposited by electron beam evaporation. While chromium layer improves the adherence to the substrate, the germanium layer ensures enough electrical conductivity during the plating and it does not oxidize during the Polyimide etching in an oxygen rich environment.

Polyimide resist/solvent solution is very thick and in order to get thin uniform layers it must be spun at high rotational speed for at least 3 min. Figure 5.9 shows the

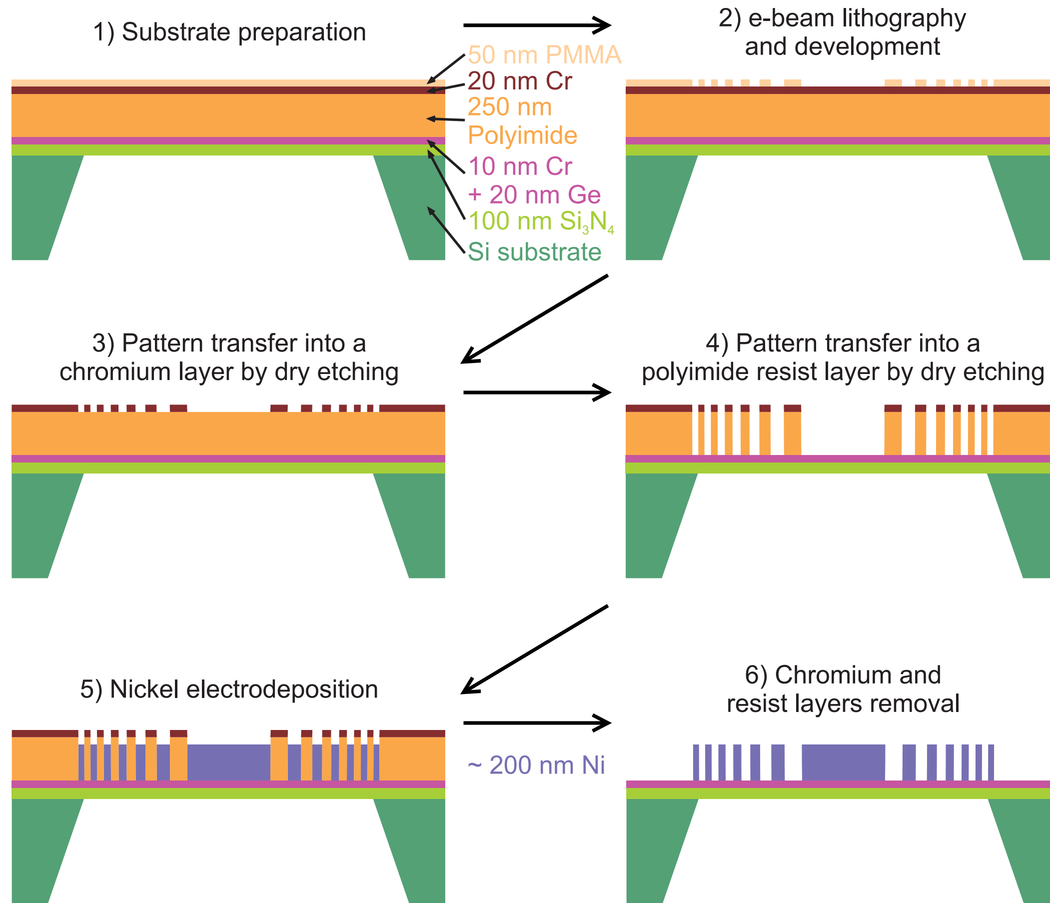

Figure 5.8: Nanofabrication approach based on metal electroplating. After the resist layer patterning by e-beam lithography, **1)**, **2)** and **3)**, the pattern is transferred to a thicker resist layer by reactive ion etching, **4)**, and the nickel structures are grown by electrodeposition, **5)**. Later on, the chromium mask and the thick resist layer are removed, **6)**.

characterization curves of the spun Polyimide layer thickness as a function of the rotation frequency. Pure Polyimide provides layer thicknesses above 1000 nm. Since we were interested in having resist layer thicknesses around 250 — 300 nm, pure Polyimide was diluted with the addition of n-methyl-2-pyrrolidone (NMP) solvent. As a matter of fact, 270 nm Polyimide layer were obtained spinning the 5:2 Polyimide:NMP solution at 6000 rpm for 180 s. After the spinning process the samples were baked for at least 2 hours at 300°C. Baking process increases the stiffness of the Polyimide resist so that high aspect ratio structures produced after the dry etching step become more robust[2].

On the top of the Polyimide resist layer, a layer of 20 nm chromium was evaporated and a last very thin layer of PMMA resist was spun ($\leq$ 50 nm). This way, the samples were ready to perform the e-beam lithography.

[2]One of main problems encountered in this fabrication method is that high aspect ratio resist structures are likely to collapse during the immersion into the electroplating solution.

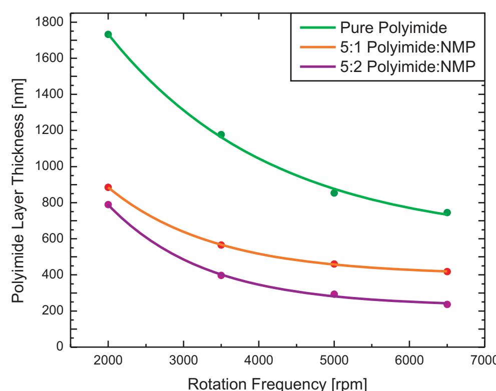

Figure 5.9: Characterization curves of the spun Polyimide layer thickness as a function of the rotation frequency. They were experimentally determined.

5.3.2 Polyimide Reactive Ion Etching

After the exposure by e-beam lithography on the PMMA layer and the pattern transfer to the underlying chromium layer, the Polyimide resist layer must be anisotropically etched. This is an essential step in the fabrication and it is achieved by low pressure oxygen plasma based reactive ion etching (RIE) process.

Reactive ion etching is a common plasma based etching technique in microfabrication. It consists of a combination of a physical and chemical processes, in which the etching is produced by the reactive species that activate and react with the sample material when they collide to its surface. By means of a radio-frequency (RF) gas discharge between two electrodes, a plasma is generated from a convenient gas mixture inside the reactor chamber. When the area of the electrodes is different a constant electric potential is created and the positively charged ions are accelerated towards the sample (which is normally located on the smaller, negatively charged electrode). Thus, reactive ion etching processes are anisotropic with an enhanced etching rate along the direction of the electric potential and therefore perpendicular to the sample surface. Many different gas mixtures can be used depending on the particular material to be etched. Oxygen-based processes are very useful to etch polymer-like material such as PMMA, photoresists, or in our case Polyimide.

Within this work we were using an Oxford Plasmalab 100 RIE system. In order to achieve a higher anisotropic process a high RF power and a very low oxygen pressure were used. With these conditions, higher aspect ratio can be reached even for the narrowest grooves since the mean free path of the ion and their directionality are increased. Main parameters of the process are summarized in table 5.1. In order to avoid an excessive heating of the Polyimide layer the sample was back cooled using a flow of helium through a hole in the aluminium holder.

Experimentally determined etching rates are around 50 nm/min, but etching times were prolonged for 10% of the required etching time to ensure that the etched zones

Polyimide Reactive Ion Etching	
O_2 Flow	5 sccm
Pressure	5 mTorr
RF Power	200 W
Temperature	290 K (He cooling assisted)
He Pressure	0.5 mTorr
DC Bias	700 V
Time	6 — 7 min
Etching Rate	$\sim$ 50 nm/min

Table 5.1: Main parameters in the reactive ion etching of the Polyimide resist layer by a low pressure oxygen plasma.

were completely clean since otherwise the metal plating would not properly start. This remark is specially important for the outermost rings, which are as narrow as 50 nm.

5.3.3 Nickel Electroplating Deposition

At the *Labor für Mikro- und Nanotechnologie* at the *Paul Scherrer Institut*, the electroplating bath was prepared following the instructions of the vendor, Enthone Inc. About two litres of electrolyte solution were prepared and the bath was always kept at a temperature of 45 — 50°C and with magnetic stirring. The solution pH was monitored and stabilized at 3.50 before each electrodeposition.

During the electroplating process, the samples were attached to holder together with a quarter of a silicon wafer coated with the same seed layer. Both the sample and the silicon wafer quarter were electrically contacted as cathode while the anode was made of a titanium mesh basket which was full of nickel pellets. Figure 5.10 shows the recipient containing the electrolytic solution and one sample ready for the electroplating process. The silicon wafer quarter is useful in controlling the electroplating rate, which results to be proportional to the electrical current density and in turn, proportional to the area that is being plated. Using the silicon wafer quarter, we ensured the same plating rate for all the samples in spite of different details in their patterns, since the area of the micro- and nanostructures that were being plated was negligible in comparison to the extremely large area of the silicon wafer quarter. That is, the quarter wafer is essential to have reproducible conditions during the nickel electroplating process.

Several samples were successfully electroplated. Just before dipping the sample into the electrolyte solution the magnetic stirring was switched off to avoid the collapse of the Polyimide structures, which could be induced by the movements in the fluid. The electrical current intensity was set to 50 mA (which corresponds to an electrical current density of 2.78 mA/cm^2) for 2 min 30 s obtaining a 200 nm thick nickel structures. Thus, the deposition rate is around 80 nm/min.

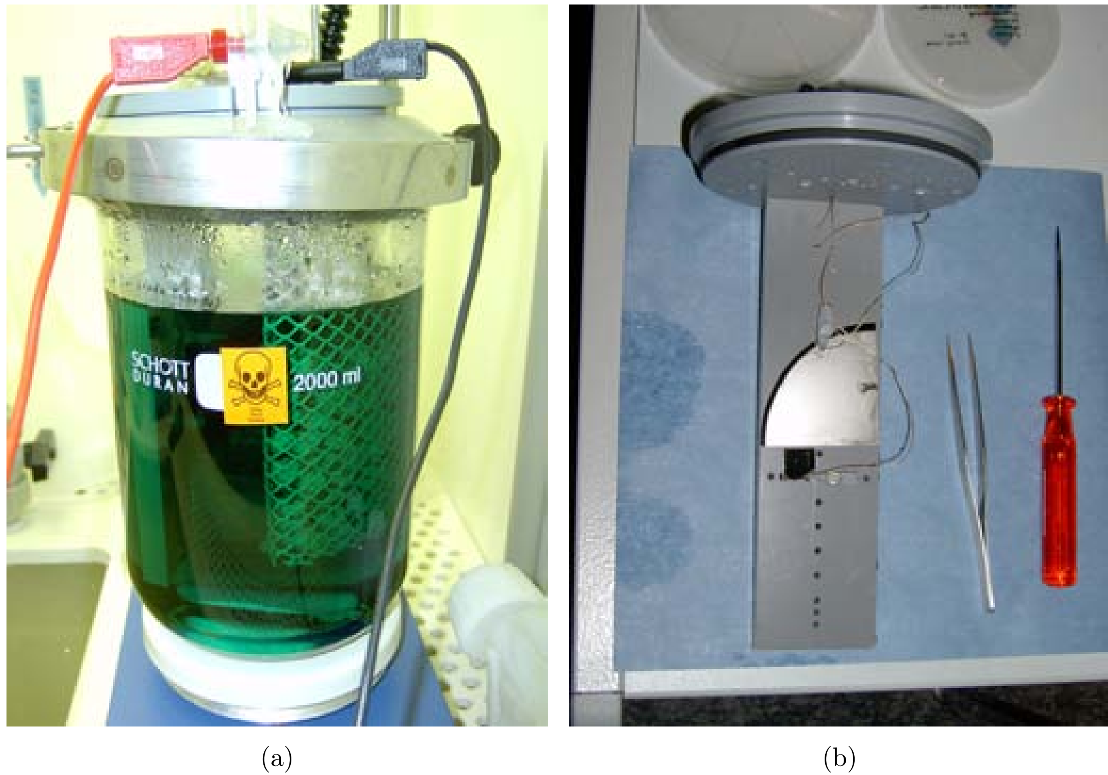

(a) (b)

Figure 5.10: (a) Recipient containing the electrolyte solution. (b) Sample attached to cathode holder ready to be electroplated. A silicon wafer quarter is also contacted in the cathode to ensure the reproducibility of electroplating conditions.

After the nickel electroplating, the chromium mask removal was not always straightforward. Two different explanations are possible: either a chromium oxide layer was formed during the oxygen plasma etching or an extremely thin nickel layer was plated on the top of Polyimide mold due to chromium layer conductivity. The result was that the standard chlorine-based reactive etching was not enough for the chromium layer removal. In one hand, it would be useful to expose square frame around the patterned structures to avoid any conductivity on the top of Polyimide mold around the patterned structures, in case the second explanation turns to be true. On the other hand, an argon plasma at very low pressure and high RF power acting for 2 min was found to be useful to remove the chromium layer before the standard chlorine-based RIE. Later, the Polyimide was removed by oxygen plasma and the nickel structures were ready.

Figure 5.11 shows the scanning electron microscopy images of the resulting nickel structures, which have a thickness of 200 nm. Smallest zones are 50 nm wide and as a result, structures with an aspect ratio of 4 are feasible to be produced by this manufacturing process.

Figures 5.12, 5.13, and 5.14 show a 100 μm diameter Fresnel zone plate with an outermost region of 50 nm. The height of the structures is again 200 nm and the outermost regions are perfectly defined. This structure is supported by a thin silicon nitride membrane and ready to be used as x-ray focusing lens.

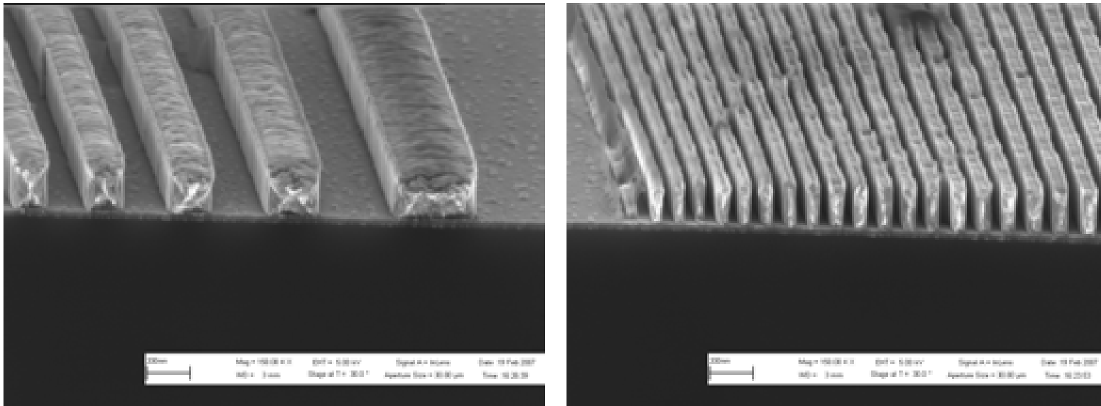

Figure 5.11: Detail of the central and outermost zone regions of a linear Fresnel zone plate produced by means of nickel electroplating using a Polyimide mold. Nickel structures are 200 nm height with a smallest zone width of 50 nm.

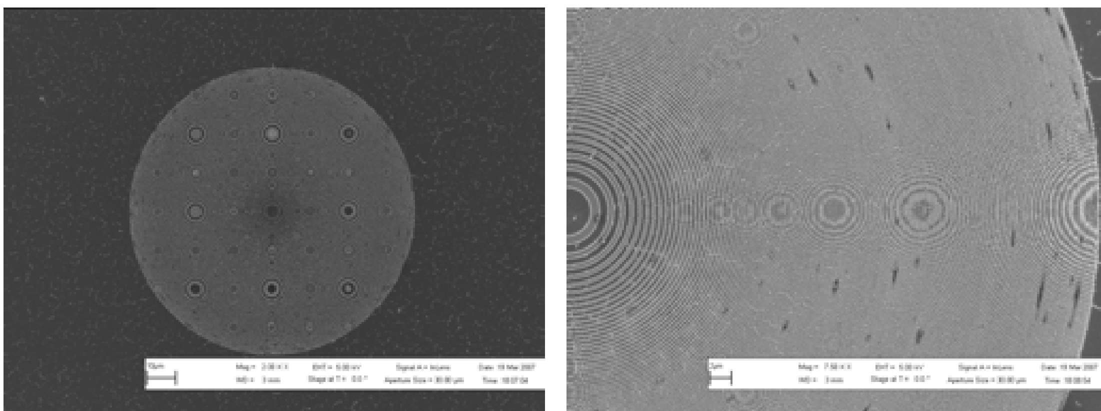

Figure 5.12: Scanning electron microscopy images of a 100 μm diameter Fresnel zone plate made of nickel by electrodeposition. This structure is supported by a thin silicon nitride membrane of 100 nm thickness.

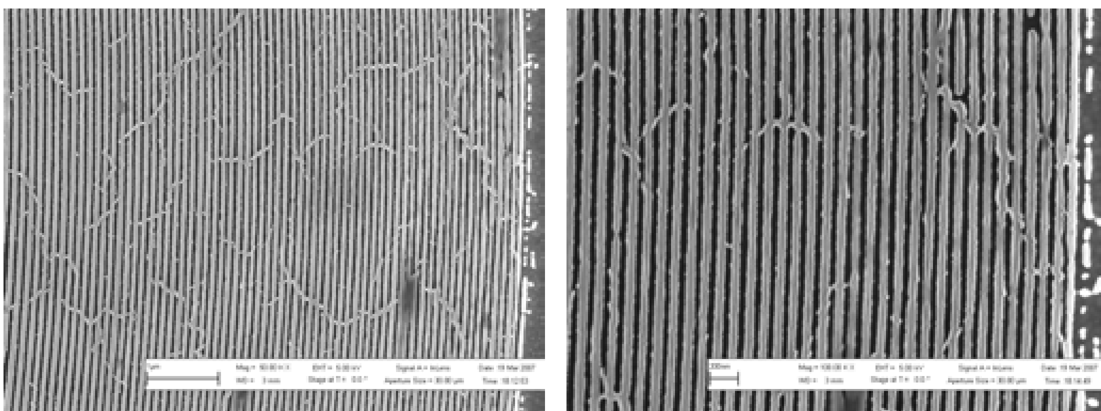

Figure 5.13: Detail of the outermost regions of a nickel Fresnel zone plate with a minimum line width of 50 nm and 200 nm in height. The nickel zones are perfectly patterned.

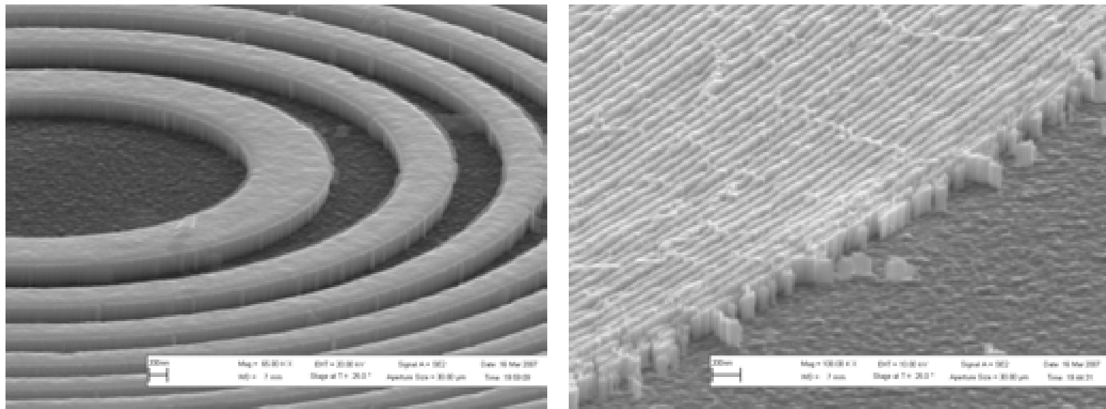

Figure 5.14: Detail of the central and the outermost regions of a nickel Fresnel zone plate.

In summary, the nickel electroplating technique using a Polyimide mold is much more effective than the previous ones and at least features down to 50 nm can be produced with an aspect ratio of 4. However, nickel electroplating using a PMMA mold should be further investigated because it is a much simpler process and it could probably provide better results than the ones that have been shown as soon as smaller features could be patterned into the PMMA resist layer during the electron beam lithography step.

CHAPTER 6

Silicon Fresnel Zone Plates

In this chapter we describe in detail a second fabrication technique to produce diffractive optics for soft x-ray radiation. We demonstrate the feasibility of producing Fresnel zone plates made of a silicon single crystal substrate. These silicon structures are produced by means of reactive ion etching and outermost zone widths down to 30 nm have been achieved. We show that they perform well at the current synchrotron radiation sources and we argue that, due to their robustness, they are likely to perform well at the next generation of x-ray sources[1], where extremely high heat load radiation beams are expected.

The fabrication results are extensively presented and discussed while showing images of the scanning electron microscopy inspections of the silicon structures. We demonstrate that at least aspect ratios up to 6 are feasible to be produced for 30 nm wide structures.

In addition, silicon Fresnel zone plate lenses were tested in both full-field and scanning transmission x-ray microscopy. Sample features down to 35 nm have been resolved in scanning transmission x-ray microscopy and a beamshaping condenser lens was used to illuminate the sample during the full-field transmission x-ray microscopy experiments. Work and results presented in this chapter are part of the publications *Vila-Comamala et al.* [103] and *Jefimovs et al.* [104].

Eventually, the production of silicon Fresnel zone plate structures is a requirement for the fabrication technique described in the next chapter, which could be used to push the ultimate spatial resolution in x-ray microscopes.

[1] 4th generation of x-ray sources are based on the Free Electron Laser (FEL) principle.

The work presented in this chapter was done at the *Labor für Mikro- und Nanotechnologie* at the *Paul Scherrer Institut* in Villigen (Switzerland). In addition, x-ray microscopy experiments were carried out at the *PolLux Beamline* of the *Swiss Light Source* at the *Paul Scherrer Institut* and at *TWINMIC Microscope* at *ELETTRA Sincrotrone* in Trieste (Italy).

6.1 Fresnel Zone Plates made of a Silicon Single Crystal Substrate

Nowadays, a new generation of x-ray sources based on the Free Electron Laser (FEL) principle are projected or under construction [83, 84, 85, 86, 87]. As shown in figure 6.1, in these sources an electron beam is guided through a linear accelerator, which can be as long as a few kilometers. Electromagnetic radiation is generated when the electron beam travels through a very long insertion device, that is, an array of magnets where the electron beam undulates and emits highly coherent x-ray radiation as in a conventional visible laser. In particular, x-FEL sources are expected to boost the field of x-ray imaging, as they will provide femtosecond x-ray pulses with peak powers many orders of magnitude higher than in any synchrotron today (see graph in figure 6.1).

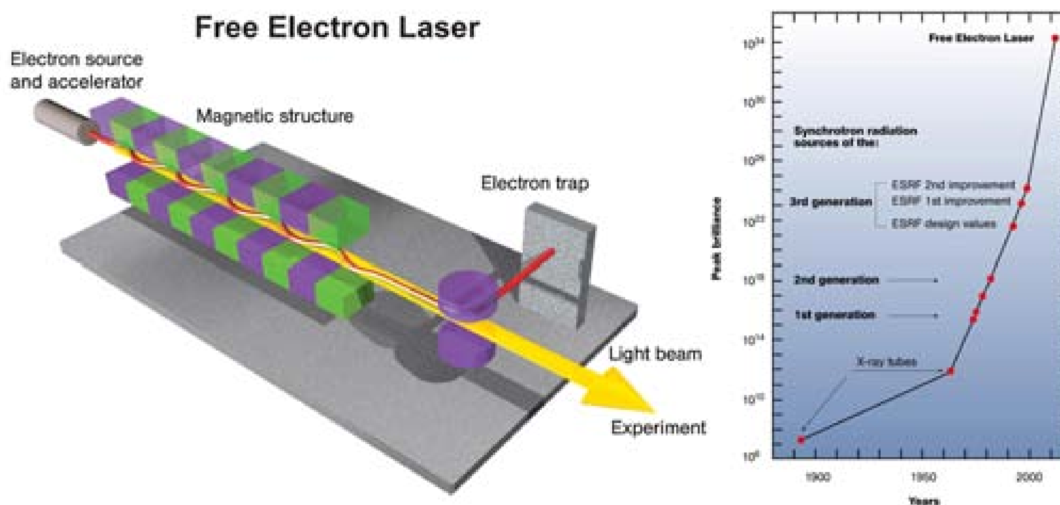

Figure 6.1: Scheme of an x-ray source based on the free electron laser principle. The electron beam in a linear accelerator is producing highly coherent electromagnetic radiation while is being guided through a very long insertion device (left). Peak brilliances of the x-ray sources (right). The x-FEL sources are expected to have peak brilliances of about ten orders of magnitude higher than any of the existing 3rd generation synchrotron sources.

As in a visible laser, another important property is that the radiation emitted by the x-FEL sources will be fully coherent over a beam cross-section which could be as big as one millimeter. However, the use of extremely intense radiation beams produced in x-FEL sources will pose severe problems of damage to the currently available x-ray optical

elements, which are expected to have a lifetime as short as a single x-FEL pulse [14]. As a result, robust x-ray optical components able to resist high heat loads will be a strong requirement at the x-FEL beamlines.

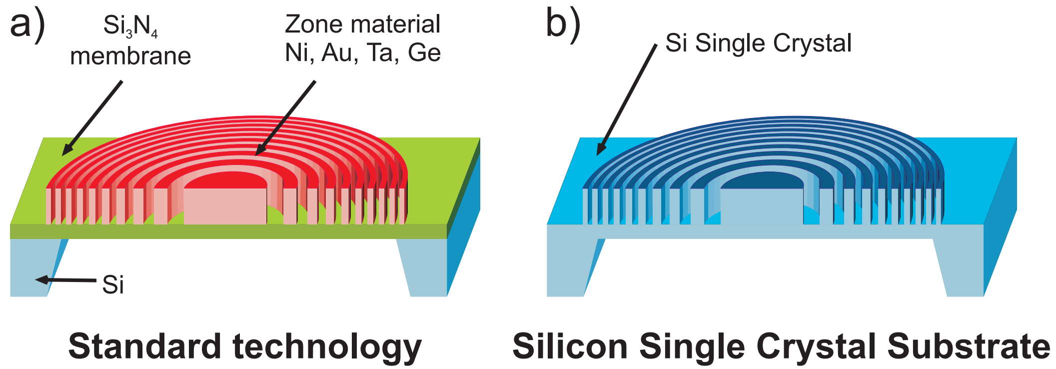

Figure 6.2: **a)** Conventional technology to produce Fresnel zone plates combines several layers of different materials. **b)** A Fresnel zone plate made of silicon single crystal substrate is likely to withstand the extremely high heat load radiation generated by x-FEL sources.

Material	Specific Heat Capacity $[\frac{J}{kg\cdot K}]$	Thermal Conductivity $[\frac{W}{m\cdot K}]$	Coefficient of Linear Expansion $[\frac{J}{\mu m\cdot K}]$
Silicon Nitride, Si_3N_4	710	30.0	2.8
Silicon, Si (Z=14)	794	148.0	2.5
Nickel, Ni (Z=28)	460	90.7	13.4
Germanium, Ge (Z=32)	321	64.0	6.1
Tantalum, Ta (Z=73)	153	57.5	6.3
Gold, Au (Z=79)	132	317.0	14.2

Table 6.1: Thermal properties (at 300 K) of common materials in Fresnel zone plate fabrication. Since silicon has a good thermal conductivity and a low coefficient of linear expansion, silicon Fresnel zone plates are expected to be suitable for x-FEL radiation beams.

As explained in the previous chapters, Fresnel zone plate patterns are commonly defined by electron beam lithography and transferred into an absorbing or phase shifting material such as Au, Ni, Ta or Ge by electroplating [53, 48, 82] or reactive ion etching processes [88]. In addition, they are usually supported by a thin ($\leq$ 100 nm) membrane of silicon nitride, Si_3N_4, which yields sufficient transmission of the soft x-ray beam. Thus, they are made combining layers of several materials with two or more interfaces, like shown in figure 6.2a). Heavy materials, which are normally used to fabricate Fresnel zone plates, while thermally very stable, absorb a significant fraction of incident beam. On the other hand, despite silicon nitride membranes only interact weakly with the incident beam, they have poor thermal conductivity. The existence of several interfaces can hinder the dissipative heat flow and structures can be damaged due to different

thermal deformations. In here, we propose the use of a silicon single crystal substrate to manufacture high resolution Fresnel zone plate lenses for soft x-ray radiation, like shown in figure 6.2b). Previously, linear and round zone plates made of monocrystalline silicon [89, 90] and refractive lenses made of diamond [91] were fabricated and their performance was tested in hard x-ray microscopy. Table 6.1 shows the specific heat capacity, the thermal conductivity and the linear coefficient of thermal expansion of common materials for x-ray Fresnel zone plates. When comparing to the other materials, silicon, as a low Z material, absorbs less energy from the incoming beam and due to its higher heat capacity less increase of the temperature is expected. Besides, good thermal conductivity enhances the heat dissipation and with a low thermal expansion coefficient little deformation of the structures is expected. On the other hand, the use of a single crystal membrane substrate, which is free of interfaces and grain boundaries, ensures uniform thermal conductivity and homogeneous thermal expansion.

With all these arguments we expect that, under the high heat loads produced by the x-FEL radiation beams, the silicon structures will perform better than the conventional metal Fresnel zone plates used in existing synchrotron based soft x-ray microscopes.

6.2 Silicon Fresnel Zone Plate Fabrication

Manufacturing steps of a Fresnel zone plate made from a silicon single crystal are schematically shown in figure 6.3.

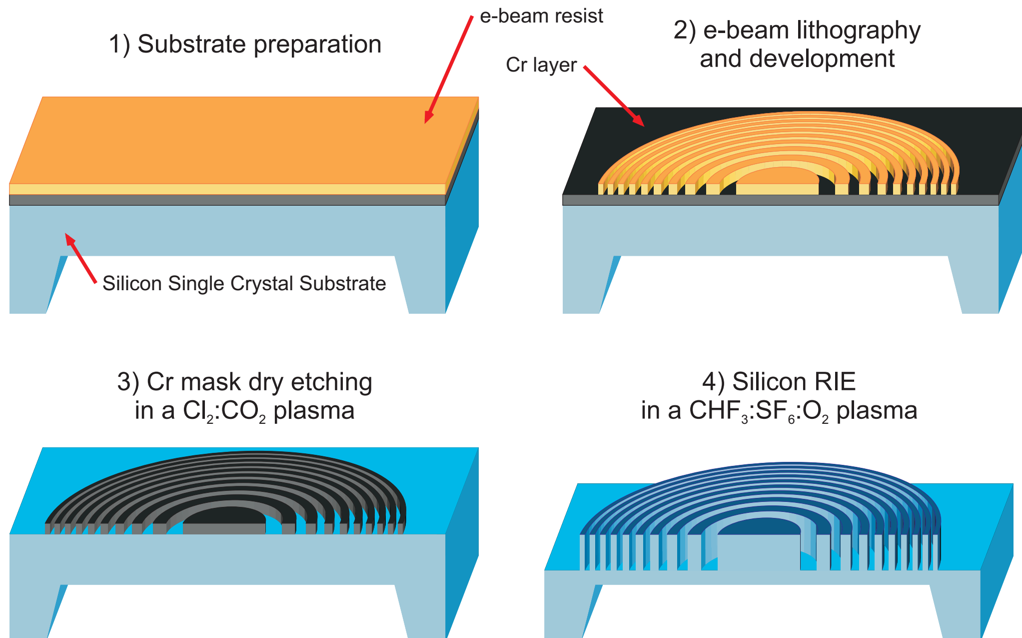

Figure 6.3: Manufacturing steps of a Fresnel zone plate made from a silicon single crystal substrate.

First, the silicon membranes are prepared by etching a boron doped (100)-silicon wafer substrate in aqueous potassium hydroxide (KOH) solution saturated with isopropanol. Later, the Fresnel zone plate structure is patterned by means of electron beam lithography using PMMA or Calixarene resists and transferred into silicon by reactive ion etching using a thin (20 nm) intermediate chromium hard mask.

Having a look at section 3.1.3 and when comparing to nickel, silicon Fresnel zone plates require a much higher aspect ratio in order to provide similar diffraction efficiencies for soft x-ray radiation. At 500 eV photon energy, 200 nm high silicon structures would only have a diffraction efficiency of 6%. In addition, 400 nm high silicon structures would provide a diffraction efficiency of 17% while a maximum diffraction efficiency of 22% is expected for 600 nm high structures. Thus, for outermost zone widths around 50 nm aspect ratios above 8 are required. Detailed information of the manufacturing steps in order to fulfill these specifications are presented in the next sections.

6.2.1 Silicon Membrane Fabrication

Availability of silicon membranes is a prerequisite for the silicon Fresnel zone plate fabrication. Within this work, they were prepared in-house following the procedure described by *Bassous et al.* [90]. Silicon membrane manufacturing steps are schematically shown in figure 6.4.

The original substrate consisted of a 250 μm thick (100)-silicon wafer being one of the sides highly boron-doped. The boron concentration was above 10^{20} cm^{-3} in a superficial layer of 1 — 4 μm thickness and both wafer sides were coated with a silicon nitride layer 250 nm thick.

Optical lithography was performed on the non-boron doped side of a whole silicon wafer to define an array of square areas of several sizes, which would become membranes, and lines, which would serve as guiding paths for cleaving the wafer in smaller pieces. Then, the exposed pattern was transferred to the silicon nitride layer by reactive ion etching using an Oxford Plasmalab 100 RIE system. The plasma etching was divided in 2 steps. During a first step an oxygen plasma cleaned any resist remains on the exposed areas. A second step performed the actual etching of the silicon nitride layer. Detailed parameters of both recipes are summarized in table 6.2.

After silicon nitride etching, the photoresist layer was removed using an oxygen-based recipe in a resist stripping machine. After that, the silicon wafer was ready to be dipped into the aqueous potassium hydroxide (KOH) solution to generate the actual membranes.

Silicon anisotropic wet etching in KOH-based solution[2] is a well-known technique

[2] Two other relevant silicon etchants are ethylene diamine pyrochatechol (EDP), and tetramethyl ammonium hydroxide (TMAH). They are all anisotropic etchants which attack silicon along preferred crystallographic directions. Besides, they all show an important decrease in the etching rate in highly boron-doped regions (dopant concentration $> 5 \cdot 10^{19}$ cm^{-3}). However, we were reluctant to the use of EDP-based solutions because they are toxic and corrosive and on the other hand, TMAH-based solutions were not available in the lab.

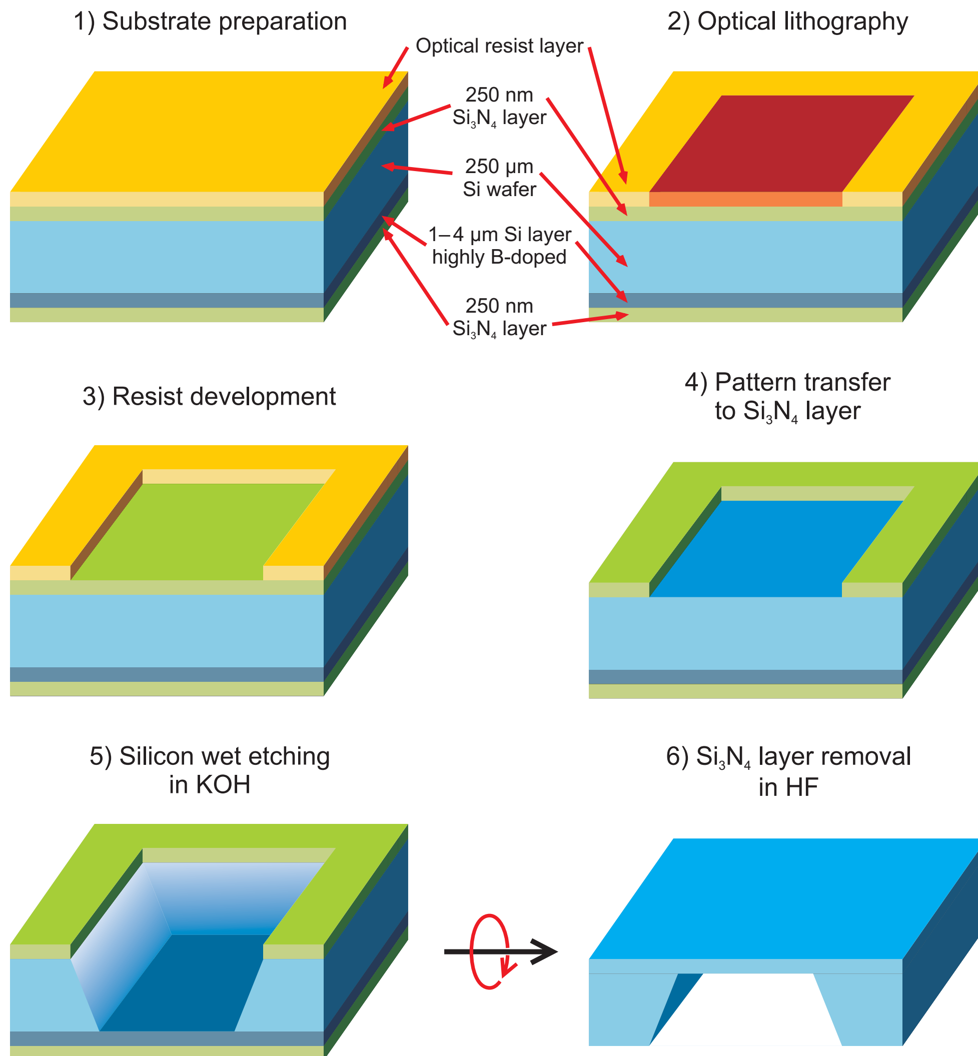

Figure 6.4: Manufacturing steps of silicon membranes from a single crystal substrate. After the optical lithography that defines the size of the membranes, the silicon wafer is etched in KOH-based solution using the silicon nitride layer as a mask.

in micro- and nanofabrication [27]. The etching rate depends on the concentration and temperature and is usually around 1 μm/min for 20 — 40% by weight aqueous KOH solutions at temperatures of 85 — 115° C. Anisotropic etching is achieved due to the fact that etching rate depends on the orientation crystallographic plane of the surface. The crystallographic (111) planes show a much slower etching rate than the planes (100) or (110), creating the typical openings shown in figure 6.5. Common masking materials for anisotropic wet etchants are silicon dioxide and nitride, being the latter one superior for longer etching times.

In the laboratory, we prepared one litre of 20% aqueous KOH solution in a transpar-

	1st Step Photoresist Cleaning	2nd Step Si_3N_4 RIE
CHF_3 Flow	—	40 sccm
O_2 Flow	5 sccm	3 sccm
Pressure	100 mTorr	100 mTorr
RF Power	100 W	100 W
Temperature	300 K	300 K
DC Bias	420 V	360 V
Time	1 min	20 min
Etching Rate	∼ 200 nm/min	∼ 17 nm/min

Table 6.2: Detailed parameters of the recipe for the reactive ion etching of the silicon nitride layer. The actual etching was performed after applying an oxygen plasma to remove any resist remains on the exposed areas.

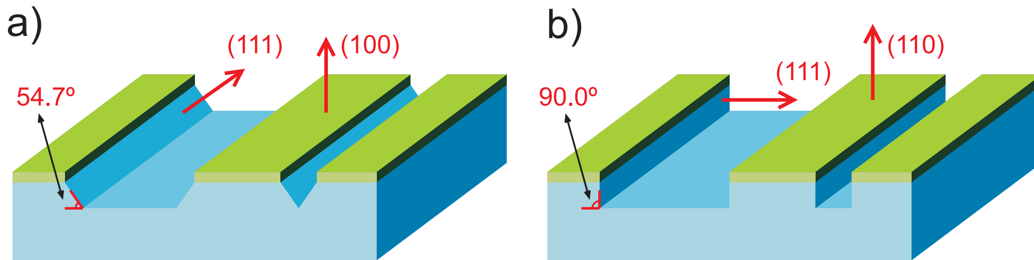

Figure 6.5: Anisotropic etching of silicon in a KOH solution due to the different etching rates for different crystallographic planes. **a)** When etching a surface with (100)-planes a typical trapezoid opening with an angle of 54.7° is obtained. **b)** When etching (110)-planes a totally vertical sidewalls can be achieved.

ent vessel and it was heated up to 70° C. Before immersing the wafer into the solution, the native silicon oxide that is formed on any silicon surface must be removed to avoid the formation of unwanted structures by dipping the wafer into a BOE solution[3]. In principle, an immersion of 30 s in the BOE solution should be enough to remove the native silicon oxide, however, due to the fact that an oxygen rich environment was used to clean the photoresist in the previous step, much longer times of 2 min 30 s were required, without affecting the silicon nitride layer. After that, the silicon wafer was quickly rinsed in water and immersed into the KOH solution avoiding its drying.

When dipping the silicon wafer into the KOH solution bubbles should instantaneously appear from the areas where the silicon nitride layer has been previously removed. Bub-

[3]Buffer oxide etch (BOE) solution is a mixture of hydrofluoric acid (HF) and water with a buffer agent, like for example NH_4F. The HF is a silicon oxide and silicon nitride etchant and the buffer agent is added to maintain the HF concentration and to control the pH.

bles are made of the hydrogen resulting from the reaction,

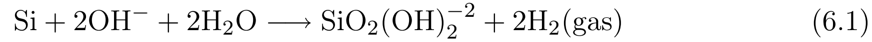

$$Si + 2OH^{-} + 2H_2O \longrightarrow SiO_2(OH)_2^{-2} + 2H_2(gas) \quad (6.1)$$

The estimated etching rate was 800 nm/min and thus, 4 hours 30 min were necessary to attack almost 250 μm. In order to increase the selectivity between the silicon and the boron-doped silicon, isopropyl alcohol (IPA) was added as soon as some light was shinning through the silicon membranes (10 — 20 μm thick). The amount of IPA must be enough to saturate the aqueous solution[4]. The KOH solution saturated with IPA can not be used right from the beginning because when etching more than 100 μm deep is very likely to produce hillocks and unwanted roughness on the surface that is being etched. After adding the IPA, the selectivity between silicon and the boron-doped silicon is enough so that at some point the bubbling stops and the silicon wafer full of membranes can be extracted from the KOH solution. The wafer must be quickly taken out and immersed in water for several times (one should prevent the wafer from drying before the rinsing in water, because some residues can be deposited on the top of the membranes which are very difficult to remove after the wafer drying).

Eventually, the silicon nitride layers covering the silicon can be removed by dipping the wafer in 50% hydrofluoric acid[5] (HF) solution for 15 min and the silicon membranes with thicknesses ranging from 1 to 3 μm are ready for further processing.

6.2.2 E-beam Lithography and Chromium Reactive Ion Etching

E-beam lithography exposures on the silicon single crystal membrane substrates were done using the LION LV-1 e-beam tool as extensively described in sections 4.2.2.2 and 4.3.2. While the details of the substrate preparation and e-beam exposure were given in the mentioned sections, in here, it is important to give a couple of remarks about the e-beam lithography and the pattern transfer to chromium layer which are specially important for the fabrication of the silicon Fresnel zone plates.

First, we intend to explain a bit further about the dose correction (see figure 4.8) that was necessary when exposing Fresnel zone plates with outermost zone widths under 50 nm. The dose correction factor, D_{cor}, given by equations 4.1 and 4.2 as a function of the angle θ must be implemented by splitting each ring of the structure in a finite number of circular segments, and arranging the dose for each one. Not considering this dose correction leads to unsuccessful exposures like shown in figure 6.6(b), which, as a matter of fact, would preclude us from patterning of Fresnel zone plates with line widths in the sub-50 nm range. Without the dose correction, the effective dose variation of 8% is enough to overexpose the line pattern for some orientations. Note that in figure 6.6(b) designed line widths are only achieved in the directions for which no dose correction is required.

[4]When the KOH solution is saturated, a clear interface between the KOH solution and the pure IPA appears.

[5]HF must be handled with extreme carefulness, since it is a very hazardous and toxic substance.

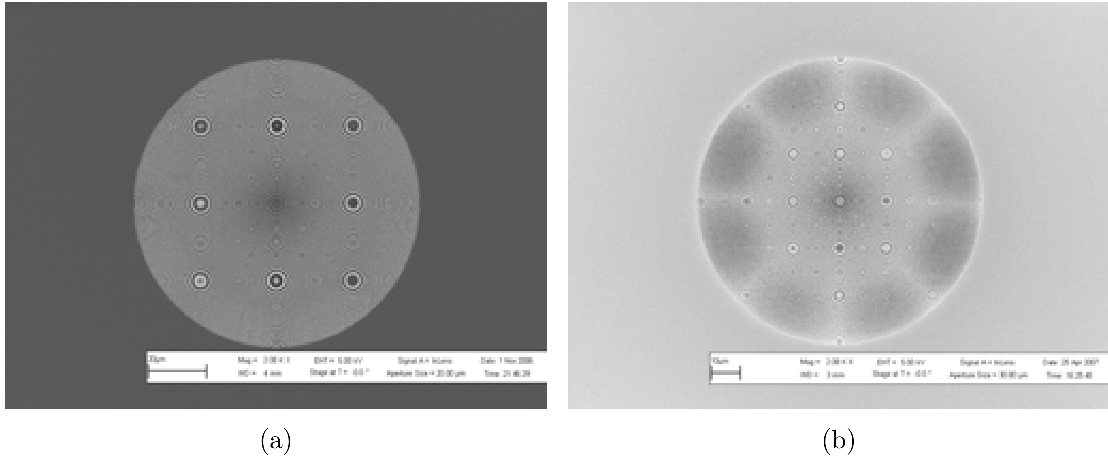

(a) (b)

Figure 6.6: (a) Scanning electron microscopy image of a Fresnel zone plate with 50 nm outermost zone width. In this case, the dose correction is not required. (b) Image of a Fresnel zone plate with 30 nm outermost zone width. From the Moiré fringes, one can observe that the lines are only well patterned in the directions where no dose correction is needed (that is, axis, 45° and −45° orientations). The regions corresponding to intermediate angles are clearly overexposed for line widths below 50 nm.

Two different approaches were used to split the rings of the Fresnel zone plate pattern and introduce the dose factor. They are both shown in figure 6.7. In b), we divide each ring in 32 circular paths subtending equal angles and introducing the value of the dose correction factor, D_{cor}, of the central angle. However, when looking at the shape of dose correction function in the graph of figure 4.8, one realizes that it would be preferable to split the rings in circular segments which subtend an angle range that requires a similar dose correction factor. In this way c), each ring is divided so that the sectors that require the highest dose correction become wider than the ones for which no correction is demanded. In figure 6.7, the dark blue regions are exposed at the nominal dose, while the lighter blue sectors are exposed applying the suitable lower dose according to the dose correction factor.

Figure 6.8 shows the result of applying the dose correction factor to a 100 μm diameter Fresnel zone plate pattern with an outermost zone width of 30 nm. One immediately realizes that a substantial improvement have been achieved when comparing to figure 6.6(b) since the overexposed regions have disappeared in both splitting approaches. A detailed inspection of the structures shows that the second one is slightly better because the line width is better preserved for the different orientations.

The second issue in this section concerns the pattern transfer to the chromium layer lying beneath the e-beam exposed resist layer. The chromium layer is going to serve as mask during the silicon reactive ion etching. If the chromium reactive ion etching is too short, the reactive species will not reach the silicon surface and the silicon etching will fail, as in figure 6.9(a). If the chromium reactive ion etching is too long the resist layer could be partially removed and the whole chromium layer will be thinned down. A thinner chromium layer translates into a destruction of the smaller lines since the

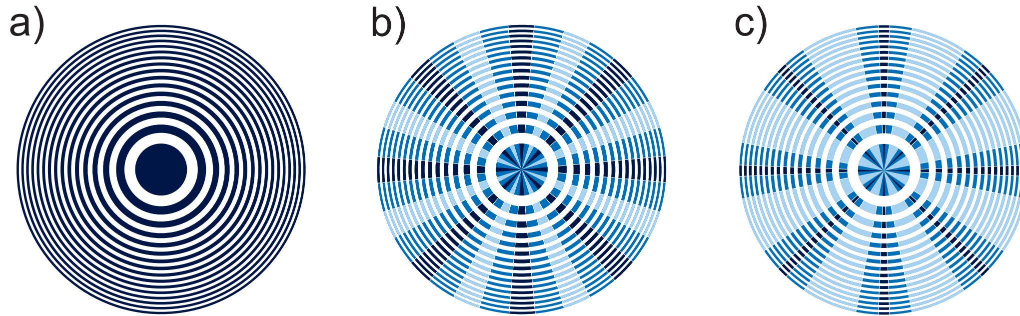

Figure 6.7: The dose correction factor introduced in section 4.2.2.2 was implemented during the Fresnel zone plate exposure by dividing the rings in two different ways. **a)** e-beam exposure without dose correction. **b)** e-beam exposure splitting the structure in 32 circular paths subtending equal angles. **c)** e-beam exposure splitting the structure in 32 circular paths taking into account the function shape of the dose correction factor. In both **a)** and **b)**, the dark blue regions are receiving a higher dose than the light blue ones.

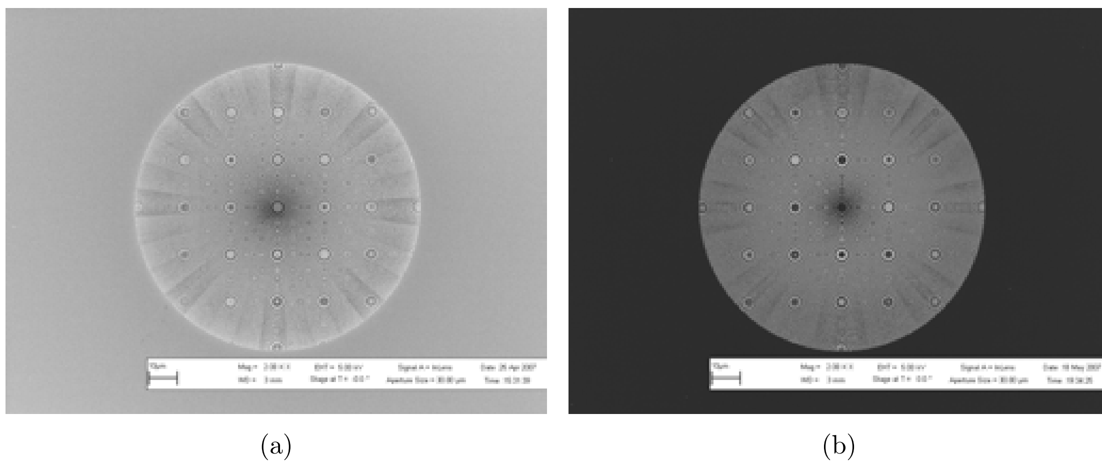

Figure 6.8: Scanning electron microscopy images of a Fresnel zone plate pattern with an outermost zone width of 30 nm. The dose correction factor was implemented using the two different approaches suggested in figure 6.7.

selectivity between chromium and silicon will be decreased and the chromium layer will be completely removed after several minutes of silicon etching. This is shown in figure 6.9(b). Thus, the pattern transfer to the chromium layer is a very critical step in the silicon Fresnel zone plate fabrication.

We were using a 20 nm thick chromium layer. One could use a thicker chromium layer but then a thicker resist layer would also be necessary. In addition, it is not clear that we could achieve a good pattern transfer for the smallest line width. The BMP Plasmafab 100 machine has two electrodes of equal size, leading to negligible bias-voltage and in consequence a more or less isotropic etching, which is not compatible with very small structures (under 100 nm) with aspect ratios above 1.

Chromium etching times ranged from 35 to 50 s depending on each sample. A general

procedure was to etch the sample for a short time (35 s), to check the result with a scanning electron microscopy inspection and to etch longer in case it was necessary.

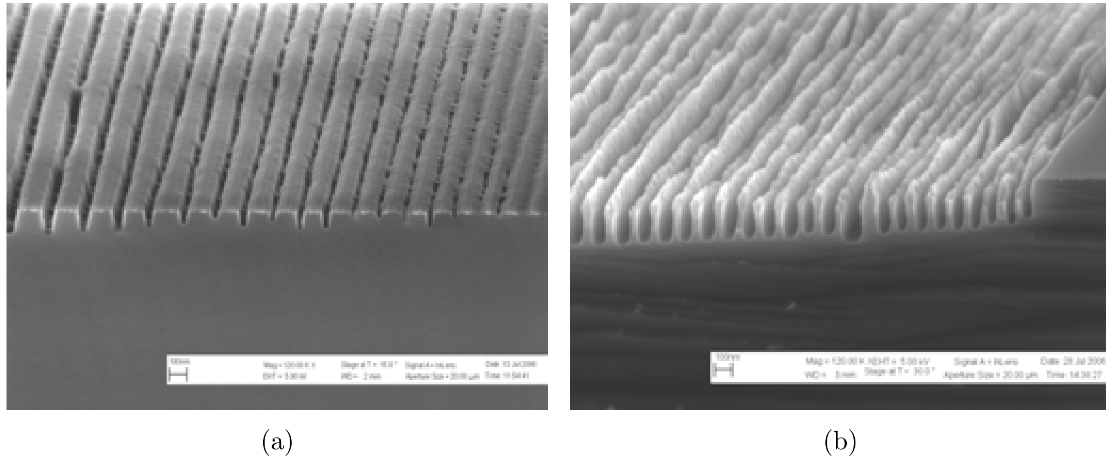

(a) (b)

Figure 6.9: The pattern transfer to chromium layer is a key point in the silicon Fresnel zone plate fabrication. (a) If the chromium layer etching is too short the silicon etching will fail. (b) If the chromium layer etching is too long the smallest silicon structures will be damaged.

A final suggestion that could help in improving the results of silicon reactive ion etching would be the replacement of the chromium layer for a titanium layer which is a harder mask. Probably 5 or 10 nm titanium would be enough to etch longer times and deeper into the silicon but no real fabrication trials were done.

6.2.3 Silicon Reactive Ion Etching

The Fresnel zone plate pattern was transferred to the silicon membrane substrate by reactive ion etching in an Oxford Plasmalab 100 RIE system. A complete introduction to silicon reactive ion etching in micromachining can be found in *Janseny et al.* [93]. Here, we are interested in having a process as much anisotropic as possible, which should almost exclusively etch in the vertical direction. Isotropic and anisotropic etchings are schematically represented in figure 6.10. The anisotropic etching relies on the formation of a passivation layer on the sidewalls of the structures that prevents further etching in the horizontal direction and avoids the undercut below the mask that one typically gets in any isotropic process. When etching structures as narrow as 50 nm, even 10 nm undercut should be addressed.

To etch our silicon structures, we were using a fluorine-based plasma containing CHF_3, SF_6 and O_2 at room temperature. In this case, the anisotropic etching results from the sidewall passivation by silicon oxide species. The O_2 supplies the inhibitor film forming species that passivate the surface with a SiO_xF_y layer, while the SF_6 and CHF_3 generate ion species, SF_x^+ and CF_x^+, that suppress the formation the inhibitor film at horizontal surfaces. Further details of the use of $CHF_3/SF_6/O_2$ gas mixtures for silicon reactive ion etching can be encountered in *Lentenberg et al.* [94].

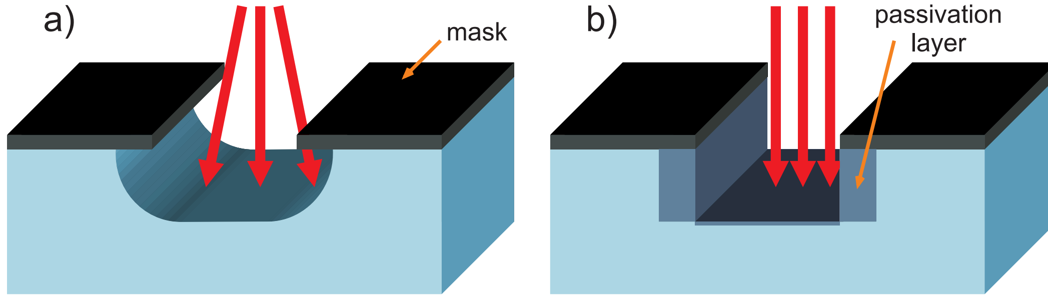

Figure 6.10: Sketch of two different etching profiles by reactive ion etching. **a)** Isotropic etching profile resulting from a non-directional process. **b)** Anisotropic etching profile relying on the formation of a passivation layer on the sidewalls of the structure so that the etching in the horizontal direction is stopped.

During the process, the parameters in the reactor chamber that could be controlled were the gas flows, the pressure, the temperature and the radiofrequency (RF) power. As mentioned in section 5.3.2, anisotropic etching is favoured when using low chamber pressures and high RF powers. Gas flows are used to regulate the relative gas concentrations inside the chamber. The sample was loaded inside the chamber lying on a silicon wafer which was replaced by a new one every 5 — 10 etching processes. The use of the silicon wafer was important to ensure the reproducibility of the process despite etching different samples. Etching times lasted from 5 to 15 min depending on the depth of the structures. Within this work, we took as starting point a recipe already employed at the *Labor für Mikro- und Nanotechnologie* and suggested in *Nöhammer* [78]. In order to have an anisotropic etching and to reduce the undercut as much as possible, a lot of tests were done until optimal results were obtained. Optimal silicon reactive ion etching recipe parameters are summarized in table 6.3.

Silicon Reactive Ion Etching	
CHF_3 Flow	40 sccm
SF_6 Flow	1 sccm
O_2 Flow	3 — 5 sccm
Pressure	15 — 30 mTorr
RF Power	100 — 200 W
Temperature	300 K
DC Bias	500 — 700 V
Time	5 — 15 min
Etching Rate	$\sim$ 25 — 40 nm/min

Table 6.3: Detailed parameters of the recipe for the silicon reactive ion etching that generates the Fresnel zone plate structure into the silicon membrane substrate.

Scanning electron microscopy images of the structures produced by silicon reactive

ion etching are extensively shown in figures 6.11, 6.12, 6.13 and 6.14. We obtained silicon structures with an aspect ratio of 8 for 50 nm wide lines. As one can observe in figure 6.11, even narrowest silicon lines have sidewalls with perfectly vertical slope. One can observe that narrower openings are shallower than wider ones. Thus, wider spacings are etching faster. This is a well-known effect, commonly referred as *RIE lag*. In our structures we had a difference in depth ranging from 50 to 100 nm when comparing the widest and narrowest openings which will translate into a decrease of the focusing diffractive efficiency of the device.

The main limitation in this technique comes from the erosion that the mask undergoes after several minutes of etching, which becomes critical for the narrowest lines. Figure 6.12 shows a structure for which the chromium mask has been totally removed and the silicon lines have been partially damaged. As suggested in the previous section, these results could be improved and deepest trenches could be achieved by using a harder mask, such as a thin titanium layer.

Figure 6.13 demonstrates one of the best results using this fabrication technique, where we were able to pattern a structure with 30 nm lines/spacings with a depth of 180 nm. Thus at least, 30 nm wide lines with an aspect ratio of 6 are feasible to be produced with a fluorine-based plasma using the chromium layer mask.

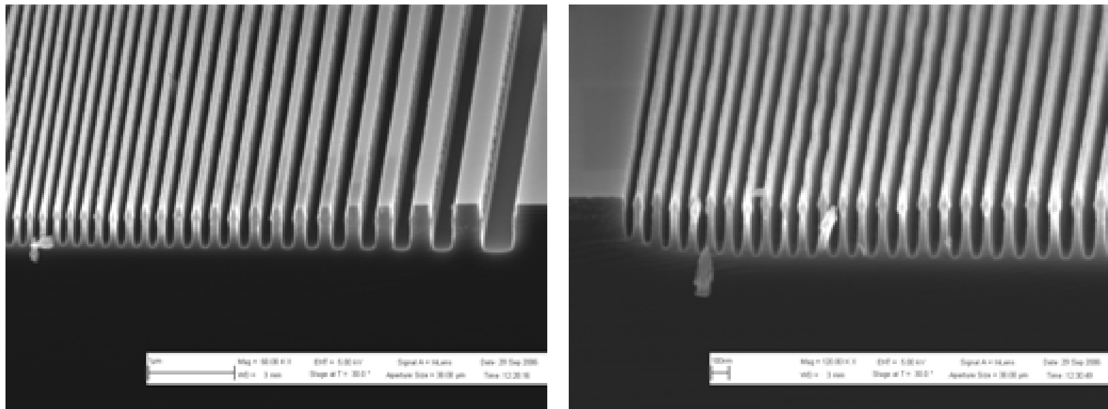

Figure 6.11: Scanning electron microscopy images of a linear Fresnel zone plate structure. The smallest trenches are 400 nm deep and 50 nm wide, that is, outermost zones have an aspect ratio of 8.

To finish this section, figure 6.14 sheds light on the limits of this nanofabrication technique. Figure 6.14(a) shows that 25 nm line/spacing silicon structures could also be patterned but their quality is poor due to the e-beam exposure. In our work, we were limited by the performance of the e-beam lithography since dense patterns of 25 nm line/spacing could not be exposed in a reproducible way. On the other hand, figure 6.14(b) shows that extremely narrow silicon walls of 15 nm could be generated and that they were able to stand. The height of the structures is 400 nm and they have a period of 190 nm.

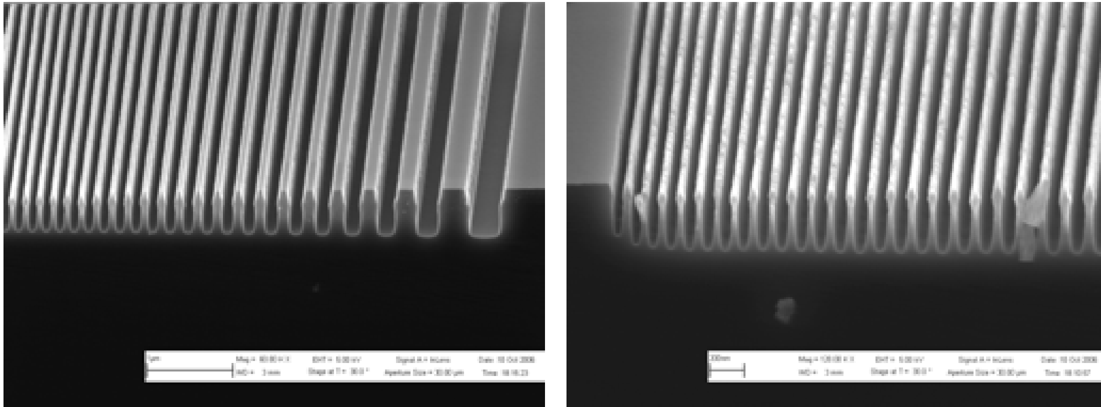

Figure 6.12: Scanning electron microscopy images of a linear Fresnel zone plate structure. When the reactive ion etching process lasts a too long time the chromium layer is removed from the ridges of narrowest lines and the silicon is partly damaged.

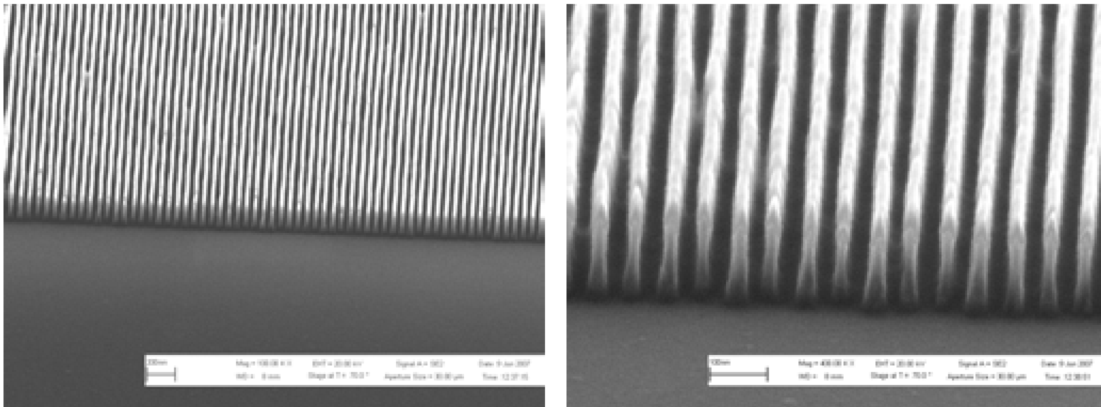

Figure 6.13: Scanning electron microscopy images of 30 nm line/spacing structures. The structure depth is 180 nm, showing the feasibility of obtaining 30 nm structures with an aspect ratio of 6.

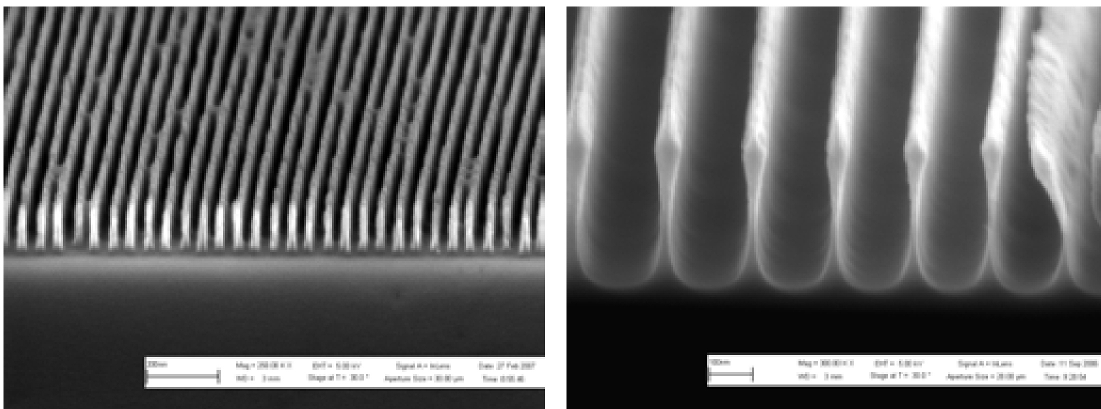

Figure 6.14: Limits of silicon reactive ion etching technique. 25 nm line/spacing grating etched 150 nm deep into silicon (left). Silicon walls which are as narrow as 15 nm in the middle part of the structure (right).

6.3 Silicon Fresnel Zone Plate Characterization

Several sets of silicon Fresnel zone plates and a few silicon beamshaping condenser lenses were produced following the manufacturing techniques explained in the previous sections. The devices were carefully inspected by optical and electron microscopy. Later, some of them were tested at the soft x-ray microscopes installed at the *PolLux Beamline* of the *Swiss Light Source* at the *Paul Scherrer Institut* (Switzerland) and at *TWINMIC experimental station* at *ELETTRA Sincrotrone* (Italy).

6.3.1 Silicon Fresnel Zone Plate

Table 6.4 shows the specifications of the two mostly patterned Fresnel zone plate designs. The values given in the table are calculated considering a photon energy of 500 eV.

Silicon Fresnel Zone Plate Specifications at 1st Diffraction Order at 500 eV (λ=2.48 nm)			
Outermost Zone Width	Δr	49.6 nm	30.0 nm
Silicon Membrane Substrate	—	$\sim$ 500 nm	$\sim$ 1000 nm
Diameter	D	100 μm	100 μm
Focal Length	f	2.000 mm	1.225 mm
Number of Zones	N	504	825
Spatial Resolution	δ_{res}	60.5 nm	36.6 nm
Depth of Focus	DOF	4.0 μm	1.4 μm
Numerical Aperture	NA	0.025	0.041
Maximum Spectral Bandwidth	$\Delta\lambda/\lambda$	$2.0 \cdot 10^{-3}$	$1.2 \cdot 10^{-3}$
Structure Height	h	300 — 500 nm	180 nm
Groove Diffraction Efficiency	η	13 — 20%	5.8%

Table 6.4: Generally, two designs of silicon Fresnel zone plates with 50 nm and 30 nm outermost zone widths were manufactured. This table summarizes the main parameters and specifications of the two patterns at a photon energy of 500 eV. They both have a diameter of 100 μm.

Both designs consist of a Fresnel zone plate with 100 μm diameter, but they have different outermost zone widths of 50 nm and 30 nm. They respectively have focal lengths of 2.0 mm and 1.2 mm at 500 eV photon energy. While a higher spatial resolution is expected for the 30 nm outermost zone width Fresnel zone plate, its diffraction efficiency theoretically expected is only 5.8% (according to the achieved zone thickness during the reactive ion etching). Nevertheless, a groove diffraction efficiency of 15% is anticipated for the Fresnel zone plate structure with 50 nm outermost zone width.

Figure 6.15 shows optical microscopy images of both designs. Optical microscopy provides a non-detailed but very fast inspection of the patterned silicon structures. Due to dimensions of the line pattern which are mostly smaller than the wavelength

of visible light only the central lines of the Fresnel zone plates can be resolved. However, using differential interference contrast the smooth colour gradients guarantees that the structures have been successfully patterned. In figure 6.5(b), small dark spots at the edges corresponds to regions of the 30 nm outermost zone width Fresnel zone plate where there is a relatively important amount of defects. Dark stripes along the main axis that become wider at the outer regions of the structures appears because of the polarized light that illuminates the sample.

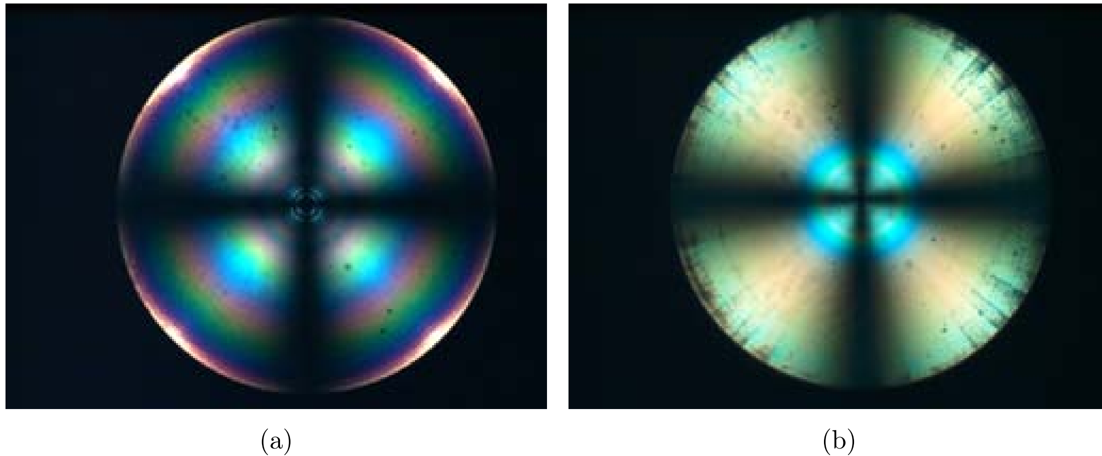

(a) (b)

Figure 6.15: Optical microscopy images of 100 μm diameter silicon Fresnel zone plates with an outermost zone width of 50 nm (a) and 30 nm (b) obtained by differential interference contrast. The color gradient ensures that the structures have been successfully produced.

Figures from 6.16 to 6.21 demonstrate the quality of the silicon structures showing several sets of scanning electron microscopy images. Figures 6.16, 6.17 and 6.18 correspond to a Fresnel zone plate pattern with an outermost region of 50 nm. In this case, a PMMA resist layer was used during the e-beam lithography. Since PMMA is a positive-tone resist, notice that the structure is *embedded* into the silicon membrane. This fact precludes us from looking at the cross-section of the structure but a profile like the one in figure 6.11 is reasonably assumed since both samples were processed following the same procedures. Thus, the expected depth of the grooves is around 300 — 400 nm. Figure 6.16 shows a general view of the silicon lens, and Moiré fringes ensure that the pattern has been successfully generated all around the structure. Concerning the manufacturing process and in particular the silicon reactive ion etching step, one can observe in figure 6.17 that the sidewalls of the silicon structures are covered with a thin *passivating* layer that prevents the etching in the horizontal direction. Figure 6.18 shows the edges of the structure with 50 nm lines/spacings perfectly patterned.

On the other hand, figures 6.19, 6.20 and 6.21 show a Fresnel zone plate structure with an outermost zone width of 30 nm that was patterned using a Calixarene resist layer for the e-beam exposure. In figure 6.19, notice that in this case the central circular zone is etched into the silicon substrate, that is, the structure has a pattern complementary to the one in the structures of the preceding images because Calixarene is a negative-tone resist. This change does not affect at all the Fresnel zone plate properties since

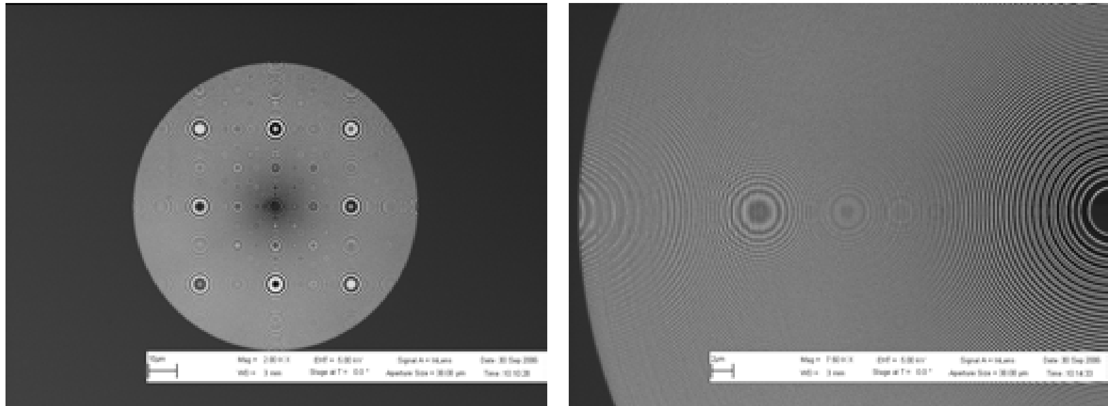

Figure 6.16: Scanning electron microscopy images of a 100 μm diameter silicon Fresnel zone plate with an outermost zone width of 50 nm. The Moiré fringes guarantee that the pattern has been successfully produced all around the structure.

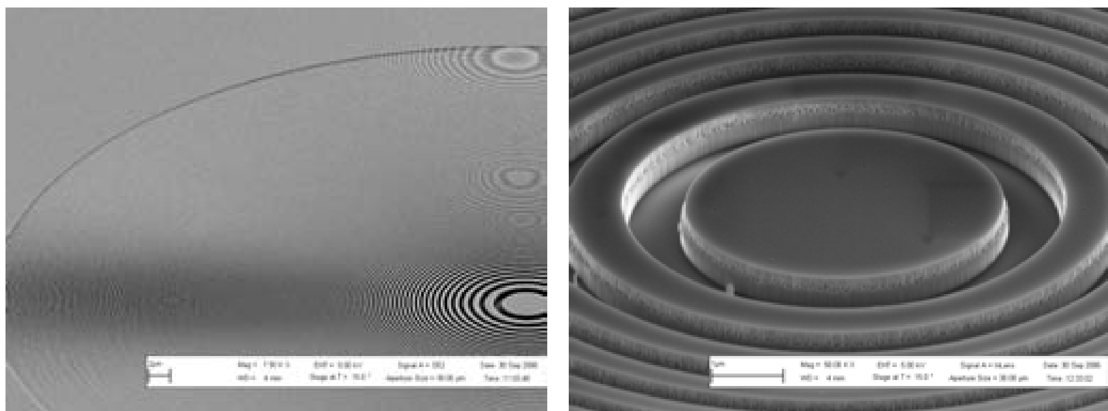

Figure 6.17: Detail of the central regions of a 100 μm diameter silicon Fresnel zone plate with an outermost zone width of 50 nm. Notice that a thin passivating layer has been grown on the sidewalls of the silicon rings (right).

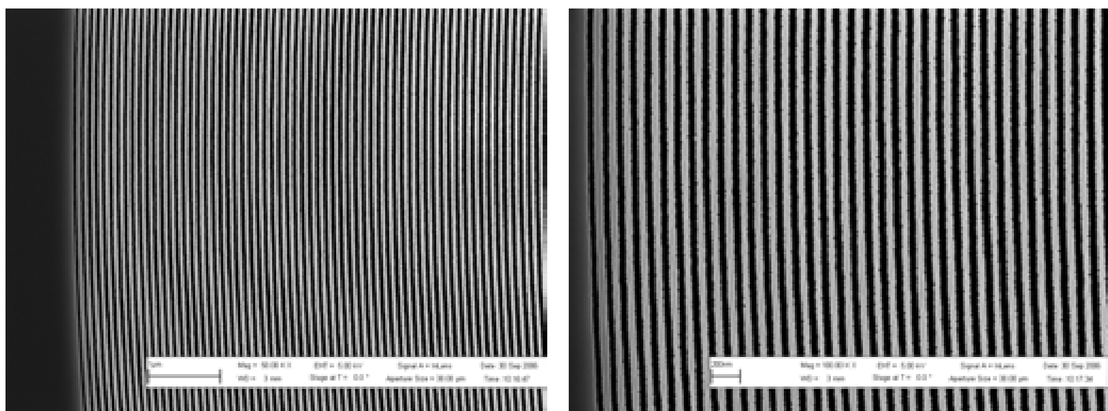

Figure 6.18: Outermost zone width of 50 nm of a 100 μm diameter silicon Fresnel zone plate. The lines are perfectly patterned into the silicon membrane.

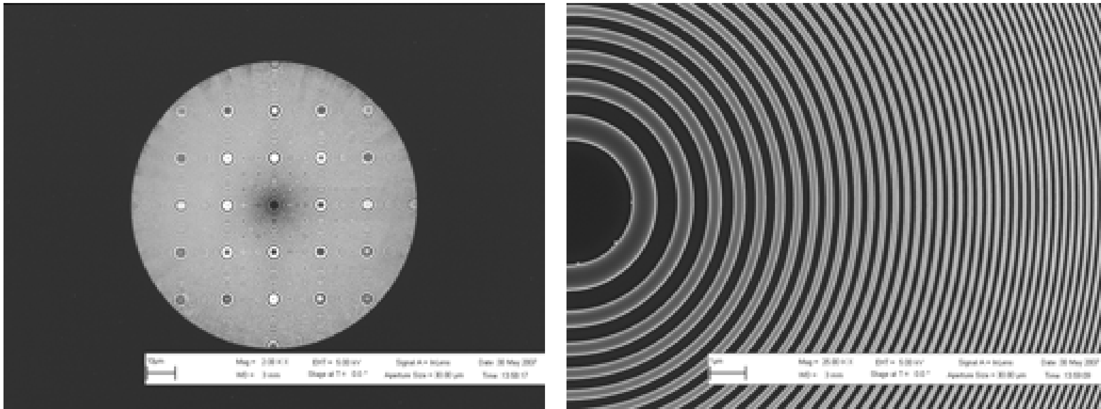

Figure 6.19: Scanning electron microscopy images of a 100 μm diameter silicon Fresnel zone plate with an outermost zone width of 30 nm.

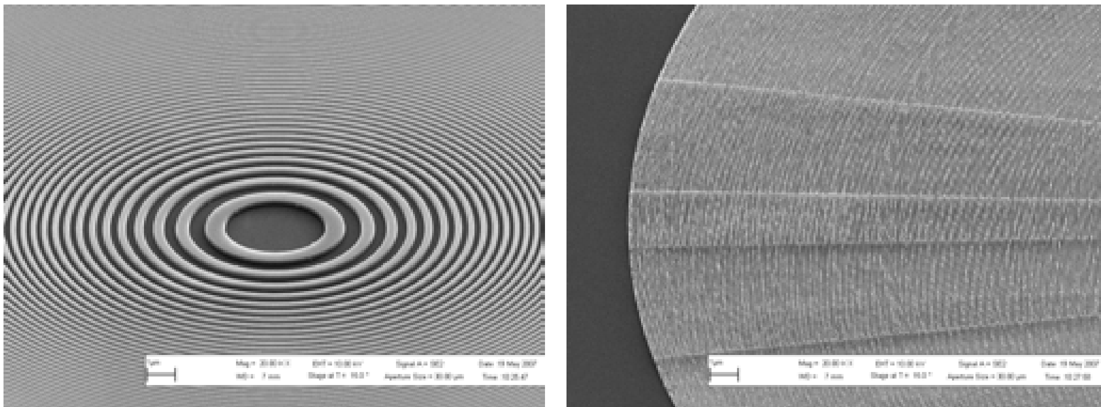

Figure 6.20: Detail of the central and the edge regions of a 100 μm diameter silicon Fresnel zone plate with an outermost zone width of 30 nm and a depth of 180 nm. The dose correction applied during the exposure that splits each ring in several pieces is visible in the outer regions of the structure (right).

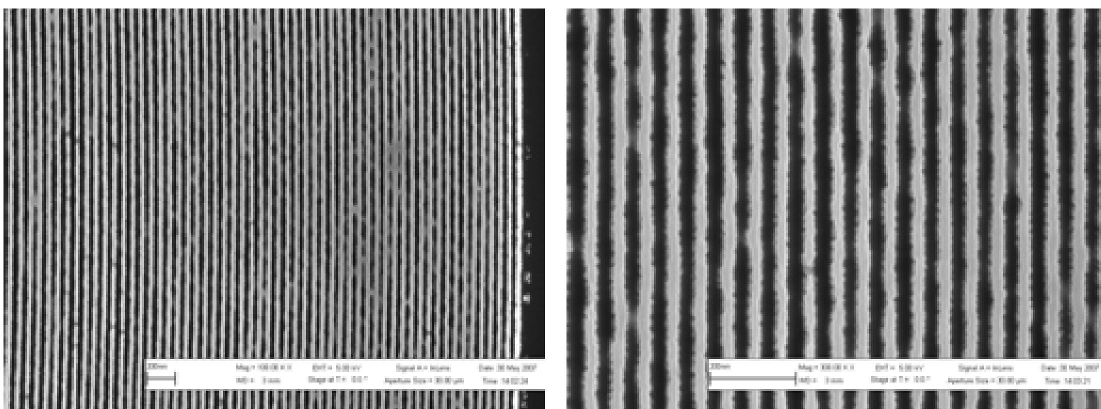

Figure 6.21: Outermost zone width of 30 nm of the 100 μm diameter silicon Fresnel zone plate. The line pattern is perfectly defined.

complementary patterns produce equivalent diffractive phenomena, as well-known in visible optics. The expected profile for the narrowest lines should be similar to the one of the grating shown in figure 6.13 with a structure height of 180 nm. In this case there are some defects in the outermost regions of the structure. They were originated during the e-beam lithography exposure, showing that the e-beam tool was operated at the limit of its capability. The radial lines visible in the outer regions of zone plate, like in figure 6.20, appears when splitting each ring during the e-beam exposure to apply the dose correction discussed in section 6.2.2. They consist of an *array* of defects again related to the e-beam system performance for such narrow line widths.

6.3.2 Silicon Beamshaping Condenser Lens

Following the design given in section 3.3, a few silicon beamshaping condenser lenses were also produced by means of electron beam lithography and silicon reactive ion etching. Table 6.5 gives the detailed parameters and specifications of the two different designs that were generated considering a photon energy of 500 eV. According to the design they should produce an intense flat-top illumination spot of 50 μm × 50 μm and 35 μm × 35 μm at their corresponding focal lengths (28.50 mm and 14.25 mm at 500 eV, respectively).

Silicon Beamshaping Condenser Lens Specifications at 500 eV (λ=2.48 nm)			
Subfield/Spot Size	d	50 × 50 μm^2	35 × 35 μm^2
Silicon Membrane Substrate	—	∼ 500 nm	∼ 500 nm
Diagonal Length	D	1414 μm	707 μm
Focal Length	f	28.5 mm	14.25 mm
Outermost Zone Width	Δr	50 nm	50 nm
Number of Zones	N	7070	3535
Depth of Focus	DOF	4.0 μm	4.0 μm
Numerical Aperture	NA	0.025	0.025
Maximum Spectral Bandwidth	$\Delta\lambda/\lambda$	$1.4 \cdot 10^{-4}$	$2.8 \cdot 10^{-4}$
Structure Height	h	300 — 500 nm	300 — 500 nm
Groove Diffraction Efficiency	η	13 — 20%	13 — 20%
Central Stop Size	d_{CS}	380 × 380 μm^2	250 × 250 μm^2
Central Stop Thickness	h_{CS}	800 nm Au	800 nm Au

Table 6.5: Two designs of beamshaping condenser lens were manufactured to produce a square flat-top illumination spot of 50 × 50 μm^2 and 35 × 35 μm^2. This table summarizes the main parameters and specifications of the two patterns at a photon energy of 500 eV.

The elements were placed on silicon substrate with a membrane area of 3 mm × 3 mm. During the manufacturing process there were no significant differences in relation to the silicon Fresnel zone plate fabrication. The only relevant detail is that the e-beam

lithography of a single element could last as long as 8 hours since the areas to be exposed were as *big* as 1 mm^2.

Figures 6.22 and 6.23 show optical and scanning electron microscopy images of a beamshaping condenser lens. In this case it has a diagonal length of 707 μm and it is divided in 400 subfields of 35 μm $\times$ 35 μm. Notice that according to the design each subfield contains a grating with the appropriate orientation and line width to deviate the first order beam into the focal spot of the element.

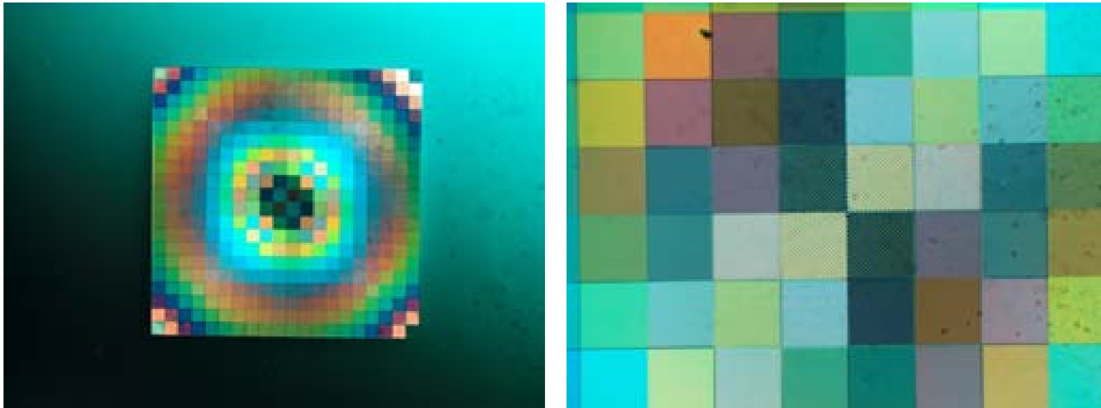

Figure 6.22: Optical microscopy images of beamshaping condenser lens obtained by differential interference contrast. The diagonal length of the device is 707 μm split in 400 subfields of 35 $\times$ 35 μm^2. Only the central subfields are resolved but the color gradient in the remaining subfields demonstrates that the element have been successfully patterned.

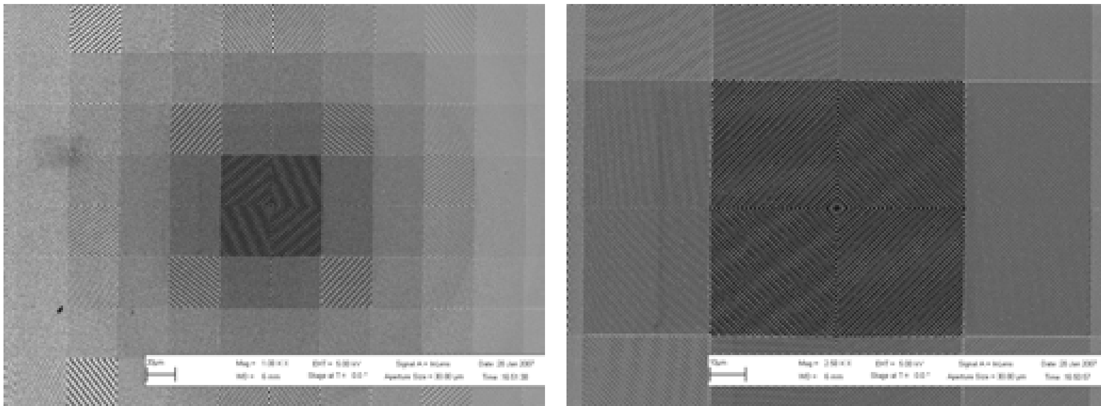

Figure 6.23: Scanning electron microscopy images of the central subfields of the beamshaping condenser lens. Notice the different orientation and line width of the gratings contained in each subfield.

As discussed at the end of section 3.3 a central stop is strongly required for the beamshaping condenser lens. In order to stop a direct x-ray beam with a photon energy of 500 eV, gold thicknesses of 500 — 1000 nm are demanded[6]. The central stop was man-

[6]X-ray transmission of 500 nm and 1000 nm thick gold layers is $0.5 \cdot 10^{-5}$ and $0.3 \cdot 10^{-10}$ at 500 eV photon energy, respectively.

ufactured on the backside of the silicon membrane after the fabrication of the beamshaping condenser lens on the frontside. The central stop was produced by gold evaporation through a square aperture conveniently aligned over the center of the beamshaping condenser lens, as schematically shown in figure 6.24. The alignment of the square aperture and the beamshaping condenser lens was manually prepared using an optical microscope in transmission. Both condenser lens and central stop were big enough so that placement inaccuracies of 10 μm are tolerable. If after the evaporation the central stop was totally misplaced, the chip could still be immersed in *Aqua Regia* solution[7], which would dissolve the central stop made of gold without damaging the silicon structure and the central stop evaporation procedure could be repeated.

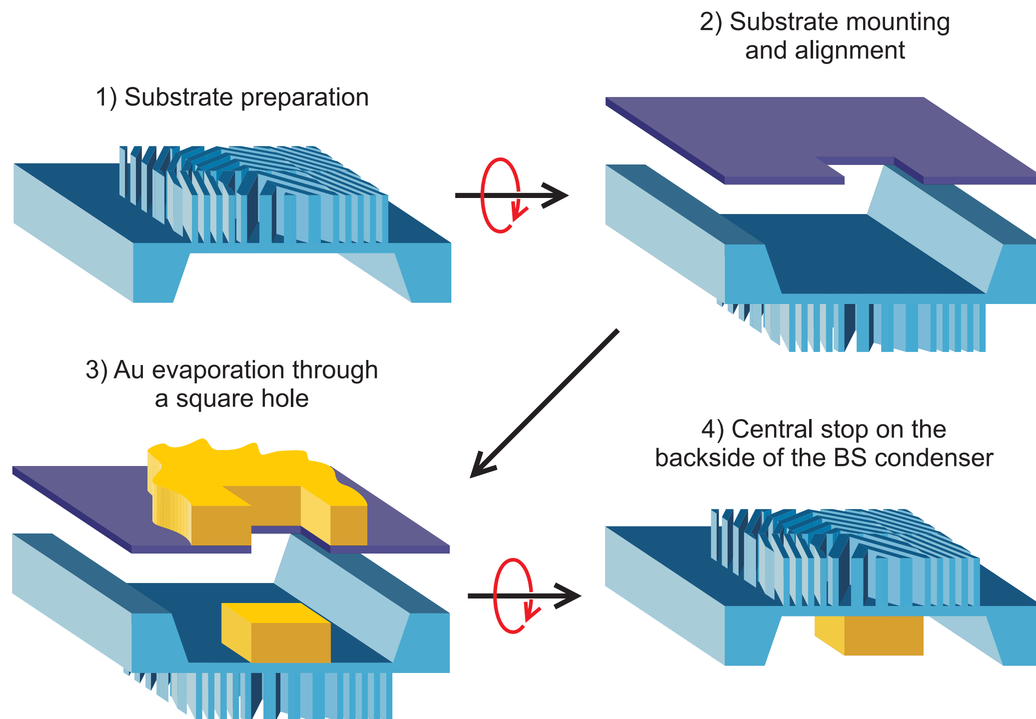

Figure 6.24: Manufacturing steps for the production of a 800 nm thick square central stop on the backside of silicon membrane where a beamshaping condenser lens is located. Gold is evaporated through a square aperture conveniently aligned.

According to the size of the beamshaping condenser lens, the size of the central stops were 380 × 380 μm^2 or 250 × 250 μm^2, respectively. Their thickness was 800 nm of gold, ensuring a residual transmission below $0.5 \cdot 10^{-5}$ at 500 eV photon energy.

[7]Aqua Regia is a corrosive solution combining nitric acid (NHO_3) and hydrochloric acid (HCl). It is usually prepared with a volumetric concentration of 1:3 NHO_3:HCl. Freshly components must be mixed just before its use since Aqua Regia solution quickly loses its effectiveness.

6.3.3 Full-Field Transmission X-ray Microscopy (TXM)

Full-field transmission x-ray microscopy (TXM) experiments were performed at the *TWINMIC Microscope* [95] installed at the *ELETTRA Sincrotrone* in Trieste (Italy). A brief introduction to TXM technique was already given in section 2.3.2 and the general scheme of a TXM experimental station was shown in figure 2.5. During our experiments, the radiation was extracted from an undulator source at the BACH beamline [96] and the photon energy was set to 720 eV for the first run of experiments. The Fresnel zone plate mounted as objective lens of the microscope was removed and replaced by a 100 μm diameter silicon Fresnel zone plate with an outermost zone width of 50 nm. The sample was illuminated with the routinely used condenser lens of the TWINMIC microscope [69]. A 100 μm pinhole was used as order selecting aperture and a soft x-ray CCD-based detector was located at 1.5 m downstream from the sample. The detector had 1300 $\times$ 1340 pixels of 20 μm^2 each, which resulted in a total active area of 26.0 $\times$ 26.8 mm^2. Typical acquisition time for a single TXM image ranged from 5 s to 30 s to ensure a good signal-to-noise ratio. Shorter acquisition times ($\sim$ 250 ms) were used during the preparation and alignment of the elements. A 10 μm radius Siemens Star[8] made of nickel and located on a thin silicon nitride membrane was used as test sample. Smallest radial period of the spokes at the innermost part of the structure was 60 nm (i.e. 30 nm lines/spacings).

The alignment of all the elements was quite effortful and time consuming but eventually the functionality of the silicon Fresnel zone plate was fully demonstrated. Figure 6.25 shows a TXM image of the nickel Siemens star obtained by using the silicon Fresnel zone plate with an outermost zone width of 50 nm. Smallest resolved lines close to center of the element correspond to 70 nm lines/spacings. So, this result fulfills the theoretically expected spatial resolution of 60 — 70 nm for a Fresnel zone plate of 50 nm outermost zone width.

Later, we replaced the condenser lens of the standard TWINMIC experimental station by a silicon beamshaping condenser lens with a subfield size of 35 μm $\times$ 35 μm, obtaining a setup like the one shown in figure 3.18. Then, figure 6.26 shows an TXM image of the nickel Siemens star when using a silicon beamshaping condenser lens to produce a square flat-top illumination and a silicon Fresnel zone plate as objective lens to generate the image on the soft x-ray CDD-based detector.

Figure 6.26 demonstrates that the beamshaping condenser lens is producing an intense square flat-top illumination. It has the expected dimensions of 35 μm $\times$ 35 μm, and the area of the illuminated spot is matched with the shadow that the central stop produces on the detector (that is, the region free of bright small spots). However, the active area of the detector is bigger and that allows us to observe the distribution of bright

[8] A Siemens star is a versatile element to test the resolution of optical instruments. It consists of a pattern of bright spokes on a dark background or vice versa, which radiate from a common center and become wider as they get further from it. Ideally, the spokes and the gaps between them become extremely narrow close to center of the structure. Radial symmetry is very convenient to check the spatial resolution in any direction.

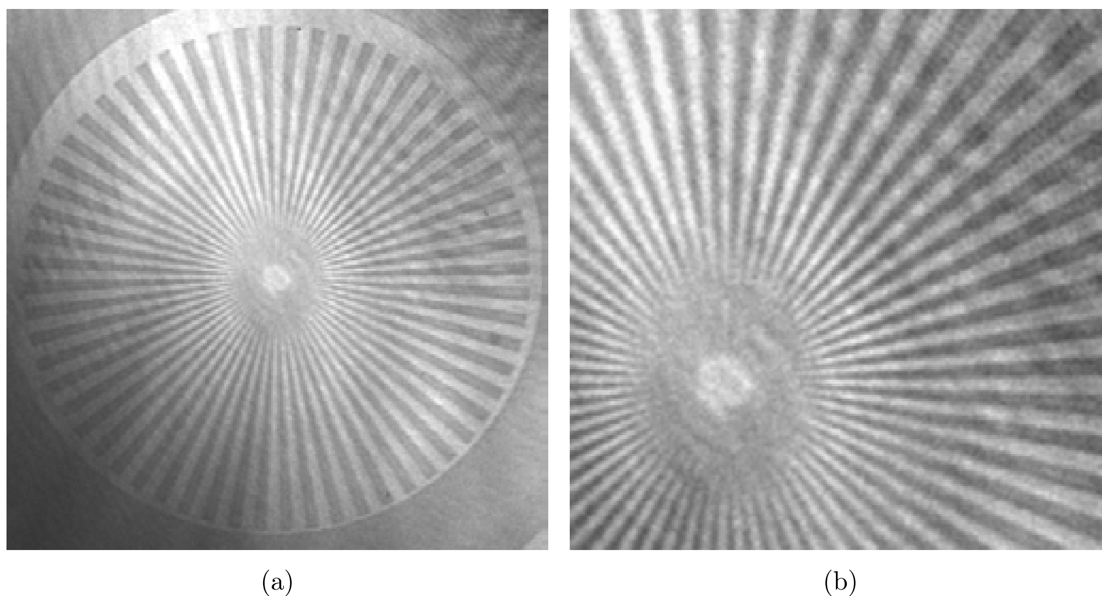

(a) (b)

Figure 6.25: TXM image of a Siemens star made of nickel (a). The image was taken using a silicon Fresnel zone plate with an outermost region of 50 nm as objective lens of the TXM setup. A photon energy of 720 eV was used. The smallest resolved lines close to the innermost part of the structure correspond to 70 nm lines/spacings. (b) Digital zoom to the central part of the image.

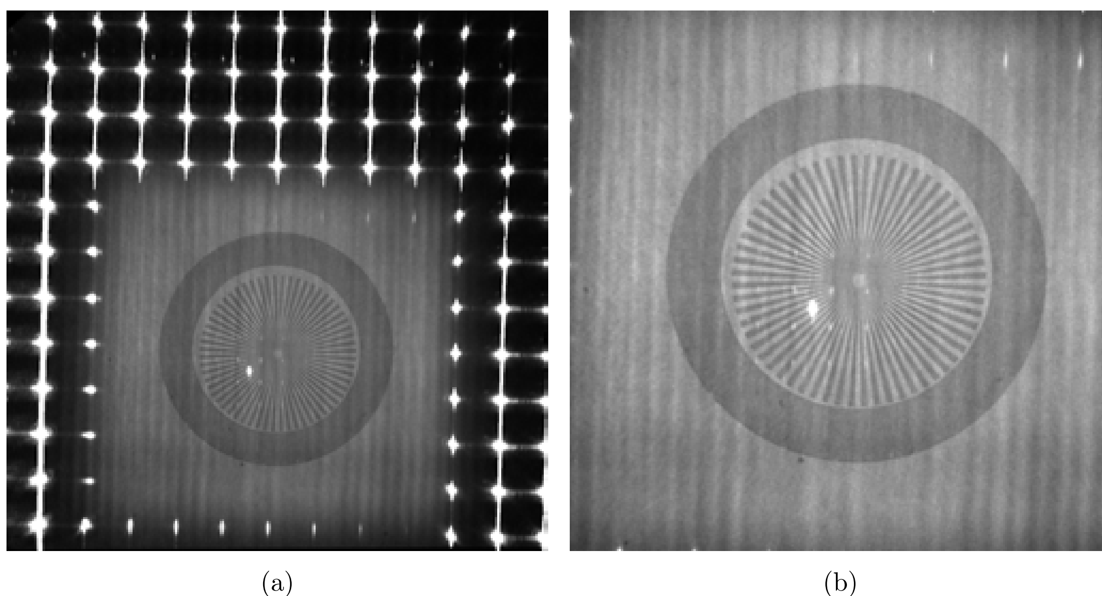

(a) (b)

Figure 6.26: TXM image of a Siemens star made of nickel (a). The image was obtained by utilizing a silicon beamshaping condenser lens to produce a square flat-top illumination on the sample and by using a silicon Fresnel zone plate as objective lens to generate the image on the detector. (b) Digital zoom to the central part of the image.

peaks coming from each subfield of the condenser, as discussed at the end of section 3.3. Close to the center of the image there is a bright spot, which probably corresponds to the transmitted direct beam through the central stop. This was totally unexpected according to the transmission calculations given in the previous section. Even considering that we were using a photon energy of 720 eV, a 800 nm thick gold layer should have a residual transmission of $0.2 \cdot 10^{-5}$. Since the BACH beamline is an undulator-based beamline[9], a feasible explanation could be that there was higher order contamination, that is, a non-negligible amount of high energy photons were not totally removed at the upstream optics of the beamline and they were reaching the experimental station.

For last run of experiments, we replaced the beamshaping condenser lens with a subfield of 35 μm × 35 μm by a bigger one with subfield dimensions of 50 μm × 50 μm and the photon energy of the x-ray was set to 500 eV. In this case the illuminated area was bigger than the active area of the detector, and the borders of the focal spot were not visible when all the elements were aligned. There was a substantial increase of the intensity on the sample since the condenser was collecting photons from a bigger cross-section of the incoming beam. Figures 6.27 and 6.28 show TXM images when illuminating the sample with the biggest beamshaping condenser lens. TXM images of a Siemens star made of silicon are shown in figure 6.27. The narrowest lines resolved at the central part of the structure have a radial period of 140 nm (70 nm lines/spacings).

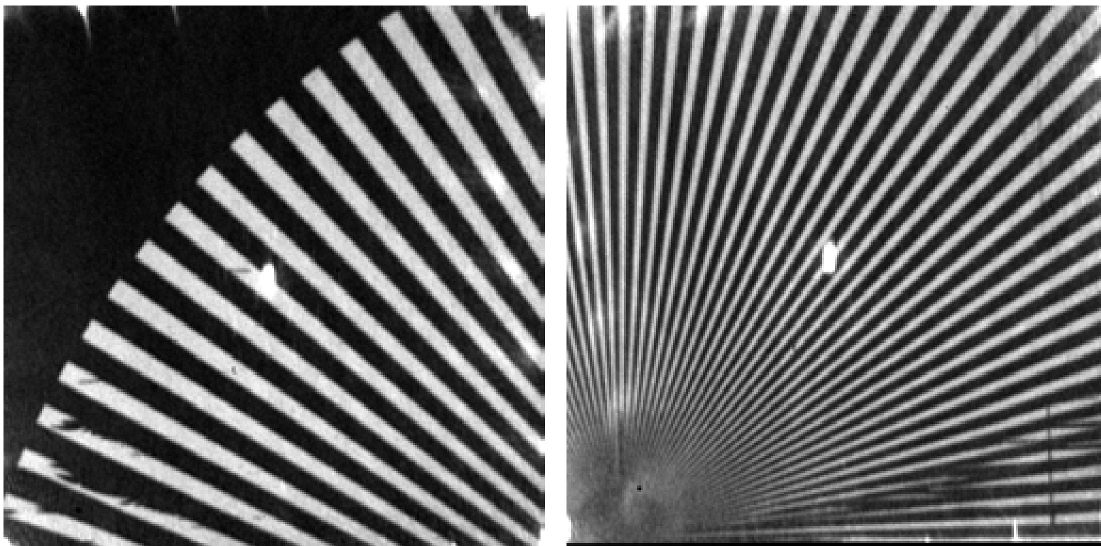

Figure 6.27: TXM image of a silicon Siemens star at 500 eV. This element was manufactured by means of e-beam lithography and silicon reactive ion etching as the optical elements presented in this chapter.

In addition, TXM images of biological material are shown in figure 6.28, demonstrat-

[9]Due to its characteristics, when an undulator source is emitting at given photon energy, E, it is also emitting a non-negligible amount of photons at energies corresponding to higher odd orders, that is, $3E$, $5E$, $7E$...

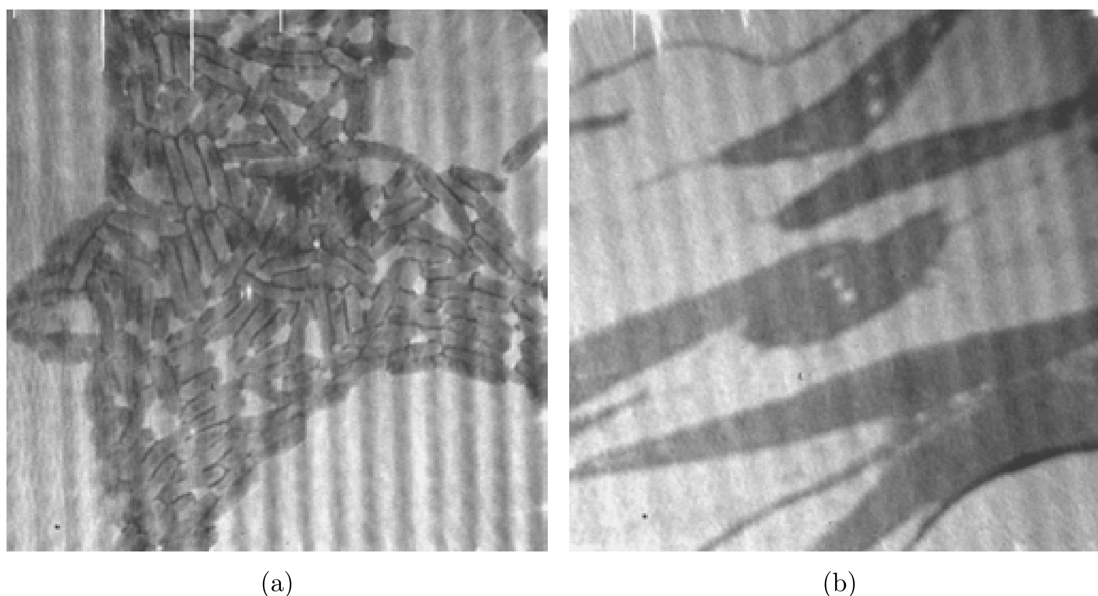

(a) (b)

Figure 6.28: TXM images of biological material at a photon energy of 500 eV (courtesy of Eva Pereiro). (a) Culture of Escherichia Coli bacteria. (b) HeLa cells (belonging to an immortal cell line used in medical research).

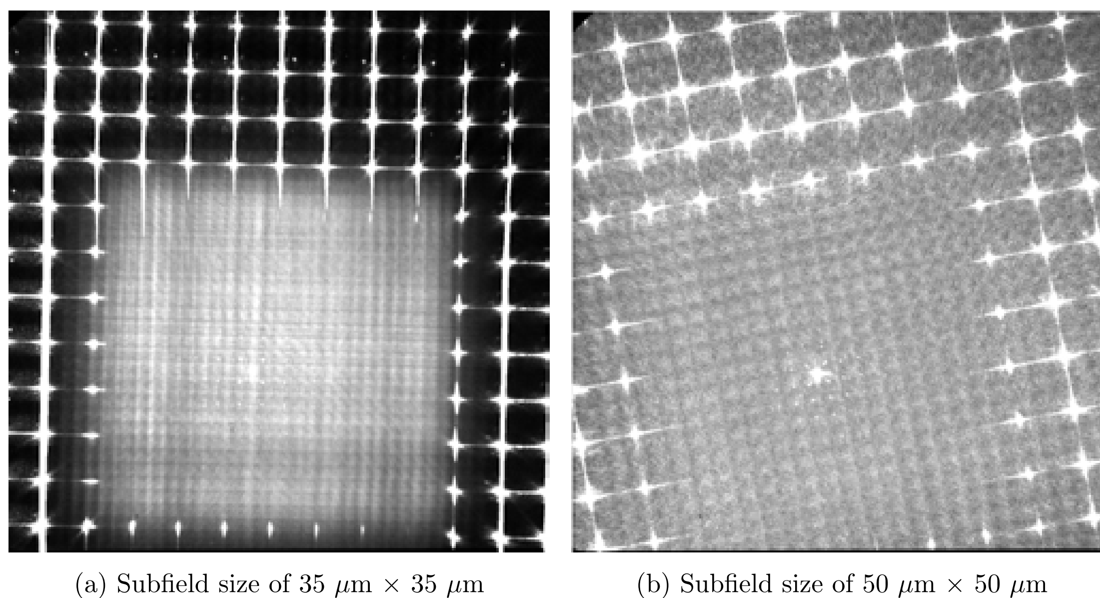

(a) Subfield size of 35 μm $\times$ 35 μm (b) Subfield size of 50 μm $\times$ 50 μm

Figure 6.29: The square flat-top illumination produced by the beamshaping condenser lenses contained some fringes that diminished the contrast in the TXM images. The fringes are interference phenomena related to coherence of the incoming radiation. They could be partly removed by introducing vibrations into the system.

ing the feasibility of using silicon-based optics in biology-oriented soft x-ray microscopes.

Eventually, we want to add a comment concerning the flat-top illumination that the beamshaping condenser lenses are producing. As it can be seen in figure 6.29 there were some interference fringes in the flat-top illumination spot which were partly degradating the contrast during the acquisition of the TXM images. These phenomena are probably related to the coherent flux produced by the undulator source which usually introduces speckle artifacts in the imaging system of soft x-ray microscopes. During the acquisition of TXM image shown above mechanical vibrations were introduced in the system to average coherent flux and to improve the illumination on the sample. However, the spatial resolution of the system was slightly decreased.

Despite being beyond of the scope of this report, further investigations in this topic would be very interesting to determine which modifications can be implemented in the beamshaping condenser lens design to improve the quality of the illumination on the sample.

6.3.4 Scanning Transmission X-ray Microscopy (STXM)

Scanning transmission x-ray microscopy (STXM) experiments were carried out at the *PolLux Beamline* [97] of the *Swiss Light Source* at the *Paul Scherrer Institut*. Main features of STXM experimental stations were given in section 2.3.2 and schematically shown in figure 2.6. As explained, the tiny focal spot produced by the Fresnel zone plate is used to probe the sample. The detector located behind the sample records the transmitted signal generating the image sequentially while the sample is accurately moved.

At the PolLux beamline the radiation is extracted from a bending magnet and an optical system composed of mirrors and gratings prepares (focuses and monochromatizes) the x-ray beam before it enters into the experimental station that contains the microscope. The photon energy of the x-ray beam was set to 500 eV. The Fresnel zone plate mounted as focusing element in the microscope was removed and replaced by several 100 μm diameter silicon Fresnel zone plates. A disadvantage of our silicon Fresnel zone plates was the lack of a central stop. Without a central stop the transmission of the zeroth order through the sample results in a contrast decrease of the STXM images. That is, in STXM imaging the central stop is not an essential component, but its use is highly recommended. In order to reduce the effects of the lack of the central stop, we replaced the standard 50 μm diameter pinhole serving as order selecting aperture by a smaller pinhole of 20 μm diameter. However, the use of a smaller pinhole as order selecting aperture implies that it has to be located closer to the sample and aligned with high accuracy not to cut the radiation cone coming from the Fresnel zone plate.

Two series of experiments were carried out at the PolLux beamline. During the first run of experiments we were using a silicon Fresnel zone plate with an outermost zone of 50 nm. In the second one a silicon Fresnel zone plate with an outermost zone of 30 nm

was mounted on the STXM experimental station. A quite higher spatial resolution was foreseen in the latter case.

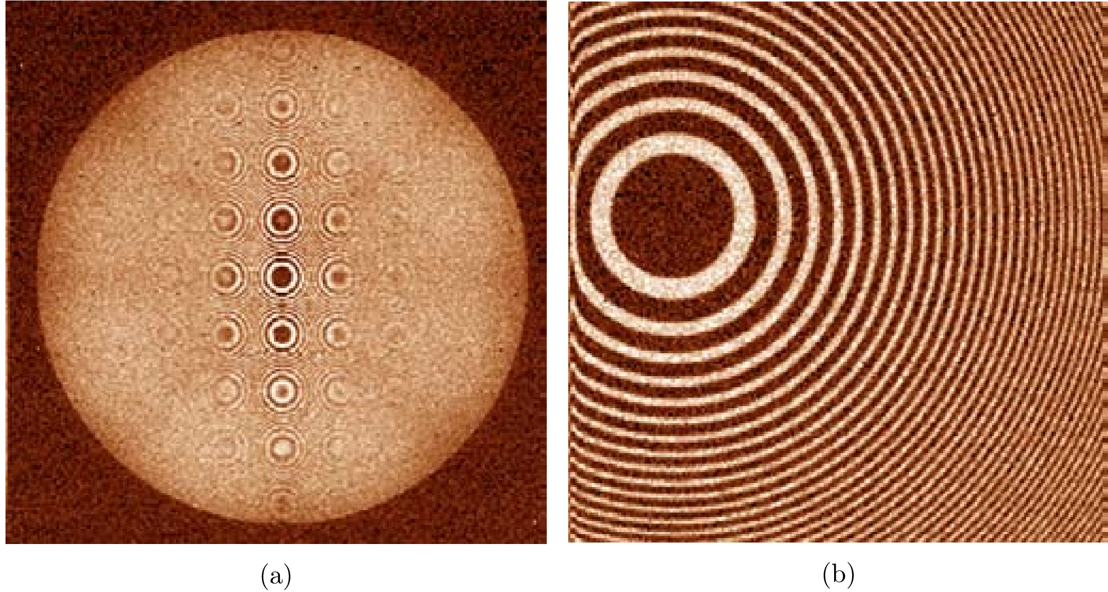

(a) (b)

Figure 6.30: STXM images of a silicon Fresnel zone plate when using a silicon Fresnel zone plate with an outermost zone width of 50 nm as a focusing element of the microscope at a photon energy of 500 eV. (a) General view of the structure. (b) Fine scan at the central region.

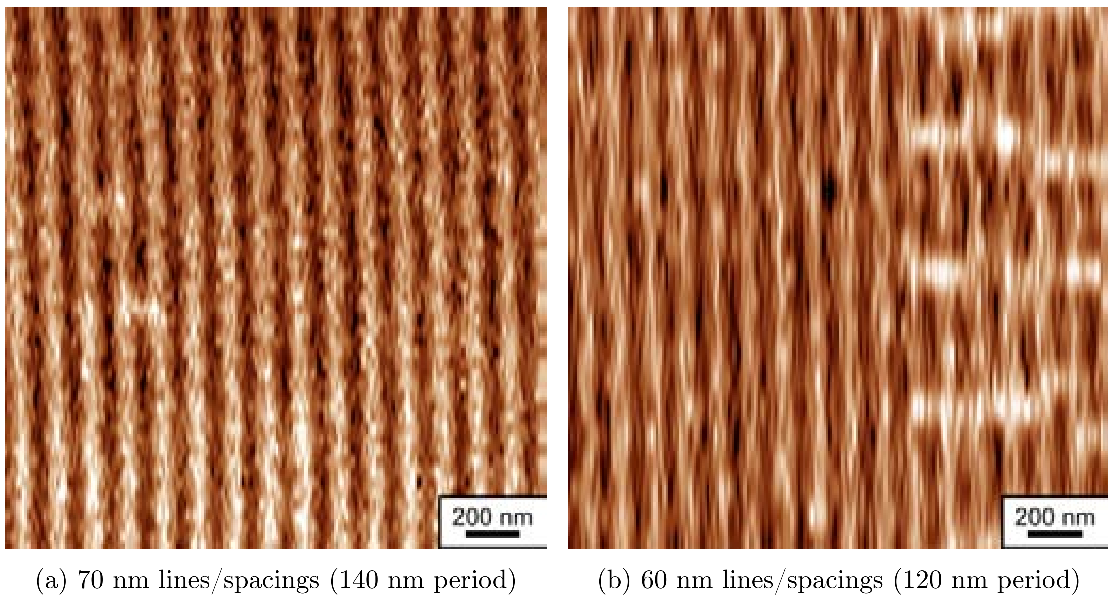

(a) 70 nm lines/spacings (140 nm period) (b) 60 nm lines/spacings (120 nm period)

Figure 6.31: STXM images of gold structures when using a silicon Fresnel zone plate with an outermost zone width of 50 nm. The gold lines have a period of 140 nm (a) and 120 nm (b) and they could not be well resolved.

Figure 6.30 shows two STXM images obtained with 50 nm outermost zone width silicon Fresnel zone plate. In this case we were using a second silicon Fresnel zone plate

as a test sample. The Moiré fringes in the left picture and the finer scan from the center of structure in the image on the right demonstrate the functionality of the silicon Fresnel zone plates to obtain valuable data in a STXM setup. Both images are made of 256 × 256 pixels, despite a different step size of 470 nm and 78 nm was respectively used. The acquisition time for each pixel was 10 ms so that the total time to record the whole image was around 12 min.

On the other hand, figure 6.31 shows two STXM images of a gold structure with lines/spacings of 70 nm (140 nm period) and 60 nm (120 nm period). This time, the images are composed of 200 × 200 pixels using a step size of 10 nm. Clearly, one can observe that the pattern is not well resolved. Despite the lines and spacings can be guessed, their borders are totally blurred. However, this is totally reasonable according to the expected spatial resolution of a Fresnel zone plate with an outermost zone width of 50 nm. The expected size of the focal spot produced by such a focusing element is around 65 nm and only bigger structures in the sample are expected to be completely resolved.

Figures from 6.32 to 6.35 show STXM images taken when using a silicon Fresnel zone plate with an outermost zone width of 30 nm. These images show several regions of a Fresnel zone plate made of gold with a minimum line width of 35 nm that we were using as test sample. Figure 6.32 shows a general view of the pattern and it is relevant because it demonstrates one of the effects that the lack of the central stop in the system is producing on the STXM images. In the border between the bright and dark areas, one can observe a shadow extending into bright side and a bright region extending into the dark area resulting from the partial shadowing of the direct beam, which has a cross-section as big as the size of the order selecting aperture. When a central stop is used the direct beam would not reach the sample and this variation of the illumination next to any border would disappear and the contrast would be enhanced.

Figures from 6.33 to 6.35 show STXM images of the line pattern of the gold structure. All images are made of 200 × 200 pixels using a step size of 10 nm so that the total scanned area is 2 μm × 2 μm. The acquisition time was 20 ms for each pixel resulting in total time of 15 min to record each image. Figure 6.33(b) must be compared with figure 6.31(b) since both images show equivalent regions of the gold structure and one clearly realizes the improvement in the spatial resolution that has been achieved by replacing the 50 nm outermost zone width Fresnel zone plate by the one with an outermost zone width of 30 nm.

Figure 6.34 shows STXM images with line patterns of 96 nm and 76 nm period. One can observe that the spatial resolution is high enough to perfectly resolve these grating structures.

Eventually, figure 6.35 demonstrates a spatial resolution of 35 nm when using a silicon Fresnel zone plate with an outermost zone width of 30 nm. Scanning electron microscopy and STXM images of the same region of the gold structures with a line pattern with a period of 70 nm are compared. Both images clearly show an equivalent level of detail of

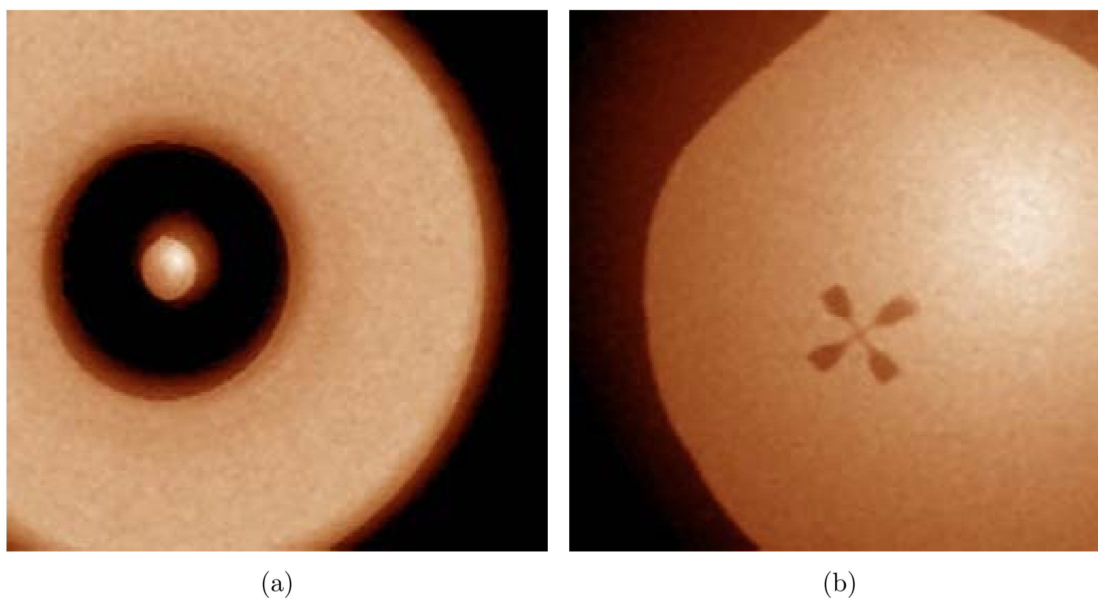

(a) (b)

Figure 6.32: STXM images of Fresnel zone plate pattern made of gold that was used as test sample while focusing the incoming x-ray radiation using a silicon Fresnel zone plate with an outermost zone width of 30 nm. (a) General view of the structure. (b) Detail of the central hole.

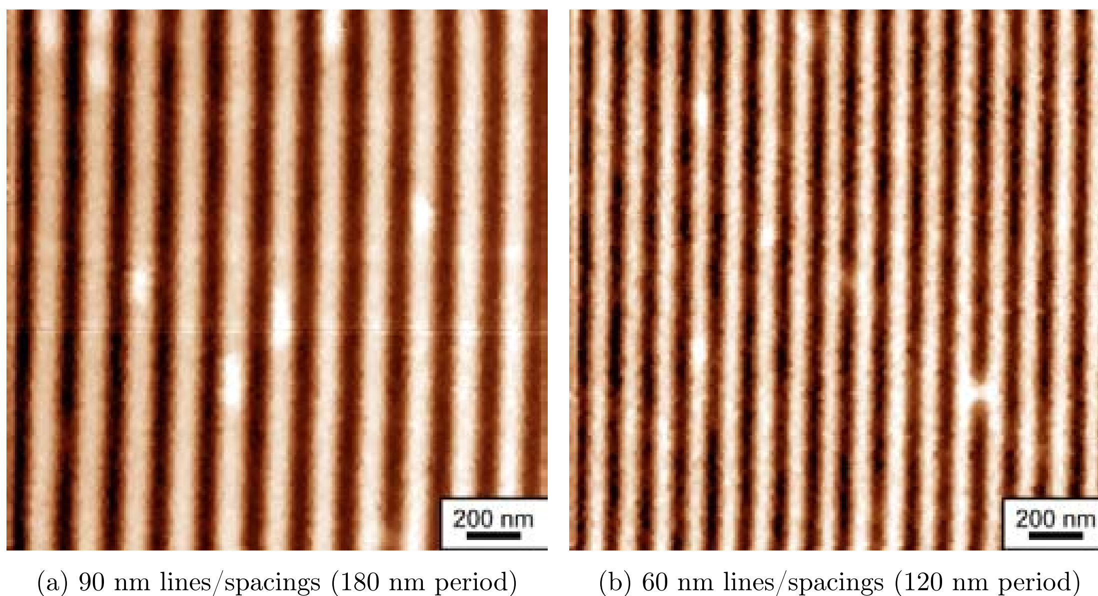

(a) 90 nm lines/spacings (180 nm period) (b) 60 nm lines/spacings (120 nm period)

Figure 6.33: STXM images of gold structures when using a silicon Fresnel zone plate with an outermost zone width of 30 nm. The gold line pattern have a period of 180 nm (a) and 120 nm (b) and they could be well resolved.

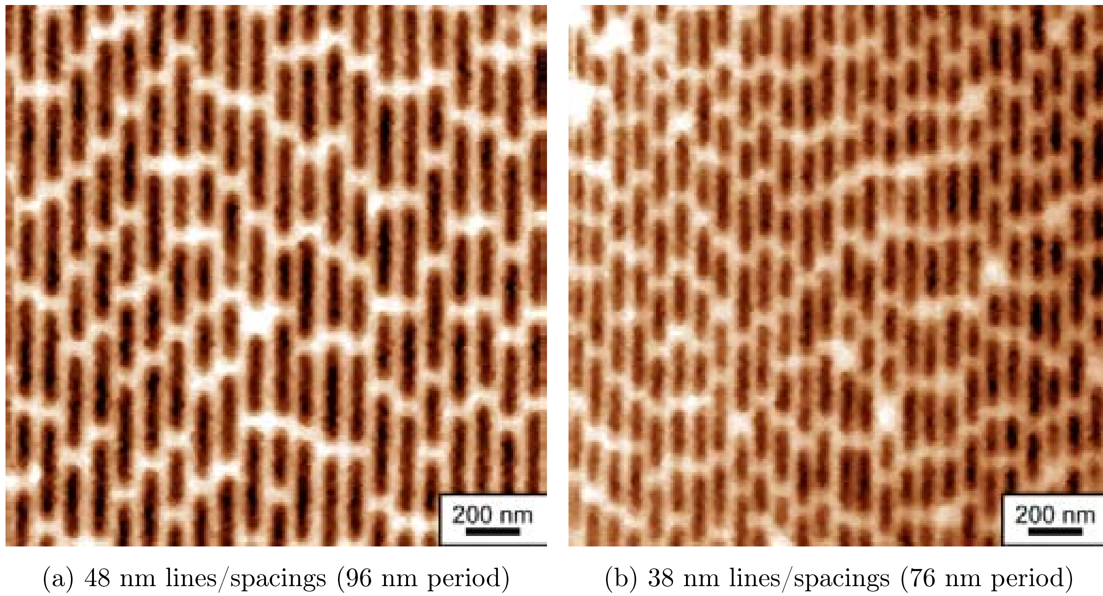

(a) 48 nm lines/spacings (96 nm period) (b) 38 nm lines/spacings (76 nm period)

Figure 6.34: STXM images of gold structures when using a silicon Fresnel zone plate with an outermost zone width of 30 nm. The gold line patterns have a period of 96 nm (a) and 76 nm (b) and they could be perfectly resolved.

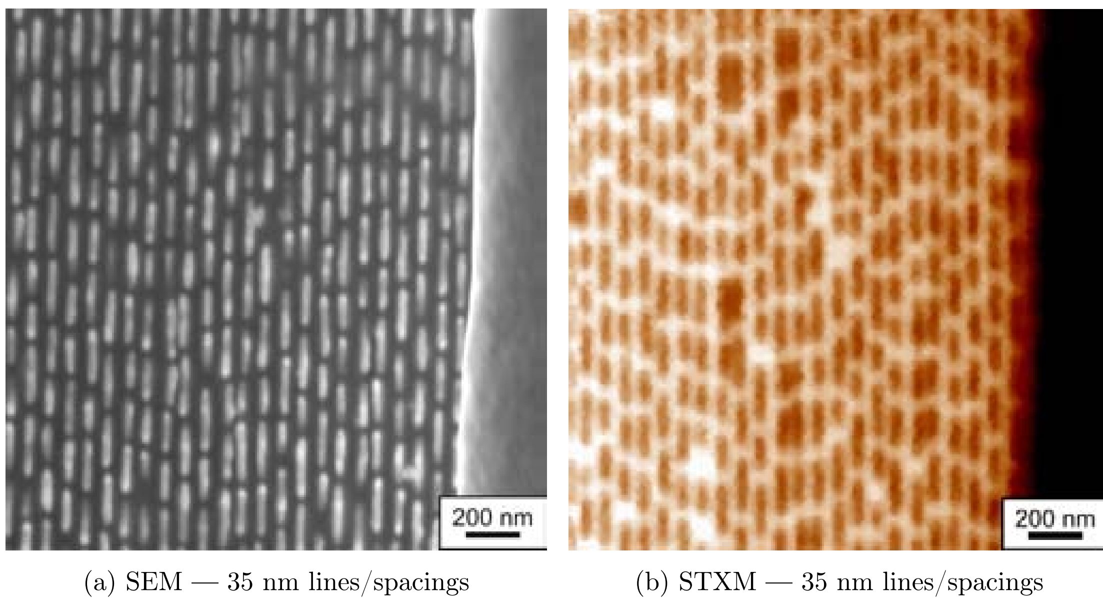

(a) SEM — 35 nm lines/spacings (b) STXM — 35 nm lines/spacings

Figure 6.35: Scanning electron microscopy and STXM images of the same region of the gold structures. The STXM image was taken at a photon energy of 500 eV using a silicon Fresnel zone plate with an outermost region of 30 nm. Both imaging techniques are resolving a pattern of 35 nm lines/spacings (70 nm period) with a similar level of detail.

the grating structure. Thus, our silicon Fresnel zone plate are completely fulfilling our expectations in terms of spatial resolution.

In the last part of the experiments we were concerned about the focusing diffraction efficiency of the silicon Fresnel zone plate. Figure 6.36 shows schematically the two intensity measurements that are required to estimate the diffraction efficiency of the focusing lens.

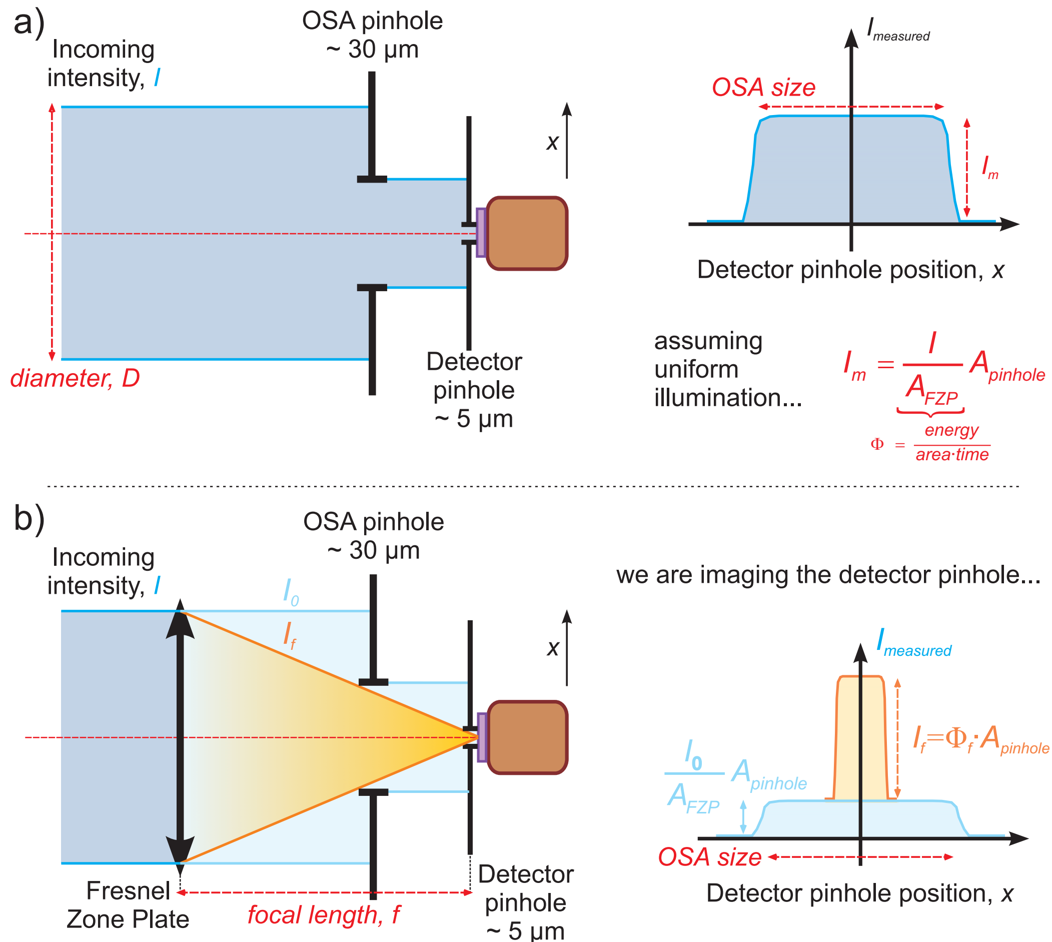

Figure 6.36: Scheme for the measurement of the diffraction efficiency of a Fresnel zone plate lens. **a)** Measurement of the total intensity, I, impinging on the focusing element. OSA pinhole is not relevant in this measurement. **b)** Measurement of the diffracted intensity, I_f, focused into the 1st order focal spot. A small pinhole is scanned along the focal plane and an intensity profile similar to the one shown in the graph is recorded. I_0 stands for the intensity of the zeroth order which is directly transmitted through the element.

The diffraction efficiency of a Fresnel zone plate is measuring how much intensity[10] is brought into the focal spot by the structure in relation to the total intensity that is impinging on it. Both intensities have to be measured accurately. Ideally one should

[10] That is, energy or amount of photons.

directly measure the total incoming intensity by using a detector that has an active area of the dimensions of the lens or by placing a pinhole with the suitable diameter in front of the detector. However, in most of cases this in not possible because the total intensity will easily saturate the detector. In order to prevent this problem, an alternative setup is shown in figure 6.36a). We are supposing a uniform incoming intensity and a small pinhole is placed in front of the detector. In the scheme we are considering that the order selecting aperture is located at proper position despite it is not relevant for the measurement. If I_m is the measured intensity through the pinhole, the total intensity, I, impinging into the lens is given by

$$I = \frac{A_{FZP}}{A_{pinhole}} \cdot I_m \tag{6.2}$$

In addition, figure 6.36b) shows the setup to measure the diffracted intensity, I_f, focused into the 1st order focal spot by scanning a pinhole along the focal plane. Then, one has that the total diffraction efficiency, η_{total}, of Fresnel zone plate is given by

$$\eta_{total} = \frac{I_f}{I} = \frac{I_f}{I_m}\frac{A_{FZP}}{A_{pinhole}} \tag{6.3}$$

As discussed in section 3.1.3, one usually distinguishes between the total diffraction efficiency and the groove diffraction efficiency, η_g, in which the absorption due to the supporting membrane has been subtracted. The x-ray radiation transmission of the membranes, T_{mem}, was estimated by measuring the transmitted intensity, I_t, through a region close to focusing structure. Thus, the groove diffraction efficiency, η_g, is obtained from

$$\eta_g = \frac{\eta_{total}}{T_{mem}} = \eta_{total}\frac{I}{I_t} \tag{6.4}$$

During our experiments at the PolLux beamline we prepared the setups of the intensity measurements for a 100 μm diameter Fresnel zone plate with an outermost zone width of 30 nm. From the specifications in table 6.4, the groove diffraction efficiency expected for such a structure is 5.8%. Table 6.6 summarizes the results of the intensity measurements and according to them the groove diffraction efficiency of the Fresnel zone plate was 3.0%.

However, the total diffraction efficiency of the element was 0.15%, that is, much lower than expected. The reason of that was the silicon membrane which appeared to be a lot thicker than expected. According to the transmission measurement the actual silicon membrane thickness was around 1.200 μm. While this was not a big problem during our experiments a much higher diffraction efficiency would be required for the daily use of the silicon lenses in a fully operational soft x-ray microscope. However, the silicon membranes can be thinned down to improve the total diffraction efficiency of the focusing element by reactive ion etching from the backside or even by using a focused ion beam[11] (FIB) system which would allow to locally thin down the membrane at the

[11] A focused ion beam system uses a beam of ions (typically gallium ions), which are emitted from a gun and focused by an electromagnetic column, to locally etch or ablate materials. It resembles a scanning electron microscope.

Silicon Fresnel Zone Plate Diffraction Efficiency Measurements at a photon energy of 500 eV		
Parameter		**Value**
Total Intensity	I	$5.06 \cdot 10^5$ counts/ms
Diffracted Intensity	I	755 counts/ms
Membrane Transmitted Intensity	I_t	$2.52 \cdot 10^4$ counts/ms
Membrane Transmission	T_{mem}	0.05
Total Diffraction Efficiency	η_t	0.0015
Groove Diffraction Efficiency	η_g	0.030

Table 6.6: Diffraction efficiency measurements for a 100 μm diameter Fresnel zone plate with an outermost zone width of 30 nm. Since the zone thickness was 180 nm, the theoretically expected groove diffraction efficiency was 5.8%. The measured value of 3% is resonable.

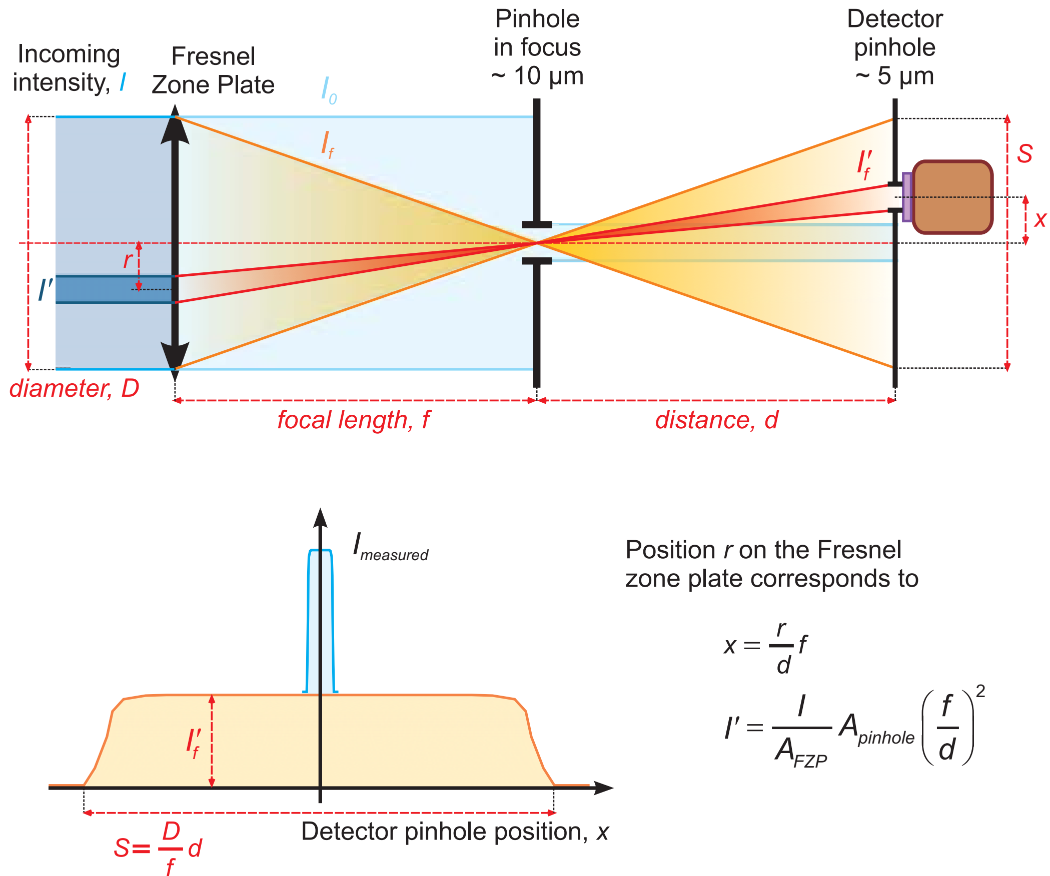

Figure 6.37: Scheme for the measurement of the local diffraction efficiency of a Fresnel zone plate lens. The diffracted intensity, I'_f, at a given distance, d, from the focal plane comes from a well defined area of the Fresnel zone plate lens.

opposite side of the Fresnel zone plate structure.

Figure 6.37 shows a second setup that allows the evaluation of the local diffraction efficiency. In comparison to the previous scheme the pinhole that is measuring the diffracted intensity is recording the signal at a distance d, from the focal point. As it can be seen in the figure, the diffracted intensity that is concentrated into the 1st order focus is creating a divergent cone of radiation as it travels away from the focal plane. The signal detected through small signal, I'_f, correspond to intensity diffracted locally from the Fresnel zone plate. Thus, with the appropriate measurements one can obtain a local estimation of diffraction efficiency of the lens. According to the parameters in figure 6.37 the local diffraction efficiency, η_{local}, is given by

$$\eta_{local} = \frac{I'_f}{I'} = \frac{I'_f}{I \frac{A_{FZP}}{A_{pinhole}} \left(\frac{d}{f}\right)^2} = \frac{I'_f}{I} \frac{A_{pinhole}}{A_{FZP}} \left(\frac{f}{d}\right)^2 \tag{6.5}$$

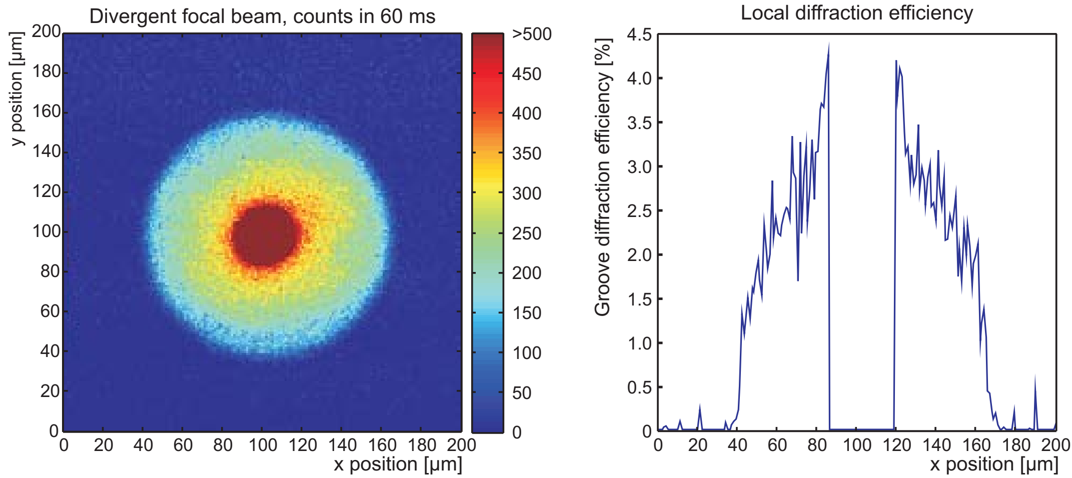

Figure 6.38: Picture of the divergent focal beam and the consequent graph giving local groove diffraction efficiency of the Fresnel zone plate.

Figure 6.38 shows the divergent focal beam and the derived local groove diffraction efficiency. In order to have a significant amount of counts the acquisition time was increased up to 60 ms per pixel. As it can be seen in the figure 6.37 when a central stop is missing the measurements at the central region are meaningless, since the most of intensity signal is due to transmission of zeroth order through the OSA pinhole which in this case can be located in the focal plane. This central part was not considered for the calculation of the local diffraction efficiency. In the graph one can observe that the diffraction efficiency is decreasing for the outer regions of the Fresnel zone plate. This fact is reasonable when one takes into account that the patterning of the outer regions which have smaller line width is more critical and sensitive to any defects. It is a common effect encountered in any Fresnel zone plate fabrication technique for x-ray radiation.

In summary, we have been showing that the silicon Fresnel zone plates are fully functional in both full-field and scanning transmission x-ray microscopes. The focusing lenses fulfilled the expected values in terms of spatial resolution, and structures as small as 35 nm have been clearly resolved in scanning transmission x-ray microscopy. In addition, we have shown that the silicon beamshaping condenser lenses produce square flat-top illumination spots, i.e. they are performing as expected to be used in full-field transmission x-ray microscopy.

CHAPTER 7

Iridium-Silicon Fresnel Zone Plates

In this last chapter we introduce and demonstrate a novel manufacturing technique which is likely to push the ultimate spatial resolution of Fresnel zone plate lenses for x-ray radiation. As explained in section 3.2, this method is based on a deposition of a thin layer of a high refractive index material onto the sidewalls of a template structure made of a low refractive index material, which leads to a doubling of the effective line density of the deposited material comparing to that of the template. Thus, the outermost zone width of the Fresnel zone plate has been divided by a factor two resulting in the subsequent improvement of the spatial resolution by a factor two.

Benefiting from the experience gained during the development of the technology extensively described in the previous chapter, we chose silicon as low refractive index material for the template. The use of a polymer resist as template material could also be considered in future works. As a high refractive index material several materials could be employed. Gold was considered as first option, and several deposition trials by means of evaporation and electroplating were done. However, due to its unique self-limiting growth mechanism, atomic layer deposition (ALD) turned out to be the best choice for our purposes, that is, in order to get a highly conformal deposition of the high refractive index material with accurately controlled film thickness. Iridium was chosen as zone material because their x-ray properties are similar to the ones of gold and because the ALD deposition for iridium has achieved a high level of control during the last years. The use of other materials, which can be deposited by ALD, should be considered in the future. Iridium-silicon Fresnel zone plates with an outermost iridium period of 40 nm and 30 nm were successfully prepared and tested in scanning transmission x-ray microscopy. Structure details as small as 15 nm (30 nm period) were clearly resolved

using a photon energy of 1 keV. This work and results are summarized in the publication *Jefimovs et al.* [105].

The work presented here was a collaboration between the *Labor für Mikro- und Nanotechnologie* at the *Paul Scherrer Institut* in Villigen (Switzerland) and the *Laboratory of Inorganic Chemistry* at the *University of Helsinki* (Finland). The silicon structures were patterned in Switzerland while the iridium atomic layer deposition was performed in Finland. Later, scanning transmission x-ray microscopy experiments to evaluate the performance of the iridium-silicon Fresnel zone plates were carried out at the *PolLux Beamline* of the *Swiss Light Source* at the *Paul Scherrer Institut.*

7.1 Iridium-Silicon Fresnel Zone Plate Fabrication

As explained in section 3.2, the basic idea in this novel fabrication technique relies on the combination of high refractive index material layer on a low refractive index template. The idea of overcoating a previously manufactured template to double the spatial frequency in grating structure was already demonstrated in preceding works. In *Flanders & Efremow* [98], they were able to generate a silicon structures with a period down to 50 nm. On the other hand in *David et al.* [99], silicon structures prepared with wet etching were coated with gold to produce 2 μm period gratings for hard x-ray phase contrast imaging. However, this is the first time that such processing technique has been employed for the production of Fresnel zone plate lenses. Manufacturing steps are schematically shown in figure 7.1.

The e-beam lithography, the pattern transfer into the chromium mask and the silicon reactive ion etching were carried out as explained in the previous chapters. An important detail is that the generated structure into silicon have a two times less dense line pattern. Concretely, while a duty cycle of 0.5 is required in an ordinary Fresnel zone plate pattern, a duty cycle of 0.25 is enough in case of the template for the zone-doubling technique. This is crucial advantage, since one should be aware that, as explained in chapter 4, low dense features are more easily patterned by e-beam lithography. The second detail was metal deposition through atomic layer deposition. In *David et al.* [99], the gold deposition was done by means of thermal evaporation and electroplating. Gold evaporation was essential to deposit a seed layer on the silicon grating structure, with 1 μm wide walls and 4 μm period. During the evaporation the sample was tilted by several degrees to ensure that the metal was also covering the sidewalls of the silicon structures. Later the structures were covered with a 1 μm thick layer of gold by electroplating, which guaranteed a uniform growth of the metal layer under the suitable conditions. This approach was first tried to cover silicon structures with similar dimensions to those of the soft x-ray Fresnel zone plates, which are almost two orders of magnitude smaller than a 4 μm period grating. Figures 7.2 and 7.3 show silicon linear gratings with periods of 60 nm and 50 nm before and after the gold evaporation and electroplating processes.

Despite the gold layer is completely covering the silicon structures a detailed inspection shows that most of the material has been deposited on the ridges of the silicon walls.

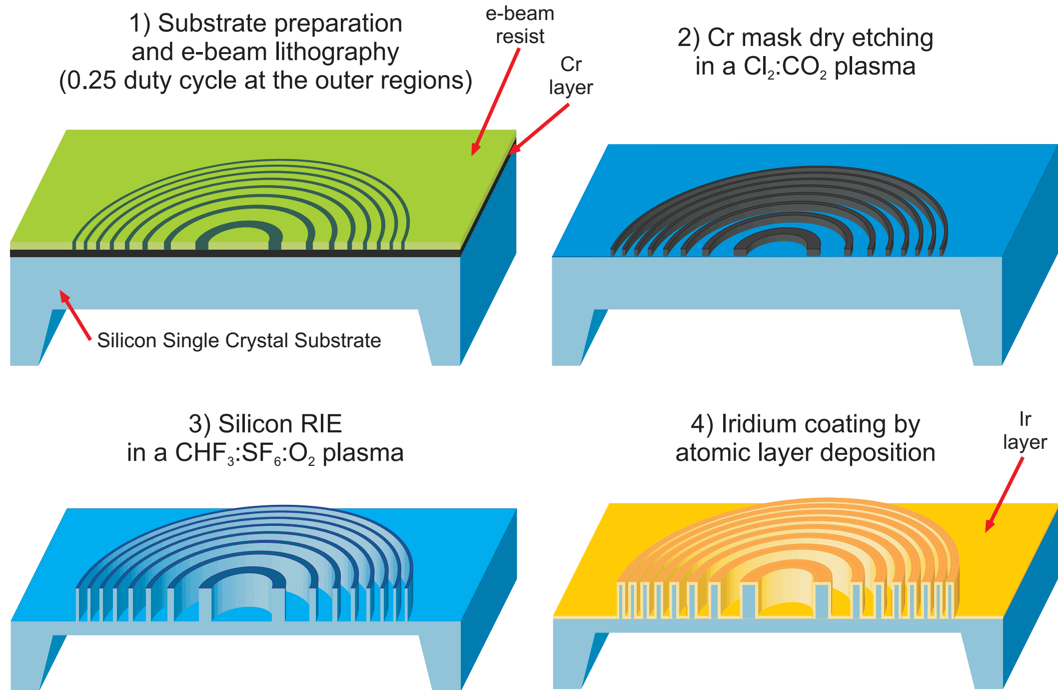

Figure 7.1: Iridium-silicon Fresnel zone plate manufacturing steps. The silicon template, which was prepared by the techniques described in chapter 6, had 80 nm period and a duty cycle of 0.25 at the outer regions. Later the structure was covered by a thin layer ($\sim$ 20 nm) of iridium by atomic layer deposition (ALD).

In addition, the thickness of the gold layer was extremely difficult to control, since only a few tens of nanometers are necessary.

On the contrary, atomic layer deposition (ALD) [100] turned out to be an alternative method which fulfilled all the requirements we had. Within this work the iridium coating by ALD was done at the *Laboratory of Inorganic Chemistry* by T. Pilvi and M. Ritala using a Picosun SUNALE^{TM} R150 reactor. A detailed overview of ALD of iridium thin films can be encountered in *Aatonen et al.* [101]. Iridium was chosen as zone material because of the high level of control of the ALD process that has been achieved for this metal and because it has good x-ray properties similar to those of gold.

Figures 7.4 and 7.5 show the scanning electron microscopy images of a 100 μm diameter silicon Fresnel zone plate pattern with an outermost period of 100 nm, before and after the iridium ALD. As required in a duty cycle of 0.25, the width of the silicon walls is 25 nm. In this first trial, the thickness of the iridium coating was also chosen to be 25 nm as well.

Due to the high level of film thickness control one can check in figure 7.5 that the remaining spacings have a width of 25 nm so that the period of the iridium structures is 50 nm (whenever the silicon template walls and the air gaps are considered equivalent).

To check the quality of the iridium layer, the structures were cross-sectioned by

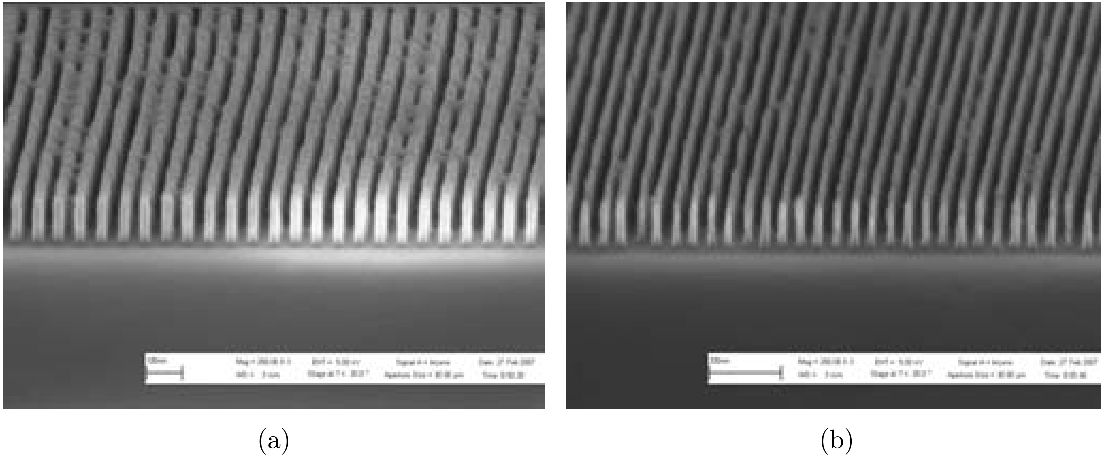

(a) (b)

Figure 7.2: Silicon linear gratings with periods of 60 nm (a) and 50 nm (b). The height is around 180 nm and the defects in the structure are due to e-beam lithography tool limitations.

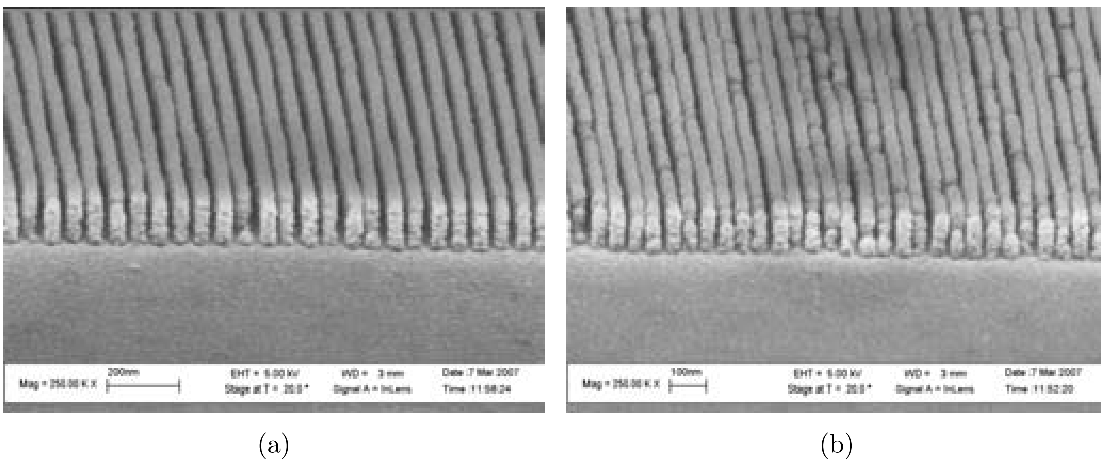

(a) (b)

Figure 7.3: Silicon linear gratings with periods of 60 nm (a) and 50 nm (b) after the gold deposition by means of evaporation and electroplating. The structures have been successfully covered with metal. However, a closer look reveals that most of the gold has been deposited on the ridges of the template structure.

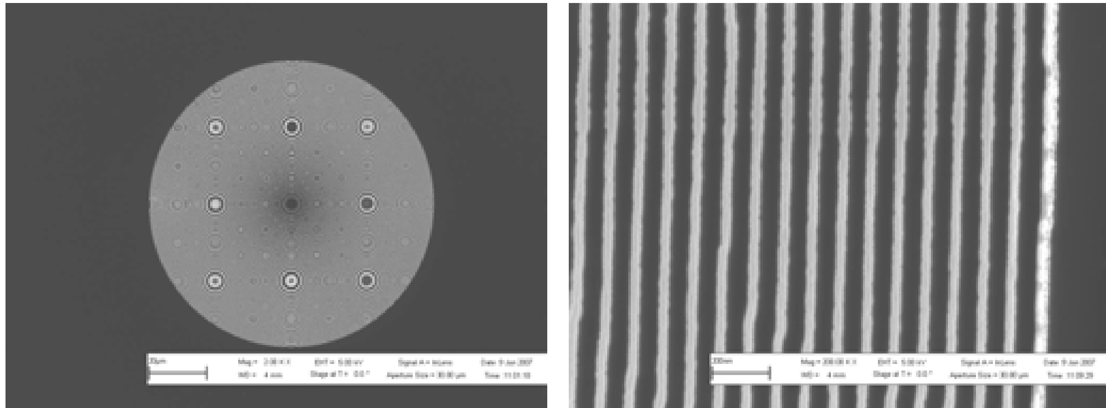

Figure 7.4: Scanning electron microscopy images of a 100 μm diameter silicon Fresnel zone plate with an outermost period of 100 nm. The duty cycle of the outer regions is 0.25 as required for zone-doubling technique.

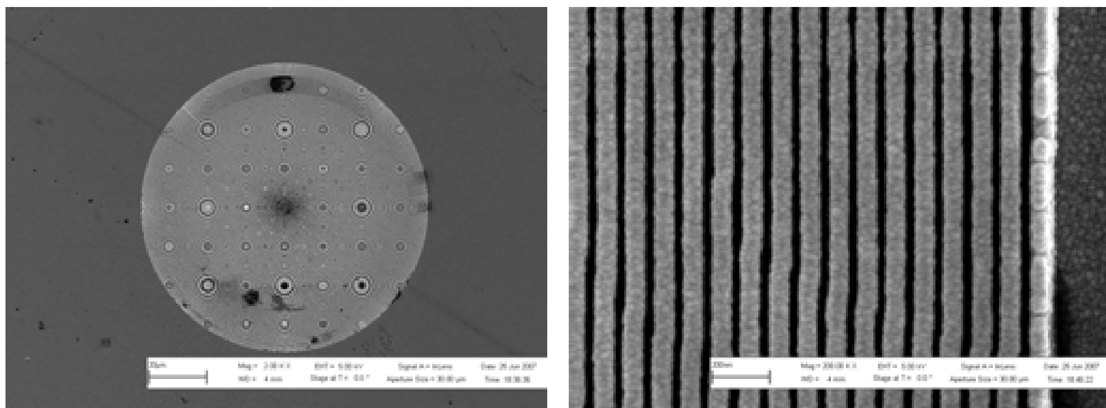

Figure 7.5: Scanning electron microscopy images of a 100 μm diameter silicon Fresnel zone plate after being coated by a thin film of iridium of 25 nm by ALD. The remaining spacings have a width of 25 nm and the silicon structures are not visible since the iridium layer is also covering the ridges of the silicon template.

focused ion beam (FIB) milling. Despite partly destroying the structure, this allowed us to observe the iridium layer deposited onto the sidewalls of the silicon template. Figure 7.6 shows the iridium structures with period of 50 nm which are attached to the sidewalls of silicon template. One can see that the quality of the ALD is fulfilling our requirements.

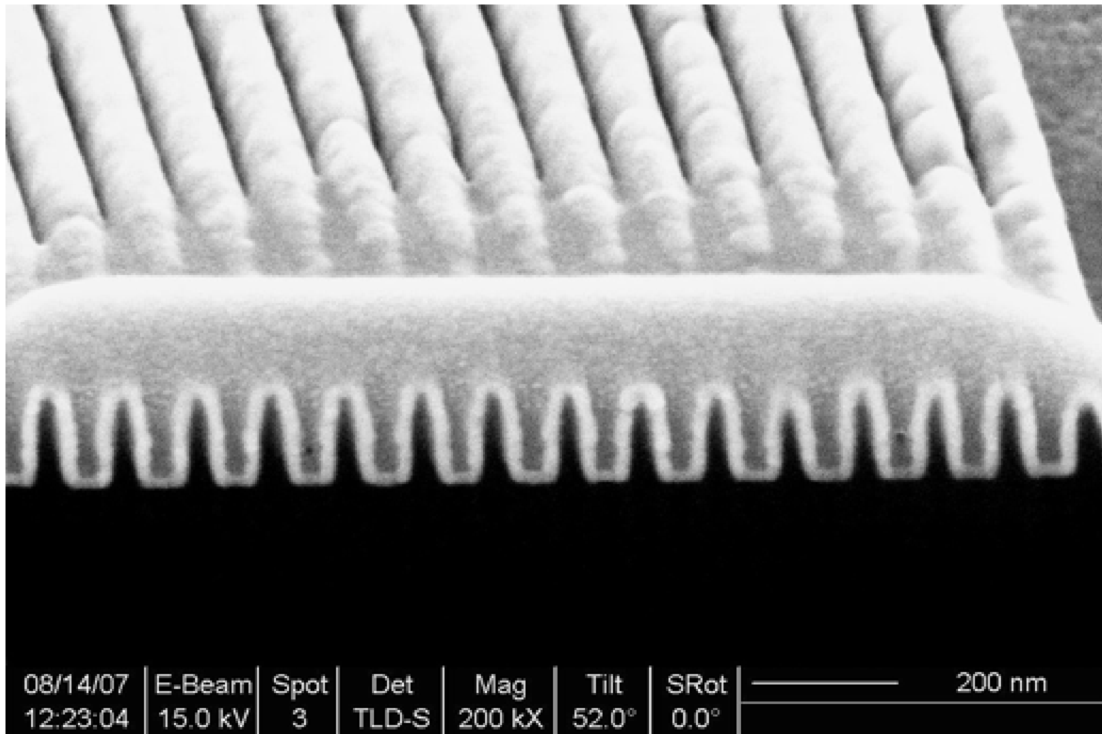

Figure 7.6: Scanning electron microscopy micrograph of an iridium-silicon Fresnel zone plate with an outermost zone width of 25 nm. A small area of the zone plate was coated with a thin platinum layer in order to ensure a clean cross-sectioning by the focused ion beam milling (courtesy of K. Jefimovs).

Thus, this result demonstrated the feasibility of applying the zone-doubling technique for the manufacturing of Fresnel zone plate patterns. After this first structure fabricated on bulk silicon, a lot of efforts were dedicated to produce a functional iridium-silicon Fresnel zone plate that could be tested in an x-ray microscope.

Up to date, the Fresnel zone plate lenses for x-ray radiation with the highest spatial resolution ever reported were achieved using two separated e-beam lithography exposure steps of complementary patterns to reduce the line density in each individual step [53]. However, extremely small alignment tolerances of only a few nanometers are required between the two exposures, making the technique inherently complicated and resulting in a low fabrication yield. On the other hand, the zone-doubling technique presented in here is very promising because it is much simpler and overcomes the difficulty of high feature density patterning without any needs of alignment. The method is very reproducible, as it only requires a single lithography step, and allows the fabrication

of large aperture diffractive optical elements with extremely high aspect ratios, which increases the efficiency of this ultrahigh resolution optics.

7.2 Iridium-Silicon Fresnel Zone Plate Characterization

Two iridium-silicon Fresnel zone plates were prepared on silicon membrane substrates. They had both a 100 μm diameter and an outermost iridium period of 40 nm and 30 nm. After their inspection with optical and electron microscopy, they were tested at the soft x-ray microscope installed at the *PolLux Beamline* of the *Swiss Light Source* at the *Paul Scherrer Institut.*

7.2.1 Iridium-Silicon Fresnel Zone Plate

The specifications of the iridium-silicon Fresnel zone plates are summarized in table 7.1. The silicon template was prepared to achieve an iridium outermost zone width of 20 nm and 15 nm so that their period should be 80 nm and 60 nm, respectively.

In here, one should emphasize that despite of the calculations of the section 3.2 which give an exhaustive analysis of the most suitable parameters, during the experimental work the aimed values were much more relaxed since the goal of these first trials was the *proof of principle* of the zone-doubling technique. Further development of the fabrication process to optimize important parameters of the focusing element such as the diffraction efficiency should be targeted in future works.

Iridium-Silicon Fresnel Zone Plate Specifications at 1st Diffraction Order at 1000 eV (λ=1.24 nm)			
Silicon Outermost Period	p	80.0 nm	60.0 nm
Iridium Outermost Zone Width	Δr	20.0 nm	15.0 nm
Silicon Membrane Substrate	—	$\sim$ 1000 nm	$\sim$ 1000 nm
Diameter	D	100 μm	100 μm
Focal Length	f	1.61 mm	1.21 mm
Number of Zones	N	1250	1666
Spatial Resolution	δ_{res}	24.4 nm	18.3 nm
Depth of Focus	DOF	1.29 μm	0.72 μm
Numerical Aperture	NA	0.062	0.138
Maximum Spectral Bandwidth	$\Delta\lambda/\lambda$	$0.8 \cdot 10^{-3}$	$0.6 \cdot 10^{-3}$
Structure Height	h	200 nm	200 nm
Groove Diffraction Efficiency	η	$\sim$ 8.0 %	$\sim$ 8.0%

Table 7.1: Two designs of iridium-silicon Fresnel zone plate with 20 nm and 15 nm outermost zone widths were manufactured. This table summarizes the main parameters and specifications of the two patterns at a photon energy of 1 keV. They both have a diameter of 100 μm.

Figures 7.7 and 7.8 show the silicon Fresnel zone plate patterns before the iridium coating by atomic layer deposition. One can observe that the quality of the structures of the Fresnel zone plate with 80 nm silicon period is better than the 60 nm period one. The second one has more defects and some silicon walls are wider than required. Both defects and line width inaccuracies are related to the e-beam lithography step. As a result, we decided to coat the silicon templates by 20 nm and 12 nm of iridium, respectively.

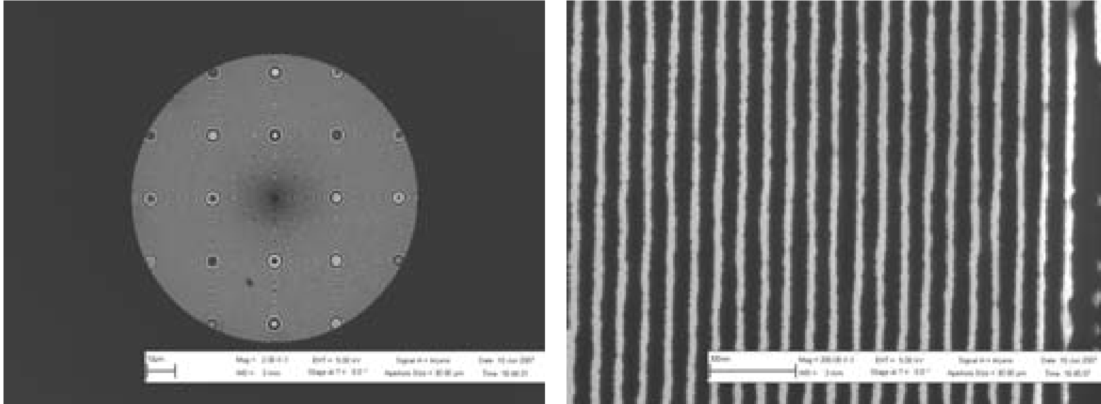

Figure 7.7: Scanning electron microscopy images of a 100 μm diameter silicon Fresnel zone plate template with an outermost period of 80 nm. As required the line width is 20 nm in the silicon template structure.

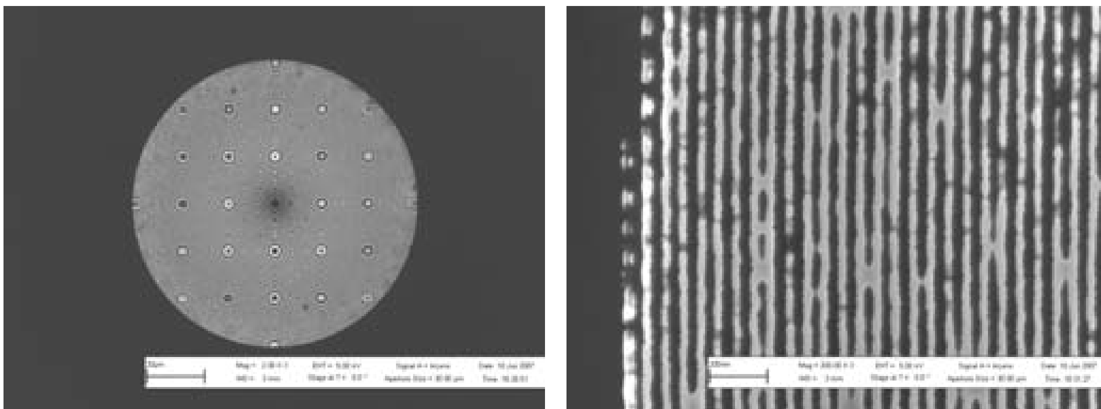

Figure 7.8: Scanning electron microscopy images of a 100 μm diameter silicon Fresnel zone plate template with an outermost period of 60 nm. In this case, the line width should be 15 nm in the silicon template structure. However, the actual structures are a bit wider (18 — 22 nm) and there are some defects in the pattern. Both problems are related to the e-beam lithography tool limitations.

Figure 7.9 shows the focused ion beam milling cross-sections of the silicon templates after the coating of iridium by ALD[1]. Again the quality of the structures of the Fresnel zone plate with 80 nm silicon period is better than the 60 nm period one. However, in

[1]Chronologically, the cross-sectioning of the structures was done after the scanning transmission

figure 7.9(b) an iridium period as small as 30 nm has been successfully generated showing the feasibility of producing extremely short periods by the zone-doubling technique.

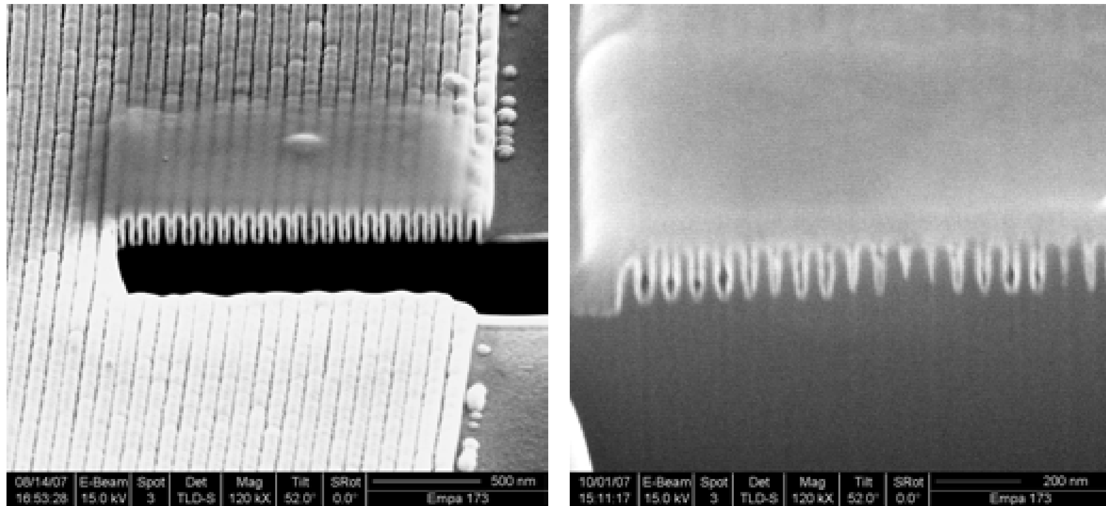

(a) 80 nm Si period / 40 nm Ir period (b) 60 nm Si period / 30 nm Ir period

Figure 7.9: Scanning electron microscopy images of cross-sections produced by focused ion beam milling of the iridium-silicon Fresnel zone plate. In (a) there is a perfectly patterned structure with an iridium outermost period of 40 nm. (b) shows a Fresnel zone plate pattern with an iridium outermost period of 30 nm. In this case, one can observe defects on the structure, that is, some silicon walls are too wide (courtesy of K. Jefimovs).

Thus, a couple of iridium-silicon Fresnel zone plate patterns were successfully produced and they were ready to be experimentally tested in an x-ray microscope.

7.2.2 Scanning Transmission X-ray Microscopy (STXM)

Scanning transmission x-ray microscopy experiments with the iridium-silicon Fresnel zone plates were identical to the ones described in section 6.3.4 to evaluate the performance of the silicon diffractive optical elements. In this case, the iridium-silicon Fresnel zone plates were used to concentrate the x-ray radiation of 1 keV photon energy and to produce the tiny spot that was used to probe the sample in the scanning transmission x-ray microscope at the *PolLux Beamline* of the *Swiss Light Source*.

A photon energy of 1 keV was chosen because 200 nm thick iridium-silicon structures should give a maximum diffraction efficiency for energies around this value[2]. In addition, using a photon energy of 1 keV has the advantage that the focal length is above 1.0 mm even for Fresnel zone plates with an outermost zone width of 15 nm[3]. On the other

x-ray microscopy experiments shown in next section, despite the damaging of a such tiny area of the Fresnel zone plate pattern should only affect very little the performance of the focusing device.

[2]The theoretically expected diffraction efficiency is around 8% for 200 nm thick iridium-silicon structures.

[3]A 100 μm Fresnel zone plate with an outermost zone width of 15 nm has a focal length as short as 600 μm at a photon energy of 500 eV.

hand, energies around 1 keV are useful and interesting for chemical mapping of some metals (Fe, Co, Ni, Cu or Zn have their L absorption edges at photon energies ranging from 700 eV to 1 keV).

A small pinhole of 20 μm diameter was accurately aligned as order selecting aperture since the iridium-silicon Fresnel zone plate were missing a central stop. As discussed in chapter 6, the lack of a central stop decreases the contrast in STXM images. The entrance slits of the experimental station were closed enough to ensure the Fresnel zone plate was illuminated by spatially coherent beam so that the resulting focal spot size was diffraction limited. Otherwise, the Fresnel zone plate would be forming an image of the source on the focal plane which could be quite much bigger than the expected spot size. Complementary, one can also argue that the demagnification of the source must be enough so that the geometric image of source should be smaller than the diffraction limited focal spot. At the PolLux beamline experimental station the entrance slits are located 1 m upstream of the Fresnel zone plate, which have focal length of around one 1.0 mm. Thus, the Fresnel zone plate is roughly demagnifying the source by a factor 1000, and the size of the entrance slits should not be much bigger than 20 μm if the expected diffraction limited spot size is 20 nm. One could be tempted of decreasing the size of the entrance slits quite below 20 μm to guarantee the diffraction limited focal spot size was achieved, however the flux of photon would be dramatically reduced. Thus, the entrance slit size must be small enough in order to ensure the diffraction limited focal spot size but at the same time large enough to probe the sample with the highest photon flux (so that the acquisition time of the STXM images can be as short as possible).

7.2.2.1 15 nm Outermost Zone Width Ir-Si Fresnel Zone Plate

During the first run of experiments we mounted the 100 μm diameter iridium-silicon Fresnel zone plate with an outermost zone width of 15 nm. Besides, we used as a sample a Fresnel zone plate made of gold with a minimum line width of 35 nm at the outermost regions of the pattern[4].

Figures from 7.10 to 7.14 show several STXM images of the gold structures.

While figure 7.10(a) shows the general view of the gold Fresnel zone plate that was used as a sample, in figure 7.10(b) there are 120 nm period structures that were perfectly resolved. Both images are made of 200 $\times$ 200 pixels using step sizes of 500 nm and 10 nm, respectively. Since we were using 20 ms of acquisition time for each pixel, the total time to acquire the images was around 15 minutes. Comparing figure 7.10(b) to figure 6.33(b) of the preceding chapter, which shows a STXM image taken with a silicon Fresnel zone plate, one could argue that the contrast between the image recorded at 1 keV photon energy is not very good. However, one has to take into account that 1 keV energy photons are much more transmitted through the gold zones than 500 eV

[4]That is, the same sample object that was used during the testing of the silicon Fresnel zone plates, as explained in section 6.3.4.

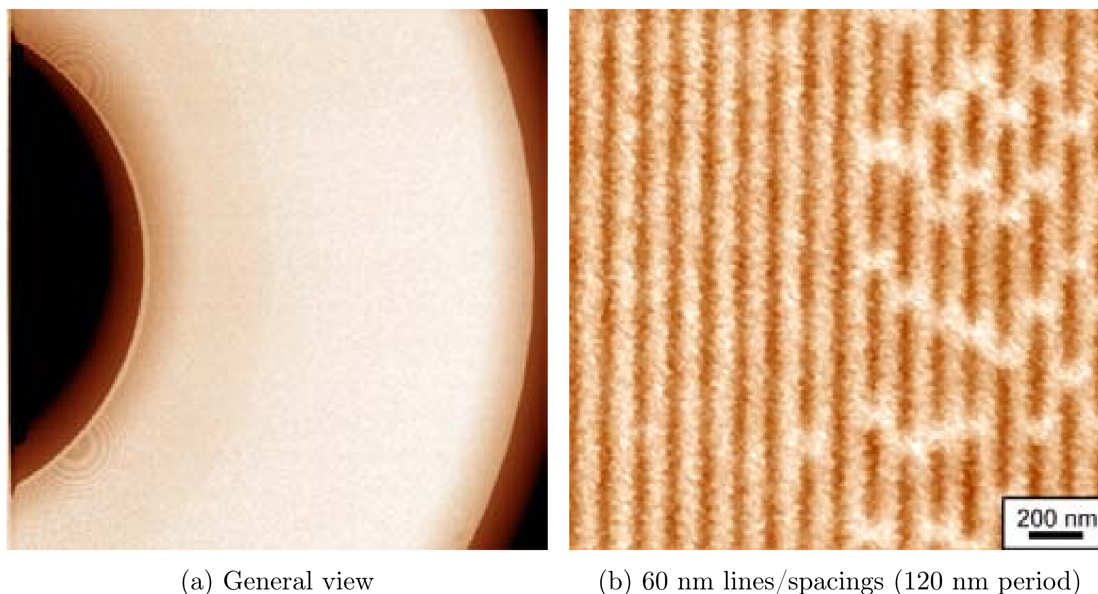

(a) General view (b) 60 nm lines/spacings (120 nm period)

Figure 7.10: STXM images of Fresnel zone plate pattern made of gold that was used as test sample while focusing the incoming x-ray radiation using a 100 μm diameter iridium-silicon Fresnel zone plate with an outermost zone width of 15 nm. (a) General view of the structure. (b) Detail of 60 nm lines/spacings.

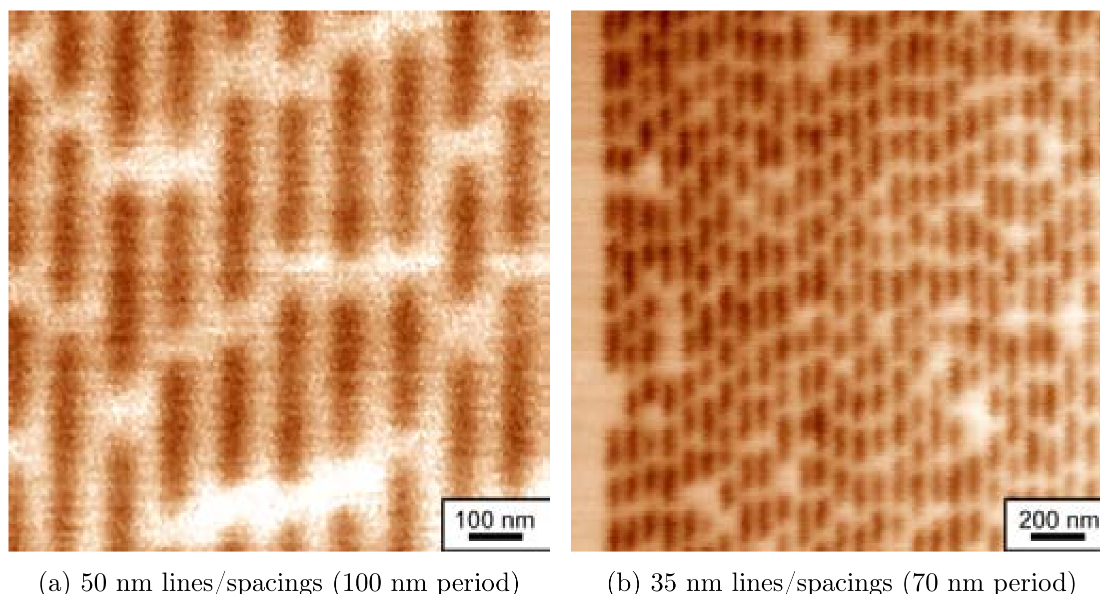

(a) 50 nm lines/spacings (100 nm period) (b) 35 nm lines/spacings (70 nm period)

Figure 7.11: STXM images of Fresnel zone plate pattern made of gold that was used as test sample while focusing the incoming x-ray radiation using a 100 μm diameter iridium-silicon Fresnel zone plate with an outermost zone width of 15 nm. (a) 50 nm lines/spacings. (b) Outermost region of the structure with 35 nm lines/spacings.

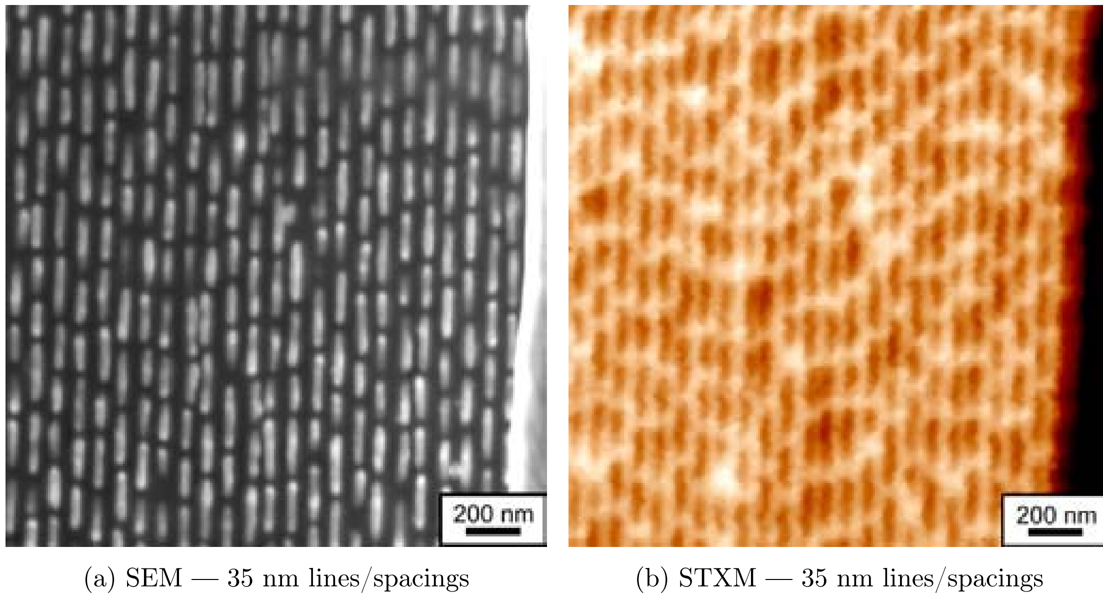

(a) SEM — 35 nm lines/spacings (b) STXM — 35 nm lines/spacings

Figure 7.12: Scanning electron microscopy and STXM images of the same region of the gold structures. The STXM image was taken at a photon energy of 1 keV using an iridium-silicon Fresnel zone plate with an outermost zone width of 15 nm. Both imaging techniques are resolving a pattern of 35 nm lines/spacings (70 nm period) with a similar level of detail.

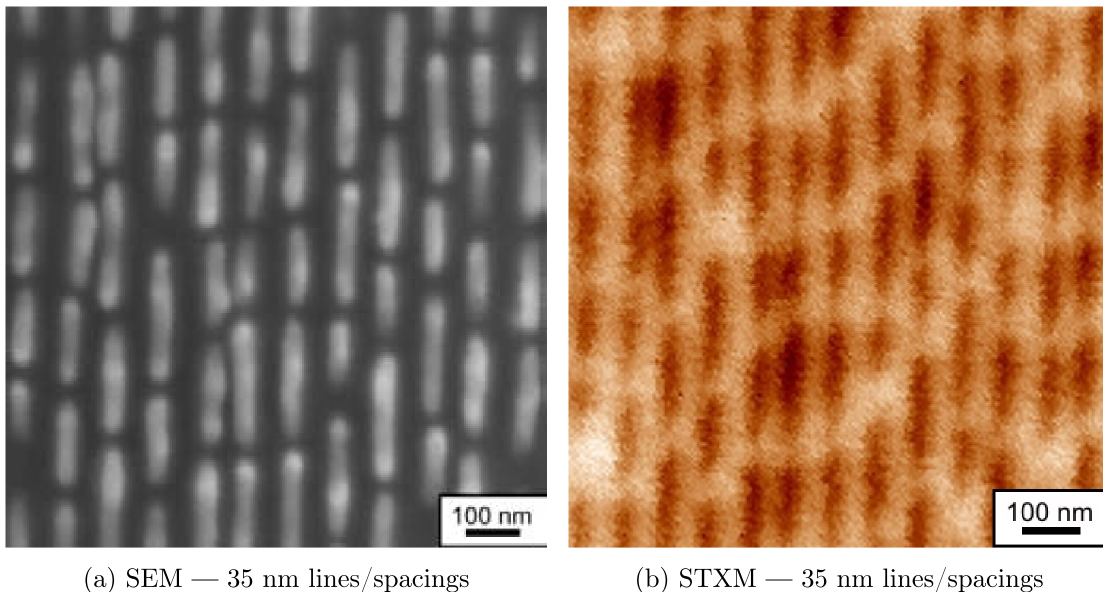

(a) SEM — 35 nm lines/spacings (b) STXM — 35 nm lines/spacings

Figure 7.13: Scanning electron microscopy and STXM images of the same region of the gold structures. The STXM image was taken at a photon energy of 1 keV using an iridium-silicon Fresnel zone plate with an outermost zone with of 15 nm. Even the narrowest gaps between slightly misplaced gold zones are visible in the STXM image.

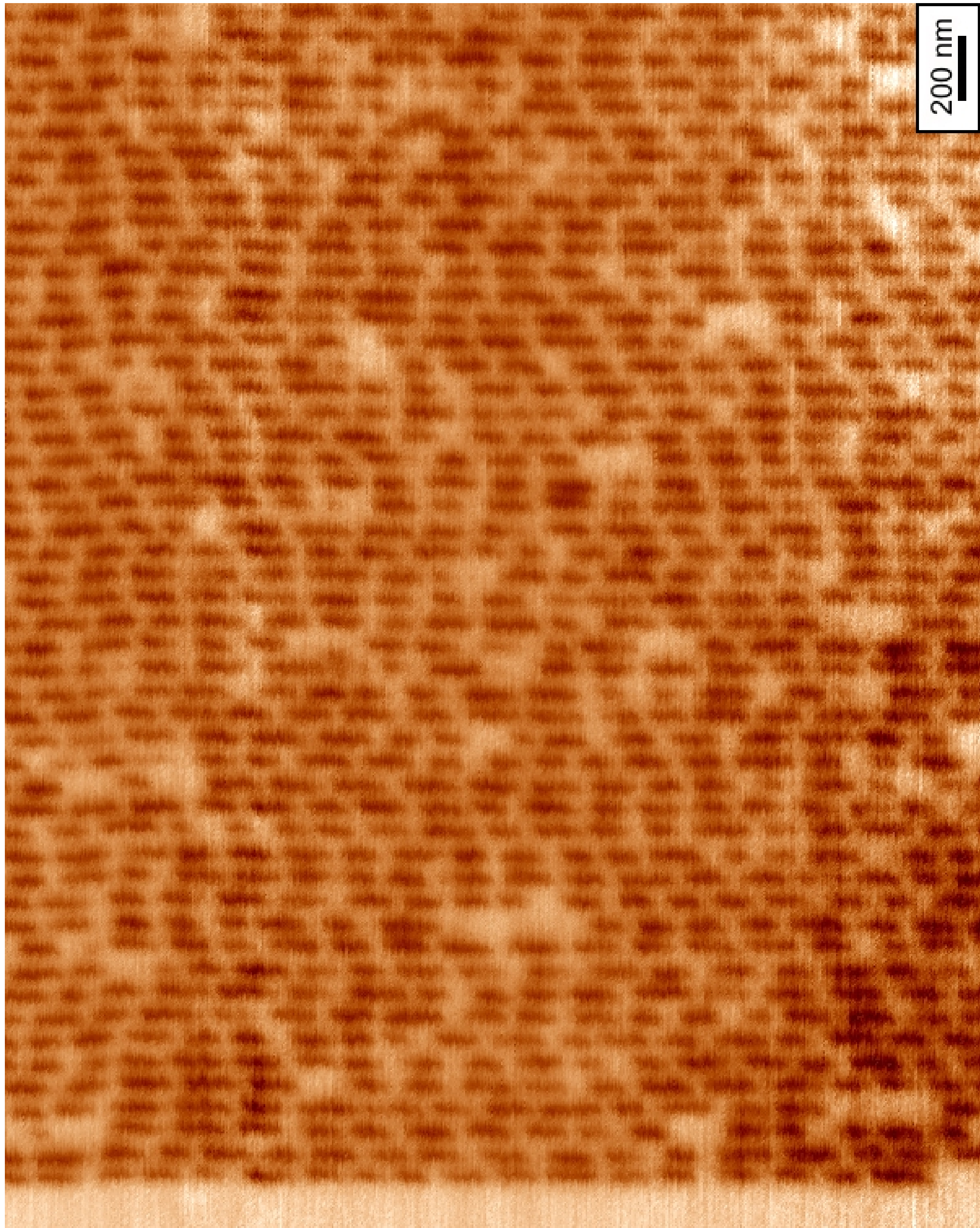

Figure 7.14: STXM image of the outermost region of Fresnel zone plate pattern made of gold. The image was taken at a photon energy of 1 keV using an iridium-silicon Fresnel zone plate with an outermost zone with of 15 nm. The image is composed of 750 × 600 pixels using a step size of 5 nm and an acquisition time of 80 ms.

energy ones[5], thus decreasing the intrinsical contrast of the gold structures. As a result, when recording the images at 1 keV photon energy a longer acquisition times where required to ensure a good signal-to-noise ratio than when recording images at 500 eV (despite this is also related to the diffraction efficiency of the device).

Figure 7.11 demonstrates that at least features down to 35 nm could be perfectly resolved by with the iridium-silicon Fresnel zone plates. Figure 7.11(a) shows a 200 × 200 pixel image of 100 nm period structures. A step size of 5 nm and acquisition time of 20 ms were employed. Figure 7.11(b) shows a 400 × 400 pixel image of 70 nm period structures utilizing a 5 nm step size and 80 ms of acquisition time.

Figures 7.12 and 7.13 are showing the same regions of gold structures when inspected by scanning electron microscopy and by scanning transmission x-ray microscopy with the iridium-silicon Fresnel zone plate. One can observe that the level of detail is similar in both approaches and that extremely small gaps are also visible in the STXM image.

Figure 7.14 is a STXM image made of 750 × 600 pixels with a step size of 5 nm and an acquisition time of 80 ms. For such a long scan, the total acquisition time was around 10 hours.

7.2.2.2 20 nm Outermost Zone Width Ir-Si Fresnel Zone Plate

The second run of experiments were performed exchanging the iridium-silicon Fresnel zone plate with 15 nm outermost zone width for the second one which has an outermost zone width of 20 nm. As discussed in the preceding section, and according to the scanning electron microscopy inspection, the iridium-silicon Fresnel zone plate with 15 nm outermost zone width had much more defects than the 20 nm outermost zone width one. Thus, we were expecting a better performance for this second focusing element.

At this point we decided to mount the 100 μm diameter iridium-silicon Fresnel zone plate with 15 nm outermost zone width as sample, since it was the structure with the smallest patterned features that was available and thus the perfect element to test the spatial resolution of our novel diffractive optical element. After mounting both iridium-silicon Fresnel zone plates as focusing element and as sample we arranged the focal length, which was expected to be 1.6 mm for the 20 nm outermost zone width iridium-silicon Fresnel zone plate at 1 keV photon energy.

Shortly after rearranging the focusing and aligning the order selecting pinhole we observed an increase of the STXM image quality. We were convinced that this was directly related to the quality of the iridium-silicon Fresnel zone plate that was used as focusing device, which was much better that the previous one.

Figure 7.15(a) shows the general view of the iridium-silicon Fresnel zone plate that was used as a sample and figure 7.15(b) shows details of the central region of the structure which is full of defects. The brighter regions correspond to those areas where the line

[5] 200 nm gold thick structures are only transmitting 0.8% at 500 eV energy photon, while 12% of the incoming photons are transmitted at 1 keV energy radiation beam.

pattern into the silicon has not been properly generated. Since there was no gap to fill during the iridium deposition they are made of silicon and they are much more transmissive.

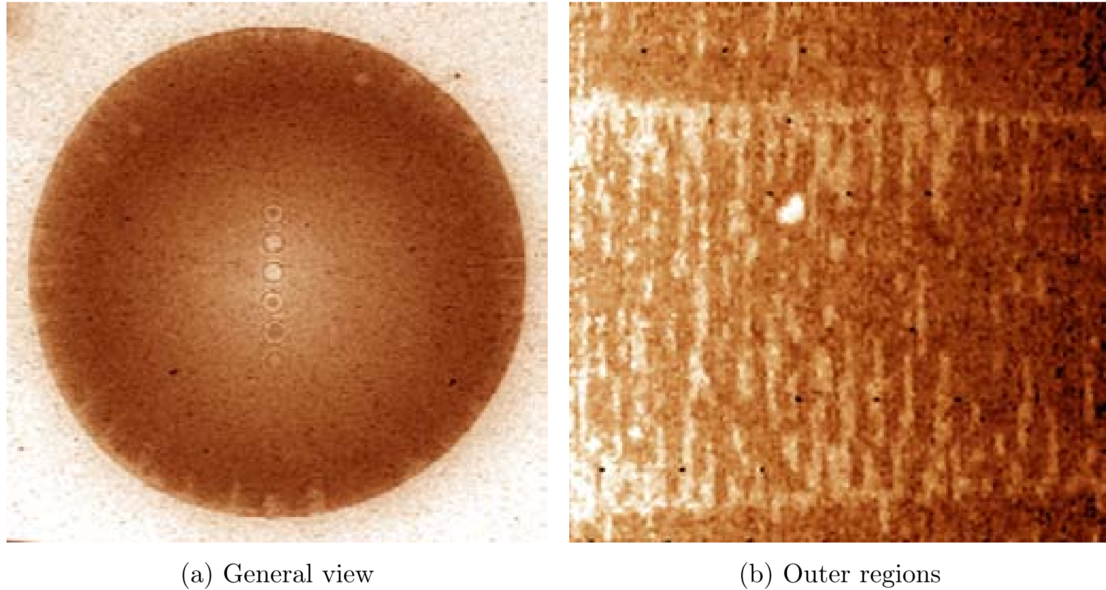

(a) General view (b) Outer regions

Figure 7.15: STXM images of an iridium-silicon Fresnel zone plate when focusing the incoming beam of 1 keV photon energy using an iridium-silicon Fresnel zone plate with an outermost zone width of 20 nm. (a) General view of the sample. (b) Central region image showing the defects of the iridium-silicon structures due to the e-beam lithography step.

Figures 7.16, 7.17 and 7.18 are comparing the scanning electron microscopy image with the STXM image of the same regions of the iridium-silicon Fresnel zone plate that was mounted as sample. Scanning electron microscopy images show structures with two times larger periodicity than the STXM images. Due to the very short penetration depth of the electron beam only the surface of the iridium layer is visible and no information of the underlying silicon template can be extracted. Nevertheless, x-rays photons do penetrate the thin iridium layer. As a result, the silicon template is clearly visible in the STXM image and the iridium lines deposited onto the sidewalls of the template can be distinguished. STXM images in figures 7.16, 7.17 and 7.18 are showing the periodicity of the iridium structures with 20 nm lines/spacings, 17 nm lines/spacings and even 15 nm lines/spacings, respectively. Thus, structures with periods down to 30 nm can be perfectly resolved, result which fulfills by far the expected spatial resolution of the iridium-silicon Fresnel zone plates. In fact, these images are showing *the best spatial resolution ever achieved in scanning transmission x-ray microscopy up to date.* All STXM images were taken using a step size of 5 nm and an acquisition time of 20 ms for each pixel.

Figure 7.19 deserves special attention since it shows a special characteristic of the Fresnel zone plates produced by means of the zone-doubling technique. As pointed out in section 3.2 and figure 3.15 there exist two focal planes for the iridium-silicon Fresnel

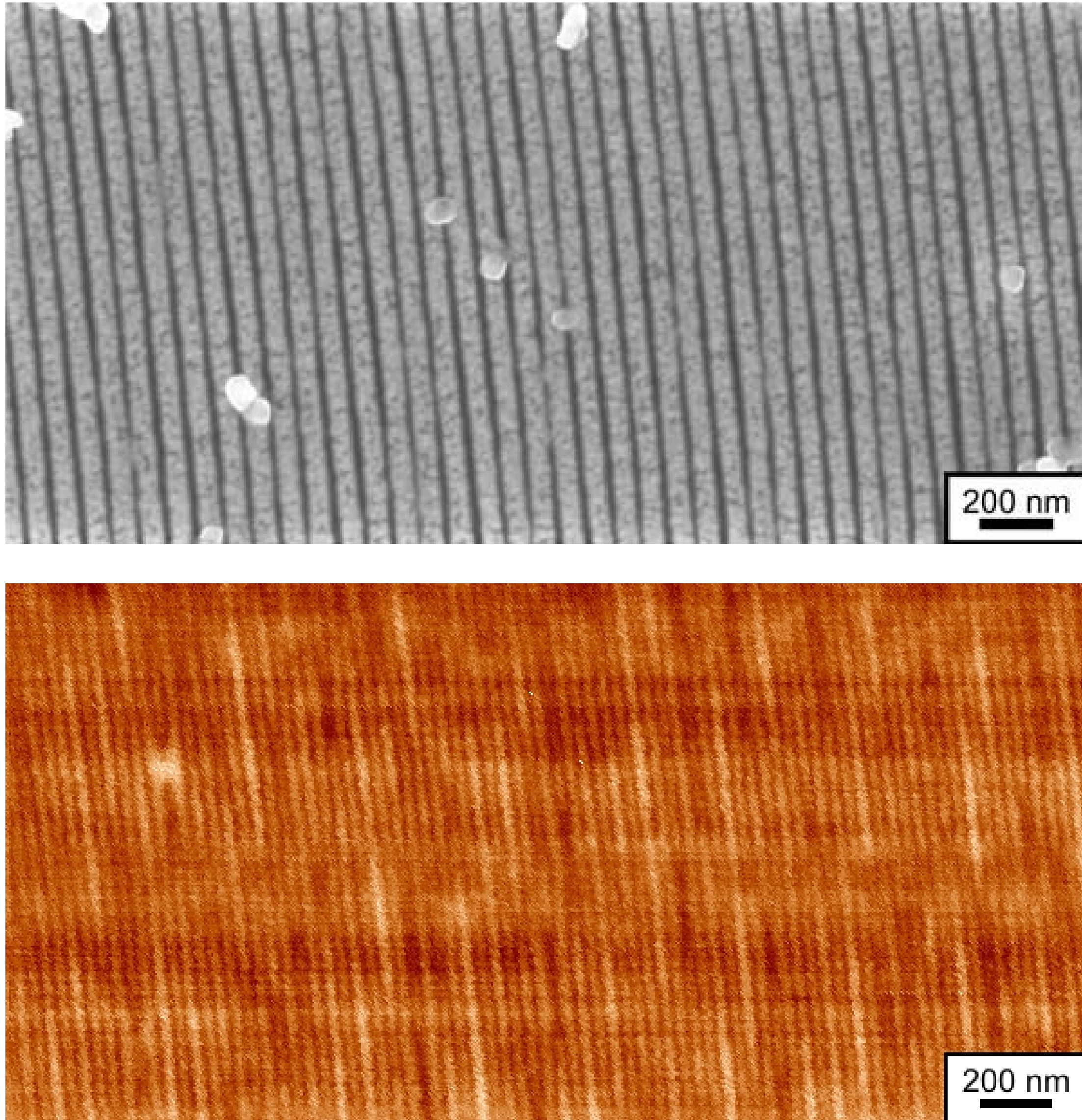

Figure 7.16: Scanning electron microscopy and STXM images of the same region of the iridium-silicon Fresnel zone plate. The STXM image was taken when focusing the incoming beam of 1 keV photon energy using another iridium-silicon Fresnel zone plate with an outermost zone width of 20 nm. The scanning electron microscopy image shows two times larger periodicity (80 nm), as electrons do not penetrate the iridium layer deposited on top of the silicon template lines. However, x-rays photons do penetrate through both the silicon template and the thin iridium layer, revealing the iridium lines deposited onto the sidewalls of the silicon template with 20 nm lines/spacings (40 nm period). The STXM image is composed of 600 $\times$ 300 pixels and was recorded employing a step size of 5 nm and an acquisition time of 20 ms.

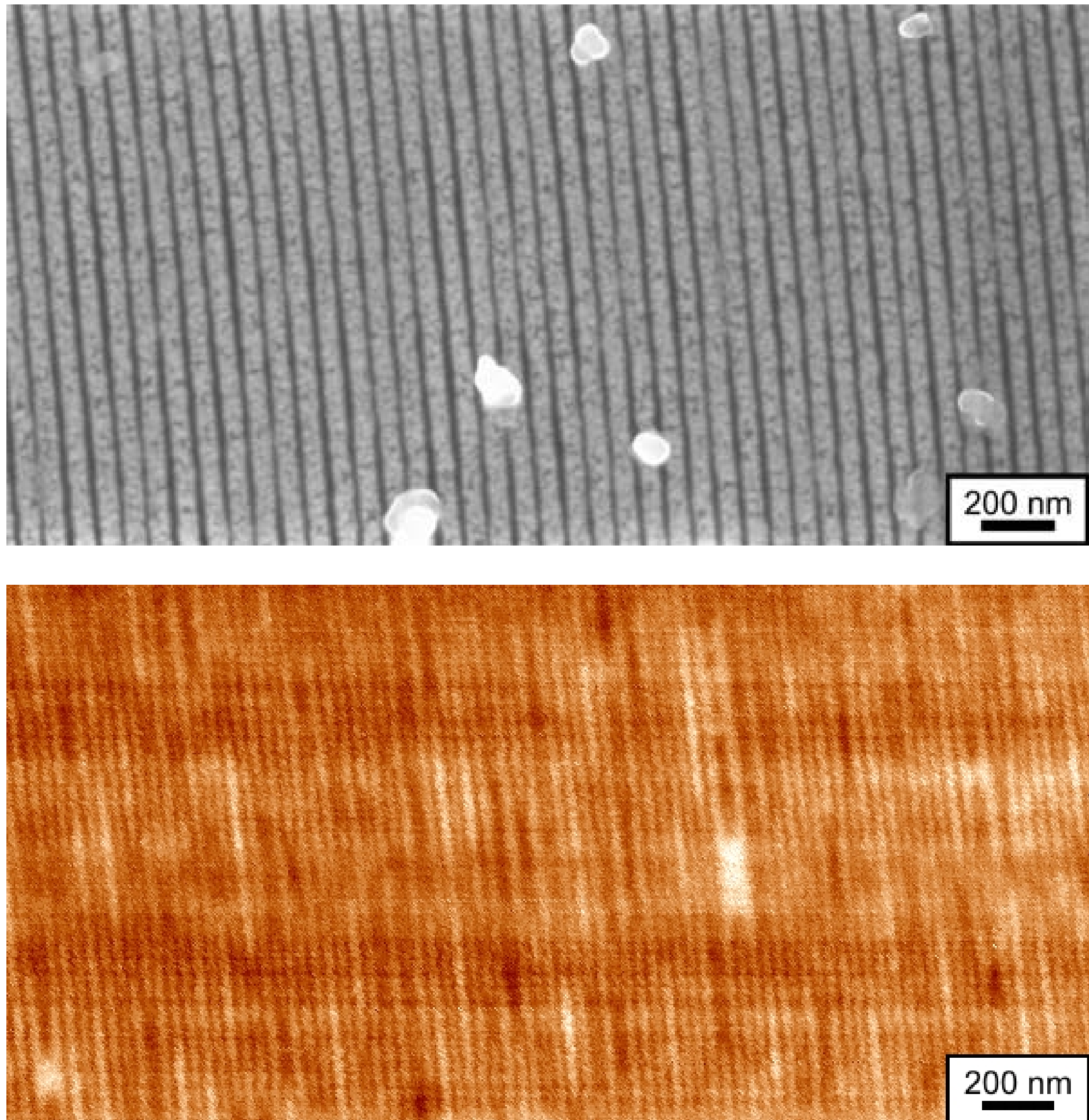

Figure 7.17: Scanning electron microscopy and STXM images of the same region of the iridium-silicon Fresnel zone plate. The STXM image was taken when focusing the incoming beam of 1 keV photon energy using another iridium-silicon Fresnel zone plate with an outermost zone width of 20 nm. The silicon template period is 70 nm so that in this case the iridium structure is made of 17 nm lines/spacings (35 nm period). The STXM image is composed of 600 × 300 pixels and was recorded employing a step size of 5 nm and an acquisition time of 20 ms.

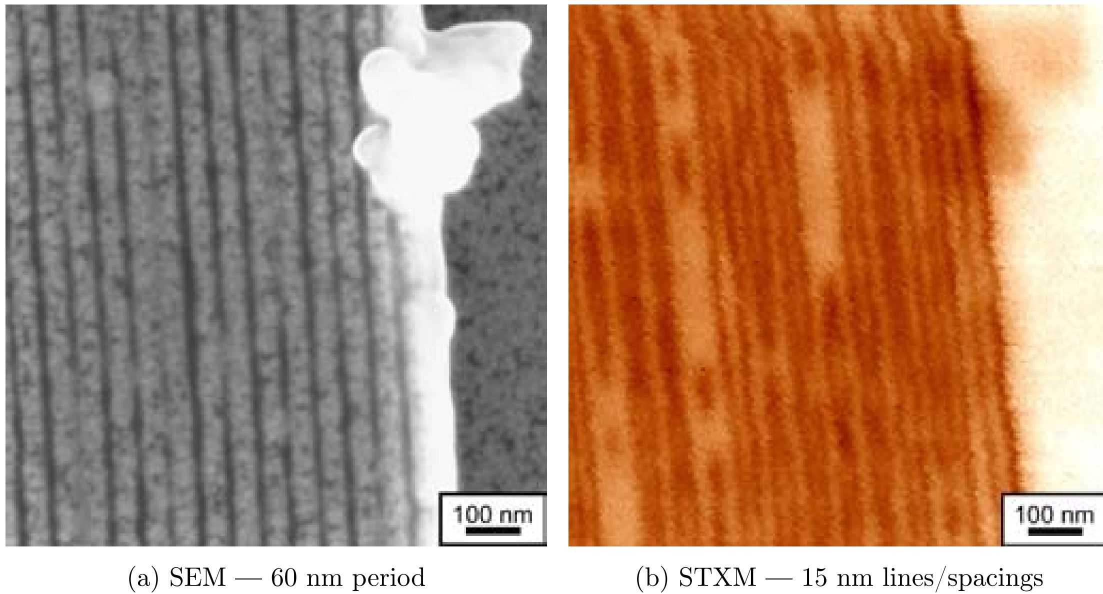

(a) SEM — 60 nm period (b) STXM — 15 nm lines/spacings

Figure 7.18: Scanning electron microscopy and STXM images of the same outermost area of the iridium-silicon Fresnel zone plate. The STXM image was taken when focusing the incoming beam of 1 keV photon energy using an iridium-silicon Fresnel zone plate with an outermost zone width of 20 nm. The silicon template period is 60 nm so that 15 nm lines/spacings (30 nm period) of the iridium structure are resolved. Note that the STXM image allows us to observe the defects on the sample which are not that easily realized in the scanning electron microscopy image. The STXM image is composed of 200 × 200 pixels and was recorded employing a step size of 5 nm and an acquisition time of 20 ms.

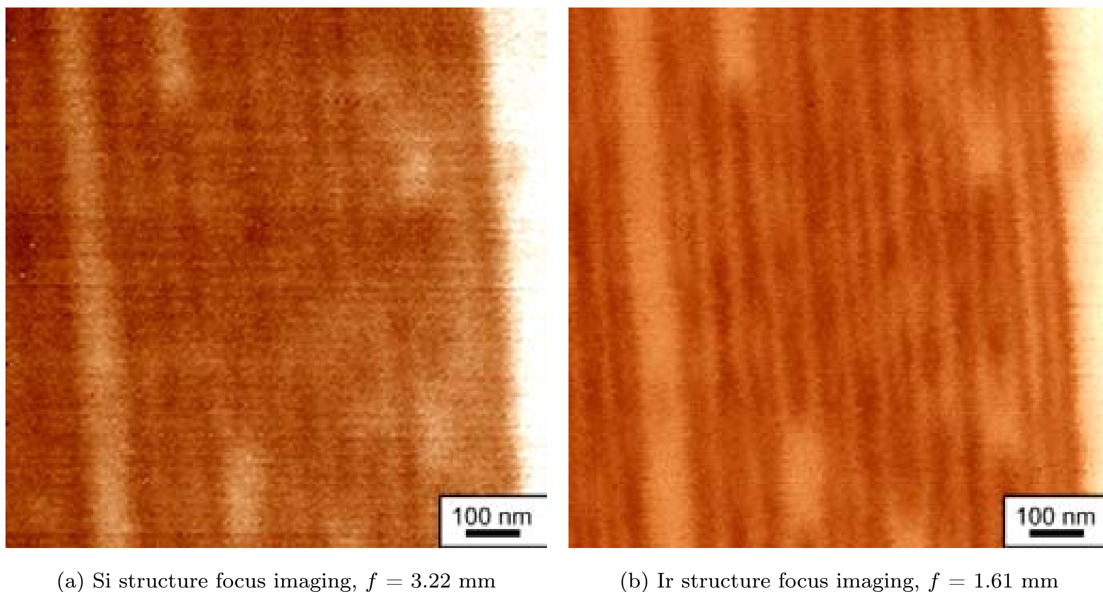

(a) Si structure focus imaging, $f = 3.22$ mm (b) Ir structure focus imaging, $f = 1.61$ mm

Figure 7.19: This figure compares the STXM images of the same region of the iridium-silicon when using the silicon structure focus (a) and the iridium structure focus (b). Whereas a focal spot size of around 40 nm is foreseen for the former one, a size of 20 nm is expected in the latter case. Demonstrating the preceding statement, one can clearly observe that the spatial resolution is much better when imaging with iridium structure focus.

zone plate, a first one corresponding to the iridium pattern and a second corresponding to the silicon template. After recording a STXM image using the focal spot produced for the iridium pattern at a focal distance of 1.61 mm, the sample position was moved to a distance of 3.22 mm where the focal plane corresponding to silicon template should be located. After arranging the focusing, realigning the order selecting aperture, and reducing the size of the entrance slits [6] by a factor 2, a second STXM image was taken. As it can be seen in the images, the spatial resolution that can be achieved by using the silicon template as focusing structure is much worse than the one corresponding to the iridium pattern. This result is in perfect agreement with theoretically expected focal spot sizes, which should be of 40 nm for the silicon template and 20 nm for the iridium pattern. Clearly a focal spot size of 40 nm is too big to resolve 30 nm period structures.

Diffraction efficiency measurements were performed for the 100 μm diameter iridium-silicon Fresnel zone plate with an outermost zone width of 20 nm. The measurements were done following identical steps described at the end of section 6.3.4 and the results are summarized in table 7.2. The total diffraction efficiency, η_t, of the structure was 0.8%, while the groove diffration efficiency, η_g, was 2.7%. This value represents a 35% of the theoretically expected groove diffraction efficiency from our calculations, which is a very feasible result taking into account that ideal structures can never be experimentally manufactured. The silicon thickness of the membrane substrate was around 1.5 μm and we had an additional layer of 20 nm iridium at the backside of the membrane. As for silicon Fresnel zone plate, such a thickness was not a problem during our experiments but it would not be very convenient for daily operation of the microscope. Again, the local etching of the silicon membrane at the backside of the diffractive structure by means of a focused ion beam tool would be a very elegant method to overcome this limitation.

Iridium-Silicon Fresnel Zone Plate Diffraction Efficiency Measurements at a photon energy of 1 keV

Parameter		Value
Total Intensity	I	$2.69 \cdot 10^5$ counts/ms
Diffracted Intensity	I	2200 counts/ms
Membrane Transmitted Intensity	I_t	$8.17 \cdot 10^4$ counts/ms
Membrane Transmission	T_{mem}	0.304
Total Diffraction Efficiency	η_t	0.008
Groove Diffraction Efficiency	η_g	0.027

Table 7.2: Diffraction efficiency measurements for a 100 μm diameter iridium-silicon Fresnel zone plate with an outermost zone width of 20 nm.

[6] Since the focal length of the silicon template is two times longer, the demagnification is decreased by a factor 2. To ensure the same conditions and a diffraction limited focal spot size, the size of the entrance slits must be reduced by a factor 2 as well. The decrease in the photon flux can be overcome by increasing the acquisition time.

Finally, figure 7.20 shows a STXM image of a large area of outermost region of the iridium-silicon Fresnel zone plate. Smallest features, that are perfectly resolved, are made of 15 nm lines/spacings (30 nm period). The image is composed of 1200 $\times$ 800 pixels and it was recorded using a step size of 5 nm and an acquisition time of 20 ms for each pixel. Total time to record the image was around 5 hours 30 minutes. This image is the best example of the potential of the zone-doubling technique for the fabrication of Fresnel zone plate lenses for x-ray radiation.

In summary, we demonstrated a novel fabrication technique based on the zone-doubling through material deposition on a prepatterned template for the manufacturing of Fresnel zone plates. 100 μm diameter iridium-silicon Fresnel zone plates were successfully produced and the STXM experiments demonstrated that ultrahigh spatial resolution are feasible to be achieved by using them as focusing elements.

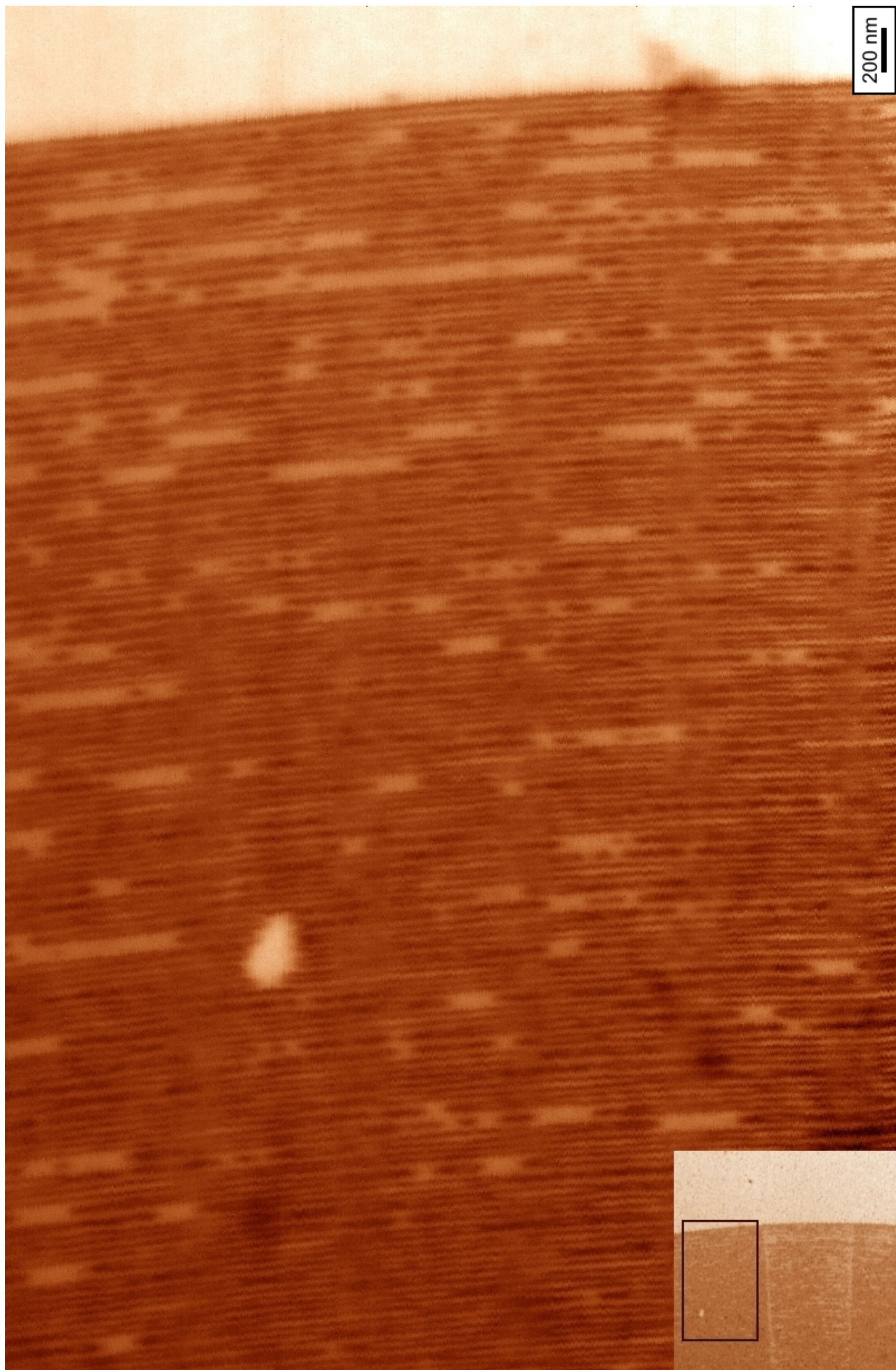

Figure 7.20: STXM image of an iridium-silicon Fresnel zone plate with an outermost zone width of 15 nm, which is used as sample object. A second iridium-silicon Fresnel zone plate with an outermost zone width of 20 nm is used as focusing element at a photon energy of 1 keV. 15 nm lines/spacings (30 nm period) are perfectly resolved. The STXM image is composed of 1200 × 800 pixels with a step size of 5 nm and an acquisition time of 20 ms for each pixel.

Conclusions and Outlook

Nanoscience and nanotechnology in the areas of electronics, magnetism, chemistry, biology and medicine are one of the most active fields in research worldwide since there are well based expectations of the technological breakthroughs derived from their findings. However, nanoscience and nanotechnology require probing tools that match the devices or samples under production or investigation.

Within this context, synchrotron radiation is an excellent instrument to probe matter and extract a lot of information from many samples that could not be under analysis using a conventional low-intensity lab x-ray source. Synchrotron radiation sources generate the most brilliant x-ray beams presently available. Many scientists are using synchrotron radiation as an essential tool in their research in physics, chemistry, biology or material science. In particular, x-ray microscopy has developed as imaging technique with a higher spatial resolution than ordinary light microscopy and providing a high penetrating power and a chemical sensitivity that can not be reached in electron microscopy. One of the essential components in x-ray microscopes are the Fresnel zone plates which are diffractive optical elements that can focus the x-ray radiation. These devices must be produced using microfabrication techniques.

There are only a few research groups all around the world that are actively working in the production of diffractive optical elements for x-ray radiation and Fresnel zone plate lenses are only commercially available at a high cost. In addition, their lifetime in an x-ray microscope in operation is rather short. In-house production of Fresnel zone plates is not always feasible: in one hand, a micro- and nanofabrication laboratory and some knowledge in diffractive optical elements are required; on the other hand, access to a synchrotron light source is necessary to check the performance of the devices.

This thesis is a result of first efforts for the in-house production of diffractive optical elements for x-ray radiation in the ALBA Synchrotron Light Source, which will be operative in 2010. This work was done in collaboration with the *Centro Nacional de Microelectrónica de Barcelona (CSIC - CNM)* and the *Grup d'Òptica del Departament de Física de la Universitat Autònoma de Barcelona*. In addition, an essential part of this work was done in close collaboration with Dr. C. David and Dr. K. Jefimovs from the *Labor für Mikro- und Nanotechnologie* at the *Paul Scherrer Institut* in Villigen (Switzerland).

The Fresnel zone plate structures were generated by combining electron beam lithography and several pattern transfer techniques. Three different approaches were used to produce the

Fresnel zone plate lenses. They were made of nickel, silicon, and combining silicon/iridium structures.

Pattern generation of Fresnel zone plates by electron beam lithography is quite challenging since a dense pattern of lines as thin as possible must be produced, and it becomes one of the main limitations in the production of Fresnel zone plates that provide high spatial resolution.

Within this work, nickel Fresnel zone plate were prepared using the most widespread technology and similar results to those of the experienced research groups were obtained. Despite these structures were not experimentally tested, their manufacture should be considered to provide lenses to the x-ray microscope in ALBA in the future.

We also prepared Fresnel zone plate made from a silicon single crystal. Full-field and scanning transmission x-ray microscopy experiments were performed using optical elements made of silicon demonstrating that these lenses perform well at the current x-ray sources. In the full-field setup a resolution of 60 nm was obtained using a silicon Fresnel zone plate with an outermost zone width of 50 nm. Complementary, images with spatial resolution of 35 nm lines/spacings were obtained in scanning transmission x-ray microscopy using a silicon Fresnel zone plate with an outermost zone width of 30 nm. Due to the robustness of these optical elements we believe that they will be suitable optical devices for the 4th generation of x-ray sources that are based on the Free Electron Laser principle. Using the same technology, we also prepared a diffractive optical element which can be used as condenser lens and that produces a square-flat top illumination. The design is quite simple, since it consists of a big area split in square gratings with a suitable line orientation and period to deviate the first order light into a common focal spot. The feasibility of producing such elements has been shown. During full-field transmission x-ray microscopy experiments the beamshaping condenser lens was successfully used to concentrate the radiation into the sample producing the expected illuminated square area.

In addition, we developed a novel method to produce Fresnel zone plate lenses which provide a higher spatial resolution than conventional lenses. The basic idea in this technique is to cover a prepatterned low refractive index template with a layer of high refractive index material. This method has some advantages since the pattern to be generated by electron beam lithography is much less demanding in terms of feature density. In this project, the collaboration of T. Pilvi and Dr. M. Ritala from the *Laboratory of Inorganic Chemistry* of the *University of Helsinki* was crucial to obtain a uniform layer of iridium on the prepatterned silicon template. A couple of iridium-silicon Fresnel zone plate structures were tested in an x-ray microscopy beamline. In particular, we were able to fabricate silicon/iridium structures with an outermost zone width of 20 nm and during the experiments at the *PolLux Beamline* of the *Swiss Light Source* we were able to resolve 15 nm lines/spaces, which is **the best spatial resolution ever achieved in scanning transmission x-ray microscopy up to date**. This technique is very promising and even better results could be achieved in the near future.

Thus, this work is a good starting point for future manufacture of Fresnel zone plate and other diffractive elements in ALBA synchrotron light source. In addition, we are convinced that other kind of interesting diffractive optical elements can be manufactured and we believe that the zone-doubling technique could be a powerful method to further increase the spatial resolution of the x-ray microscopy experimental stations. There is plenty of room at the bottom, there is plenty of room for improvement.

Acknowledgements

A few weeks ago, I could not even imagine myself writing these lines. If I am doing so, it means that the manuscript is almost ready and that the time has come to thank all the people who have been helping and supporting me during the development of this thesis. Four years of work in three different research institutes and one year stay in Switzerland implies that many people has been contributing to my work. I just hope that nobody will be missing in the following.

First, I want to thank my three supervisors: Salvador, Juan and Xavier. They all have been supporting me during these years (and they all suffered my stubbornness during the correction of the manuscript).

In the Labarotari de Llum Sincrotró I must thank the constant support I received from the other Ph. D. ~~students~~: Felisa, Ferran and Zeus and also the help and advice from Nico, who was always there when a question came up. I also feel very grateful to Ramon, who was always taking care of any computer problem I had and who was eagerly reparing my computer just one week ago avoiding my nervousness to become a panic attack. In addition, I am specially thankful to Enric, who was the only person gently caring about the economical situation of the students in the lab, to Eva, who contributed to the experiments in Elettra, and to Jordi, who was kindly helping with the LaTeX preparation of this manuscript.

From the Centro Nacional de Microelectrónica, I have to thank Francesc Perez-Murano, who always showed interest in the project and Marta Duch and Marta Gerbolés, who were both always working hard to process my samples. I also feel specially grateful to Gemma, who was always there to help me in anything during my training and operation of the electron beam lithography system.

From the Physics Department of the Universitat Autònoma de Barcelona I am grateful to Francesc Pi, who gently prepared the electron beam evaporation of gold and nickel at the very beginning of this work.

Looking 900 kilometers further, I have to thank all the staff from the Labor für Micro- and Nanotechnologie at Paul Scherrer Institut since they make me feel like at

home during my year stay. I am specially grateful for the help and advice that I got from Ana, Anja, Eugen, Dirk, my officemate Christian, Harald, Roger, Bianca, Fredy, Vaida, Harun, Laura, Celestino, Edith, Thomas and Stefan.

From the experiments at the synchrotrons, I am thankful for the patience and advice of Jörg Raabe, Marco Stampanoni and Federica Marone from the Swiss Light Source and of Burkhard Kaulich from Elettra. I am also grateful to the people from the cSAXS group of the Swiss Light Source: Franz, Oliver, Ian, Martin and Andreas since during the meetings I was always getting interesting criticism that helped to improve my work.

Many thanks to Tero Pilvi and Mikko Ritala from Helsinki, which I have not yet met personally but they contribute to an essential part of the presented work with a fast and extremely efficient response.

From the non-scientific environment, I have to thank my parents and all my friends which have been always supporting me. Specially to my friends in Barcelona: Nuria, Elisabet, Delfí, Marga, Marc, Laia, Marissa, Josep Rafel, Raquel, Roger, Imma, Dani and Silvia and to my friends in Switzerland: Mir, Dirk, Camille, Stefan, Maxi, Vera, Christian (2), Fátima, Elena, Shanka and Liz.

Last but not least I feel specially thankful to Christian David and Konstantins Jefimovs from the Paul Scherrer Institut. To Christian I must thank his patience, confidence and constant advice during my year stay. And to Konstantins I feel specially grateful for all the advice that I received when I was working with him in the lab, for his patience and to carefully listen to all my demands.

To all of you I must just say once again:

Thank You Very Much!!!!!

Danke Schön!!!!! Огромное Спасибо!!!!! Merci Beaucoup!!!!!

Munches Gracies!!!!! Grazie Tante!!!!! Kiitoksia Oikein Paljon!!!!!

Labai Aciu!!!!! Muchas Gracias!!!!!

Moltes Gràcies!!!!!

Joan Vilà Comamala
Barcelona
3rd December 2007

Bibliography

[1] M. H. B. Stowell, A. Miyazawa, N. Unwin. *Macromolecular structure determination by electron microscopy: new advances and recent results*, Curr. Opin. Struct. Biol. **8** (1998) 595-600

[2] B. F. McEwen, M. Marko. *The emergence of electron tomography as an important tool for investigating cellular ultrastructure*, J. Histochem. Cytochem. **49** (2001) 553-563

[3] J. L. Finney. *The complementary use of x-ray and neutron diffraction in the study of crystals*, Acta Crystallogr. B **51** (2004) 447-467

[4] A. Gutiérrez, J. A. Martín-Galgo, S. Ferrer. *La luz sincrotrón: una herramienta extraordinaria para la ciencia*, Apuntes de Ciencia y Tecnología **12** (2004) 37-46

[5] J. R. Helliwell. *Overview and new developments in softer x-ray* (2 Å$< \lambda <$ 5 Å) *protein crystallography*, J. Synchrotron Radiat. **11** (2004) 1-3

[6] J. R. Helliwell. *Synchrotron radiation and crystrallography: the first 50 years*, Acta Crystallogr. A **54** (1998) 738-749

[7] H. Schenk, R. Peschar. *Understanding the structure of chocolate*, Radiat. Phys. Chem. **71** (2004) 829-835

[8] C. Jacobsen. *Soft x-ray microscopy*, Trends Cell Biol. **9** (1999) 44-47

[9] P. Coppens, B. Iversen, F. K. Larsen. *The use of synchrotron radiation in x-ray charge density analysis of coordination complexes*, Coordin. Chem. Rev. **249** (2005) 179-195

[10] G. H. Lander. *Studies of magnetism with synchrotron X-rays*, J. Alloy. Compd. **250** (1997) 544-551

[11] E. Dooryheé, P. Marinetto, P. Walter, M. Anne. *Synchrotron X-ray analyses in art and archaeology*, Radiat. Phys. Chem. **71** (2004) 863-868

[12] J. Als-Nielsen, D. McMorrow. *Elements of modern x-ray physics*, John Wiley & Sons Ltd. *Chichester* (2001)

[13] H. Winick. *Synchrotron radiation - Present capabilities and future directions*, J. Synchrotron Radiat. **5** (1998) 168-175

[14] I. Vartanyants, I. Robinson, I. McNulty, C. David, P. Wochner, T. Tschentscher. *Coherent x-ray scattering and lensless imaging at the european XFEL facility*, J. Synchrotron Radiat. **14** (2007) 453-470

[15] P. Kirkpatrick, A. V. Baez. *Formation of optical images by x-rays*, J. Opt. Soc. Am. A **38** (1948) 766-774

[16] D. Sayre, H. N. Chapman. *X-ray microscopy*, Acta Crystallogr. A **51** (1995) 237-252

[17] J. F. Adam, J. P. Moy, J. Susini. *Table-top water window transmission x-ray microscopy: Review of the key issues, and conceptual design of an instrument for biology*, Rev. Sci. Instrum. **76** (2005) 091301

[18] W. Meyer-Ilse, D. Hamamoto, A. Nair, S. A. Lelievre, G. Denbeaux, L. Johnson, A. L. Pearson, D. Yager, M. A. Legros, C. A. Larabell. *High resolution protein localization using soft x-ray microscopy*, J. Microsc. **201** (2001) 395-403

[19] W. Yun, S. T. Pratt, R. M. Miller, Z. Cai, D. B. Hunter, A. G. Jarstfer, K. M. Kemner, B. Lai, H. R. Lee, D. G. Legnini, W. Rodriguesa, C. I. Smith. *X-ray imaging and microspectroscopy of plants and fungi*, J. Synchrotron Radiat. **11** (1998) 1390-1395

[20] H. R. Beguiristain, I. S. Anderson, C. D. Dewhurst, M. A. Piestrup, J. T. Cremer, R. H. Pantell. *A simple neutron microscope using a compound refractive lens*, Appl. Phys. Lett. **81** 4290-4292

[21] J. Miao, P. Charalambous, J. Kirz, D. Sayre. *Extending the methodology of x-ray crystallography to allow imaging of micrometre-sized non-crystalline specimens*, Nature **400** (1999) 342-344

[22] H. M. L. Faulkner, J. M. Rodenburg. *Movable aperture lensless transmission microscopy: a novel phase retieval algorithm*, Phys. Rev. Lett. **93** (2004) 023903

[23] J. M. Rodenburg, A. C. Hurst, A. G. Cullis, B. R. Dobson, F. Pfeiffer, O. Bunk, C. David, K. Jefimovs, I. Johnson. *Hard x-ray lensless imaging of extended objects*, Phys. Rev. Lett. **98** (2007) 034801

[24] G. J. Williams, H. M. Quiney, B. B. Dhal, C. Q. Tran, K. A. Nugent, A. G. Peele, D. Paterson, M. D. de Jonge. *Fresnel Coherent Diffractive Imaging*, Phys. Rev. Lett. **97** (2006) 025506

[25] M. Muñoz, D. Einfield. CELLS Internal Report (2005)

[26] E. Pereiro, M. Hollews, S. Ferrer. *Conceptual Design Report of the MISTRAL beamline (up to monochromatic exit slit) in ALBA Synchrotron Radiation Facility*, CELLS Internal Report (2007)

[27] B. Ziaie, A. Baldi, M. Z. Atashbar. *Chapter 5. Introduction to micro / nanofabrication*, Springer Handbook of Nanotechnology, edited by: B. Bhushan. Springer - Verlag. *Würzburg* (2004)

[28] D. Attwood. *Soft X-rays and Extreme Ultraviolet Radiation*, Cambridge University Press. *Cambridge* (1999)

[29] W. R. Leo. *Techniques for Nuclear and Particle Physics Experiments*, Springer - Verlag. *Berlin* (1994)

[30] C. T. Chantler. *Detailed Tabulation of Atomic Form Factors, Photoelectric Absorption and Scattering Cross Section, and Mass Attenuation Coefficients in the Vicinity of Absorption Edges in the Soft X-Ray (Z=30–36, Z=60–89, E=0.1 keV–10 keV), Addressing Convergence Issues of Earlier Work*, J. Phys. Chem. Ref. Data **29** (2000) 597-1048

[31] A. Thompson *et al. X-ray Data Booklet*, Center for X-ray Optics, *Lawrence Livermove National Laboratory* (2001)

[32] Center for X-ray Optics, Berkeley Lab, *http://www.cxro.lbl.gov/*

[33] J. Kirz, C. Jacosen, M. Howells. *Soft x-ray microscopes and their biological application*, Q. Rev. Biophys. **28** (1995) 33-130

[34] A. G. Michette. *X-ray Microscopy*, Rep. Prog. Phys. **51** (1988) 1525-1606

[35] O. Hignette, P. Cloetens, G. Rostaing, P. Bernard, C. Morawe. *Efficient sub 100 nm focusing of hard x-rays*, Rev. Sci. Instrum. **76** (2005) 063709

[36] K. Yamauchi, H. Mimura, S. Matsuyama, H. Yumoto, S. Handa, K. Yamamura, Y. Sano, K. Endo, Y. Mori, Y. Nishino, K. Tamasaku, M. Yabashi, T. Ishikawa. *Hard x-ray focusing less than 50 nm for nanoscopy/spectroscopy*, AIP Conference Proceedings **879** (2007) 786-791

[37] O. Hignette, P. Cloetens, C. Morawe, C. Borel, W. Ludwig, P. Bernard, A. Rommenveaux, S. Bohic. *Nanofocusing at ESRF using multilayer mirrors*, AIP Conference Proceedings **879** (2007) 792-795

[38] N. Schell, F. Eichhorn, A. Bjeoumikhov, H. Prinz, C. Ollinger. *Parabolic Capillary Optics with less than 50 μm focus and large focal distance for synchrotron radiation scattering*, AIP Conference Proceedings **879** (2007) 975-980

[39] R. Huang, D. H. Bilderback. *Single-bounce monocapillaries for focusing synchrotron radiation: modeling, measurements and theorecial limits*, J. Synchrotron Radiat. **13** (2006) 74-84

[40] F. A. Hofmann, C. A. Freinber-Trufas, S. M. Owens, S. D. Padiyar, C. A. MacDonald. *Focusing of synchrotron radiation with polycapillary optics*, Nucl. Instrs. and Meth. B **133** (1997) 145-150

[41] D. H. Bilderback, A. Kazimirov, R. Gillilan, S. Cornaby, A. Woll, C. S. Zha, R. Huang. *Optimizing monocapillary optics for synchrotron x-ray diffraction, fluorescence imaging, and spectroscopy applications*, AIP Conference Proceedings **879** (2007) 758-763

[42] F. Pfeiffer, C. David, M. Burghammer, C. Riekel, T. Salditt. *Two-dimensional x-ray waveguides and point sources*, Science **297** (2002) 230-234

[43] A. Jarre, C. Fuhse, C. Ollinger, J. Seeger, R. Tucoulou, T. Salditt. *Two-dimensional hard X-ray beam compression by combined focusing and waveguide optics*, Phys. Rev. Lett. **94** (2005) 074801

[44] C. David, T. Weitkamp, B. Nöhammer, J. F. van der Veen. *Diffractive and refractive x-ray optics for microanalysis applications*, Spectr. Acta A **61** (2006) 1505-1510

[45] B. Lengeler, C. Schroer, J. Tümmler, B. Benner, M. Richwin, A. Snigirev, I. Snigireva, M. Drakopoulos. *Imaging by parabolic refractive lenses in the hard x-ray range*, J. Synchrotron Radiat. **6** (1999) 1153-1167

[46] V. Nazmov, E. Rezkinova, A. Last, J. Mohr, V. Saile, R. Simon, M. DiMichiel. X-ray lenses fabricated by LIGA technology, AIP Conference Proceedings **879** (2007) 770-773

[47] J. P. Lee, G. B. Kim, J. H. Kim, S. S. Chang, S. J. Lee. *Fabrication of compound refractive x-ray lenses using LIGA process and performance tests*, AIP Conference Proceedings **879** (2007) 981-984

[48] A. Holmberg, M. Lindblom, S. Rehbein, H. M. Hertz. *Nickel Zone Plates for Compact Soft X-Ray Microscopy*, IPAP Conf. Series **7** (2006) 124-126

[49] K. Jefimovs, O. Bunk, F. Pfeiffer, D. Grolimund, J. F. van der Veen, C. David. *Fabrication of Fresnel zone plates for hard X-rays*, Microelectron. Eng. **84** (2007) 1467–1470

[50] C. David, A. Souvorov. *High-efficiency Bragg-Fresnel lenses with 100 nm outermost zone with*, Rev. Sci. Instrum. **64** (1999) 4168-4173

[51] G. Schmahl, D. Rudolph, P. Guttmann, G. Schneider, J. Thieme, B. Niemann. *Phase contrast studies of biological specimens with the x-ray microscope at BESSY*, Rev. Sci. Instrum. **66** (1995) 1282-1286

[52] U. Vogt, M. Lindblom, P. A. C. Jansson, T. T. Tuohimaa, A. Holmberg, H. M. Hertz, M. Wieland, T. Wilhein. *Towards soft x-ray phase-sensitive imaging with diffractive optical elements*, IPAP Conf. Series **7** (2006) 91-93

[53] W. Chao, B. D. Harteneck, J. A. Liddle, E. H. Anderson, D. T. Attwood. *Soft X-ray microscopy at a spatial resolution better than 15 nm*, Nature **435** (2005) 1210-1213.

[54] E. Di Fabrizio, S. Cabrini, D. Cojoc, F. Romanato, L. Businaro, M. Altissimo, B. Kaulich, T. Wilhein, J. Susini, M. De Vittorio, E. Vitale, G. Gigli, R. Cingolani. *Shaping x-rays by diffractive coded nano-optics*, Microelectron. Eng. **67-68** (2003) 87–95

[55] O. Carnal, M. Sigel, T. Sleator, H. Takuma, J. Mlynek. *Imaging and focusing of atoms by a Fresnel Zone Plate*, Phys. Rev. Lett. **67** (1991) 3231-3234

[56] P. D. Kearney, A. G. Klein, G. I. Opat, R. Gähler. *Imaging and focusing of neutrons by a zone plate*, Nature **287** (1980) 313-314

[57] J. Kirz. *Phase zone plates for x-rays and extreme UV*, J. Opt. Soc. Am. **64** (1974) 301-309

[58] F. Pfeiffer, C. David, J. F. van der Veen, C. Bergemann. *Nanometer focusing properties of Fresnel zone plates described by dynamical diffraction theory*, Phys. Rev. B **73** (2006) 245331

[59] C. Bergemann, H. Keymeulen, J. F. van der Veen. *Focusing x-ray beams to nanometer dimensions*, Phys. Rev. Lett. **91** (2003) 204801

[60] E. Di Fabrizio, D. Cojoc, S. Cabrini, B. Kaulich, J. Susini, P. Facci, T. Wilhein. *Diffractive optical elements for differential interference contrast x-ray microscopy*, Opt. Express **11** (2003) 2278-2288

[61] E. Di Fabrizio, D. Cojoc, S. Cabrini, M. Altissimo, B. Kaulich, T. Wilhein, J. Susini, O. Dhez. *Phase and intensity control through diffractive optical elements in x-ray microscopy*, J. Electron Spectrosc. Relat. Phenom. **144-147** (2005) 957-961

[62] A. A. Firsov, A. A. Svintsov, S. I. Zaitsev, A. Erko, V. V. Aristov. *The first synthetic x-ray hologram: results*, Opt. Commun. **202** (2002) 55-59

[63] H. H. Solak, C. David, J. Gobrecht. *Fabrication of high resolution zone plates with wideband extreme ultraviolet holography*, Appl. Phys. Lett. **85** (2004) 2700-2702

[64] M. Born, E. Wolf. *Principles of Optics, 7th Edition*, Cambridge University Press, (1999) 595

[65] E. H. Anderson, D. L. Olynick, B. Harteneck, E. Veklwrov, G. Denbenaux, W. L. Chao, A. Lucero, D. Attwood. *Nanofabrication and diffractive optics for high-resolution x-ray applications*, J. Vac. Sci. Technol. B **18** (2000) 2970-2975

[66] G. C. Yin, T. M. Tang, F. R. Chen, K. S. Liang, F. W. Duewer, M. Feser, H. P. D. Shieh. *Energy-tunable transmission x-ray microscope for differential contrast imaging with near 60 nm resolution tomography*, Appl. Phys. Lett. **88** (2006) 241115

[67] C. Rau, V. Crecea, K. M. Peterson, P. R. Jemian, C. P. Richter, U. Neuhäusler, G. Schneider, X. Yu, P. V. Braun , I. K. Robinson. *A Full-Field KB-FZP microscope for hard x-ray imaging with sub-100 nm resolution*, IPAP Conf. Series **7** (2006) 7-8

[68] B. Niemann, P. Guttmann, S. Rehbein, C. Knöchel. *Concept an realization of the novel rotating condenser-monochromator at the Göttingen TXM at BESSY II*, J. Phys. IV **104** (2003) 273-276

[69] U. Vogt, M. Lindblom, P. Charalambous, B. Kaulich, T. Wilhein. *Condenser for Koehler-like illumination in transmission x-ray microscopes at undulator sources*, Opt. Lett. **31** (2006) 1465-1467

[70] Y. Arntz, J. D. Seelig, H. P. Lang, J. Zhang, P. Hunziker, J. P. Ramseyer, E. Meyer, M. Hegner, Ch. Gerber. *Label-free protein assay based on a nanomechanical cantilever array*, Nanotechnology **14** (2003) 86-90

[71] S. Yasin, D. G. Hasko, F. Carecenac. *Nanolithography using ultrasonically assited development of calixarene negative electron beam resist*, J. Vac. Sci. Technol. B **19** (2001) 311-313

[72] Y. Ekinci, H. H. Solak, C. Padeste, J. Gobrecht, M. P. Stoykovich, P. F. Nealey. *20 nm Line/space patterns in HSQ by EUV interference lithography*, Microelectron. Eng. **84** (2007) 700–704

[73] V. Auzelyte, M. Elfman, P. Kristiansson, C. Nilsson, J. Pallon, N. Arteaga Marrero, M. Wegdén. *Exposure parameters for MeV proton beam writing on SU-8*, Microelectron. Eng. **83** (2006) 2015–2020

[74] P. P. Ilinski, B. Lai, N. J. Bassom, J. Donald, G. Athas. *X-ray zone plate fabrication using focused ion beam*, Proceedings of SPIE Vol. **4145** (2001) 311-315

[75] M. A. McCord, M. J. Rooks. *Chapter 2: electron beam lithography*, Hanbook of Microlithography, Micromachining and Microfabrication, Volume **1**: Microlithography, Ed. P. Ray-Choudhury, SPIE Publications (1997)

[76] G. Rius Suñé. *Fabricació d'estructures nanoelectromecàniques amb litografia per feix d'electrons*, Master Thesis at the Universitat Autonòma de Barcelona (2005)

[77] K. Jefimovs. *Fabrication of surface relief diffractive optical elements and their applications*, Ph. D. Thesis at the Faculty of Science of the University of Joensuu (2003)

[78] B. Nöhammer. *Diffractive and refractive lenses for hard x-rays with ultra-high efficiencies*, Ph. D. Thesis at the Faculty of Science of the University of Neuchâtel (2004)

[79] J. Fujita, Y. Ohnishi, Y. Ochiai, E. Nomura, S. Matsui. *Nanometer-scale resolution of calixarene negative resist in electron beam lithography*, J. Vac. Sci. Technol. B **14** (1996) 4272-4276

[80] WolframMathWorld, Bézier Curve *http://mathworld.wolfram.com/BezierCurve.html*

[81] C. David, D. Hambach. *Line width control using a defocused low voltage electron beam*, Microelectron. Eng. **46** (1999) 219-222.

[82] M. Peuker. *High-efficiency nickel zone plates with 20 nm minimum outermost zone width*, Appl. Phys. Lett. **78** (2001) 2208-2210

[83] The European X-Ray Laser Project XFEL, Hamburg (Germany), *http://xfel.desy.de/*

[84] The BESSY Soft X-ray Free Electron Laser, Berlin (Germany), *http://www.bessy.de/front_ content.php?idcat=31*

[85] FERMI@Elettra, Trieste (Italy), *http://www.elettra.trieste.it/FERMI/*

[86] Low Emittance Gun - PSI Free Electron Laser Project, Villigen (Switzerland), *http://fel.web.psi.ch/*

[87] Linac Coherent Light Source, Stanford (USA), *http://www-ssrl.slac.stanford.edu/lcls/index.html*

[88] T. Weitkamp, B. Kaulich, O. Dhez, C. David. *First tantalum zone plates for the TWINMIC x-ray microscope project*, Microelectron. Eng. **73-74** (2004) 651-655.

[89] C. David, E. Ziegler, B. Nöhammer. *Wet-etched diffractive lenses for hard x-rays*, J. Synchrotron Radiat. **8** (2001) 1054-1055

[90] I. Snigireva, A. Snigirev, G. Vaughan, M. Di Michiel, V. Kohn, V. Yunkin, M. Grigoriev. *Stacked Fresnel Zone Plates for High Energy X-rays*, AIP Conference Proceedings **879** (2007) 998-1001

[91] B. Nöhammer, J. Hoszowska, A. K. Freund, C. David. *Diamond planar refractive lenses for third- and fourth-generation X-ray sources*, J. Synchrotron Radiat. **10** (2003) 168-171

[92] E. Bassous, A. C. Lamberti. *Highly selective KOH-based etchant for Boron-doped silicon structures*, Microelectron. Eng. **9** (1989) 167-170.

[93] H. Jansen, H. Gardeniers, M. de Boer, M. Elwenspoek, J. Fluitman. *A survey on the reactive ion etching of silicon in microtechnology*, J. Micromech. Microeng. **6** (1996) 14–28.

[94] R. Legtenberg, H. Jansen, M. de Boer, M. Elwenspoek. *Anisotropic reactive ion etching of silicon using $SF_6/O_2/CHF_3$ gas mixtures*, J. Electrochem. Soc. 142 (1995) 2020-2028

[95] B. Kaulich, D. Bacescu, J. Susini, C. David, E. Di Fabrizio, G. R. Morrison, P. Charalambous, J. Thieme, T. Wilhein, J. Kovac, D. Cocco, M. Salome, O. Dhez, T. Weitkamp, S. Cabrini, D. Cojoc, A. Gianoncelli, U. Vogt, M. Podnar, M. Zangrando, M. Zacchigna, M. Kiskinova. *TwinMic - A European Twin X-ray Microscopy Station Commissioned at ELETTRA*, IPAP Conf. Series **7** (2006) 22-25

[96] M. Zangrando, M. Finazzi, M. Zacchigna, E. Di Fabrizio, D. Cocco, R. Rochow-Carbone, M. Kiskinova, B. Kaulich, R. H. Menk, F. Parmigiani. *Multipurpose experimental station for soft x-ray microscopy on BACH beamline at Elettra*, Proceedings of SPIE Vol. **4506** (2001) 154-162

[97] U. Flechsig, C. Quitmann, J. Raabe, M. Böge, R. Fink, and H. Ade. *The PolLux microspectroscopy beamline at the Swiss Light Source*, AIP Conf. Proc. **879** (2007) 505-508 .

[98] D. C. Flanders, N. N. Efremow. *Generation of $<$ 50 nm period gratings using edge defined techniques*, J. Vac. Sci. Technol. B **1** (1983) 1105-1108

[99] C. David, J. Bruder, T. Rohbeck, C. Grünzweig, C. Kottler, A. Diaz, O. Bunk, F. Pfeiffer. *Fabrication of diffraction gratings for hard x-ray phase contrast imaging*, Microelectron. Eng. **84** (2007) 1172-1177

[100] M. Leskelä, M. Ritala. *Atomic layer deposition chemistry: recent developments and future challenges*, Angew. Chem. Int. Ed. **42** (2003) 5548-5554

[101] T. Aaltonen, M. Ritala, V. Sammelselg, M. Leskelä. *Atomic layer deposition of iridium thin films*, J. Electrochem. Soc. **151** (2004) G489-G492

Publications Related to this Thesis

[102] J. Vila-Comamala, X. Borrisé, F. Pérez-Murano, J. Campos, S. Ferrer. *Nanofabrication of Fresnel zone plate lenses for x-ray optics*, Microelectron. Eng. **83** (2006) 1355–1359

[103] J. Vila-Comamala, K. Jefimovs, J. Raabe, B. Kaulich, C. David. *Silicon Fresnel zone plates for high heat load x-ray microscopy*, accepted to Microelectron. Eng. (2007)

[104] K. Jefimovs, J. Vila-Comamala, M. Stampanoni, B. Kaulich, C. David. *Beam-shaping condenser lens for full-field transmission x-ray microscopy*, J. Synchrotron Radiat. **15** (2008) 106-108

[105] K. Jefimovs, J. Vila-Comamala, T. Pilvi, J. Raabe, M. Ritala, C. David. *Zone-doubling technique to produce ultrahigh-resolution x-ray optics*, Phys. Rev. Lett. **99** (2007) 264801

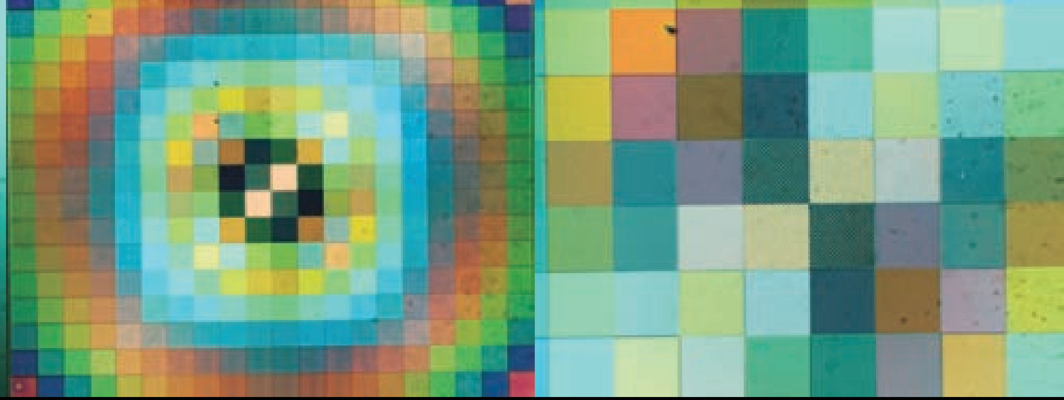

1µm
Mag = 50.52 K X
WD = 4 mm
EHT = 5.00 kV
Stage at T = 10.0 °
Signal A = InLens
Aperture Size = 20.00 µm
Date :30 Oct 2006
Time :18:56:10